Appendix G

Cap Erosion and Flood Modeling

TECHNICAL MEMORANDUM

HYDRODYNAMIC AND SEDIMENT TRANSPORT EVALUATION: CAPPING/ARMORING ANALYSES OF THE LOWER PASSAIC RIVER

June 8, 2007
MPIN0021

HydroQual
Environmental
Engineers & Scientists

CONTENTS

Section Page

ATTACHMENT A	SEDZLJ Incorporation into ECOMSEDZLJ
ATTACHMENT B	Bed Elevation Changes, Maximum Erosion and Bottom Shear Stresses for Ambrose Sand Cap
ATTACHMENT C	Bed Elevation Changes, Maximum Erosion and Bottom Shear Stresses for Upland Borrow Sand Cap
ATTACHMENT D	Bed Elevation Changes, Maximum Erosion and Bottom Shear Stresses Under Different Depth and Capping/Armoring Scenarios

FIGURES

TABLES

SECTION 1

INTRODUCTION

As part of the Lower Passaic River (LPR) Restoration Project, a study of the tidal 17 miles of the river, the USEPA is evaluating early remediation of the contaminated sediment deposited in the lower eight miles of the river. The Focused Feasibility Study (FFS) calls for consideration of several alternative capping/dredging options in the first 8.3 miles of the LPR. They include capping and armoring using 2-4 ft of sand and/or rock between River Mile (RM) 0 and 8.3. This study has two main objectives:

- To provide an evaluation of the stability of the proposed sand cap and to identify those areas where erosion of the sand cap is likely, so that the sand cap can be stabilized with a layer of rock cobble armor; and
- Determine changes in water elevation along the length of the LPR that would occur under high flow and/or storm surge events that, in conjunction with the capping and armouring, may result in additional flooding of the low lying areas along the LPR.

Several extreme flow conditions were considered, including 100- and 500-year flows. Flooding due to 100-and 500-year storm surges was also considered in the study.

The hydrodynamic model used in this study is an extension of the model being developed for the lower 17 mile Passaic River and the Newark Bay remedial investigation (RI)/feasibility study (FS). The details of the model setup and calibration have been reported previously (HydroQual, 2007). The major extension of the LPR and Newark Bay hydrodynamic model used in this analysis was to expand the model grid to include the 500-year flood plain as determined by the Federal Emergency Management Administration (FEMA).

The sediment transport model used in this study is known as SEDZLJ (Jones and Lick, 2001). For the purposes of this study SEDZLJ was incorporated into HydroQual's hydrodynamic modeling code, ECOM, and the resulting modeling code is known as ECOMSEDZLJ.

As mentioned above, the hydrodynamic model being developed for the LPR and Newark Bay RI/FS was extended to include the 500-year flood plain. The first step, after extending the model grid, was to demonstrate the applicability of the model by calibrating the model against available field data. The model was also validated by application of the model to Hurricane Donna, which occurred in 1960. In addition, model estimates of the spatial extent of flooding, as forced by FEMA estimates of the 500-year flow and storm surge, were compared against the FEMA 500-year flood plain.

The resulting hydrodynamic model was then applied, together with the sediment transport model, SEDZLJ, to evaluate cap stability of two different classes of sand; one from the Ambrose Channel of New York/New Jersey Harbor and one available from upland sources. The results of the sediment transport model were used to identify areas with unacceptable rates of sand cap erosion. These areas would then be pre-dredged to a depth of 2-ft, capped with 2-ft of sand, and armored with 2-ft of rock cobble.

After the sand cap/rock armor analysis was completed, the hydrodynamic model was utilized again to investigate the impact that the cap/armor would have on flooding of low lying areas in the LPR under different conditions of high river flow from the LPR and storm surge from New York/New Jersey Harbor and the New York Bight Apex. It should be noted that the effects of future sea-level rise on potential flooding have not been considered in this analysis.

SECTION 2

HYDRODYNAMIC MODEL CONFIGURATION

In order to address the potential flooding issues in the LPR basin resulting from placement of a cap, the FEMA's 500-year flood area map was obtained (Figure 2-1). The source of the data set is Q3 Flood Data derived from the Flood Insurance Rate Maps published by FEMA (1996). Figure 2-1 indicates that the 100- and 500-year flood plain area in the LPR basin is confined to a fairly nar row area along both sides of the river for most of the length of the LPR; however, near the mouth of the Passaic River and in the Hackensack basin the flood-area is wide and covers much of the low lying marshes and tidal creeks in the Meadowlands.

The model grid developed for the study is shown in Figure 2-2. Also shown on the plot are land surface elevations relative to the National Geodetic Vertical Datum (NGVD) 1929. The elevations were deduced from land survey data compiled by the US Army Corps of Engineers (USACE) in 1990 as a part of the USACE's Passaic River Flood Control Project (Figure 2-3). The survey maps consist of 2 ft interval contours of the land elevations in the study area. The survey data in lower sections of the river, up to RM 5, were available in electronic data format. However, in the upstream sections of the river, only paper copies of the survey maps were available. Land elevation contours were digitized for this study in those sections within the FEMA 500-year flood areas. These detailed land survey maps helped configure the hydrodynamic model to be used in the flood analysis portion of this study. Figure 2-4 shows an example of the USACE survey map at the Riverside County Park of Lyndhurst near RM 11. The figure shows both the aerial photography of the area as well as the digitized land elevation contours. The lower panel of Figure 2-4 depicts the vertical profile on both sides of the river following the transect (A-A') shown in the upper panel of Figure 2-4.

Model depths of the river proper were estimated from surveys compiled by the USACE. The Passaic River surveys were conducted in 2004 and Hackensack River data were collected in the mid-1990s. The model also accounts for wetting and drying of appropriate grid cells based on bathymetric and tidal conditions so there are a few grid cells in the Passaic River where grid cells can become exposed during low tides. Bottom sediment texture data collected in the LPR were reviewed (Aqua Survey, 2006) during the grid design effort in order to reflect proper representation of the bottom properties. Bottom texture data show that, in upper section of the LPR, below the Dundee Dam and upstream of RM 8, there are significant portions of the river that consist of coarse gravel and rock material. Figure 2-5 shows the extent of the coarse bottom in the LPR. The unshaded areas in the figure indicate fine grained material such as silt and fine sands. Bottom drag coefficients of the upstream sections containing rock and gravel were scaled up to 0.1 (unitless) and the rest of the silt and fine grained sand bottom areas were specified with a baseline coefficient of 0.0025.

The computational model consists of 68×170 grid cells in the horizontal plane and 11 equally spaced σ-levels in the vertical plane (*i.e.*, 10 vertical segments). The model open boundaries are located at entrance to the Kill van Kull from New York Harbor and the entrance to Arthur Kill from Raritan Bay at South Amboy.

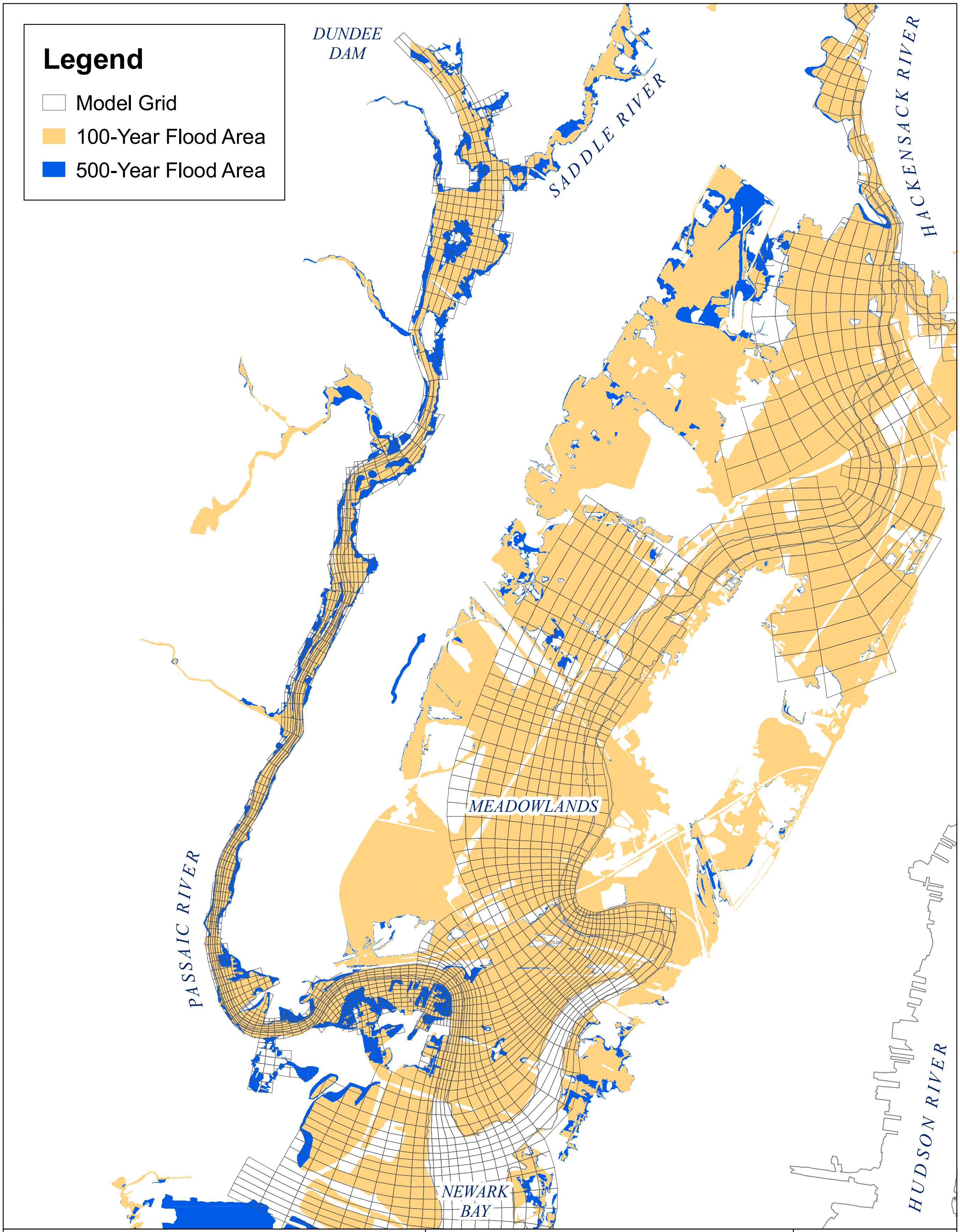

Figure 2-1. FEMA 100- and 500-year flood area with hydrodynamic model grid.

Data: FEMA Q3

HydroQual

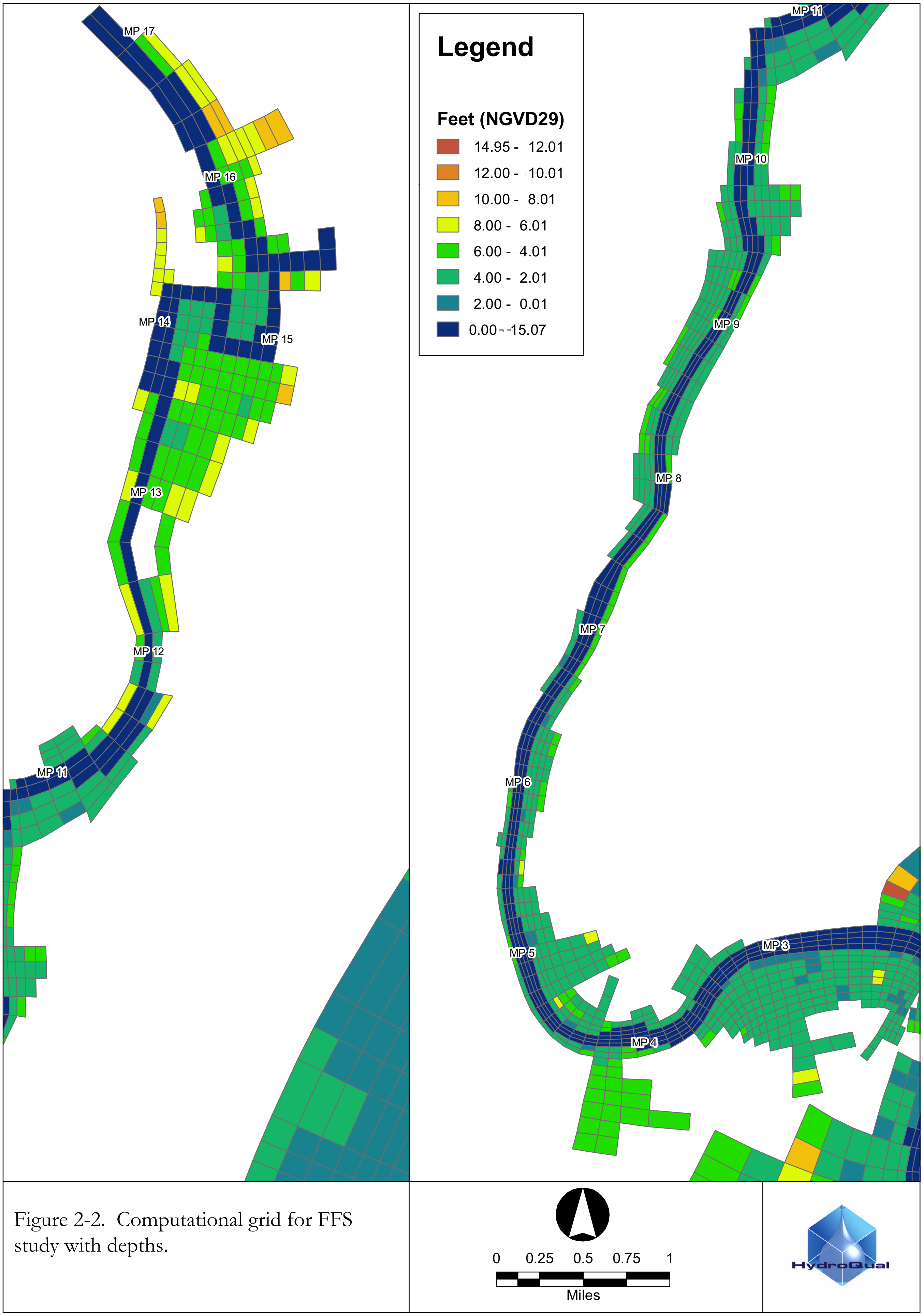

Figure 2-2. Computational grid for FFS study with depths.

HydroQual

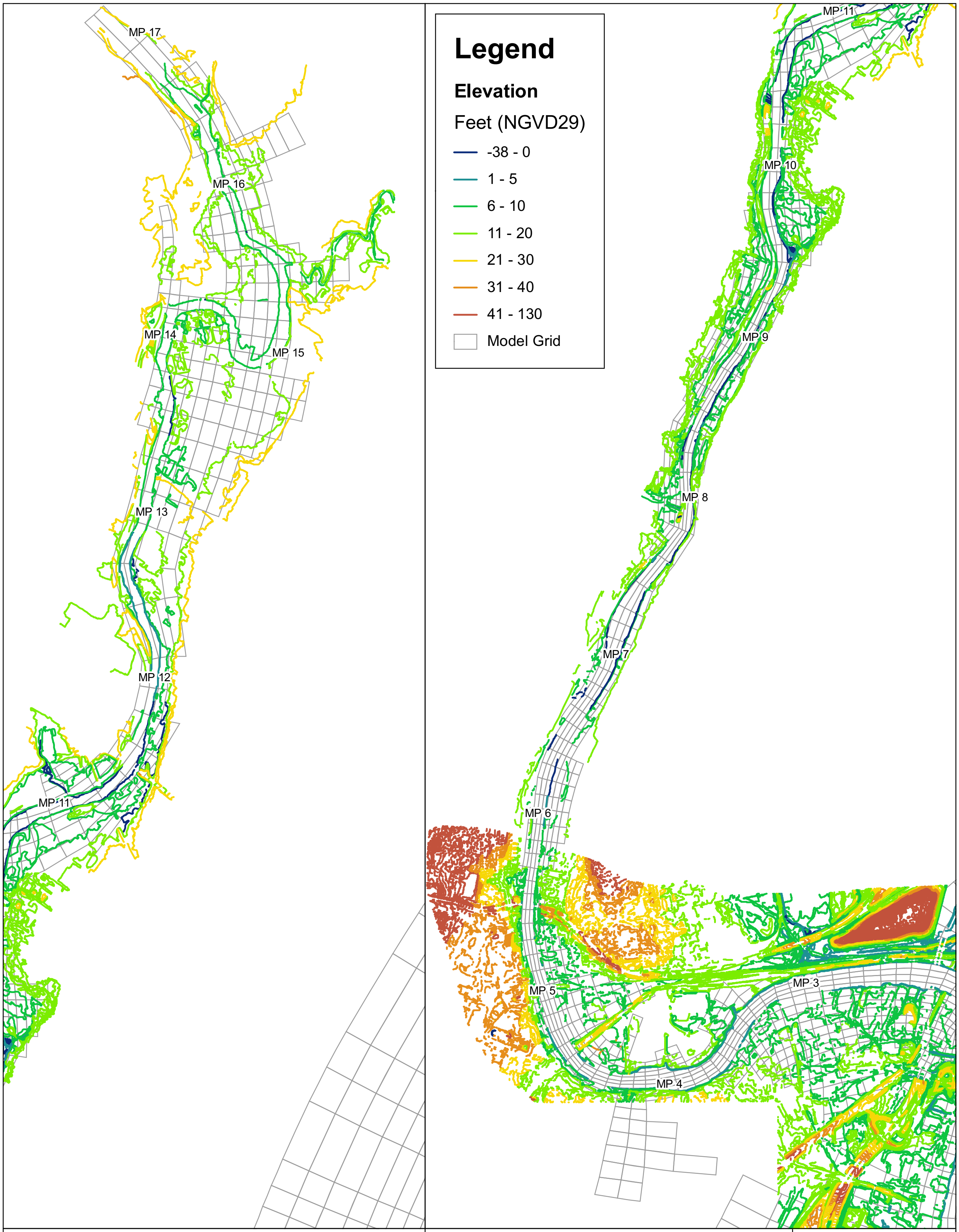

Figure 2-3. Overview of the USACE land survey data with hydrodynamic model grid.

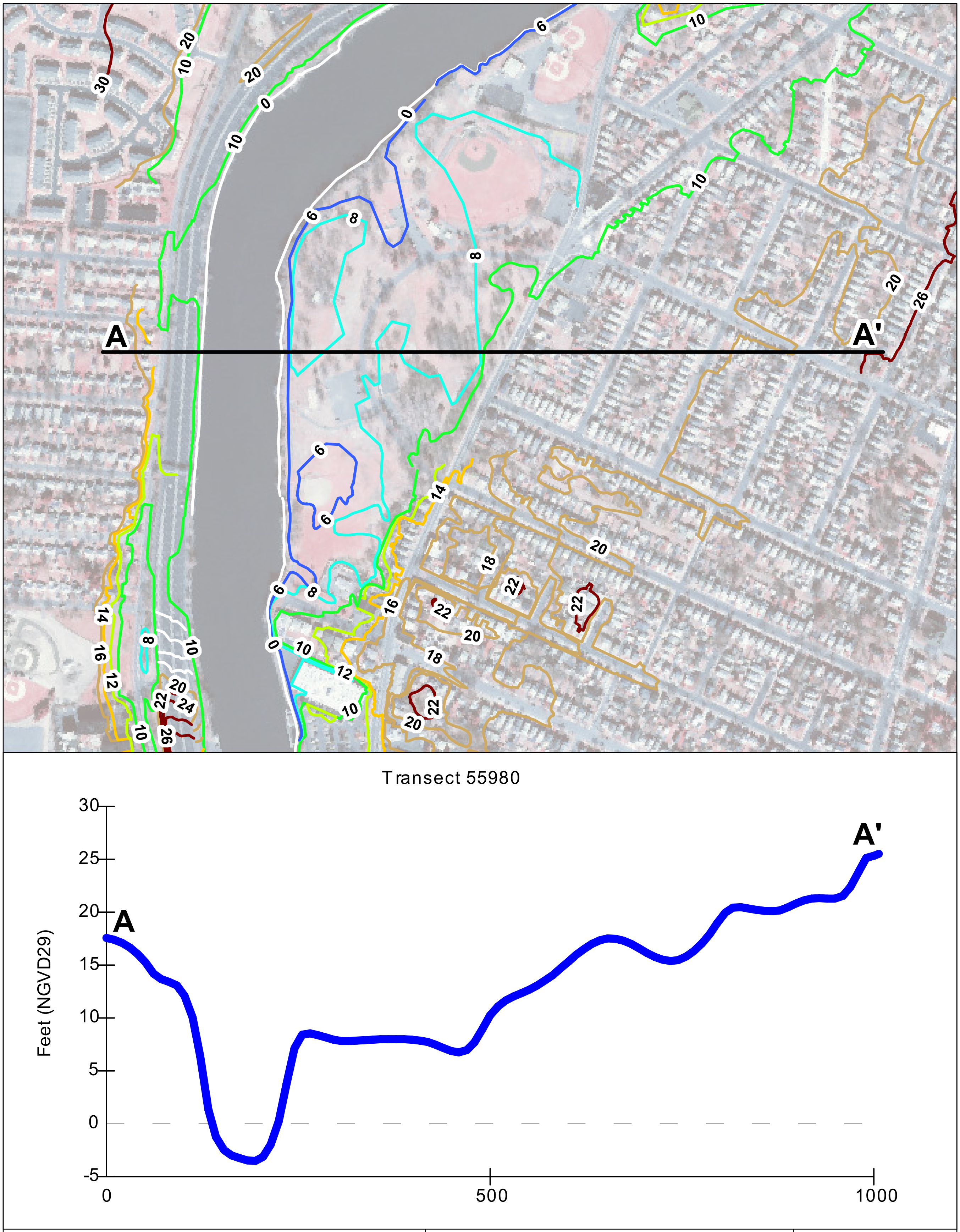

Figure 2-4. Detailed view of the USACE land survey data near RM 11 and cross -section of the land elevation.

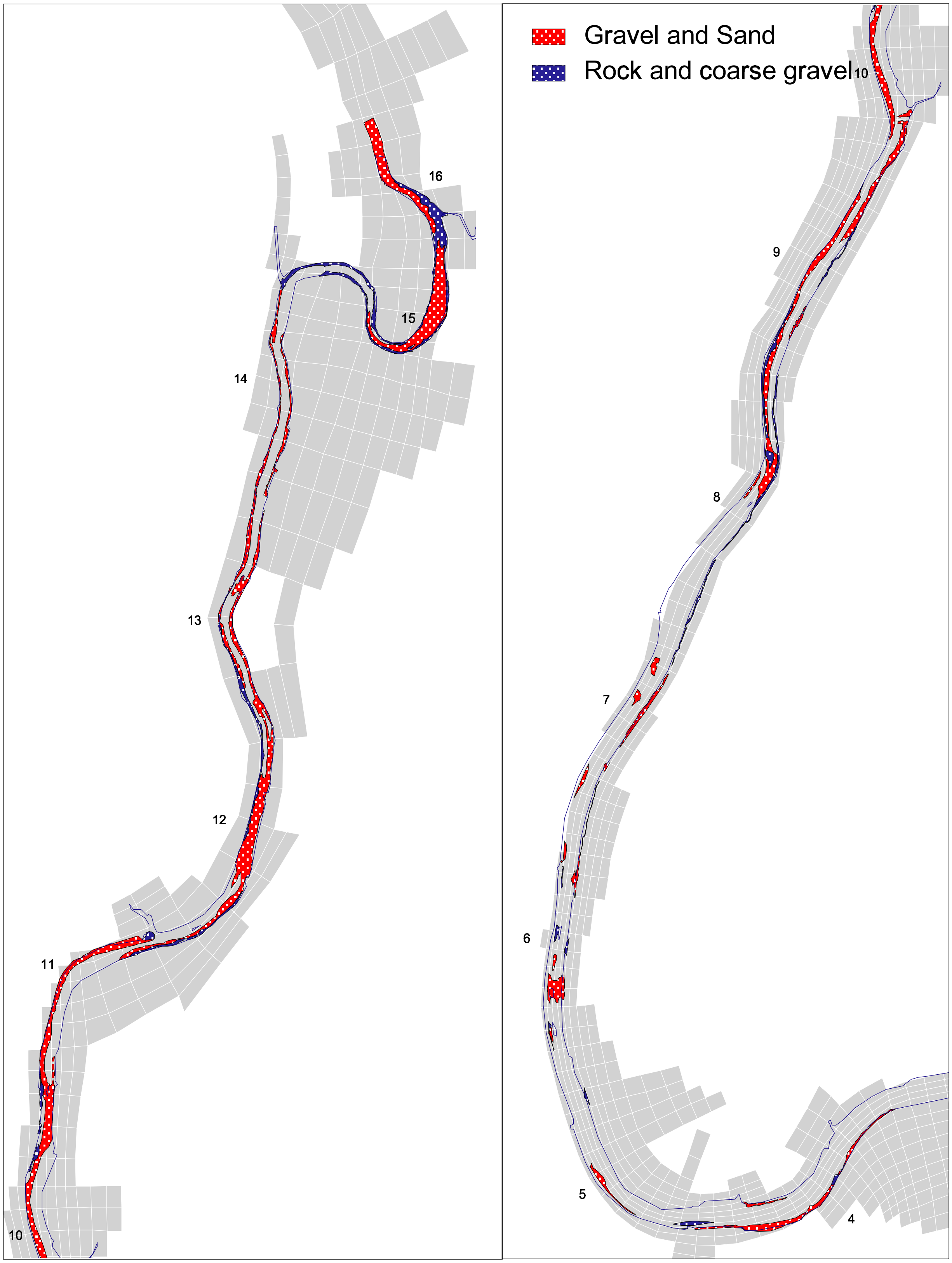

Figure 2.5. A map showing the distribution of rock , coarse gravel , gravel and sand in the Lower Passaic River.

SECTION 3

HYDRODYNAMIC MODEL CALIBRATION

The model was calibrated for a 30-day simulation using field data collected in the summer of 2004. A high quality data set, collected by the Rutgers University Institute of Marine & Coastal Sciences (IMCS), between mid-August and September 2004, was used for the calibration. This data set consisted of three bottom-mounted pressure sensors, three temperature and conductivity sensors and two bottom-mounted ADCPs (Figure 3-1).

3.1 BOUNDARY CONDITIONS AND MODEL FORCINGS

Hourly water surface elevations and temperature and salinity (Figure 3-2) along the two open-water boundaries at the Kill van Kull and South Amboy were extracted from the Water Year 2004 archives of HydroQual's LPR hydrodynamic model (HydroQual, 2007).

Freshwater inflows, both from riverine and non-point sources, were extracted from the input data used for the LPR hydrodynamic model. The bottom panel of Figure 3-2 shows the total boundary inflows from the upper Passaic River and the Hackensack River and the total flow from combined sewer outfalls (CSO) and stormwater outfalls (SWO) for the Passaic and Hackensack River basins. Lacking observed river inflow temperatures, a three-day moving average of air temperature observed at Newark International Airport was specified as inflow water temperatures (Figure 3-3).

Hourly meteorological parameters from Newark International Airport were used to compute air-sea heat exchanges as well as surface forcing functions. The parameters included wind speed and direction, air temperature, relative humidity, barometric air pressure, and cloud cover (Figure 3-3).

Detailed discussions on the boundary forcing data can be found in HydroQual's hydrodynamic report for the LPR study (HydroQual, 2007).

3.2 CALIBRATION RESULTS

3.2.1 Tidal Elevations

Water surface elevations were collected at the three pressure sensors M1, M3, and M5 in the LPR (Figure 3-1). Figure 3-4 illustrates the computed surface elevations and the measurements over a 30-day calibration period, September 1st to 30th, 2004. In the figure, blue lines are the model results while the red lines are observations. The mean range of tide in the LPR and the Newark Bay areas is between 1.5 and 1.8 m. The figure shows that the maximum water surface variation at those gauges is about 3.3 m during the calibration period. The water surface elevation during spring tides can be more than 1.0 m above mean sea level (MSL). The model-data comparisons, shown in Figure 3-4, also indicate that the amplitudes of the tide, the ranges between spring and neap tidal cycles, and times of high and low water are very well reproduced at those three locations in the river. A few exceptions can be noted around days 26-30 at M3 and days 28-29 at M5 when observed data at those stations show an increase in water elevations not reproduced by the model. Careful review of the observed elevations suggests that the pressure sensors deployed at M3 and M5 may have shifted their positions during the survey. The upstream freshwater flows shown in Figure 3-2 indicate that there was a second high flow event during the calibration period around day 18. While the increase in the observed water elevations at M3 and M5 around day 28 may coincide with the flow event at day 28, the other event around day 18 does not show a corresponding increase in the observed water elevations at any of the gauges. Moreover, the sudden increase in water elevations observed at M3 around day 26 occurred a few days earlier than the peak of the Passaic River flow measured at Little Falls. Although it can't be proved conclusively, these observations suggest the possibility that the M3 and M5 pressure sensors may have shifted slightly during the survey.

3.2.2 Current Velocities

Current velocity data at two locations in the LPR were available for calibration of the hydrodynamic model. The data collection instruments were two bottom moored acoustic current meters and were deployed during September 2004. The locations of the current meters are shown in Figure 3-1 (M2 and M3).

Time-series of hourly current velocities were measured at the surface, mid-depth and bottom layers, 4.1 m, 2.6 m and 0.9 m from the bottom, respectively, at Station M2. The computed results and the observed data are shown in Figure 3-5a, where positive values depict a downstream current and negative values depict an upstream current. In Figures 3-5a and 3-5b, the blue lines are the model results and the red lines are the observations. Figure 3-5a indicates that there were strong tidal currents in the LPR during the calibration period. Due to fresh water inflows around day 28 (see Figure 3-2), the maximum ebb tidal velocities at the surface were about 1.25 m/s and the maximum flood tidal velocities were about 0.85 m/s. In the vertical, it can be noted that velocities decrease with increasing depth. At the bottom layer, the maximum ebb tidal velocities were about 0.8 m/s and the maximum flood tidal velocities decreased to about 0.65 m/s. At M2, the model slightly overestimates ebb tide velocities near the surface and bottom layers around days 2, 14, and 28 during spring tidal periods. In general, the figure indicates good model performance in reproducing tidal currents, their time of occurrence, and the variations between spring and neap tidal cycles. Three sub-tidal events were recorded at days 7, 18 and around 28. At M2, the model computed slightly higher bottom velocities than those observed at 0.9 m above bottom.

Shown in Figure 3-5b are the time-series of hourly current velocities at surface, mid-depth and bottom layers, 6.0 m, 3.0 m and 1.0 m from the bottom, respectively, for Station M3. At this upstream location, surface tidal currents are not as strong as those observed at the downstream current meter, M2. The maximum ebb tidal velocities at the surface are about 1.0 m/s and the maximum flood tidal velocities are about 0.70 m/s. As depth increases, current velocities decrease. However, at the bottom layer, the maximum ebb and flood tidal velocities are larger than those computed at M2, 1.0 m/s and 0.75 m/s, respectively.

Only 14 days of mooring data were collected at M3 in September 2004. Figure 3-5b shows that the model reproduces the amplitudes and phases of velocity observed near the bottom quite well. At surface and mid-depth layers, the phase of current is well simulated, but the amplitude is over-estimated. Both the computed and observed current velocities show a sub-tidal event around day 28.

3.2.3 Temperature and Salinity

Continuous observations of surface and bottom water temperature and salinity were made at six locations in the LPR from August through October 2004. The locations of these stations are shown in Figure 3-1 and are denoted as M1, M2, M3, M4, Bridge St. (BS) Bridge, and M5 from downstream to upstream. The data collected at these stations in September 2004 were used to calibrate the hydrodynamic model for temperature and salinity.

The model-data comparisons of hourly temperature and salinity at these locations are shown in Figures 3-6 and 3-7, respectively. The blue lines represent the computed values and the red lines the observations at surface and bottom layers. In order to correlate changes in temperature and salinity with the model forcing terms, the upstream river inflow data are also shown with the temperature and salinity plots.

During the simulation period, temperatures were basically maintained above 20ºC in the LPR except for a decrease around day 19 due to a high flow event. The model and data indicate small differences in surface and bottom temperatures showing relatively weak thermal stratification in the river. Figure 3-6 indicates that the model computed surface and bottom temperatures follow closely the observed temperature for most of the simulation period. However, the model does not quite capture the temperature variations following the high flow event. The discrepancy in the computed and the measured temperatures around the day 19 flow event may be attributed to a lack of information concerning the proper water temperature to be assigned to freshwater inflows (see the previous section). The model-data differences are relatively small at downstream locations (M1, M2 and M3) but become more apparent at upstream locations (M4, Bridge St. Bridge and M5) closer to the source of the inflow, *i.e.*, water over the Dundee Dam.

Figure 3-7 indicates that freshwater flow and estuarine circulation have a significant influence on the salinity variations. Strong salinity stratification is shown at the downstream station during the high flow event. At M1, the surface salinity can decrease to near 0 practical salinity unit (psu) while the corresponding bottom salinity has a value of about 13.5 psu around day 18. The observed tidal variation in the surface salinity at M1 can be as much as 12 psu most of the time. This represents the tidal excursion of high salinity water entering the river from Newark Bay during flood tide and low salinity water moving downstream from the upstream LPR during ebb tide. Moving upstream, salt intrusion and vertical stratification become weaker and freshwater flow influence becomes more dominant. At M5 and Bridge St. Bridge, the surface-to-bottom salinity differences are only about 1-2 psu during the low flow period and salinities at surface and bottom approach 0 psu during the high flow period. Corresponding to each high flow event, Figure 3-7 also shows corresponding decreases in observed and computed salinity. The surface salinity can decrease from 17 psu to close to 0 psu at the downstream stations and from 7 psu to 0 psu at the upstream stations.

In general, the model was able to reproduce both the surface and bottom salinity at all stations very well in the LPR except during a few occasions at M1 and M2 at the bottom. The computed temporal variations in surface salinity as well as vertical stratification due to tidal movement of water are in good agreement with the observations. In particular, the model reproduced the high freshwater inflow events that occurred on days 8, 18 and 28. In response to freshwater flow, both the timing and magnitude of salinity fluctuations were accurately represented by the model. At station M5 and Bridge St. Bridge, the most upstream locations of the survey where not many data were available, the computed salinities agree reasonably well with the observed data. The extent of the salt intrusion into the LPR was well represented by the model. This suggests that the physical configuration (geometry) of the LPR is adequately addressed and hydrodynamic transport and mixing characteristics are well resolved in the model.

3.3 STATISICAL ANALYSIS

Statistical analyses were performed in order to assess the model performance in terms of model/data comparisons. The model computed values of temperature, salinity, velocity and elevation were compared against the observations at several locations.

The statistical parameters considered included the root mean square error (RMSE), the relative RMSE, and the correlation coefficient. The RMSE, a measure of the error between the model and observed data, can be expressed mathematically as:

$$\mathrm{RMSE} = \sqrt{\frac{\sum (C_{OBS_i} - C_{MODEL_i})^2}{n}},$$

where C_{OBS} is the observed variable, C_{MODEL} is model calculated variable, and n is number of paired variables. The relative RMSE (%) is defined as the RMSE divided by the data range and measures the model performance in terms of reproducing the observations accounting for the variability in the observations. The correlation coefficient measures the strength of the linear association between the predicted and actual values.

3.3.1 Tidal Elevations

Table 3-1 highlights the results of the statistical analysis for tidal elevations at three tidal gauge stations (M5, M3 and M1) in terms of the above mentioned parameters. The tidal elevation data were compared with the model results for the period of one month, starting September 2004. The number of data points used in the statistical analysis, based on the data, along with the statistical parameters are presented in the table.

Table 3-1. Statistical Evaluation of Model Performance for Water Elevation

Station	No. Data Pairs	Data Range (m)	RMSE (m)	Rel. RMSE (%)	Correlation Coefficient
Upper Tidal Gauge (M5)	3887	2.66	0.22	8.2	0.92
Middle Tidal Gauge (M3)	1296	2.69	0.26	9.7	0.90
Lower Tidal Gauge (M1)	3456	2.55	0.18	7.1	0.96

For the three stations, the mean RMSE and the mean correlation coefficient are 0.22 m and 0.93, respectively. It is to be noted that the model performance in terms of reproducing the tidal elevations is better at M5 and M1 as compared to M3. The average relative RMSE is 8.3%.

The results of the statistical correlation analysis in the form of scatter plots are presented in Figure 3-8. As can be observed, the model and data values seem to be closely correlated. Most of the point comparisons lie within close proximity to the one-to-one line in the plot, emphasizing the fact that the model predicted values are in close agreement with the data measurements.

Table 3-2 compares results of harmonic analyses of computed and observed water surface elevations at the tidal gauge stations. The amplitudes and phases of four major tidal constituents, the principle lunar (M_2) and solar (S_2) semi-diurnal components and luni-solar (K_1) and principle lunar(O_1) diurnal components, are presented in the table. The dominant tidal constituent is M_2, with observed amplitude varying from 0.80 m at the M5 tide gauge to 0.72 m at the M1 gauge. For the M_2 tide, the maximum error in amplitude is about 0.06 m, and the maximum phase error is about 2° (4 minutes). Among all four tidal constituents, amplitude errors never exceed 0.06 m, while phase errors are always less than 1 hour.

For the semi-diurnal components M_2 and S_2, the comparison between observed and calculated phase shows the maximum phase error not exceeding 7° (or 15 minutes). At several instances, the calculated phase error is less than a couple of degrees, signifying the robustness of the model in capturing the dominant tidal components. In general, the harmonic analysis shows that the model reproduces the observed water surface elevations at the M5 and M1 tide gauges better than it does at the M3 tide gauge, which is consistent with the results from the previous statistical analysis.

The results of harmonic analysis obtained in this study compare well with the results of the earlier NY Harbor Study (Blumberg et. al., 1999), where the M2 amplitude differences are less than 10 cm and phase differences are less than 15° (or 30 minutes).

Table 3-2. Comparison of Harmonic Constants for Water Elevation

M_2 Component

Station	Observed		Calculated	
	Amp (m)	Phase (deg)	Amp (m)	Phase (deg)
Upper Tide Gauge (M5)	0.80	243	0.76	242
Middle Tide Gauge (M3)	0.80	241	0.74	239
Lower Tide Gauge (M1)	0.72	236	0.66	234

S_2 Component

Station	Observed		Calculated	
	Amp (m)	Phase (deg)	Amp (m)	Phase (deg)
Upper Tide Gauge (M5)	0.20	264	0.18	271
Middle Tide Gauge (M3)	0.20	261	0.18	268
Lower Tide Gauge (M1)	0.17	257	0.16	257

K_1 Component

Station	Observed		Calculated	
	Amp (m)	Phase (deg)	Amp (m)	Phase (deg)
Upper Tide Gauge (M5)	0.09	120	0.05	101
Middle Tide Gauge (M3)	0.08	116	0.05	99
Lower Tide Gauge (M1)	0.09	113	0.05	98

O_1 Component

Station	Observed		Calculated	
	Amp (m)	Phase (deg)	Amp (m)	Phase (deg)
Upper Tide Gauge (M5)	0.05	105	0.05	97
Middle Tide Gauge (M3)	0.06	97	0.05	96
Lower Tide Gauge (M1)	0.05	94	0.04	88

3.3.2 Current Velocities

The current velocity measurements were compared with the model predicted values to evaluate the model performance in terms of reproducing the current velocity in the system. The velocity measurements were made at two different locations at several depths.

The outcomes of the statistical analysis for current velocities are illustrated in Table 3-3. The model output was extracted at three depth levels and a comparison between the model and data values was performed.

The resulting RMSEs, relative RMSEs, and correlation coefficients are presented in Table 3-3. As can be seen in the table, the RMSEs vary from 0.15 m/s to 0.23 m/s, with a mean of 0.19 m/s and relative RMSEs vary from 8.5 % to 13.1 %, with a mean of 11.3 %. The correlation coefficient ranges from 0.74 to 0.87. The table indicates that the downstream station (M2) has relatively smaller RMSEs and relative RMSEs, and higher correlation coefficients as compared to the upstream station (M3). The RMSE values also demonstrate that the model performs better in simulating the current velocities at the bottom as compared to mid-depth or surface; however, the model and data values seem to be better correlated at the surface than at the bottom or mid-depth. The statistical analysis of currents obtained in this study compare well with the results of the earlier New York Harbor(NYH) study (Blumberg et. al., 1999), where the RMSE on the current meters deployed in the East River varied between 0.15 m/s and 0.43 m/s. The correlation coefficients of current velocities in the NYH study were above 0.95.

Table 3-3. Statistical Evaluation of Model Performance for Current Velocity

Station	No	Data Range	RMSE (m/s)	Rel. RMSE	Correlation Coefficient
M3					
Surface(5.5m)	648	1.68	0.22	13.1	0.86
Mid-depth(2.5m)	648	1.69	0.22	13.0	0.81
Bottom(0.5m)	648	1.63	0.18	11.0	0.74
M2					
Surface(3.62m)	1436	2.06	0.23	11.2	0.87
Mid-depth(2.12m)	2141	1.99	0.17	8.5	0.86
Bottom(0.37m)	2112	1.39	0.15	10.8	0.81

The results of the statistical correlation analysis at different depth levels for both the stations have been presented in the form of scatter plots in Figure 3-9. As can be observed, the model and data values seem to be closely correlated. Most of the points are well distributed around the one-to-one line in the plot, emphasizing the fact that the model predicted values are in good correspondence with the data measurements.

3.3.3 Temperature and Salinity

The model was calibrated by comparing model results to temperature measured by sensors collected at six locations in the region during the month of September 2004. Table 3-4 presents the statistical evaluation of model performance in terms of RMSE, relative RSME and correlation coefficient between computed and observed water temperature at surface and bottom. The RMSE in water temperature predictions varies from 1.6 ºC to 5.0 ºC, with relative RMSE varying from 9.3 % to 31.3%. In general, the model does a better job simulating the surface temperatures and the model predictions at the downstream stations are better than the upstream stations. Figure 3-10 shows the statistical correlation between the model and data values. The model and data values seem to be relatively well correlated to each other at the downstream stations (M1, M2, and M3) but at some times significantly deviate from the 1-to-1 correlation line at the upstream stations (Bridge St. Bridge and M4). This is likely due to uncertainties in the freshwater temperature specified in the model, which has been discussed in the previous section.

Table 3-4. Statistical Evaluation of Model Performance for Temperature

Station	No. of Data	Data Range (Deg C)	RMSE (Deg C)	Rel. RMSE	Correlation Coefficient
BS					
Surface	335	5.1	1.6	31.3	0.50
Bottom	338	7.8	1.6	20.7	0.39
M5					
Surface	No data				
Bottom	35	3	0.5	15.0	0.85
M4					
Surface	623	8.1	1.2	14.5	0.73
Bottom	338	7.8	1.4	18.1	0.53
M3					
Surface	359	3.6	0.7	18.5	0.62
Bottom	359	3.8	0.7	19.1	0.64
M2					
Surface	695	7.8	1.0	12.3	0.81
Bottom	695	7.8	1.0	13.1	0.81
M1					
Surface	695	7.9	0.7	9.3	0.87
Bottom	198	5.3	0.7	12.7	0.87

Comparisons between the model predicted and measured salinity values were made at six locations in the study area for the month of September, 2004. Table 3-5 presents the statistical evaluation of model performance in terms of RMSE, relative RSME and correlation coefficient between computed and observed salinity at surface and bottom. The RMSE in salinity predictions varies from 1.1 psu to 4.6 psu, while the relative RMSE varies from 13.07 % to 38.40%. Similar to the behavior of model predicted temperature, it can be noticed that the model does a better job simulating the surface salinity as compared to the bottom salinity. Figure 3-11 shows the statistical correlation between the model and data values. The figure indicates that model-data correlation is better at surface than at bottom where the observed salinity is generally higher than computed (see Figure 3-7).

Table 3-5. Statistical Evaluation of Model Performance for Salinity

No	Station	No. of Data	Data Range (psu)	RMSE (psu)	Rel. RMSE	Correlation Coefficient
1	BS					
	Surface	318	6.4	1.1	17.1	0.68
	Bottom	36	9.7	3.0	30.7	0.55
2	M5					
	Surface	No data				
	Bottom	35	4.5	1.6	34.8	0.53
3	M4					
	Surface	605	12.1	1.6	13.5	0.85
	Bottom	36	9.7	3.7	38.4	0.63
4	M3					
	Surface	366	12.5	2.2	17.3	0.83
	Bottom	360	16.0	5.3	33.1	0.71
5	M2					
	Surface	677	16.5	2.5	15.2	0.88
	Bottom	695	16.2	4.6	28.5	0.69
6	M1					
	Surface	677	17.1	2.2	13.1	0.88
	Bottom	198	18.7	3.1	16.7	0.67

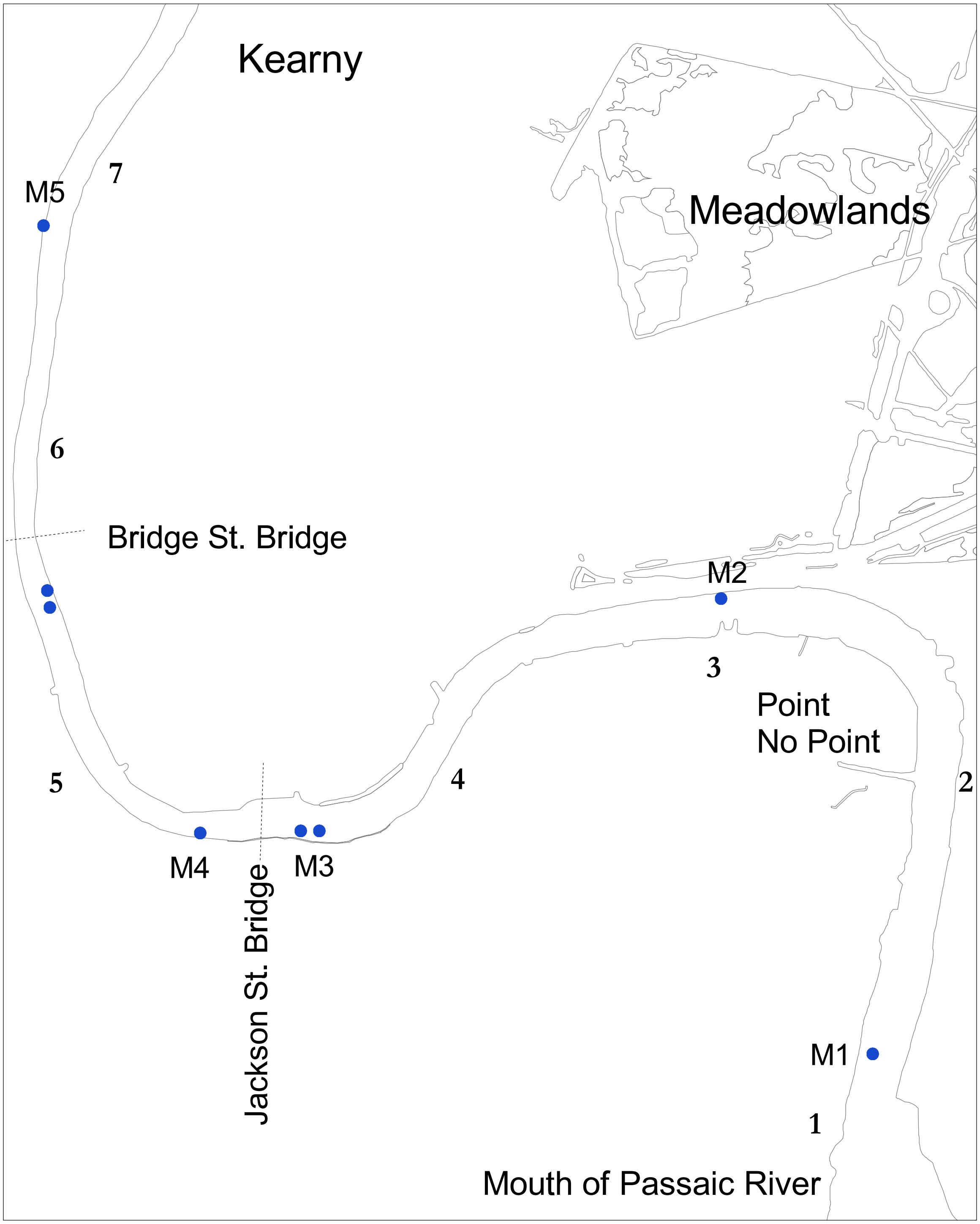

Figure 3-1. Locations of the 2004 IMCS field sampling stations in the Lower Passaic River.

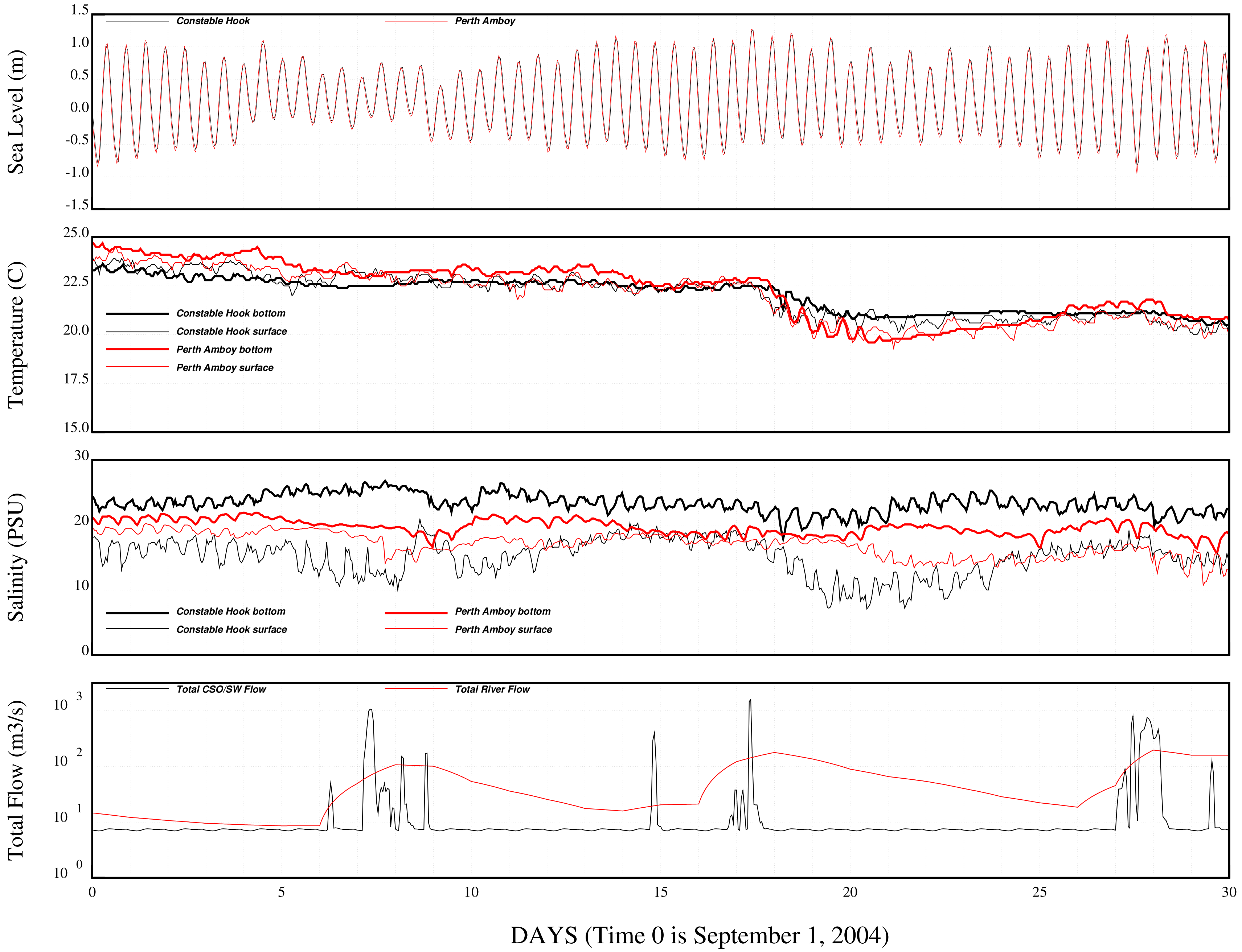

Figure 3-2. Boundary forcing data used for the model calibration.

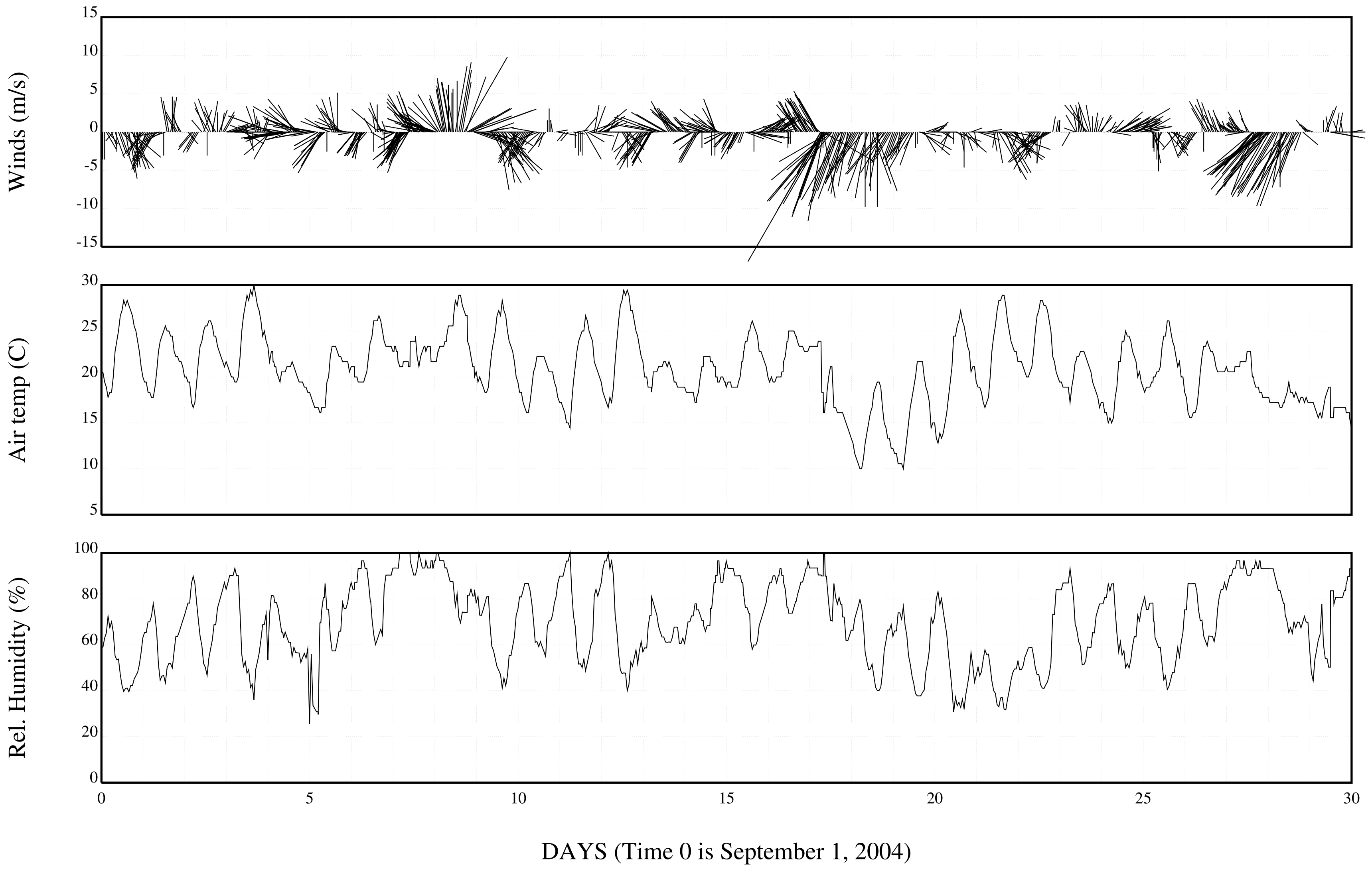

Figure 3-3. Meteorological data used for the model calibration.

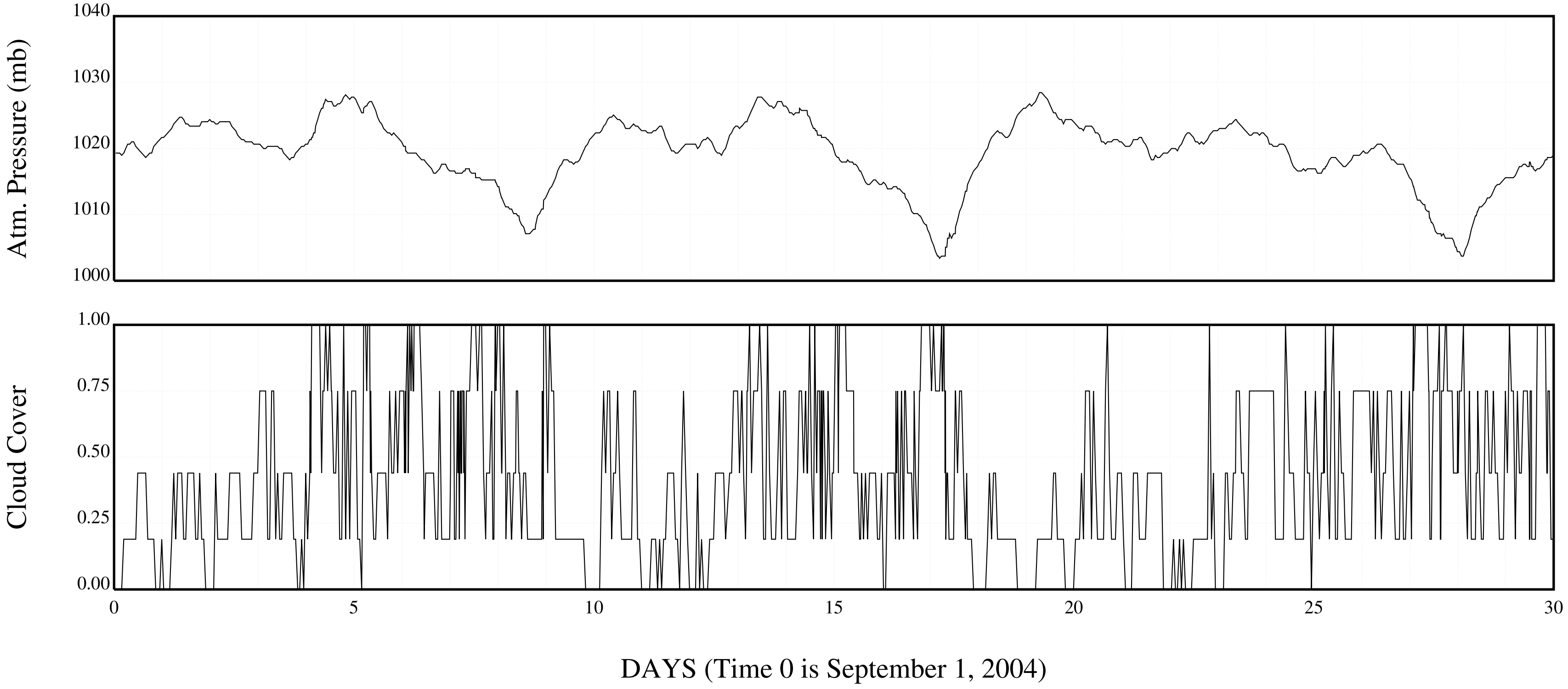

Figure 3-3 (continued). Meteorological data used for the model calibration.

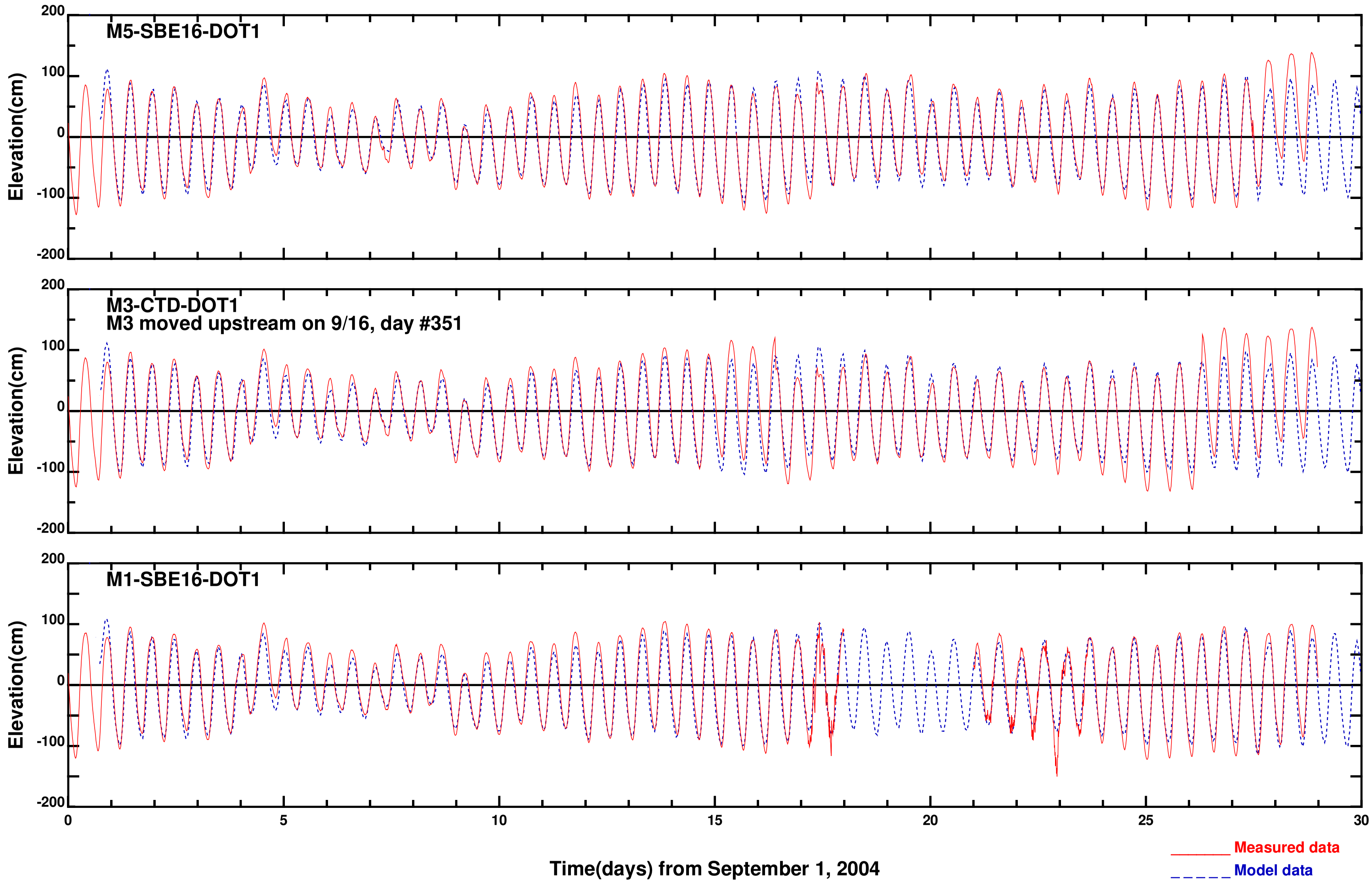

Figure 3-4. Comparison of computed water elevations with observed data.

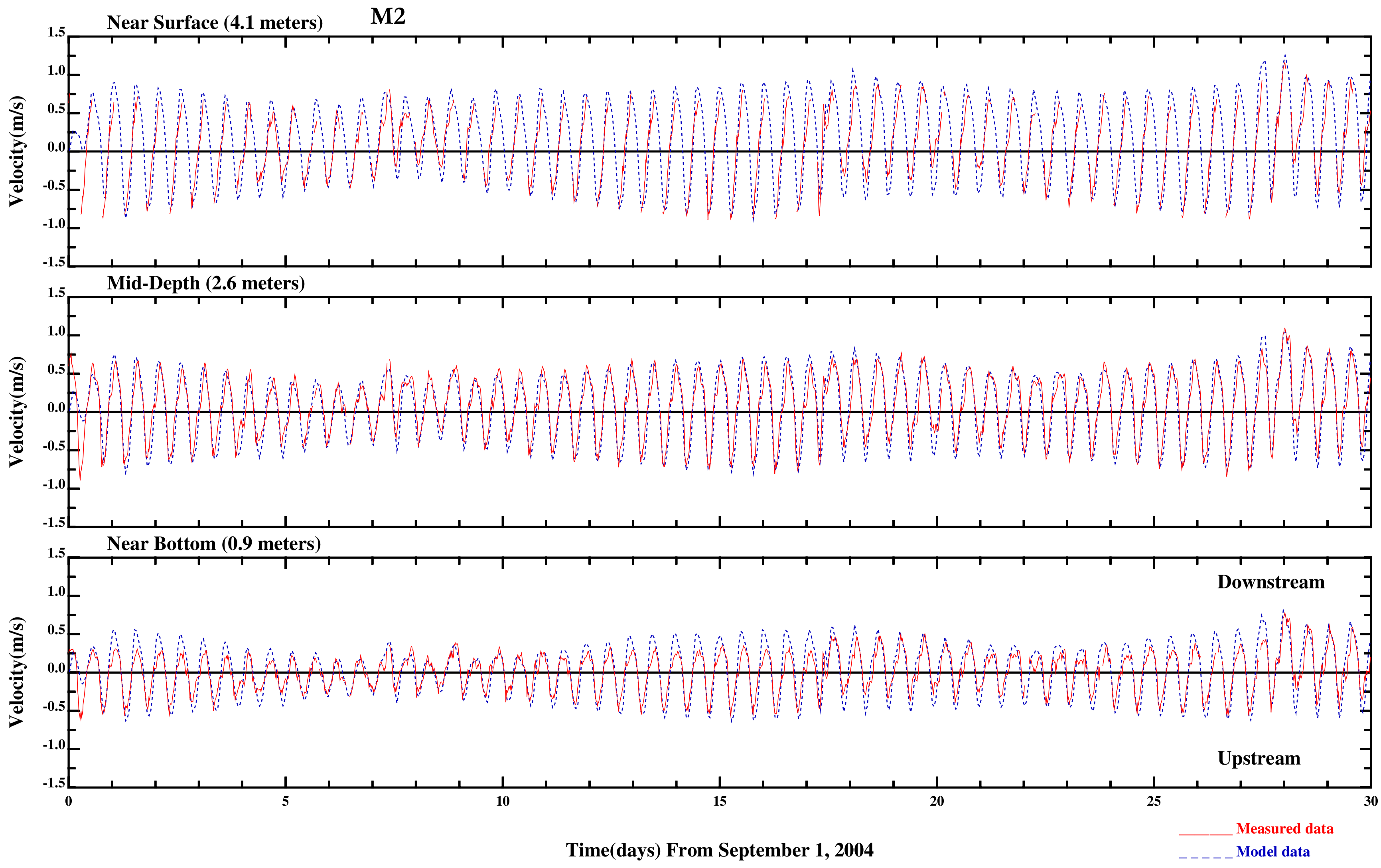

Figure 3-5a. Comparison of computed current velocities at three depths with observed data at M2.

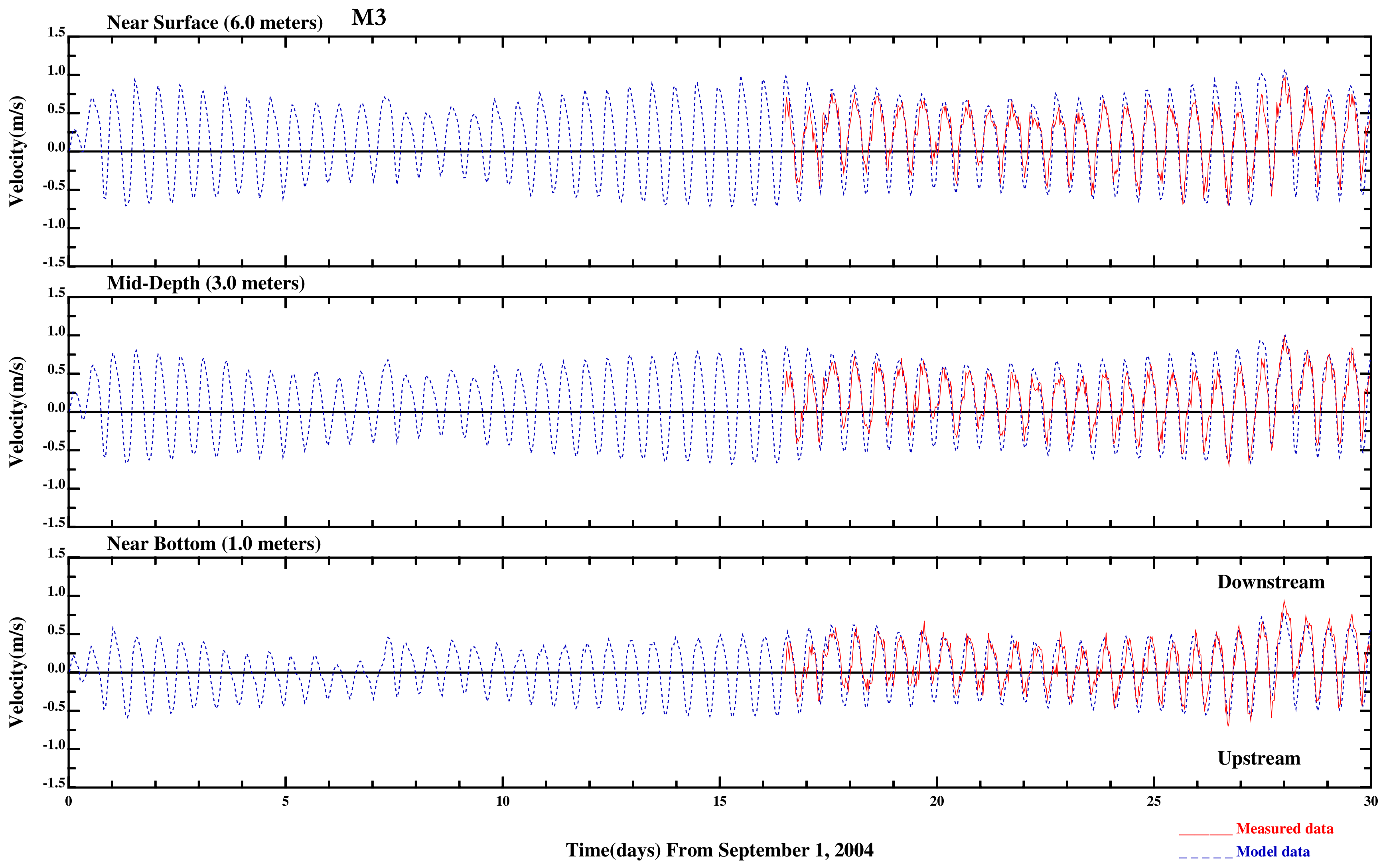

Figure 3-5b. Comparison of computed current velocities at three depths with observed data at M3.

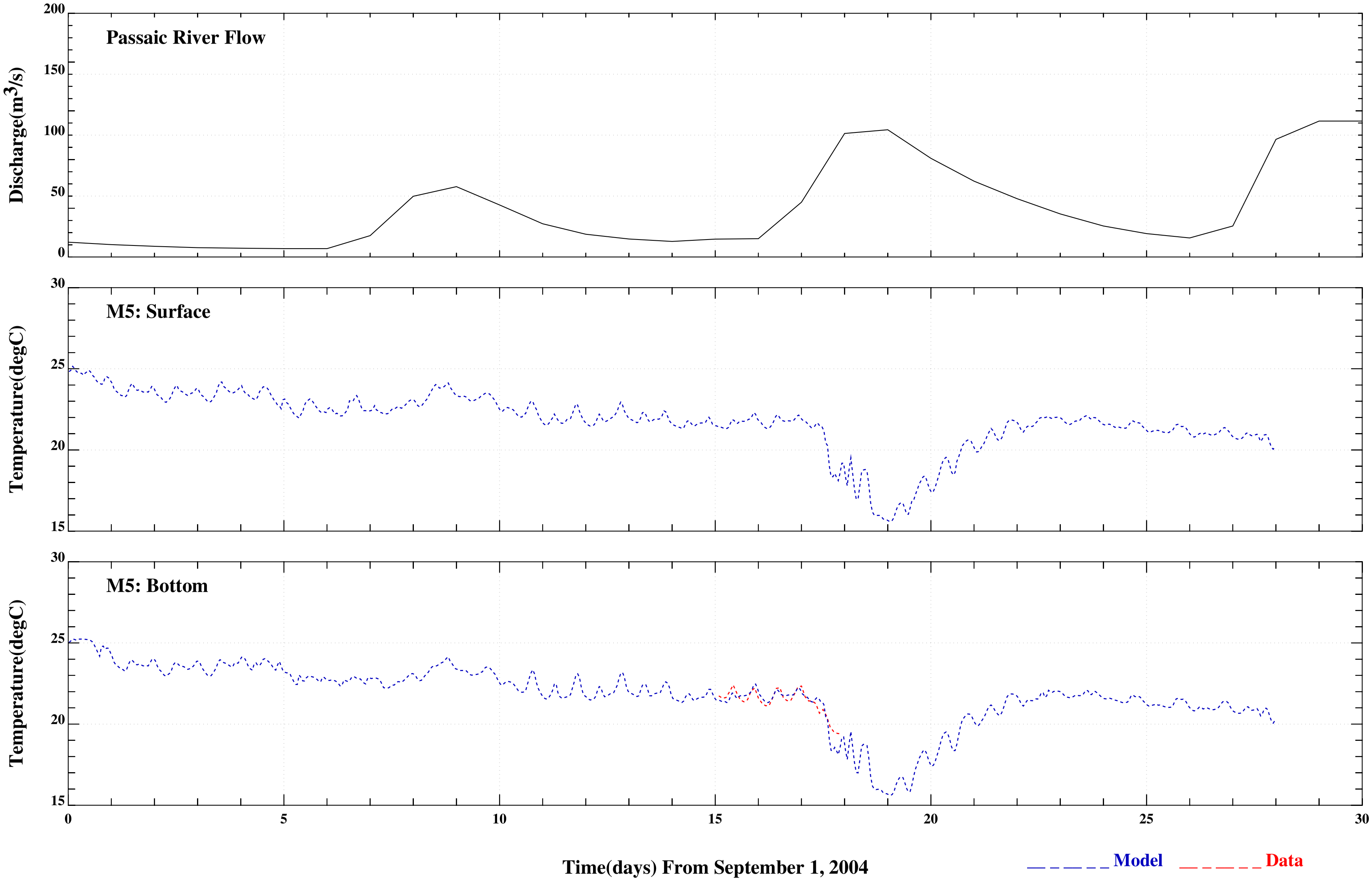

Figure 3-6. Comparison of computed water temperature with observed data.

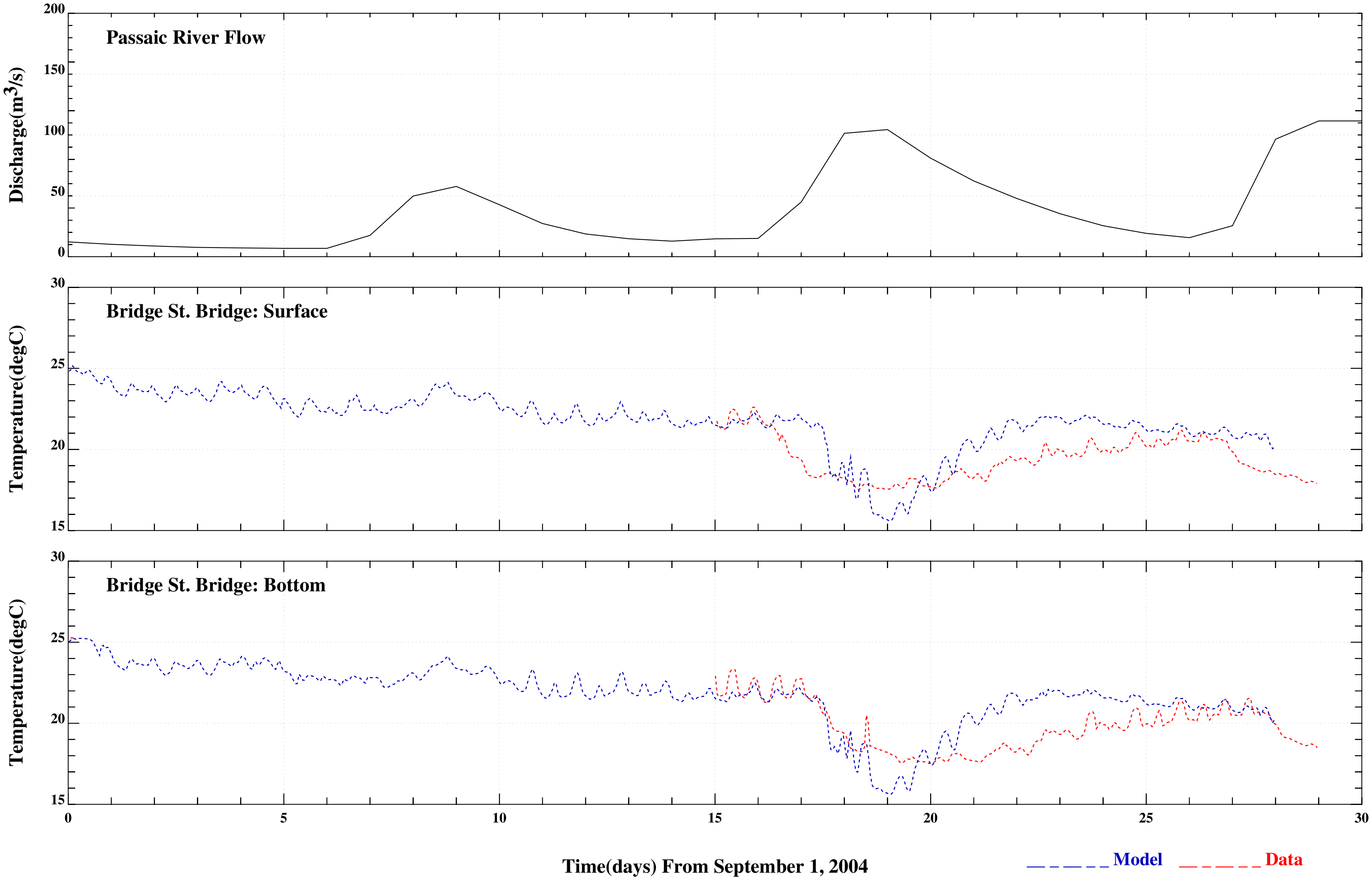

Figure 3-6. Comparison of computed water temperature with observed data (continued).

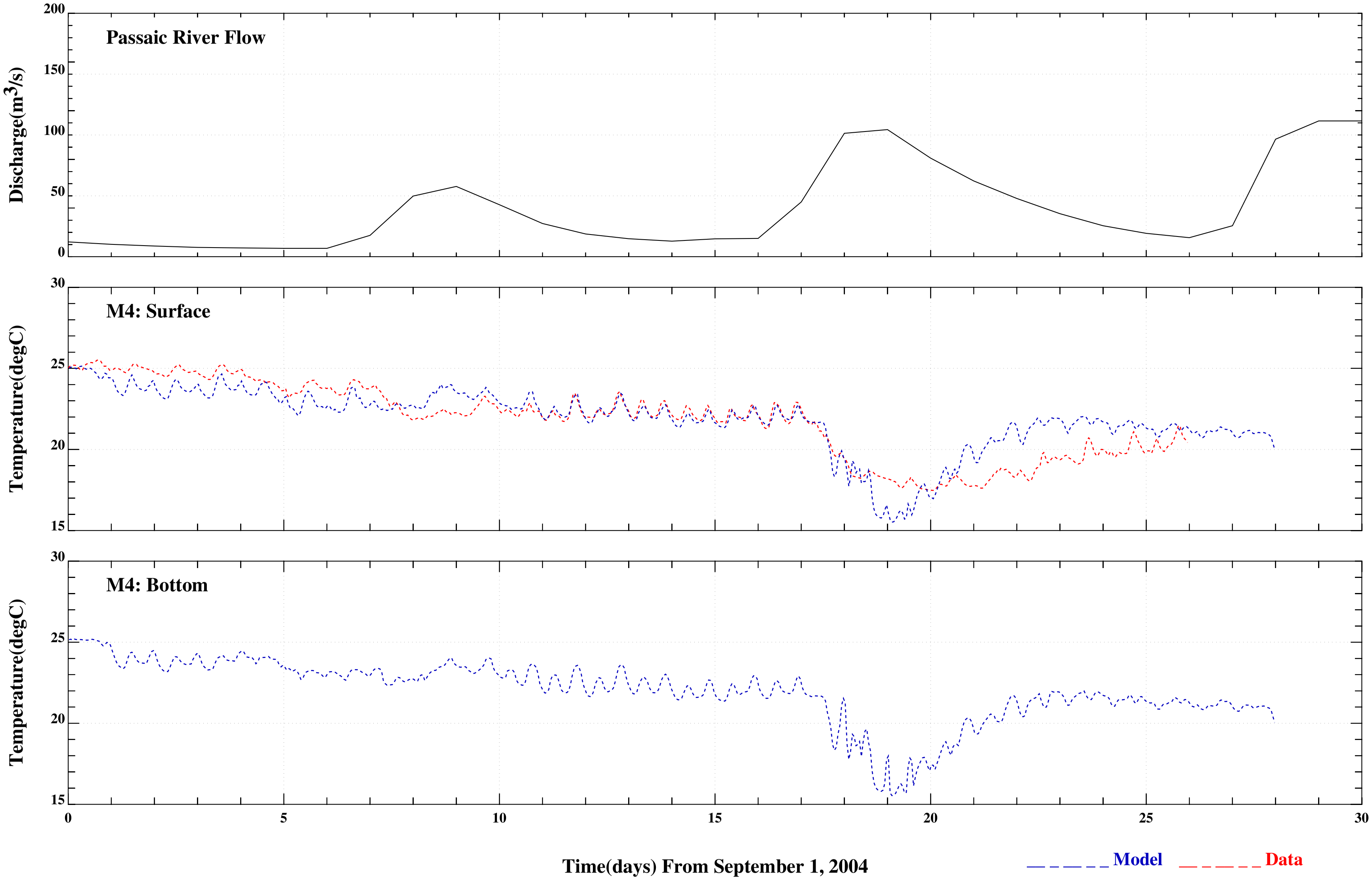

Figure 3-6. Comparison of computed water temperature with observed data (continued).

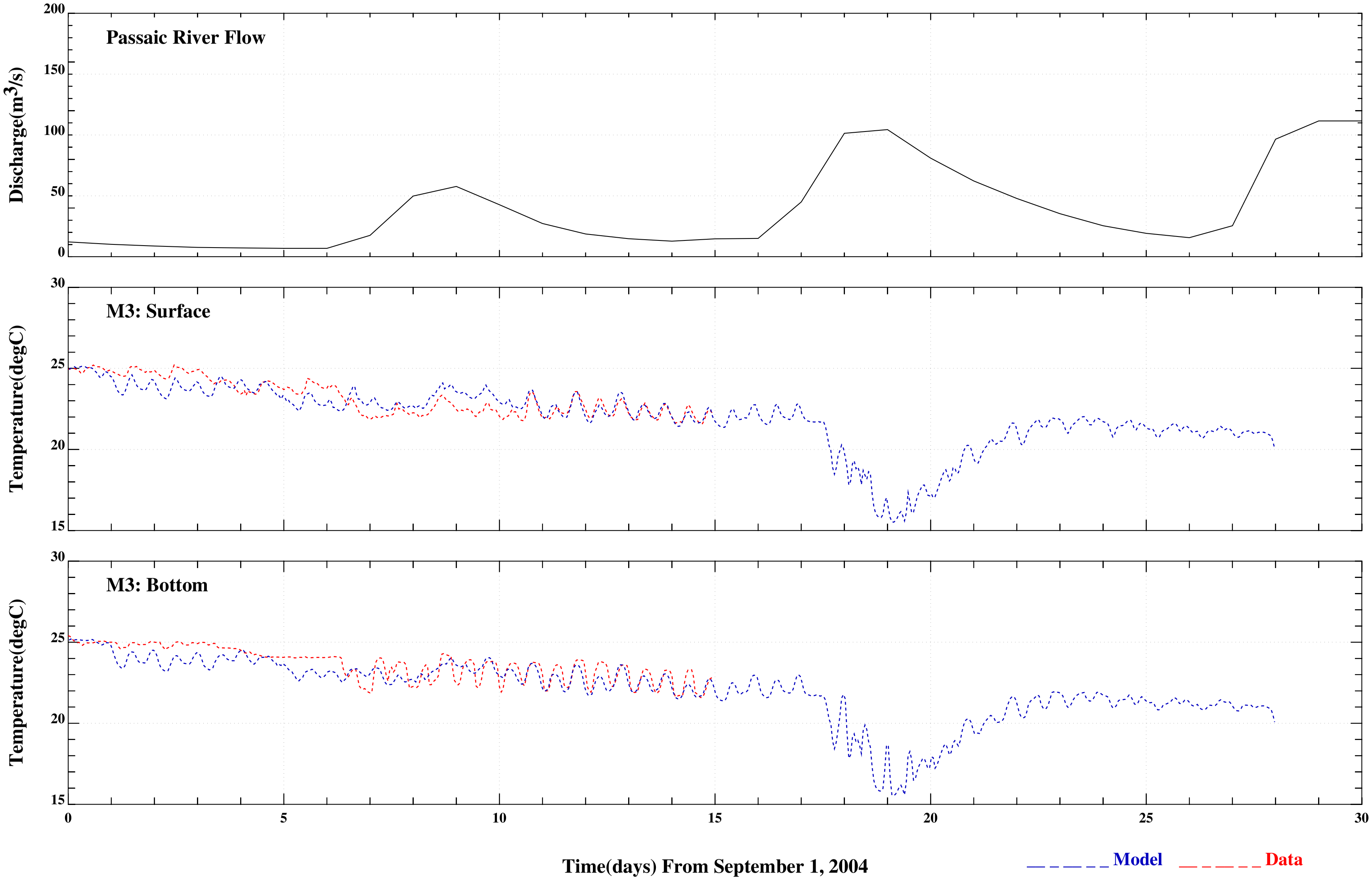

Figure 3-6. Comparison of computed water temperature with observed data (continued).

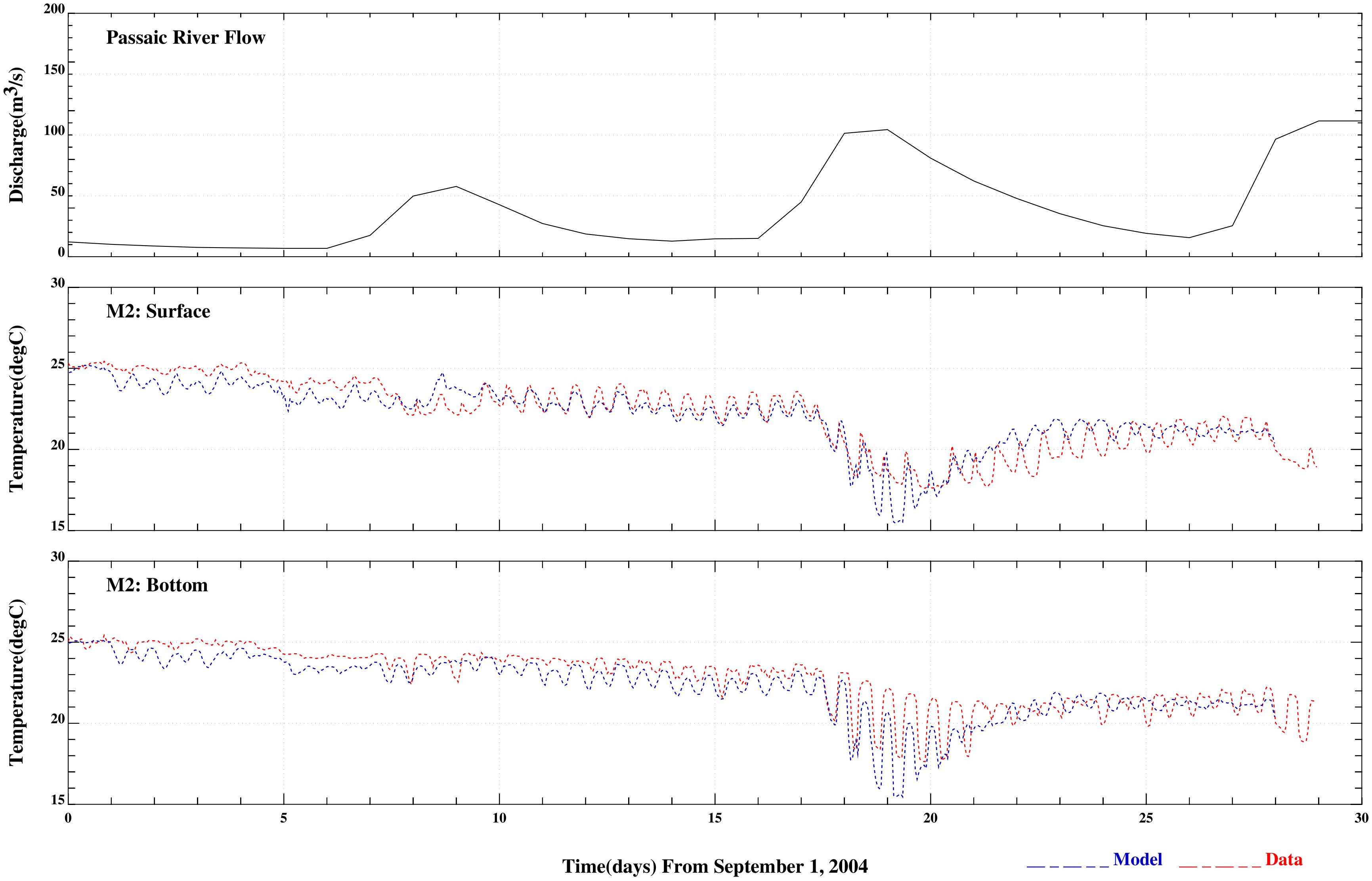

Figure 3-6. Comparison of computed water temperature with observed data (continued).

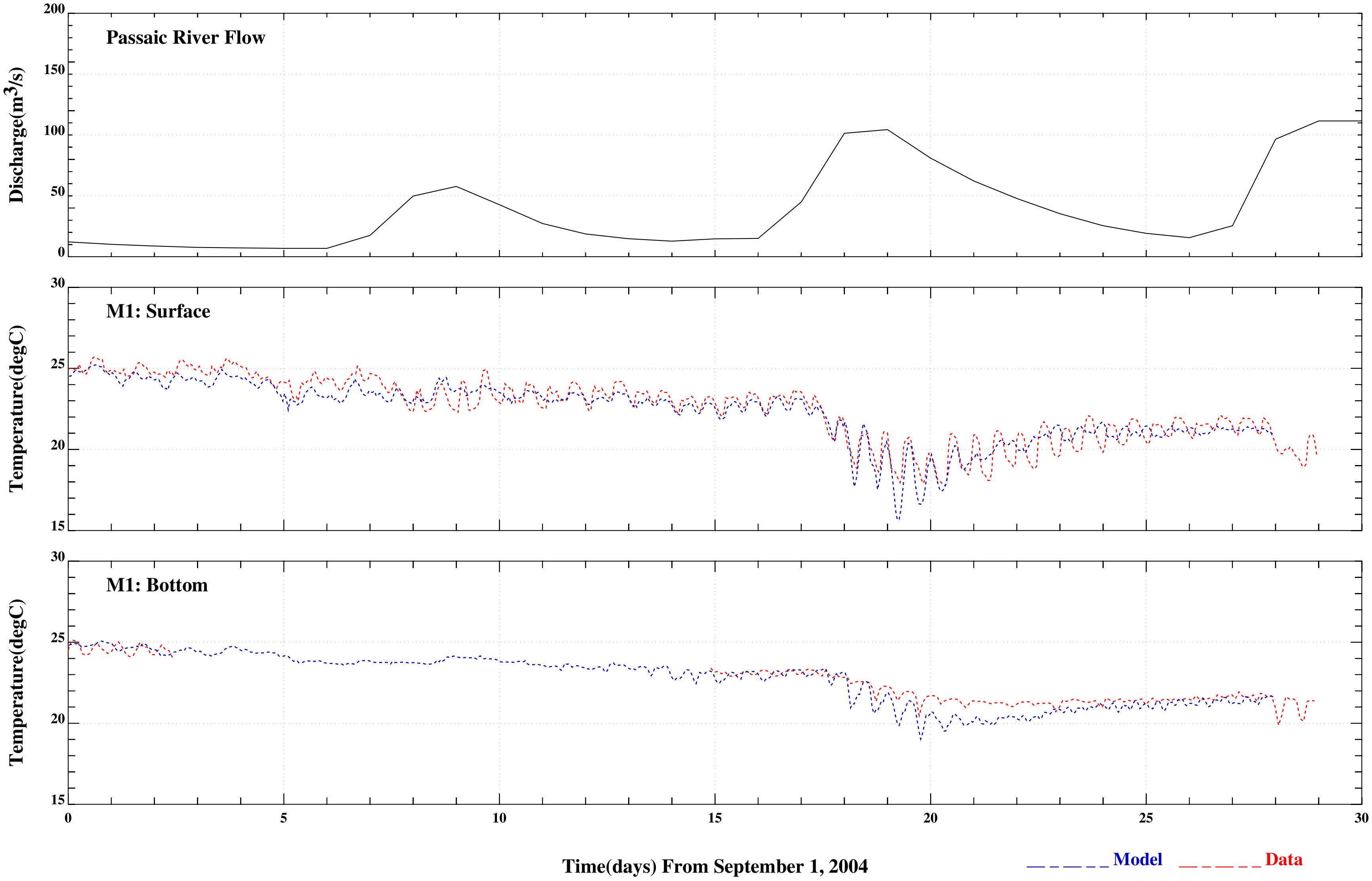

Figure 3-6. Comparison of computed water temperature with observed data (continued).

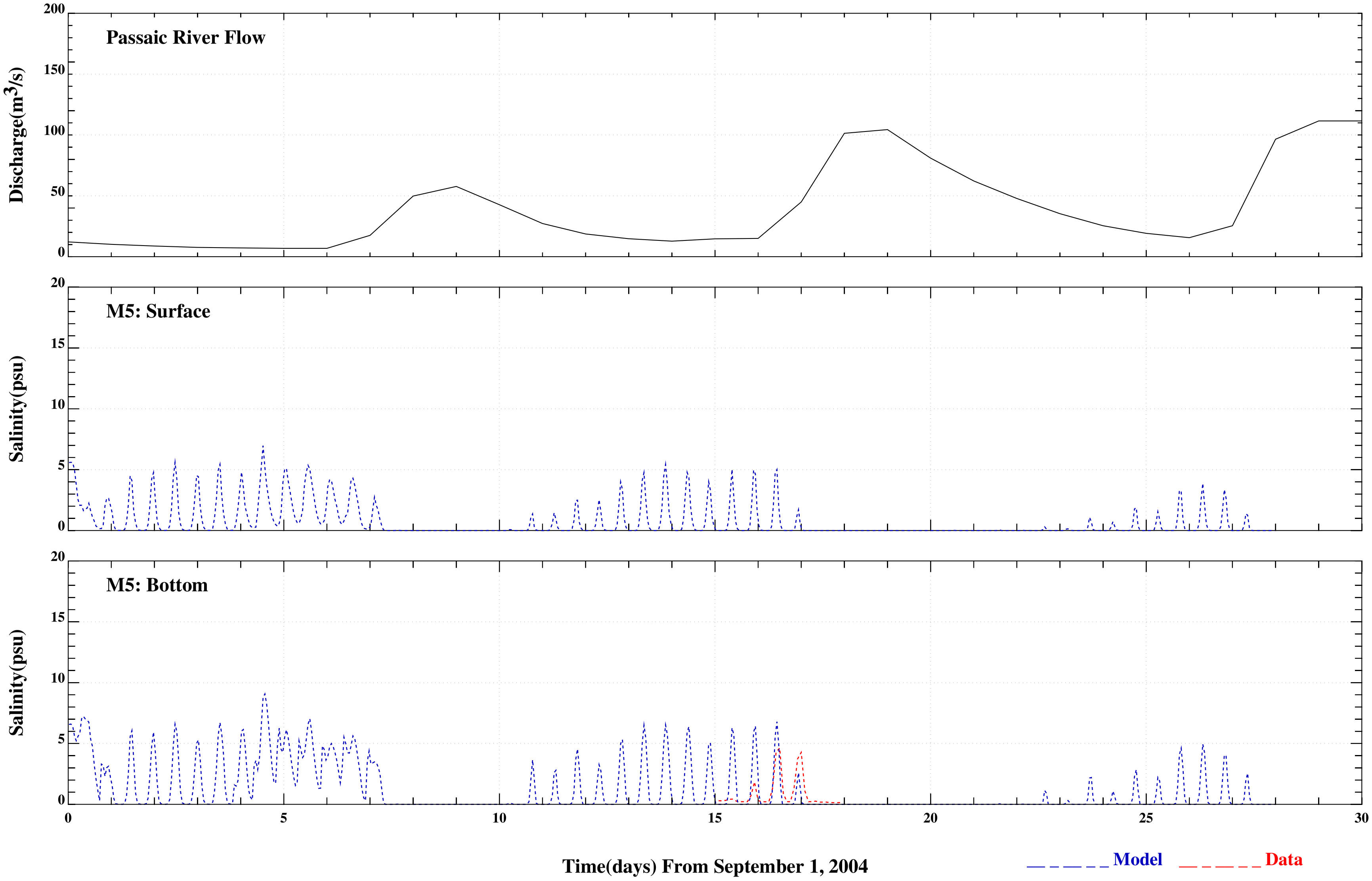

Figure 3-7. Comparison of computed salinity with observed data.

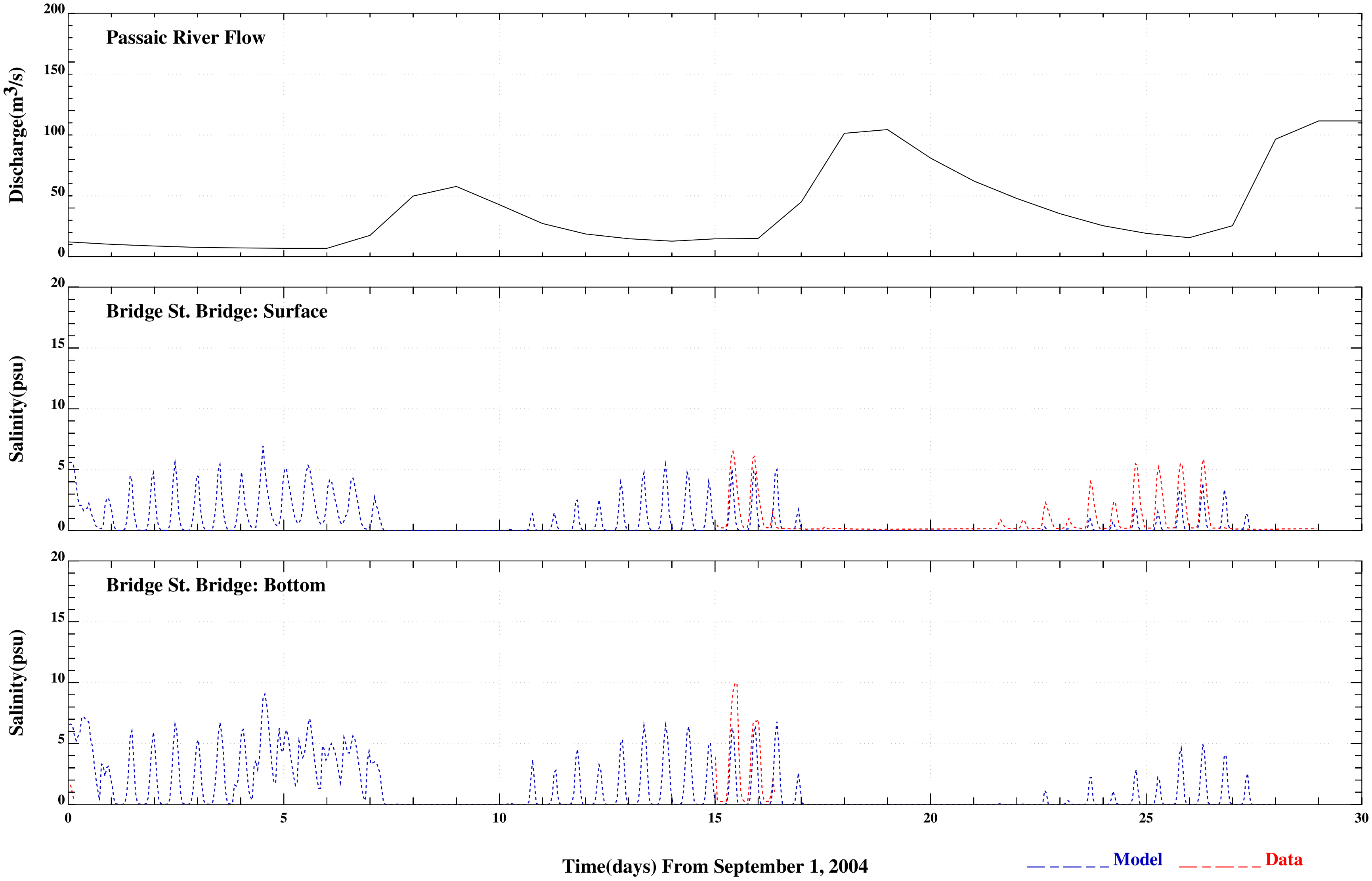

Figure 3-7. Comparison of computed salinity with observed data (continued).

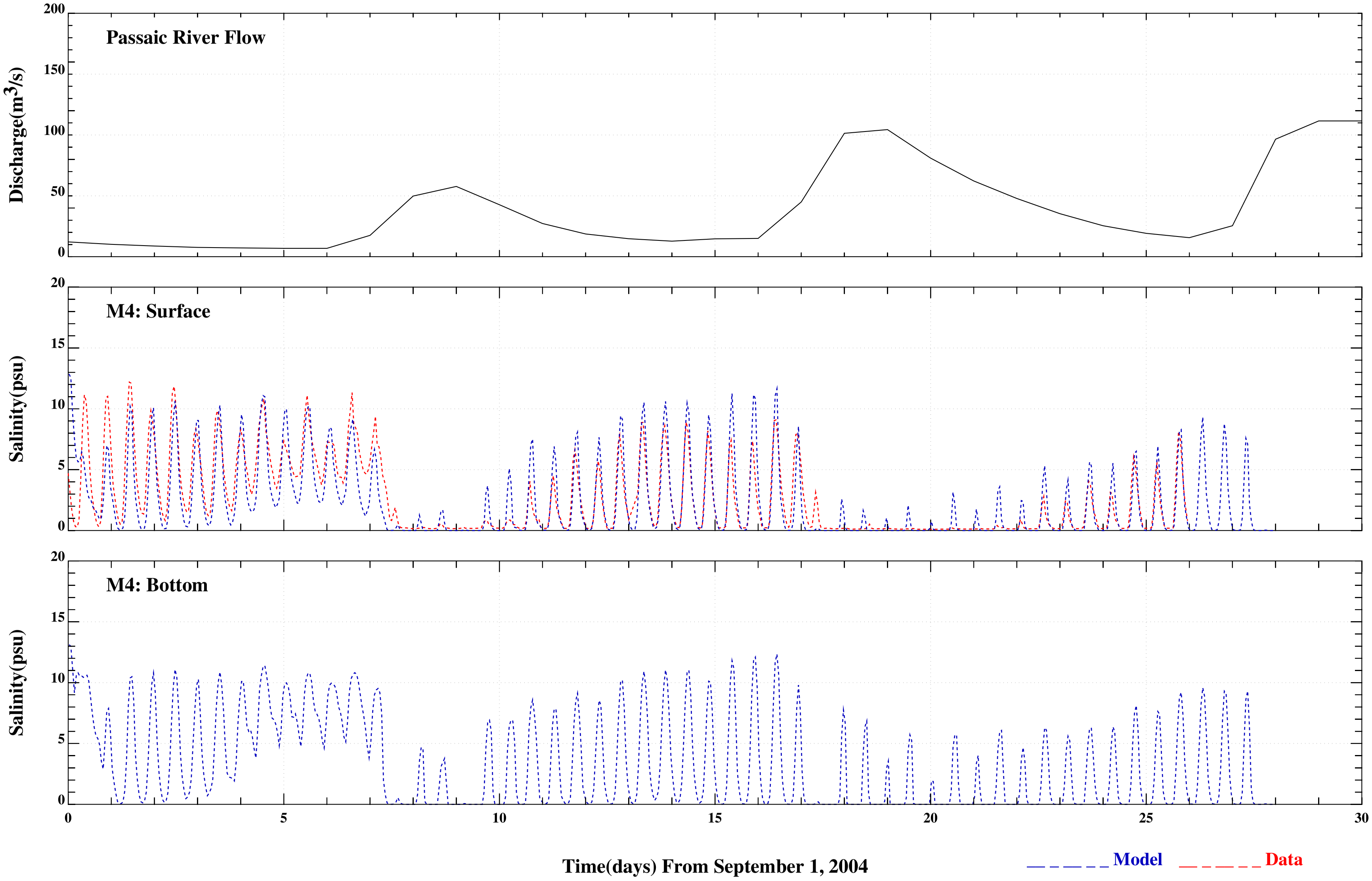

Figure 3-7. Comparison of computed salinity with observed data (continued).

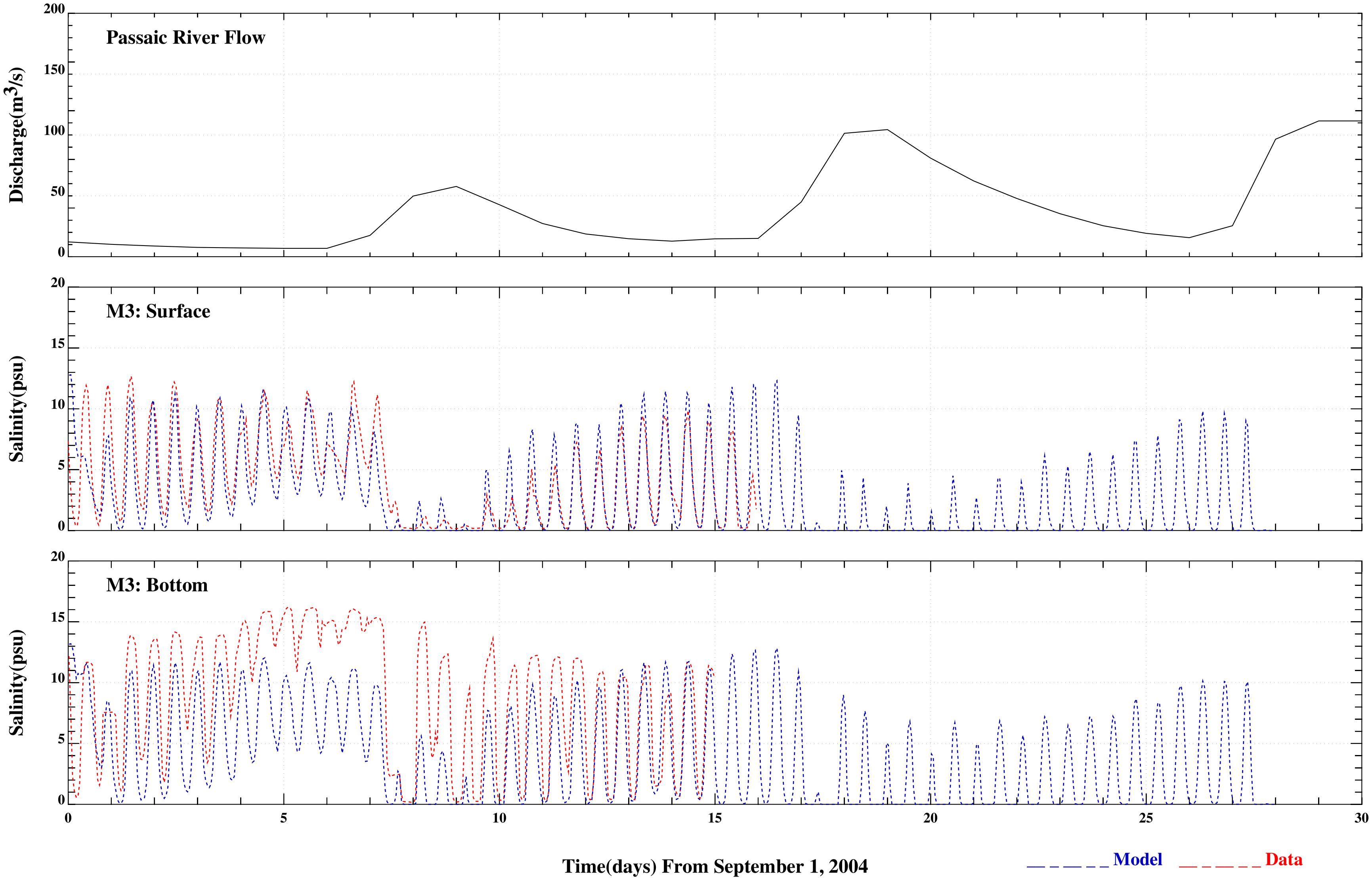

Figure 3-7. Comparison of computed salinity with observed data (continued).

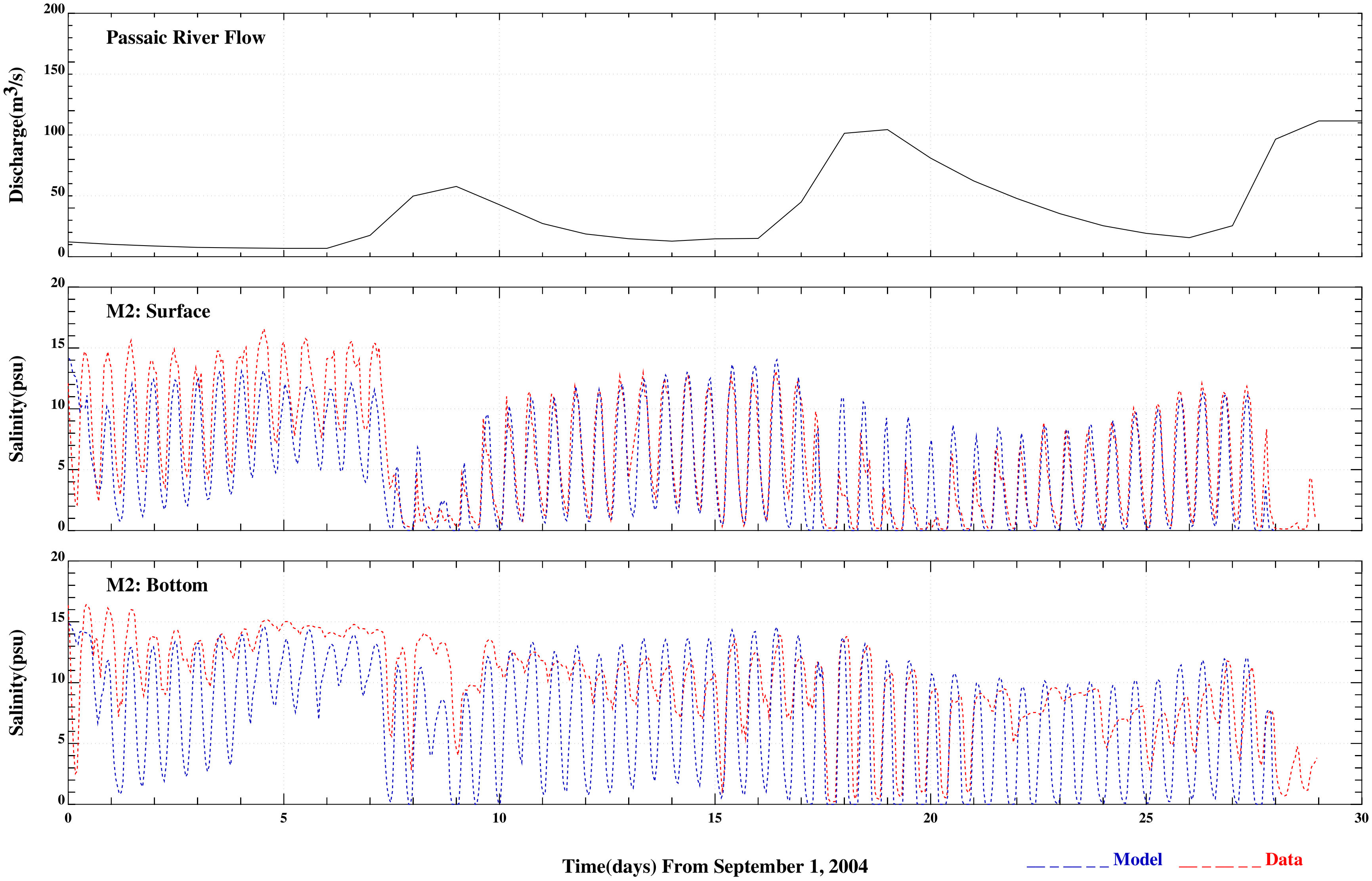

Figure 3-7. Comparison of computed salinity with observed data (continued).

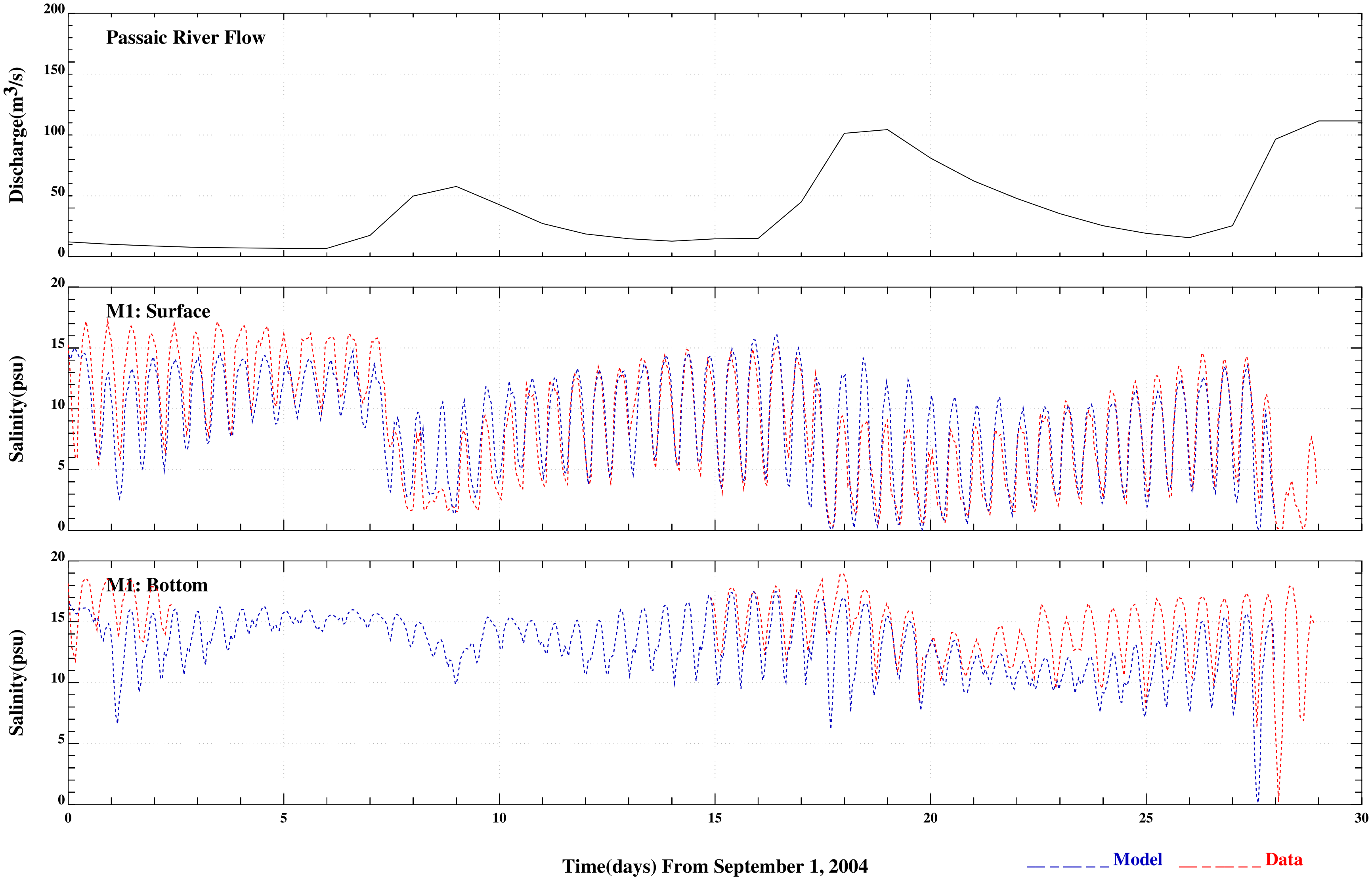

Figure 3-7. Comparison of computed salinity with observed data (continued).

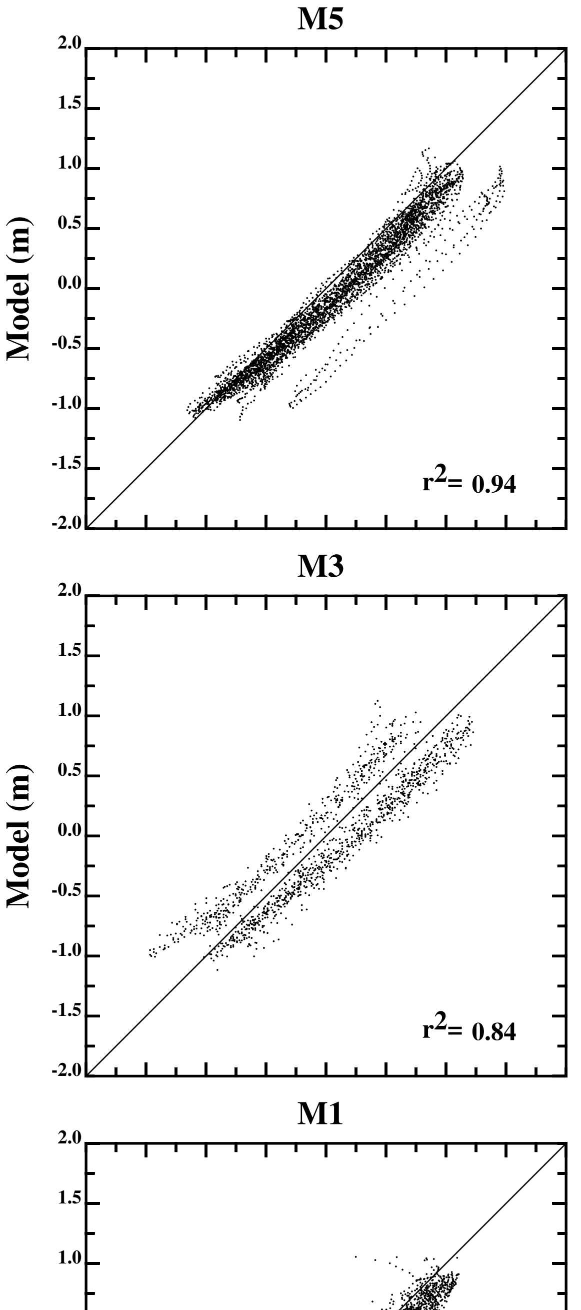

Figure 3-8. Scatter plot of computed water elevation with observed data.

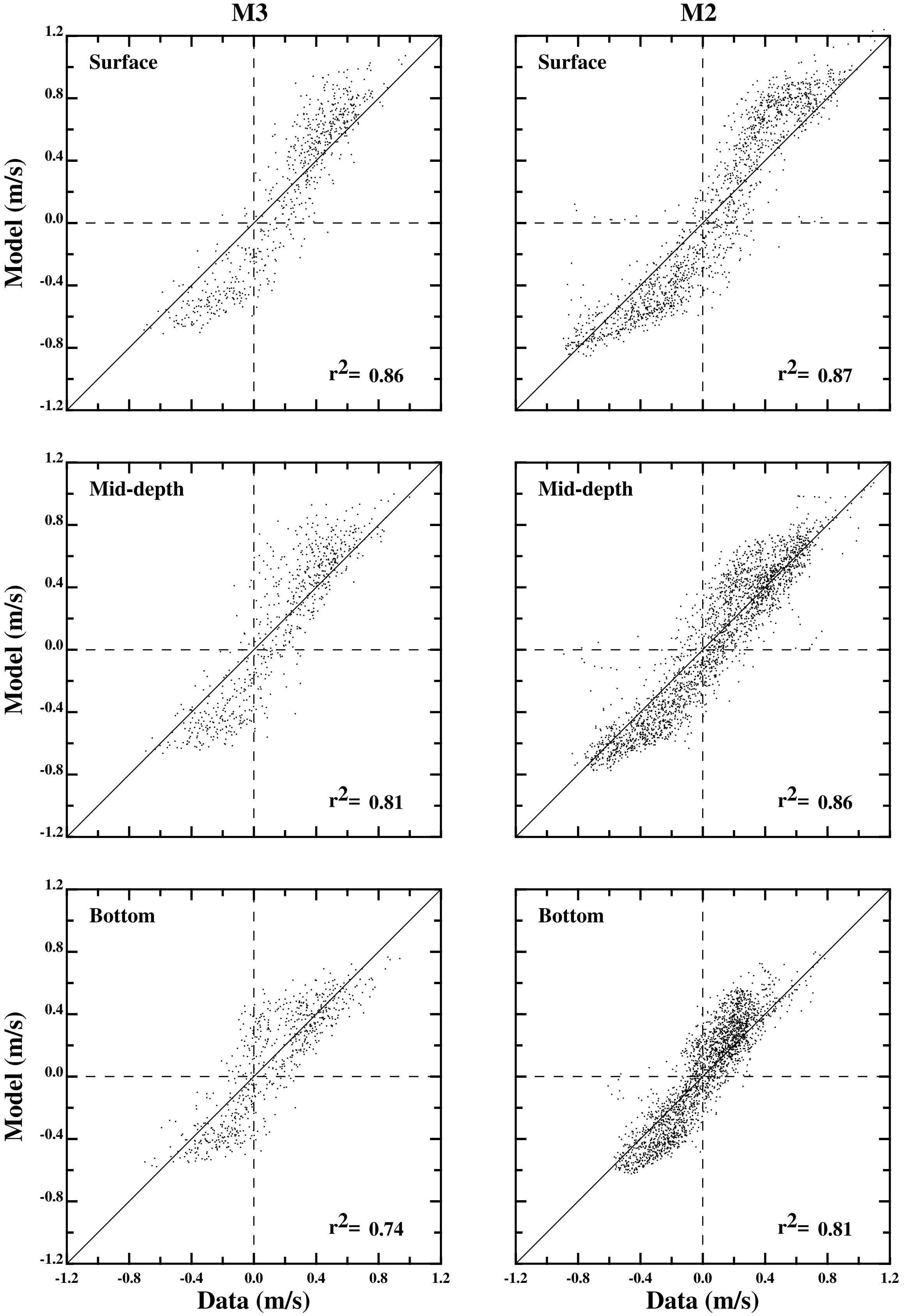

Figure 3-9. Scatter plot of computed current velocities with observed data.

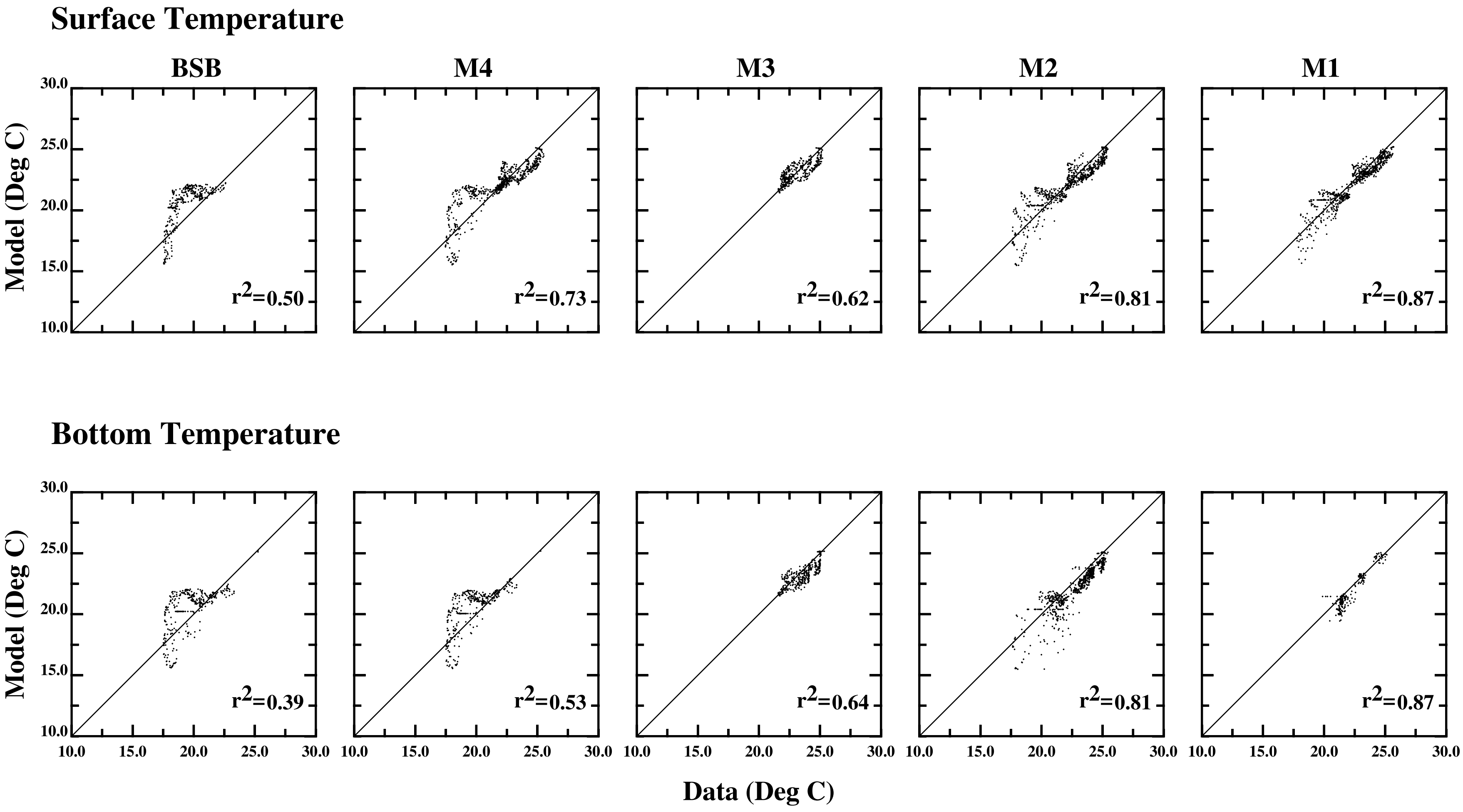

Figure 3-10 Scatter plot of computed temperature with observed data.

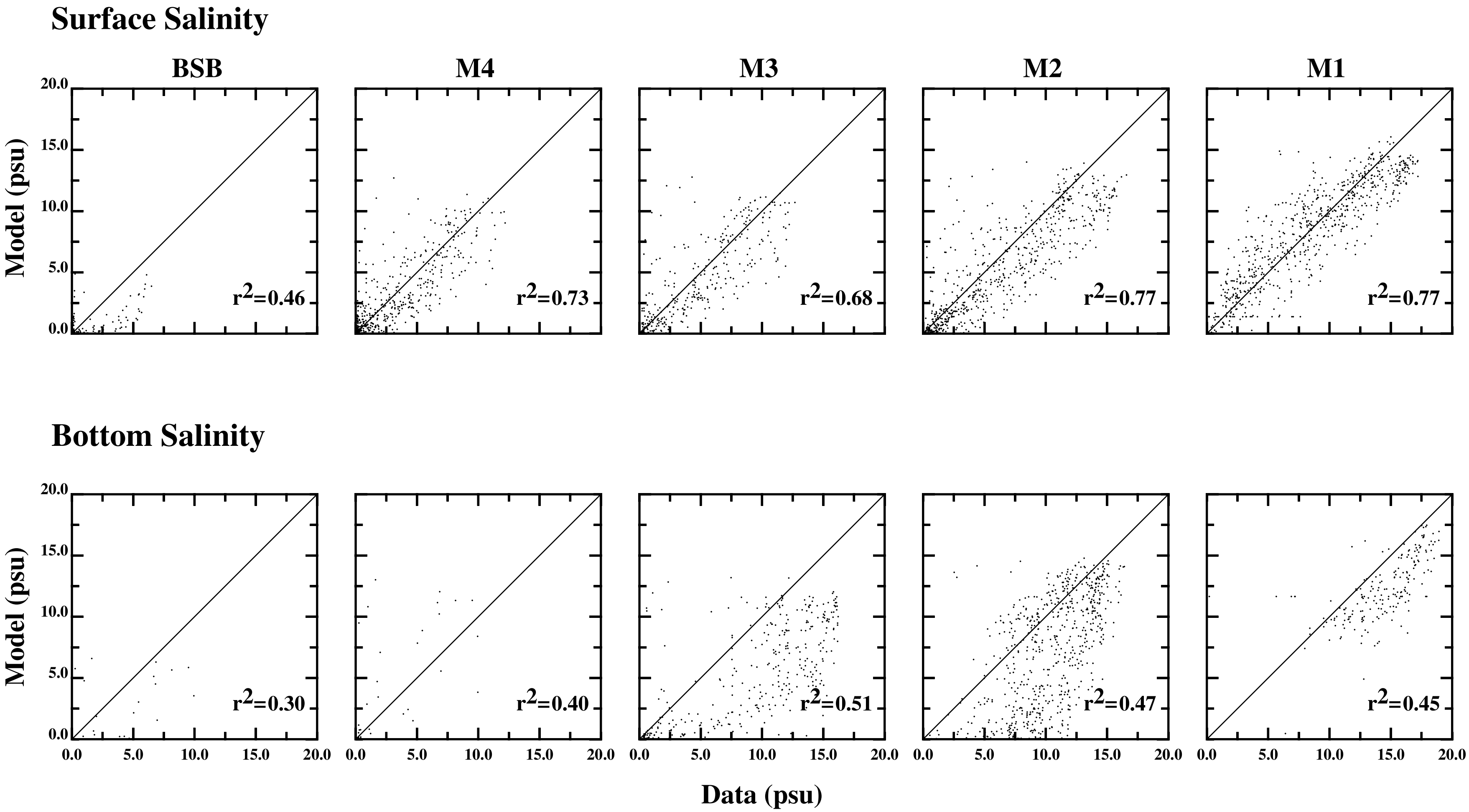

Figure 3-11 Scatter plot of computed salinity with observed data.

SECTION 4

HYDRODYNAMIC MODEL VALIDATION: HURRICANE DONNA

Hurricane Donna, which passed over the NY-area on September 12, 1960, is one of the largest storms ever to hit the region. The hurricane produced extensive coastal flooding in Florida, North Carolina, and many states along the eastern Atlantic seaboard before the eye of the hurricane passed over the eastern end of Long Island. In many parts of New York Harbor, the arrival of the peak surge coincided with the normal high tide for the day (Harris, 1963). NOAA tidal stations in the NY region report the historical maximum water elevation as being attributable to Hurricane Donna. Both the NOAA Battery and Sandy Hook stations recorded a storm surge of 2.56 m (NGVD29) during the hurricane.

Harris (1963) described the characteristics of the hurricane storm surges from 1928 through 1961 and included discussion on storm surge elevations in the NY region that were recorded during Hurricane Donna. To validate the hydrodynamic model using the passage of Hurricane Donna, a model simulation was performed using the water surface elevations observed at the NOAA Battery station and the USGS stream gauge data measured at the Little Falls (Figure 4-1). Physical conditions of the Passaic River and land elevations were assumed the same as the calibration runs. While the surge elevation was one of the highest in the records, the river inflow volumes during the Hurricane were about 5,000 cfs, which is approximately the 1.25 year return flow volume for the station. This suggests that no significant upland rainfall events in the upstream LPR drainage basin were associated with the passage of the Hurricane.

The model results show that the maximum surge elevations during Hurricane Donna are in good agreement with the observed data within the LPR (Figure 4-2). The maximum water elevation rises to 2.6 m up to RM 7 and then increases further upstream. The computed water elevation, 2.93 m, at RM 12 matches very well with the observed elevation. As shown in Figure 4-3, the model computed flooded areas in the LPR basin during Hurricane Donna are estimated to be approximately about 945 acres. However, there are no data available to compare to the modeled flooding areas.

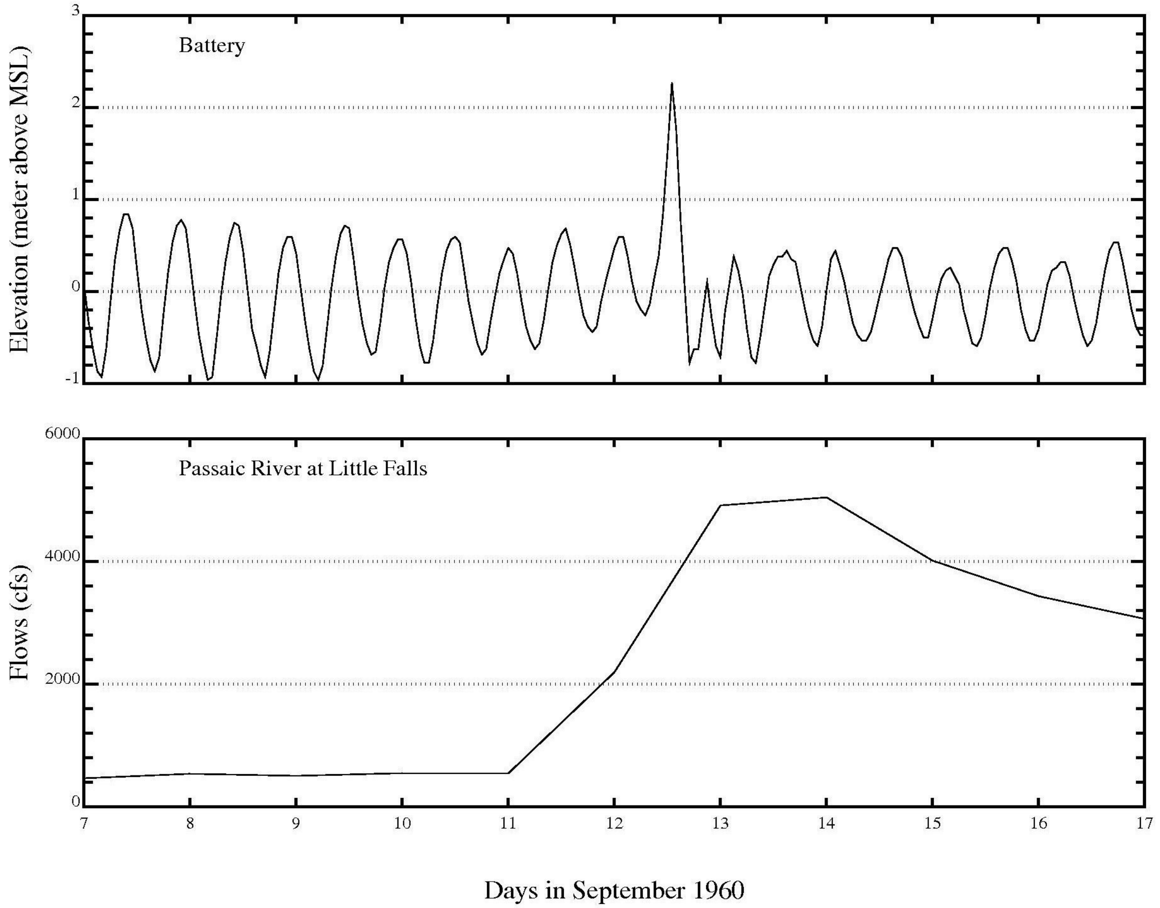

Figure 4-1. Observed water elevation at the Battery (upper frame) and the Passaic River flow at Little Falls (lower frame) during Hurricane Donna.

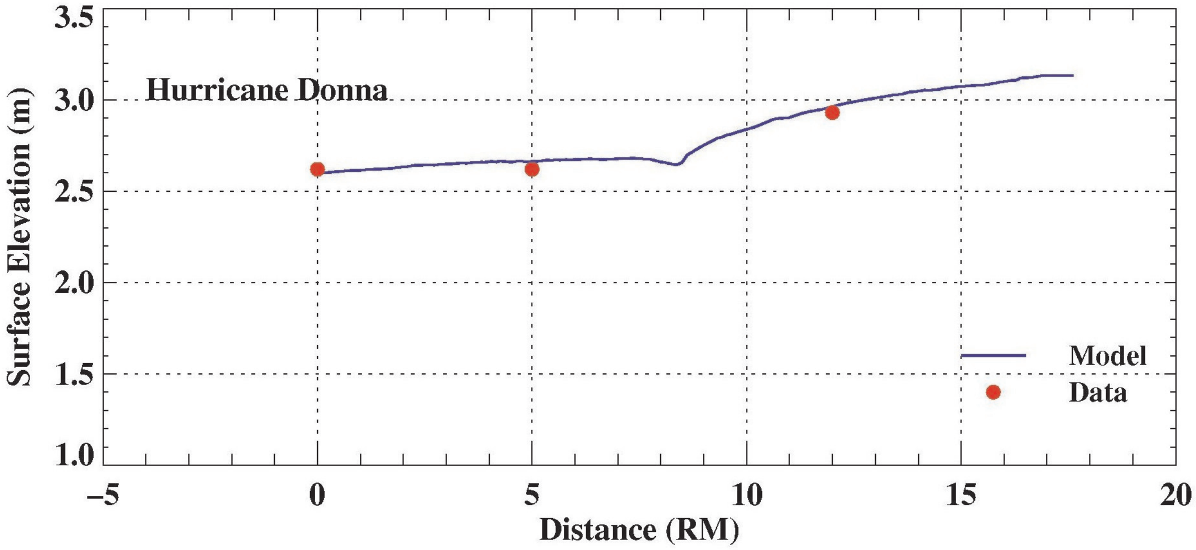

Figure 4-2. Maximum water elevations along the Lower Passaic River during Hurricane Donna.

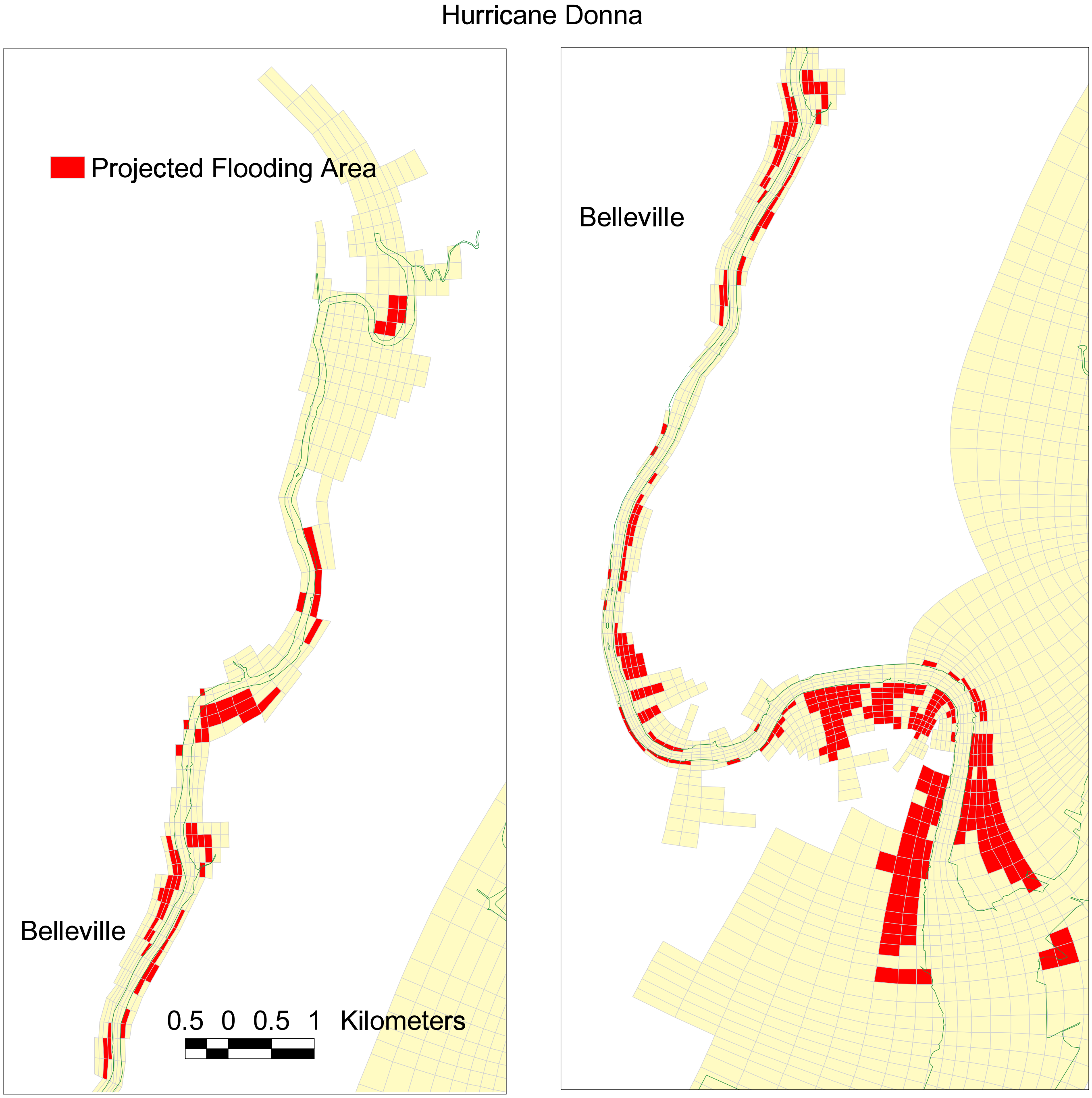

Figure 4-3. Projected flood area during Hurricane Donna.

SECTION 5

SEDIMENT TRANSPORT ANALYSIS OF CAP STABILITY AND EROSION FOR THE LOWER PASSAIC RIVER

5.1 INTRODUCTION

As part of the FFS for the LPR, USEPA is evaluating (among other options) the placement of a sand cap as a remedial alternative to address concerns associated with contaminated sediment in the river. The stability and erosion of the proposed sand capping alternatives were examined using a hydrodynamic and sediment transport model and sediment grain size analyses. Descriptions of the physical setting of the river, elements of cap design, and other aspects of the overall study are presented in the FFS.

5.2 SEDIMENT MODEL FRAMEWORK

Descriptions of the model framework, the grid, and model set-up and parameterization for cap stability and erosion analyses follow.

5.2.1 Model Description and Governing Equations

For the LPR cap stability and erosion analysis, an existing, peer-reviewed sediment transport model (SEDZLJ) (Jones and Lick, 2001) was incorporated into HydroQual's hydrodynamic model framework, ECOMSED (HydroQual, 2004). SEDZLJ uses measured erosion rates for sands obtained from the literature (Roberts et al., 1998) as the basis to compute sediment transport. The incorporation of SEDZLJ into ECOMSED was performed by Dr. Craig Jones (developer of the SEDZLJ computer code) of Sea Engineering, Inc. (SEI). The resulting computer code is termed ECOMSEDZLJ and was peer-reviewed by Dr. Earl Hayter of the USEPA.

The integration of SEDZLJ sediment transport routines into ECOMSED and other related code modifications provided four primary benefits needed to fulfill project goals:

1. Computation of erosion fluxes as a function of measured erosion rates,
2. Division of total erosion fluxes into bedload and suspended load components,
3. Simulation of bedload transport, and
4. Simulation of a user-defined number of particle size classes.

These code modifications substantially improve the ability of ECOMSEDZLJ to simulate the expected differential transport of sediments and cap materials comprised of particles with a continuum of grain sizes and subject to significant bedload transport.

The governing equations for hydrodynamics, following a system of orthogonal cartesian coordinates (*X*, *Y*, *Z*) and using the hydrostatic pressure assumption (*i.e.* the weight of the fluid identically balances the pressure) and the Boussinesq approximation (*i.e.* density differences are negligible unless the differences are multiplied by gravity), are:

Conservation of Mass (Continuity Equation)

$$\nabla \cdot \vec{V} + \frac{\partial W}{\partial Z} = 0 \tag{5-1}$$

Conservation of Momentum (Reynolds Momentum Equations)

$$\frac{\partial U}{\partial t} + \vec{V} \cdot \nabla U + W \frac{\partial U}{\partial Z} - fV = -\frac{1}{\rho_0} \frac{\partial P}{\partial X} + \frac{\partial}{\partial Z}\left(K_M \frac{\partial U}{\partial Z} \right) + F_X \tag{5-2}$$

$$\frac{\partial V}{\partial t} + \vec{U} \cdot \nabla V + W \frac{\partial V}{\partial Z} + fU = -\frac{1}{\rho_0} \frac{\partial P}{\partial Y} + \frac{\partial}{\partial Z}\left(K_M \frac{\partial V}{\partial Z} \right) + F_Y \tag{5-3}$$

$$\rho g = -\frac{\partial P}{\partial Z} \tag{5-4}$$

where: $\vec{V}$ = horizontal vector operator with velocity components *U* and *V*; ∇ = horizontal gradient operator; *U*, *V*, *W* = velocities in the *X*-, *Y*-, and *Z*-direction, respectively; *f* = Coriolis parameter; ρ, ρ_0 = potential and reference density of the fluid; *P* = pressure; K_M = vertical eddy diffusivity of turbulent momentum mixing; and F_X, F_Y = horizontal diffusion in the *X*- and *Y*-direction, respectively.

The horizontal diffusion terms represent small (sub-grid) scale processes not directly resolved by the model grid and are expressed in a form analogous to molecular diffusion:

$$F_X = \frac{\partial}{\partial X}\left(2A_M \frac{\partial U}{\partial X} \right) + \frac{\partial}{\partial Y}\left[A_M \left(\frac{\partial U}{\partial Y} + \frac{\partial V}{\partial X} \right) \right] \tag{5-5}$$

$$F_Y = \frac{\partial}{\partial Y}\left(2A_M \frac{\partial V}{\partial Y} \right) + \frac{\partial}{\partial X}\left[A_M \left(\frac{\partial U}{\partial Y} + \frac{\partial V}{\partial X} \right) \right] \tag{5-6}$$

where: A_M = horizontal diffusivity.

These equations are transformed for use in a curvilinear, orthogonal, sigma (σ)-level coordinate system as described by HydroQual (2004).

The governing equations for erosion in SEDZLJ (Jones and Lick, 2001) are:

Erosion Rate

$$E\left(\tau^{b}\right)=\left(\frac{\tau_{m+1}-\tau^{b}}{\tau_{m+1}-\tau_{m}}\right)E_{m}+\left(\frac{\tau^{b}-\tau_{m}}{\tau_{m+1}-\tau_{m}}\right)E_{m+1} \tag{5-7}$$

$$\ln E(T)=\left(\frac{T_{0}-T}{T_{0}}\right)\ln E^{L+1}+\left(\frac{T}{T_{0}}\right)\ln E^{L} \tag{5-8}$$

where: $E(\tau^{b})$ = erosion rate as a function of shear stress (τ); τ^{b} = bottom shear stress; τ_{m} = shear stress less than τ^{b}; τ_{m+1} = shear stress greater than τ^{b}; $E(T)$ = erosion rate as a function of depth in the sediment bed; T = sediment layer thickness; T_0 = initial sediment layer thickness; and the superscript L and $L+1$ denote depths in the sediment profile at the upper and low limits of the eroding sediment layer. Equations 5-7 and 5-8 can be combined to express the erosion rate as a function of both shear stress and depth. The onset of erosion is identified as the critical shear stress for erosion, τ_{ce}, and is defined as the shear stress at which erosion is initiated at a rate of 10^{-4} cm/s.

For non-cohesive particles, the critical shear stress for erosion can be estimated from the particle diameter as:

$$\tau_{ce}=\begin{cases} d & \text{for } d \le 400\,\mu m \\ 4.14d & \text{for } d > 400\,\mu m \end{cases} \tag{5-9}$$

When the shear stress acting on grains comprising the bed exceeds the critical shear stress for a given grain size, particles may be transported as bedload (in a thin layer in contact with the bed) or as suspended load (fully entrained in the water column away from the bed). The governing equations used to fractionate eroded sediments into bedload and suspended load are:

Non-Cohesive Bedload vs. Suspended Load Fractionation

$$\tau_{cs} = \begin{cases} \dfrac{1}{\rho_w}\left(\dfrac{4w_s}{d_*}\right)^2 & for\ d \le 400\,\mu m \\ \dfrac{1}{\rho_w}(4w_s)^2 & for\ d > 400\,\mu m \end{cases} \tag{5-10}$$

$$f_{SL} = \begin{cases} 0 & for\ \tau^b \le \tau_{ce} \\ \dfrac{\ln(u_*/w_s) - \ln\left(\sqrt{\tau_{cs}/\rho_w}/w_s\right)}{\ln(4) - \ln\left(\sqrt{\tau_{cs}/\rho_w}/w_s\right)} & for\ \tau^b > \tau_{cs} \\ 1 & for\ \dfrac{u_*}{w_s} \le \tau_{cs} \end{cases} \tag{5-11}$$

where: τ_{cs} = critical shear stress for transport as suspended load; w_s = particle fall velocity; d_* = particle dimensionless diameter = $d\left[(\rho_s - 1)g/\nu^2\right]$; d = particle diameter; ρ_s = particle density; f_{SL} = fraction of the total amount eroded that is transported as suspended load; and u_* = shear velocity. The fraction transported as bedload = $(1-f_{SL})$. Equations 5-10 and 5-11 can be used in conjunction with the particle grain size distribution and critical shear stress for erosion to express the erosion flux of sediment by grain size that is transported by bedload and suspended load as a function of the bottom shear stress.

The bottom shear stress acting on the bed (*i.e.* the total bed shear stress) is a function of the total hydrodynamic roughness and can be expressed in terms of two separate components: (1) form roughness; and (2) grain roughness (*i.e.* skin friction). Individual grains on the surface of the sediment bed are subjected only to the skin friction component of the total bed shear stress. The total bed shear stress is computed from the near-bed hydrodynamic velocities according to the "log law" velocity profile:

$$u(z_b) = \frac{u_{*T}}{\kappa}\ln\left(\frac{z_b}{z_0}\right) \tag{5-12}$$

$$\tau_T = \rho u_{*T}{}^2 = \rho C_d\, u(z_b)^2 \tag{5-13}$$

$$C_d = \left(\frac{\kappa}{\ln \frac{z_b}{z_0}} \right)^2 \tag{5-14}$$

where: $u(z_0)$ = near-bed flow velocity, u_{*T} = near-bed shear (friction) velocity; κ = von Karman constant = 0.4, z_b = height of the near-bed layer above the bed surface; and z_0 = bed roughness height; τ_T = total bed shear stress; ρ = density of the fluid; and C_d = coefficient of drag. In the sigma layer coordinate system of the hydrodynamic model, z_b is height above the bed at the mid-point of the bottom sigma layer.

The shear stress component associated with skin friction can be computed as a function of the total bed shear stress as follows (Grant and Madsen, 1982; Glenn and Grant, 1987):

$$u_{*S} = u_{*T} \left(\frac{\ln \frac{z_b}{z_0}}{\ln \frac{z_b}{z_{0S}}} \right) \tag{5-15}$$

$$\tau_S = \rho u_{*S}{}^2 \tag{5-16}$$

where: u_{*S} = the near-bed shear velocity attributable to skin friction; and z_{OS}= the roughness height of particles comprising the bed surface; τ_S = the skin friction shear stress.

As part of the model development process, SEI and HydroQual verified that the SEDZLJ code was properly implemented in ECOMSED by simulating and successfully reproducing the laboratory results of Little and Mayer (1972). The results of these numerical tests are presented in Attachment A. As an additional quality assurance measure, simulations were also conducted using a truncated curvilinear grid for the LPR from RM 0 to RM 12 to ensure that the enhanced transport computations within ECOMSEDZLJ code properly conserved mass. These tests both indicated that the model code functions properly.

5.2.2 Model Set-up and Parameterization

The full model grid for the cap erosion study is shown in Figure 5-1. For reference, land surface elevations relative to the National Geodetic Vertical Datum (NGVD) 1929 are also shown in Figures 2-1 and 2-2. This grid is identical to the grid described in Section 2 of this memorandum. Although the focus of the cap erosion study is the LPR, the full grid includes the Hackensack River and Newark Bay as needed to account for tides and other flow conditions that impact the river. Model depths for the river were based on surveys compiled by the USACE as described in Section 2. The model accounts for the wetting and drying of grid cells as needed to account for changing water surface elevations that occur as a result of fluctuating tidal conditions. This is a necessary aspect of model formulation because there are several shallow locations in the Passaic River where grid cells representing portions of the river bed can become exposed (*i.e.*, dry) during low points in the tidal cycle.

The computational domain consists of 68×170 grid cells in the horizontal plane and 11 equally spaced σ-levels in the vertical plane (*i.e.*, 10 vertical segments). The model open boundaries are located at the entrance to Kill van Kull from New York Harbor and the entrance to Arthur Kill from Raritan Bay at South Amboy. Throughout the remainder of this section, the visual display and descriptions of model results focus on the LPR from RM 0 to RM 8.3.

It is important to note that boat wake and wind-induced waves were not considered in this analysis. With respect to boat wakes, Dr. Craig Jones (pers. comm.) suggested that boat wake or propeller wash effects would largely act to "mix" the capping material locally, since it would be unlikely that a boat (or boats) would follow the exact same path within the river time after time. With respect to wind-induced waves, due to the narrowness of the river and due to the meandering nature of the river it is unlikely that significant wind-waves could develop.

5.2.3 Description of Modeling Scenarios

Simulations were conducted to explore the stability and erosion of a sand cap in response to flow events of different magnitude. For these analyses, Passaic River flow records from the USGS Little Falls gauging station for the period 1891 through 2005 were analyzed to determine return flows, including flood conditions, of different recurrence intervals. The drainage area at the Little Falls gage (780 square miles) accounts for 77% of the total Passaic River basin (1,013 square miles). To compute total flows for the entire basin, the flows at Little Falls were multiplied by a factor of 1.3 to account for the portion of the drainage basin below Little Falls and to represent the flow at the river mouth. For this study, total basin flows were specified as inputs at Dundee Dam (RM 17) to simplify model set-up. This is a reasonable approach since nearly all of the remaining tributary inputs to the river

(Saddle River, Third River, etc.) occur near or above the upstream limit of the cap area and direct drainage is expected to be small. This also represents a worst case for the stability analysis because the entire flow through the system occurs along the entire length of the capped area. The return flows used for this study, based on a statistical analysis (log – normal recurrence internal) of daily flow data, are summarized in Table 5-1. Further details of the return flow analysis are provided in Section 6.1.1 of this memorandum. The one-month, six-month and one-year return flows were estimated separately. This was accomplished by analyzing probability of occurrence using the recent 20 years of monthly peak flows at Little Falls. The one-month return flow was estimated as the 50th percentile, the six-month return flow as the 83.3th percentile and the one-year return flow as the 91.7th percentile, which yielded 5,060 and 5,840, and 8,050 cfs, respectively, when corrected for the below Little Falls drainage area.

Table 5-1. Lower Passaic River Return Flows for Cap Stability and Erosion Analysis

Return Period	***Flow (cfs)***	
	Little Falls	*River Mouth*
1-month	3,900	5,060
6-month	4,500	5,840
1-year	6,200	8,050
2-year	6,751	8,767
5-year	9,968	12,945
10-year	12,219	15,869
25-year	15,280	19,844
50-year	17,465	22,681
100-year	19,808	25,725

The erosion and stability of two basic capping scenarios were evaluated in the study:

1. Placement of a two foot thick sand cap across entire bed of the LPR from RM 0 to RM 8.3 (Figure 5-2), and
2. Placement of armor stone on selected model cells to protect the cap and reduce the potential for erosion. The armored areas were pre-dredged to a depth of 2 feet before 2 feet of sand and 2 feet of armor (rock cobble) are put in place. (Figure 5-2).

For scenarios that include cap placement only (no armor), the placement of the cap on the bed reduces river depths (increases bed elevations) by two feet throughout the capped area. For armor placement scenarios, it was assumed that pre-dredging would be conducted such that bed elevations in armored areas would be reduced by the specified thickness of the armor layer prior to armor placement such that bed elevations after armoring would be no greater than for the sand cap alone.

For each of these scenarios, two types of sands were evaluated as cap materials: (1) Ambrose Sand (AS) (d_{50} = 386 μm); and (2) Upland Borrow Sand (UBS) (d_{50} = 1,441 μm). Grain size distributions for these materials and corresponding particle size classes used in ECOMSEDZLJ are presented in Tables 5-2. To best represent the spectrum of particles comprising the capping sands in the model, AS was simulated as four size classes and UBS was simulated as five size classes. The armor stone was considered to be non-erodible under the flow conditions simulated (*i,e.* 6-inch angular rock). All design aspects of cap placement, thickness, the types of sand evaluated, and sizing of armor stone were specified in the FFS.

Table 5-2. Characteristics of Capping Materials

Property	*Size Class*				
	1	2	3	4	5
Ambrose Sand					
d_p (μm)	125	222	1,020	3,360	N/A
Composition By Weight (%)	10	80	6	4	N/A
τ_{ce} (dynes/cm^2)	1.2	1.7	5.4	25	N/A
w_s (cm/s)	0.9	2.3	11.3	25	N/A
τ_{cs} (dynes/cm^2)	1.2	2.4	16.8	81	N/A
Upland Barrow Sand					
d_p (μm)	150	300	1180	2360	4750
Composition By Weight (%)	5	25	35	30	5
τ_{ce} (dynes/cm^2)	1.6	1.9	6.5	16	39.4
w_s (cm/s)	1.2	3.4	12.6	20	30
τ_{cs} (dynes/cm^2)	1.6	2.8	21	53.4	121

For each size class simulated, the particle diameter given is the mean particle diameter of the grains in that class. As a rule of thumb, the largest size class is chosen as the largest size for which more than 2-3% of the mass is retained on a sieve. Similarly, the smallest size class can be chosen as the smallest size for which 2-3% of the mass is retained on the smallest sand-sized sieve. For AS, the grain size distribution is comparatively narrow with 80% of the distribution having a diameter of 222 μm and the entire distribution could be represented with four size classes. For the UBS, the size distribution was less well sorted, with up to 5% of the distribution in the range of 4,750 μm. Consequently, the UBS was represented as five size classes. Additionally, since a wider size range occurs in the upland sand, an additional size class is needed to more accurately simulate the expected coarsening of the bed that would occur over time.

Four river depth conditions were also explored as part of the analysis: (1) 8-mile Cap – Armor Area Pre-dredging Scenario: the bottom of the LPR capped from RM 0 to RM 8.3, with two feet of pre-dredging in armored areas, resulting in post-remediation depths two feet above pre-remediation bathymetry; (2) 8-mile Cap – Full Pre-dredging Scenario: the bottom of the LPR pre-dredged two to four feet from RM 0 to RM 8.3 prior to cap placement, resulting in post-remediation depths at the same elevation as pre-remediation bathymetry; (3) Current Navigation Usage – Full Pre-dredging Scenario: the bottom of the LPR pre-dredged from RM 0 to RM 8.3 prior to cap placement with a 21-31 ft navigation channel between RM 0 and RM 2.5; and (4) Future Navigation Usage – Full Pre-dredging Scenario: the bottom of the LPR pre-dredged from RM 0 to RM 8.3 prior to cap placement with a 15-31 ft navigation channel between RM 0 and RM 8.3. For both navigation usages, present depths were applied outside of the pre-dredged areas.

Tables which summarize the navigation channel depths and corresponding modeled depths for the Current Navigation Usage and Future Navigation Usage scenarios are included as Tables 5-3 and 5-4, respectively. The depth modeled corresponds to the approximate depth of the top of the cap or backfill. Further discussion on how the top of cap or backfill is determined can be found in the FFS.

Table 5-3. Relationship between Proposed Navigation Channel Depth and Modeled Depth – Current Navigation Usage (Unit: feet, MLW)

Location	Constructed Depth	Proposed Depth	Treatment in Navigation Channel	Modeled Depth for Future Use
RM 0-RM 1.2	30	30	Backfill	31
RM 1.2-RM 2.5	30	16	Cap	21
RM 2.5-RM 8.3	20	Existing Bathymetry	Cap	Existing Bathymetry

Table 5-4. Relationship between Proposed Navigation Channel Depth and Modeled Depth – Future Navigation Usage (Unit: feet, MLW)

Location	Constructed Depth	Future Use Depth	Treatment in Navigation Channel	Modeled Depth for Future Use
RM 0-RM 1.2	30	30	Backfill	31
RM 1.2-RM 2.5	30	16	Cap	21
RM 2.5-RM 3.6	20	16	Backfill	21
RM 3.6-RM 4.6	20	10	Cap	15
RM 4.6-RM 8.1	16	10	Backfill	17
RM 8.1-RM 8.3	10	10	Backfill	11

Major high flow hydrographs observed between 1891 and 2005 at the USGS Little Falls gauging station were reviewed for the shape and duration of each flow event. Most of high flow events recorded at the Little Falls station were less than five days in duration. The high flow event observed in April 1984, with a peak flow of 18,400 cfs, was selected for this study. This is the highest flow event recorded at Little Falls in recent decades. The peak of each flow event was coupled with the peak spring tide at the open boundaries, based on astronomical harmonic tidal constituents obtained from NOAA. For the AS capping, 10-day simulations were conducted for the 1-year, 25-year and 100-year return flow events and for the UBS capping, 10-day simulations were conducted for each of the nine identified return flow events. For the combination of UBS capping, armoring, and river depth conditions, 10-day simulations were conducted with the 100-year return flow event. Hydrographs for each return flow were constructed by scaling the April 1984 flow curve by the ratio of peak flows. All hydrographs have the same shape and consist of the following: ramp-up from a zero initial velocity condition (days 1-2), rising limb (days 3-5), peak (day 5), and falling limb (days 5-10).

To represent sand in capped areas, the bottom roughness height used in the model is the same as determined during the prior hydrodynamic model calibration (Z_0 = 0.001 m). To represent the expected additional roughness and flow resistance caused by large, angular stone, the bottom roughness height in armored areas (on a cell by cell basis in the model) was increased by a factor of 10 (Z_0 = 0.01 m).

Erosion characteristics (τ_{ce}) for sands were determined based on the measurements of Roberts et al. (1998). Fall velocities (w_s) for each particle type simulated were determined from the formula of Cheng (1997). Similarly, the critical shear stress for transport as suspended load (τ_{cs}) was determined from fall velocity and particle diameter as described from Equation (5-9) following the method of van Rijn (1984). A summary of these parameters is also presented in Table 5-2.

5.3 MODEL APPLICATION AND RESULTS

Computer simulations of hydrodynamics and cap sand sediment transport for the LPR were performed. Simulations were conducted across a range of flow events for combinations of sand cap materials, armor stone, and channel depth conditions. Results of the ECOMSEDZLJ model application to the study area are described below.

5.3.1 Cap Stability and Erosion Analysis: Ambrose Channel Sand

ECOMSEDZLJ was used to examine the response of sands taken from the Ambrose Channel, located at just outside the mouth of New York/New Jersey Harbor, and placed on the river bed. The model was set to run four non-cohesive particle size classes as defined in Table 5-2. Ten-day simulations were set up and conducted for three return flow events. Results for all simulations were summarized for the river bed from RM 0 to RM 8.3 in terms of the cross-river averaged net bed elevation change at the end of the simulation, the maximum bed erosion computed during the simulation period and bottom shear stress as presented in Figure 5-3. Bottom shear stresses discussed in this section refer to the "skin friction" component of the total bottom shear stress. Results for each of the three individual events showing net bed elevation change, the maximum bed erosion and bottom shear stress for each model cell are presented in Attachment B. Figure 5-4 displays the horizontal distributions of the maximum bed erosion for the 1-year and 25-year flow events. In this sequence of figures, blue shaded areas indicate net deposition while red shaded areas indicate net erosion. It should be noted that in some locations it is possible that bed erosion could occur initially as the smaller sand particle size classes are eroded but later these areas show a net increase in bed elevation from the relocation of upstream sand particles.

The model results in Figures 5-3 and 5-4 indicate that excessive transport and net erosion of an Ambrose Sand cap can be expected. At some locations along the river, nearly the entire thickness of the cap (2-feet) could be eroded by a 25-year event. Around RM 5.5, even a 1-year event has the potential to erode approximately 1-foot (~30 cm) of the sand cap.

Bottom shear stresses vary by position along the river as well as with freshwater and tidal conditions. Note that the maximum cross-sectionally-averaged bottom shear stress is greater than 40 dynes/cm^2 for the 100-year flow condition (Figure 5-3). This is substantially larger than the critical shear stress for erosion of even the largest particles used in the AS grain size distribution (maximum τ_{ce} = 25 dynes/cm^2).

These results indicate that fine to medium sand capping materials such as AS will not be stable unless substantial areas of the cap are also protected with armor stone. In this case, the extent of erosion was judged to be so severe and so extensive that no further simulations using AS as a cap material were attempted.

5.3.2 Cap Stability and Erosion Analysis: Upland Borrow Sand

ECOMSEDZLJ was also used to examine the response of UBS placed on the river bed. Similar to the AS capping scenarios, ten-day simulations were set up and conducted for each of the nine return flow events. Results for all simulations were summarized for the river bed from RM 0 to RM 8.3 in terms of the cross-river averaged net bed elevation change at the end of the simulation, the maximum bed erosion during the simulation, and the bottom shear stress as presented in Figure 5-5. UBS was divided into five grain size classes for use in the sediment transport model. The size classes and initial distributions for each capping segment were assigned as presented in Table 5-2. Results for each of the nine individual events showing net bed elevation change, maximum bed erosion, and bottom shear stress for each model cell are presented in Attachment C. In this sequence of figures, blue shaded areas again indicate net deposition and red shaded areas indicate net erosion.

Because it contains an appreciable fraction of very coarse sand and very fine gravel, the UBS is subject to less erosion and generally is expected to be more stable than AS. To further illustrate the erosion characteristics of the borrow sand, 10 representative locations along the river, as identified in Figure 5-6, were examined in more detail. Bed elevation change (BEC) and bottom shear stress (BSS) over time are shown for each of these locations in Figure 5-7. Each location was represented by a single grid cell rather than the cross-river averages presented in Figure 5-5. The cells at RM 3.06, 3.48, 3.80, 5.30 and 6.47 are located in the deep channel and at RM 1.74, 2.52, 4.56 and 6.06 are located on the side channel of the river. Basically the cells in the mid-channel correspond to higher bottom shear stress and, therefore, higher rates of erosion. The results presented in Figure 5-7 and Attachment C also indicate that in most locations, for most flow conditions, bottom shear stresses typically do not exceed the critical shear stress for erosion of the largest grain size (4,750 μm, τ_{ce} = 39.4 dynes/cm^2). However, for larger events (25-year and larger) more than 10 cm of erosion can occur at some of the locations in the capped region.

Although the very coarse sand and very fine gravel components of the UBS provide some measure of stability for the cap, at a small number of high bottom shear stress locations more severe erosion is expected. For example, for events with a 50-year or longer return interval, almost one foot (~30 cm) of the cap is still expected to erode at several locations around RM 3, RM 5 and RM 8.

To address areas with more severe erosion (*i.e.*, more than one inch (2.54 cm) of erosion for any flow event), a further series of simulations was conducted to examine the effectiveness of placement of protective armor stone over the sand cap. Based on a review of the locations subject to one inch or more erosion, areas for armor stone placement and protection were identified as presented in Figure 5-2. For these armoring simulations, 140, 104, 101 and 42 individual cells on the model grids were armored for the 8-mile Cap – Armor Area Pre-dredging, the 8-mile Cap – Full Pre-dredging, the Current Navigation Usage - Full Pre-dredging and the Future Navigation Usage - Full Pre-dredging, respectively. The navigation channel restoration areas are presented in Figure 5-8.

Armored cells were assumed to be non-erodible. To account for the expected increase in roughness and flow resistance caused by the placement of large, angular stone, the bottom roughness height (Z_0) in armored cells was increased by a factor of 10 from 0.001 to 0.01 m. To represent a worst case scenario, simulations were conducted using the UBS for the 100-year return flow under four scenarios, with and without armoring. Cross-river averaged net bed elevation change, maximum bed erosion, and maximum bottom shear stresses are presented in Figure 5-9. Net bed elevation change, maximum erosion and bottom shear stress for each scenario (capping only and capping/pre-dredging, and two capping scenarios plus armoring for the existing depth and similarly for navigation channel restoration) are presented in Attachment D. For capping scenarios, navigation channel restorations, especially the future navigation usage, significantly reduce cap erosion between RM 0 and 8.3. For capping plus armoring scenarios, armoring greatly reduces cap erosion regardless of channel depth configuration (*i.e.* with or without navigation channel restorations). To obtain the final armored cells, iterative simulations were conducted. For each iteration, HydroQual provided the maximum erosion values for each grid cell to Malcolm Pirnie, Inc. (MPI). Then, MPI identified the grid cells to be armored and a new simulation was conducted with the adjustment of armored areas. This procedure was repeated until no sand capped cells were found eroding more than 1 inch (2.54 cm) after the 10-day simulation for the 100-year return flow under the four different scenarios.

5.4 DISCUSSION

The model results indicate that severe erosion is expected for a cap composed of AS. Even under low to moderate flows such as the 1-year return flow event, approximately 10 cm of the cap could erode in areas that experience high bottom shear stresses. Over time, a sequence of small events could lead to significant cap loss. For high flow conditions and in certain locations, the entire depth of the cap could be eroded in a single event. This high potential for erosion is a reflection of the small median particle diameter (222 μm) and narrow range of grain sizes comprising this material.

In contrast, the UBS is expected to be far more stable under typical flow conditions in the Passaic River. Although significant erosion may still occur along some areas of the bed, the depth of maximum erosion is expected to be much lower than for the AS. This decreased erosion potential is a reflection of the larger mean particle diameter (1,440 μm) and broad range of grain sizes comprising this material, including very coarse sand and very fine gravel. However, along high shear stress areas of the bed, even UBS could be subject to significant erosion.

The placement of armor stone in high shear stress areas of the bed is expected to greatly increase the stability of the cap. Such armoring is expected to improve cap stability regardless of channel depth configuration. With armor, the maximum erosion was found to be less than 1 inch (2.54 cm) for the 100-year return flow.

It is worth noting that cap stability may be influenced by smaller, more frequent events as well as for larger storms. A series of smaller to moderate events may collectively contribute to more substantial erosion than any single event. This suggests that the placement of protective armor may be a necessary component of cap design for the LPR even if large events were not considered.

It should also be noted that the analysis conducted herein does not include consideration of any sands (non-cohesive) and cohesive solids that might enter the LPR system at the Dundee Dam or from rainfall related runoff from the drainage area below the Dundee Dam. Hence, the cap erosion results presented in this memorandum may be considered to be conservative in nature.

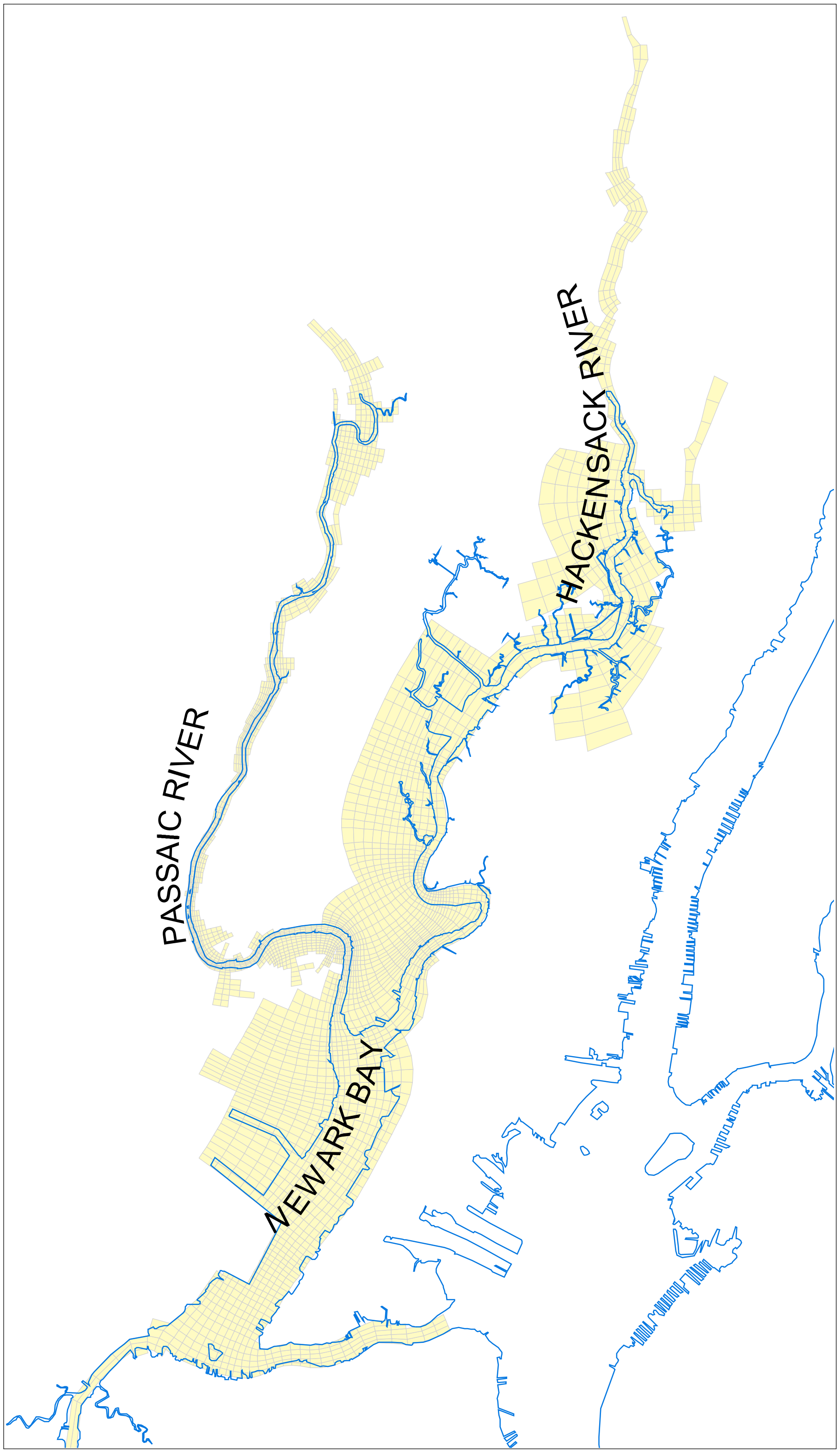

Figure 5-1. Study area of the Lower Passaic River, the Hackensack River and Newark Bay with the orthogonal curvilinear model grid.

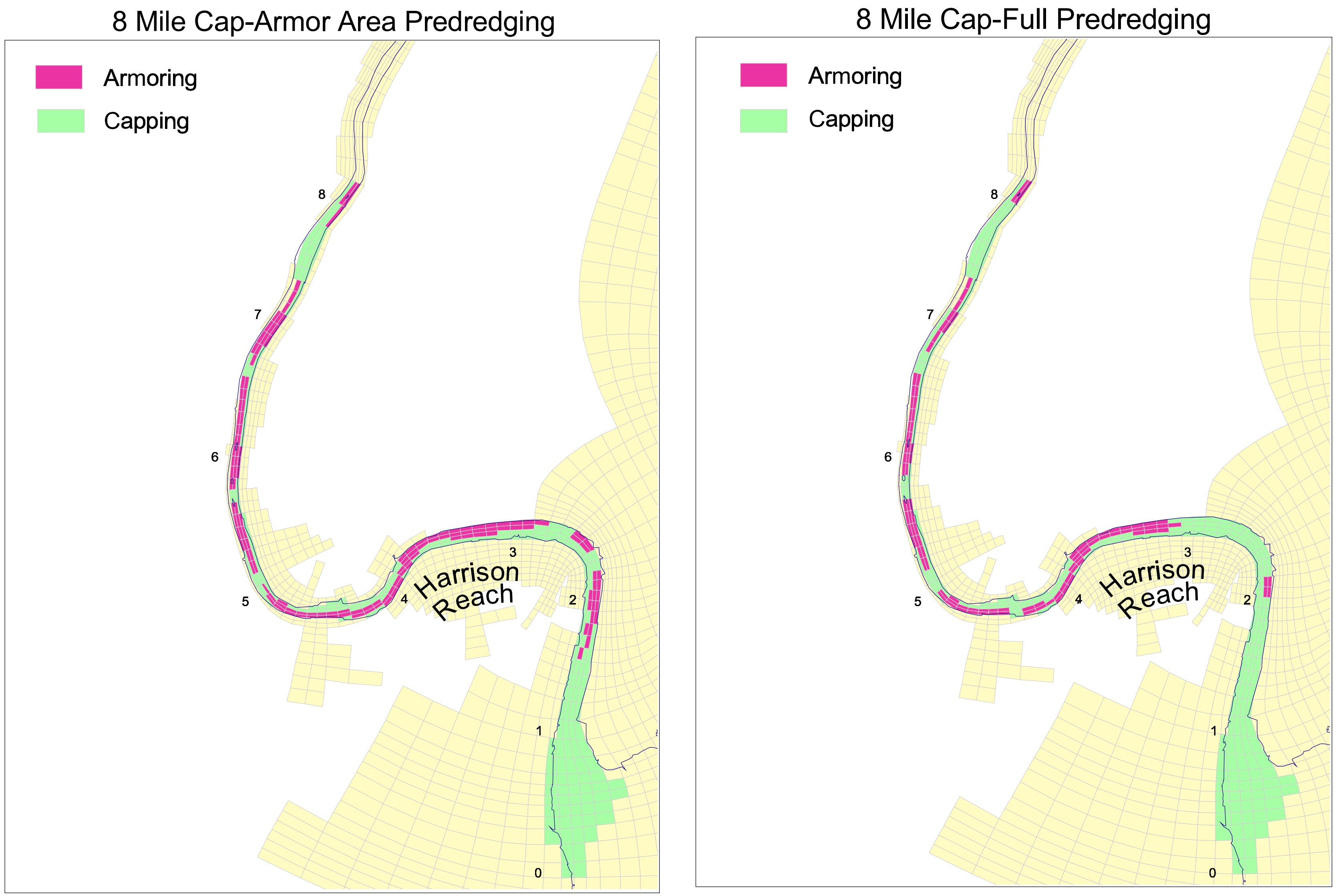

Figure 5-2. Capped and armored areas between RM 0 and RM 8.3 for different simulation scenarios.

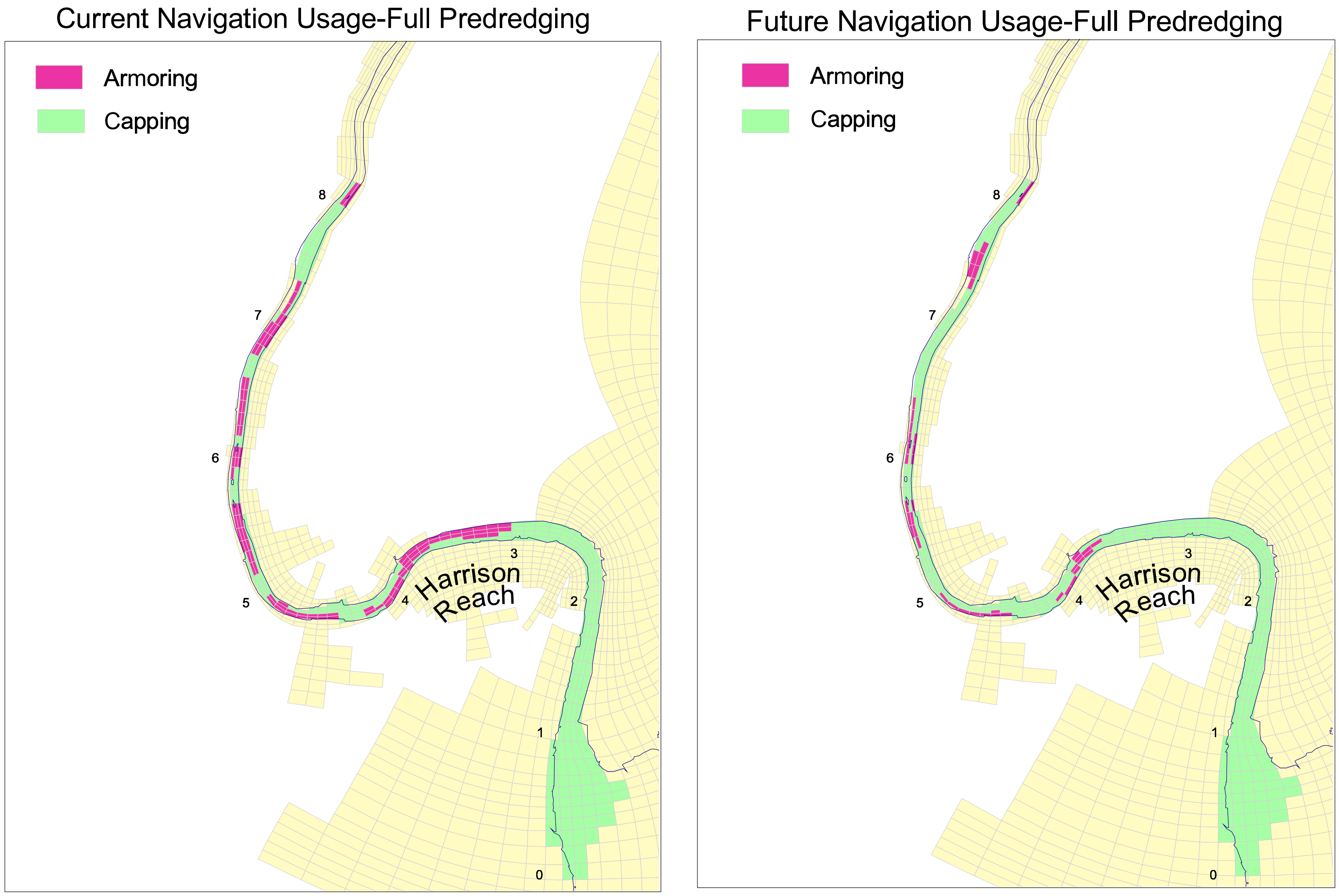

Figure 5-2. Capped and armored areas between RM 0 and RM 8.3 for different simulation scenarios (continued).

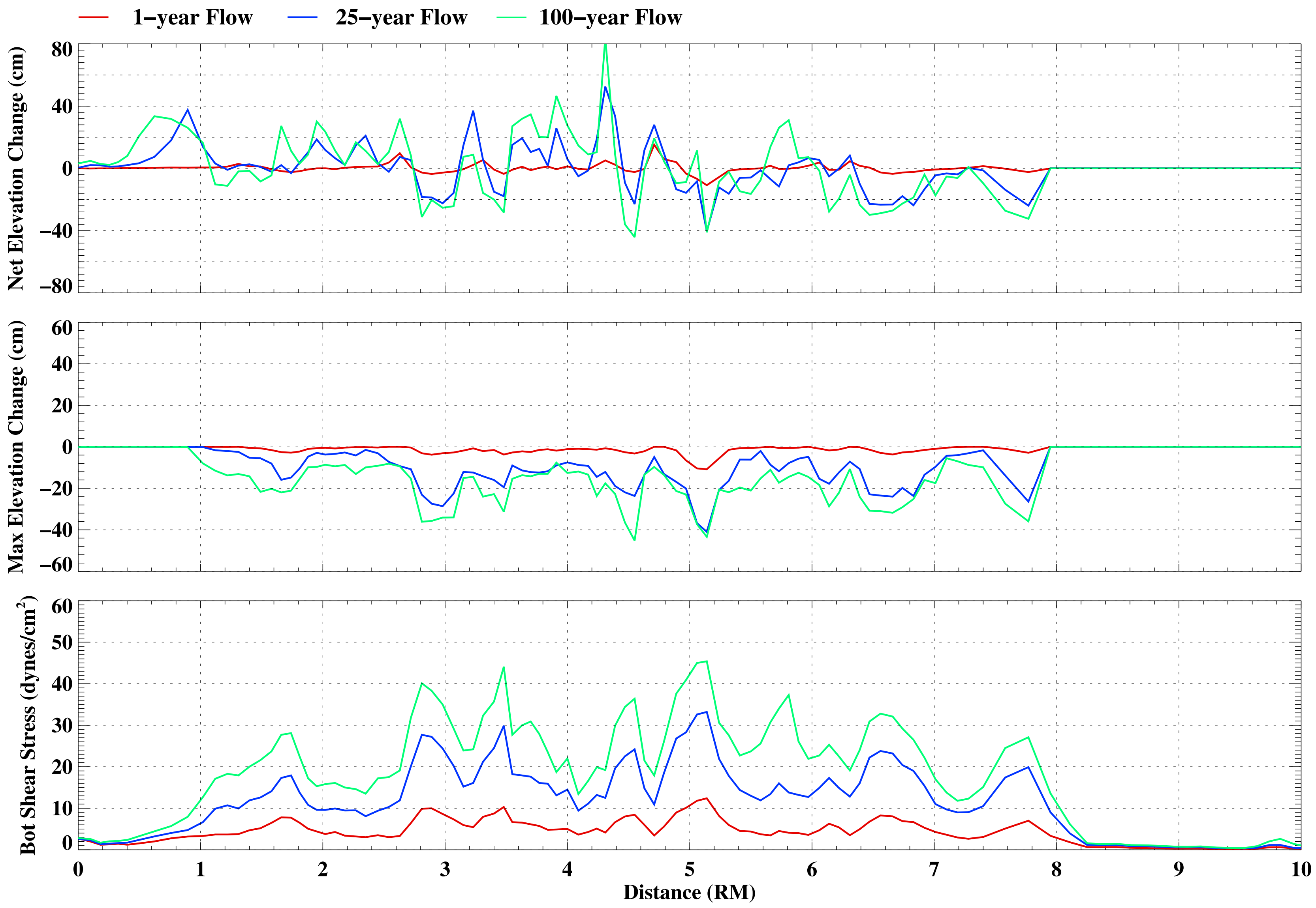

Figure 5-3. Cross-river average net bed elevation change, the maximum erosion and bottom shear stress along the river under the 1-year, 25-year and 100-year return flow conditions at the end of each simulation (Ambrose sand used as the capping material).

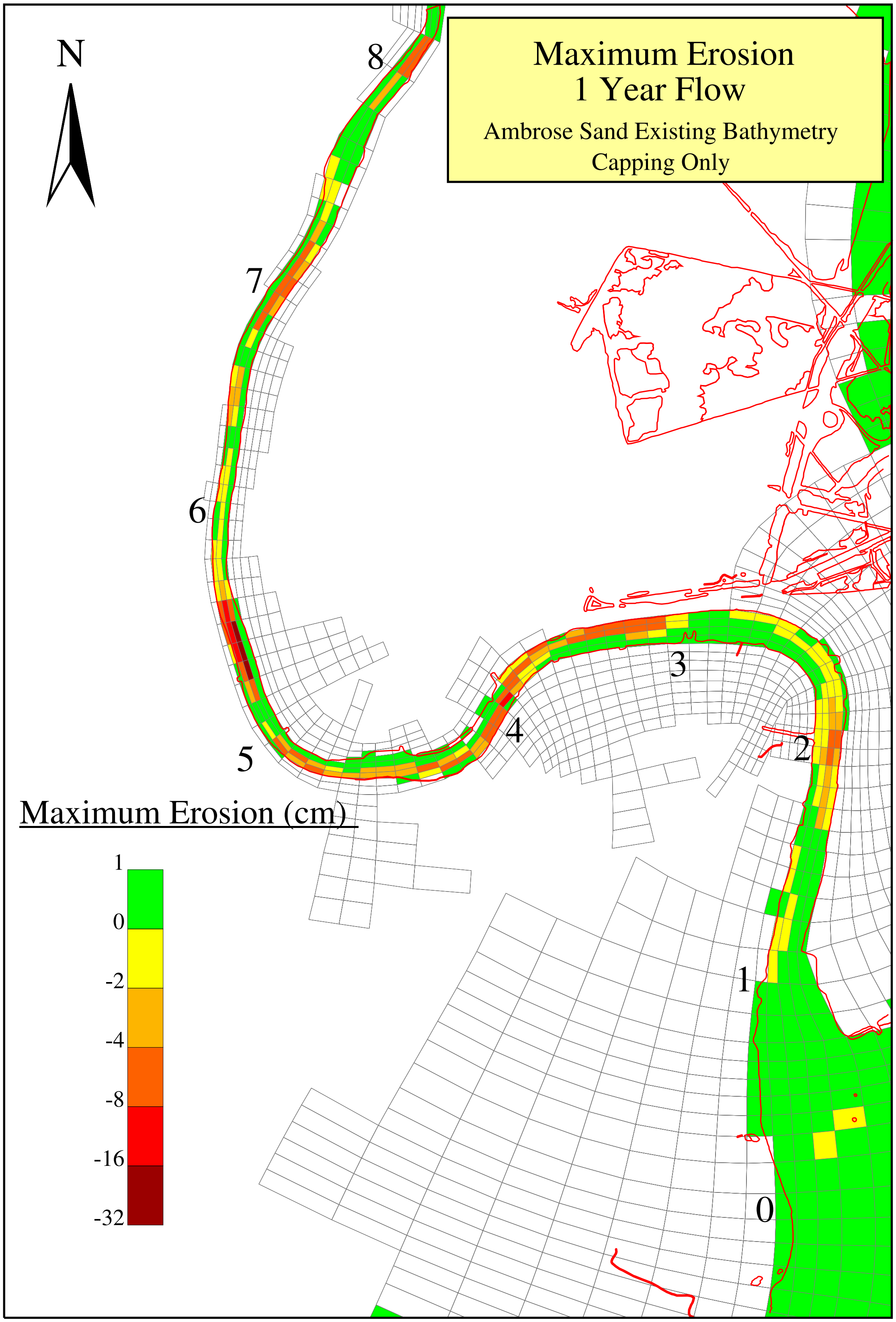

Figure 5-4a. Plan view of the maximum erosion under the 1-year return flow conditions (Ambrose sand used as the capping material).

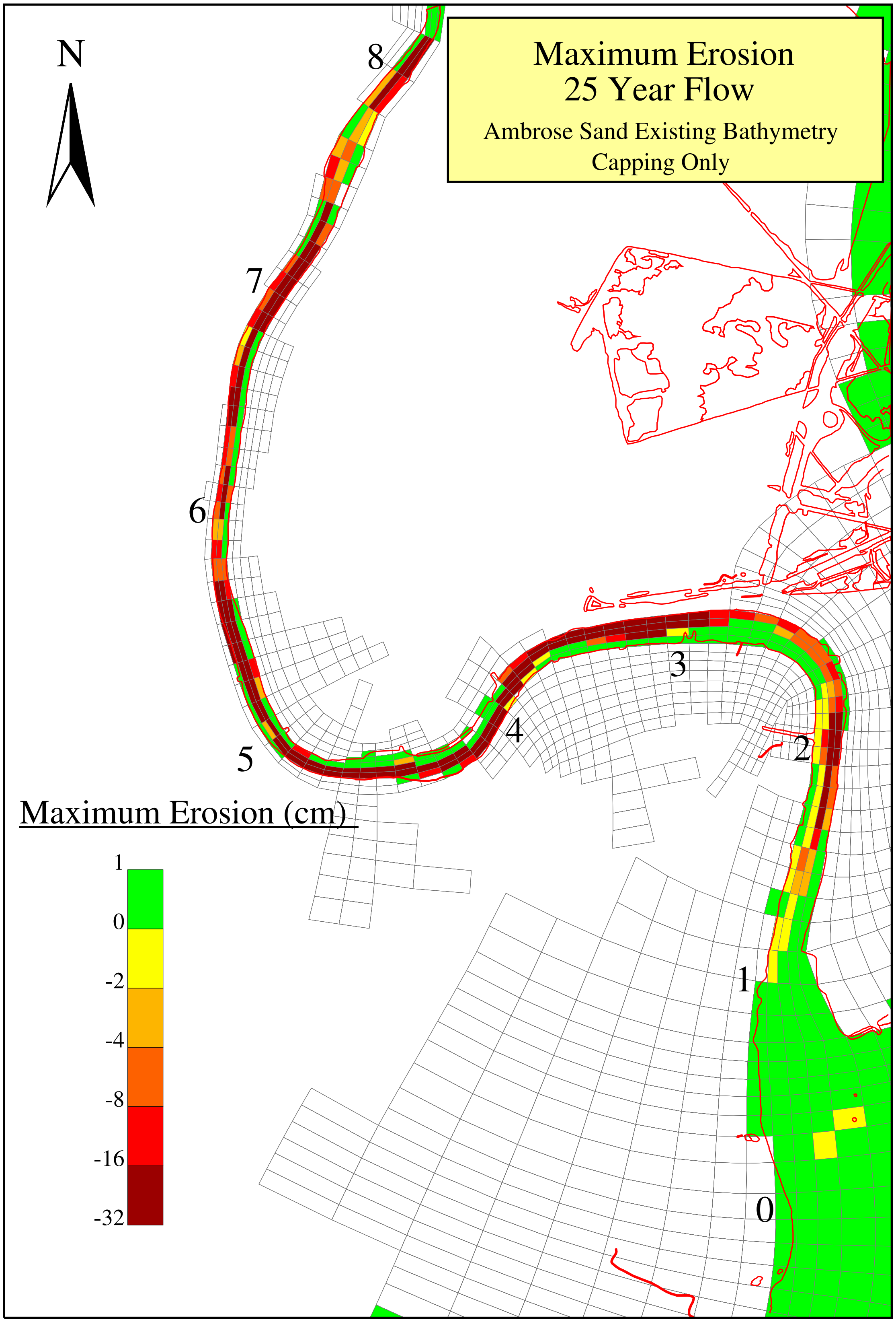

Figure 5-4b. Plan view of the maximum erosion under the 25-year return flow conditions (Ambrose sand used as the capping material).

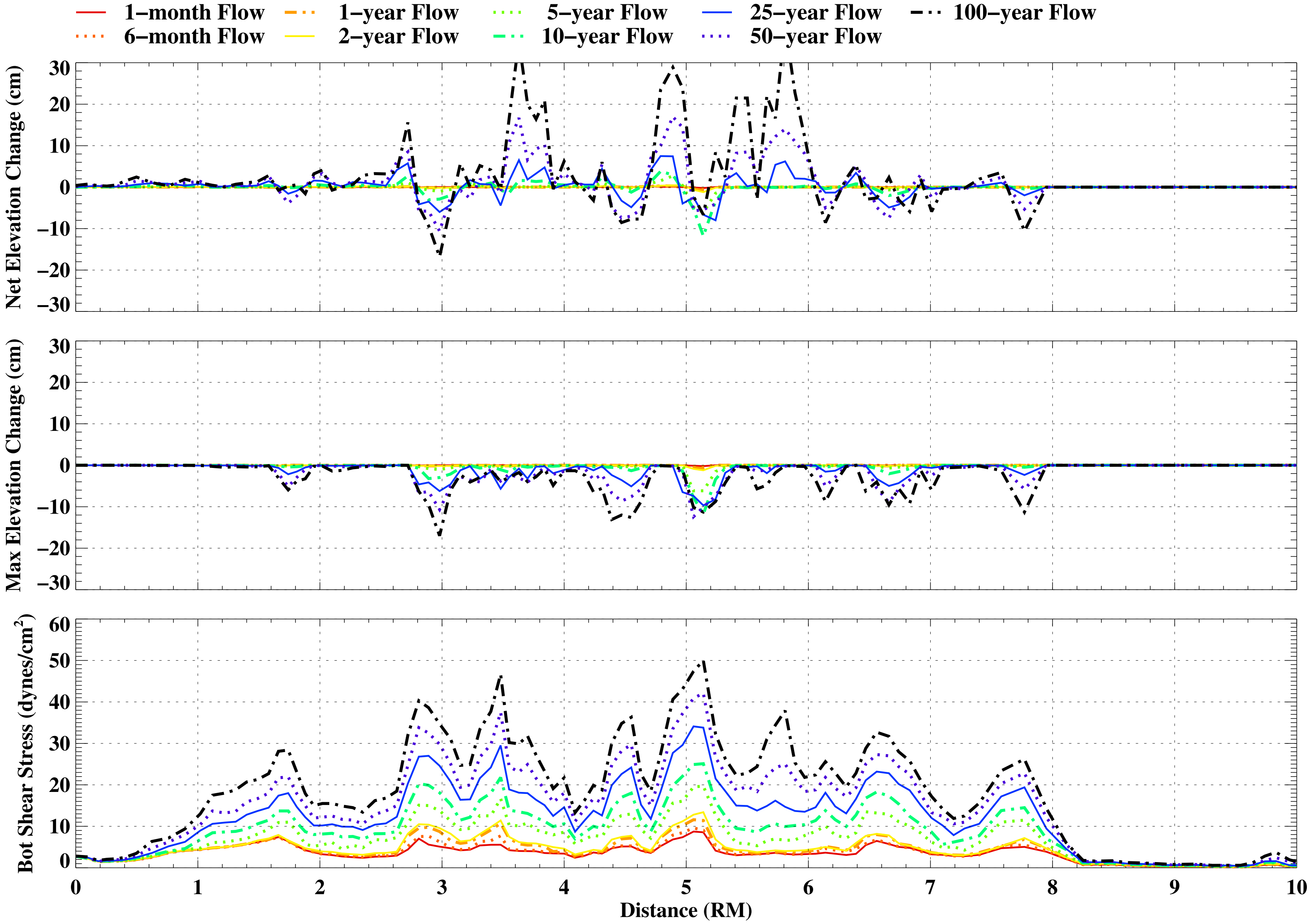

Figure 5-5. Cross-river average net bed elevation change, the maximum erosion and bottom shear stress along the river under the 1-month, 6-month, 1-year, 2-year, 5-year, 10-year, 25-year, 50-year and 100-year return flow conditions at the end of each simulation (Upland borrow sand used as the capping material).

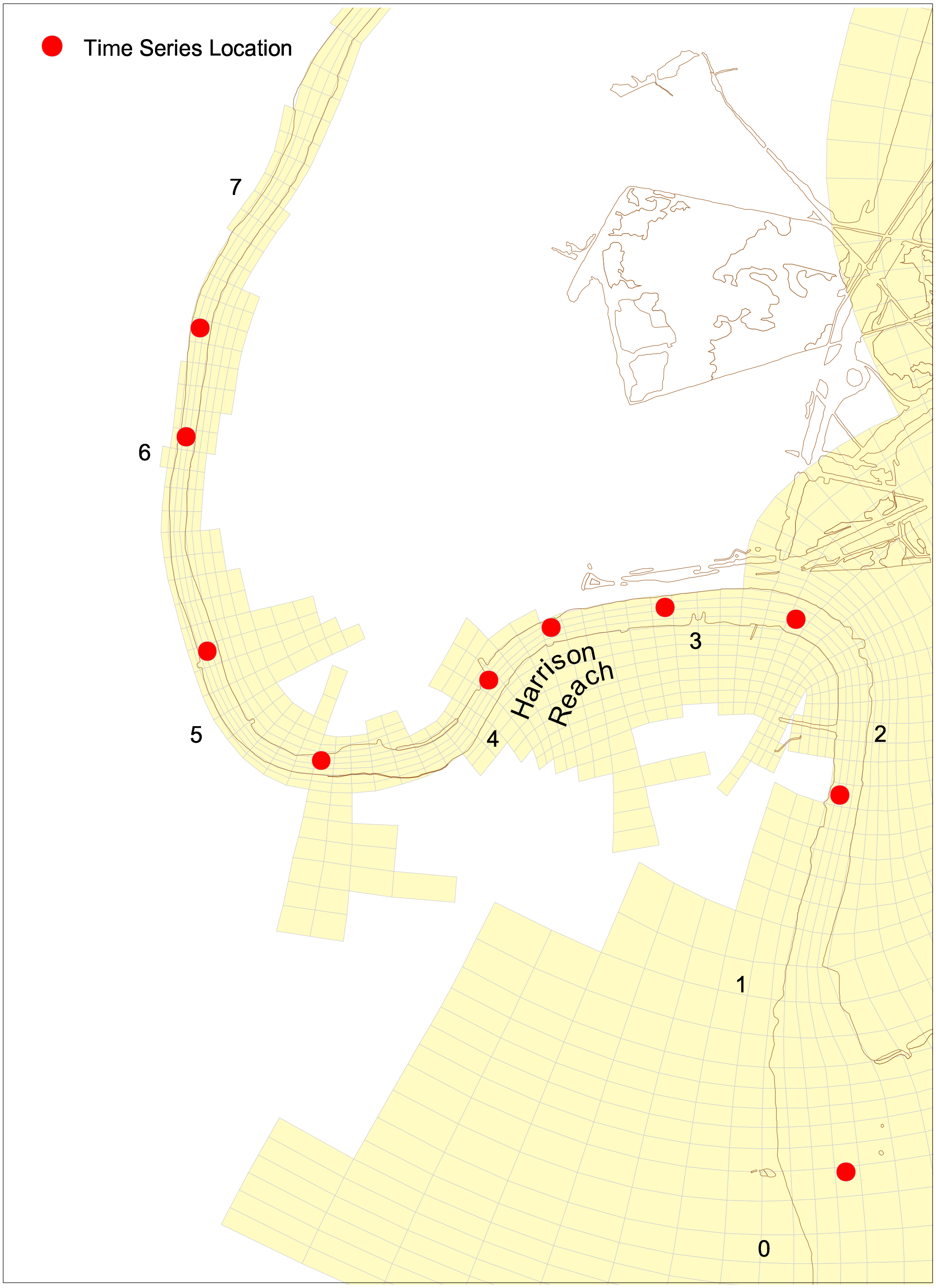

Figure 5-6. Map showing 10 selected locations along the river, where time-series are presented.

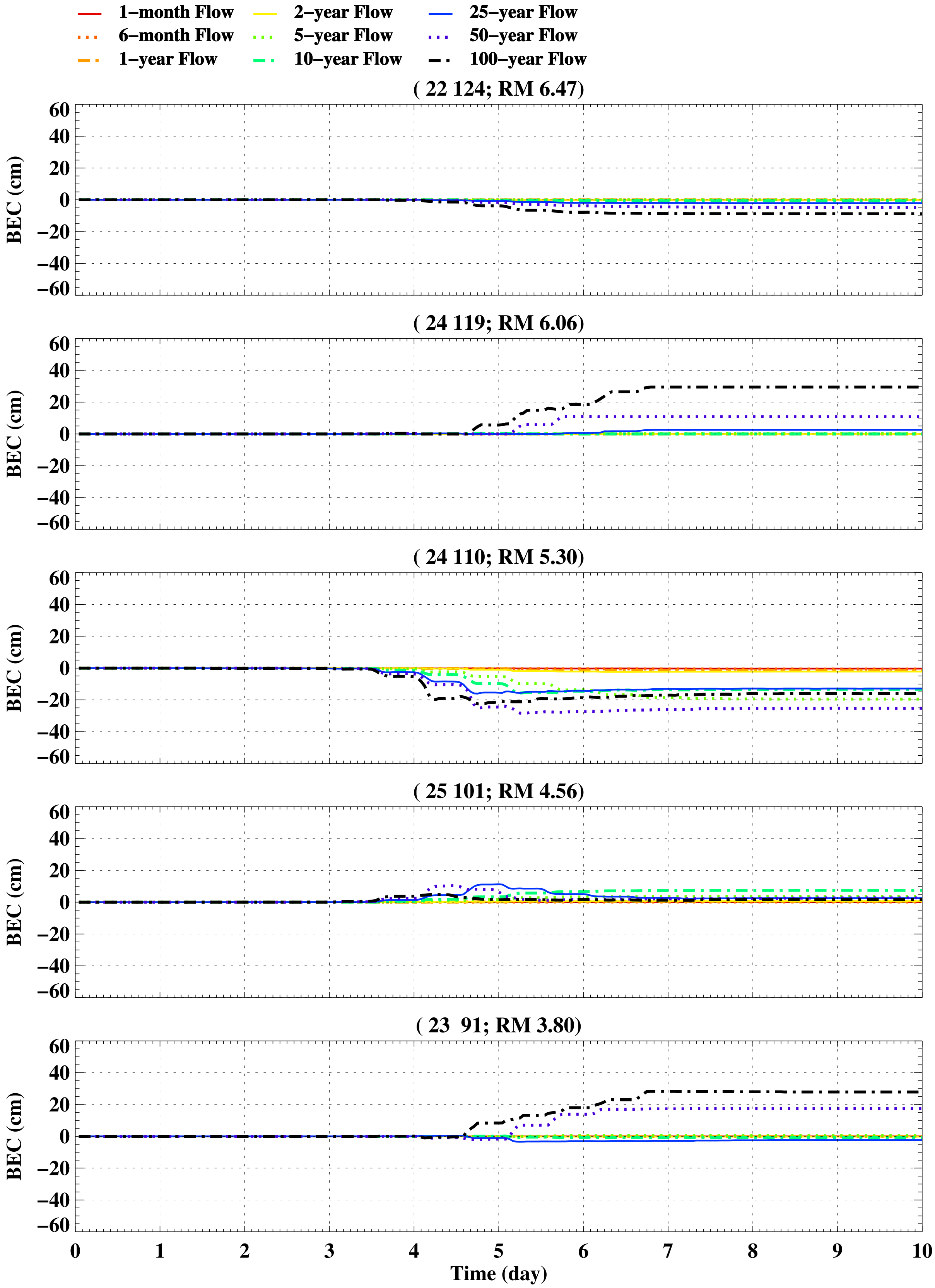

Figure 5-7. Time-series of bed elevation change (BEC) and bottom shear stress (BSS) at the 10 selected locations along the river (Upland borrow sand used as the capping material).

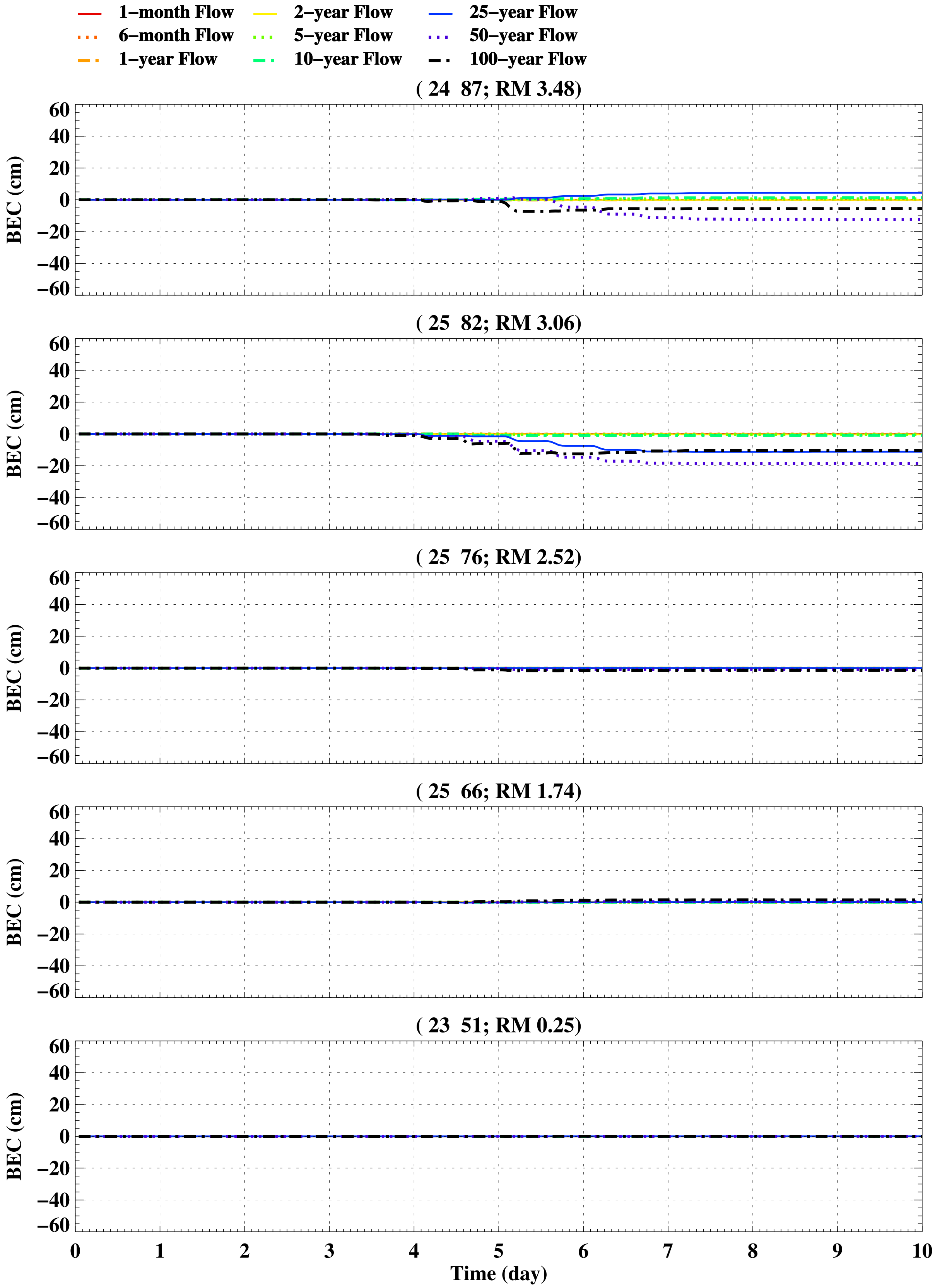

Figure 5-7. Time-series of bed elevation change (BEC) and bottom shear stress (BSS) at the 10 selected locations along the river (Upland borrow sand used as the capping material) (continued).

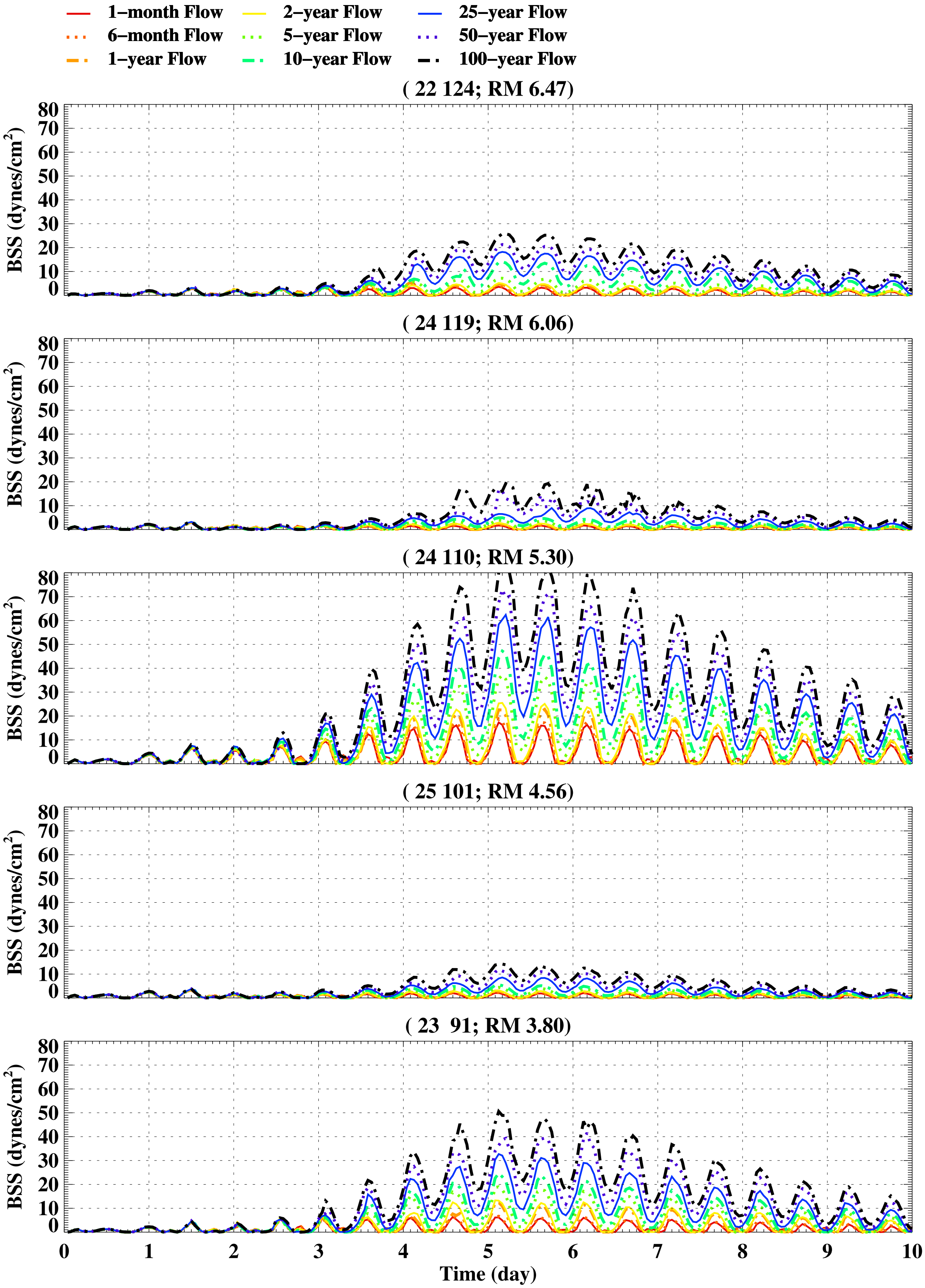

Figure 5-7. Time-series of bed elevation change (BEC) and bottom shear stress (BSS) at the 10 selected locations along the river (Upland borrow sand used as the capping material) (continued).

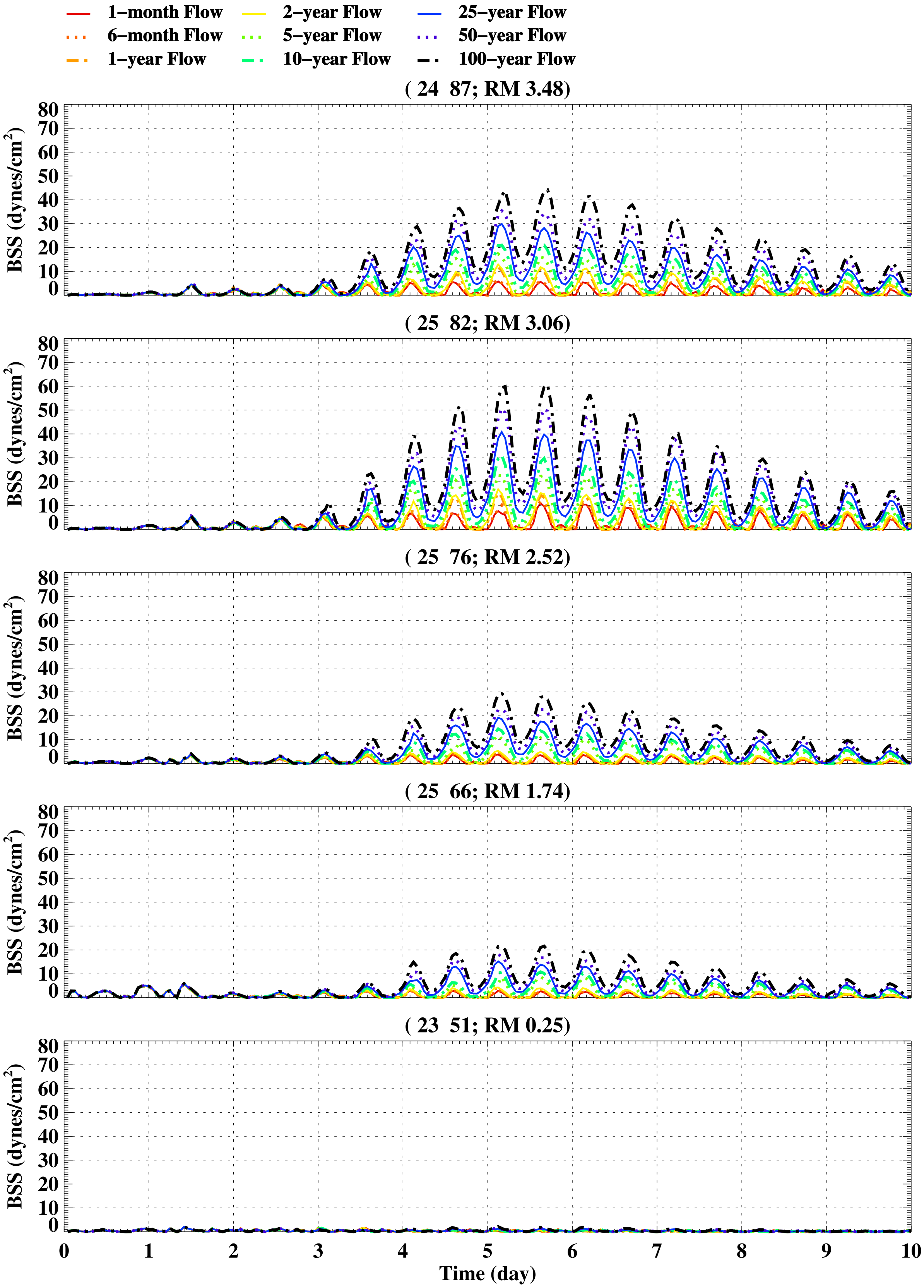

Figure 5-7. Time-series of bed elevation change (BEC) and bottom shear stress (BSS) at the 10 selected locations along the river (Upland borrow sand used as the capping material) (continued).

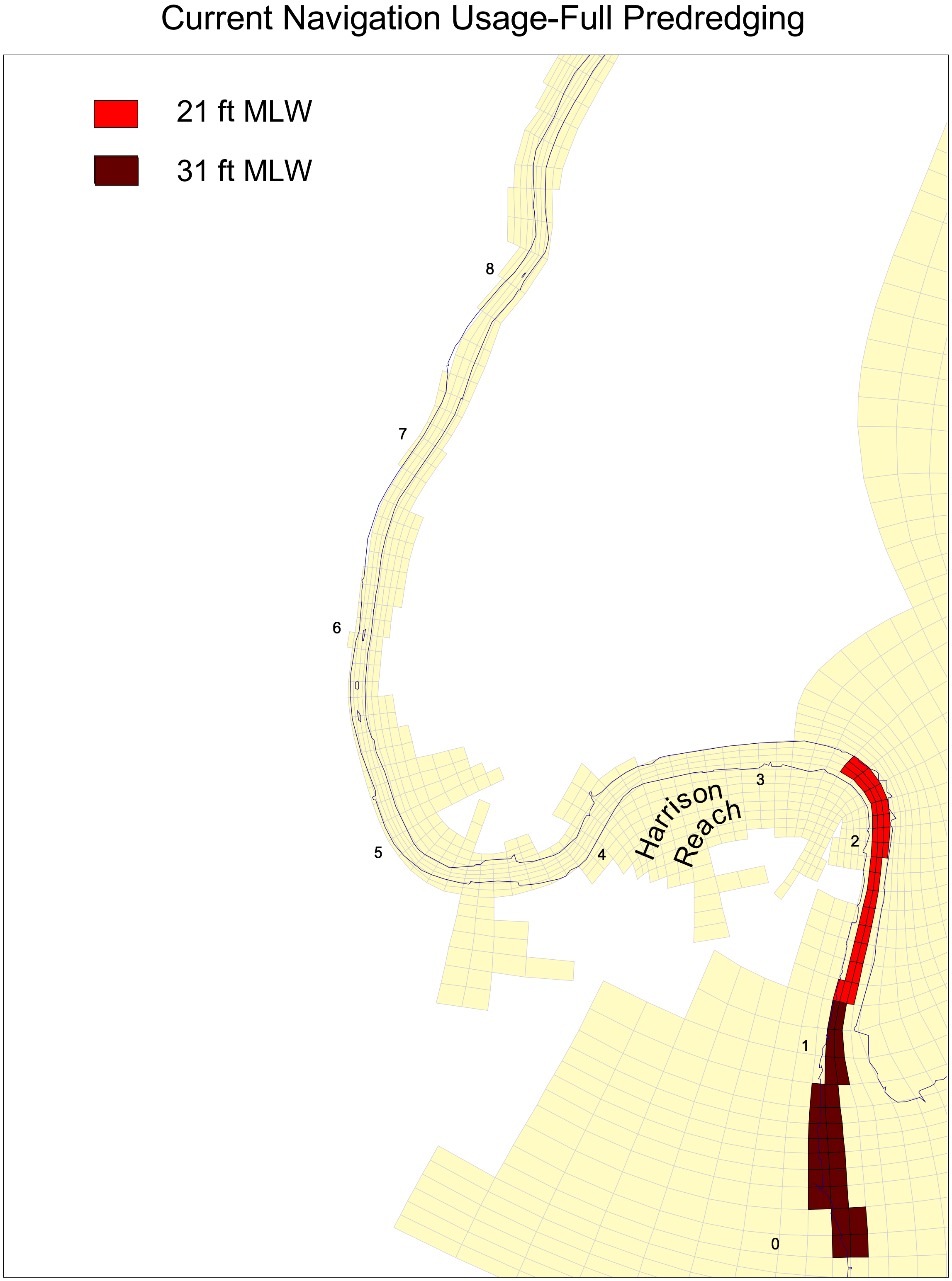

Figure 5-8a. "Current Navigation Usage" areas between RM 0 and RM 2.5.

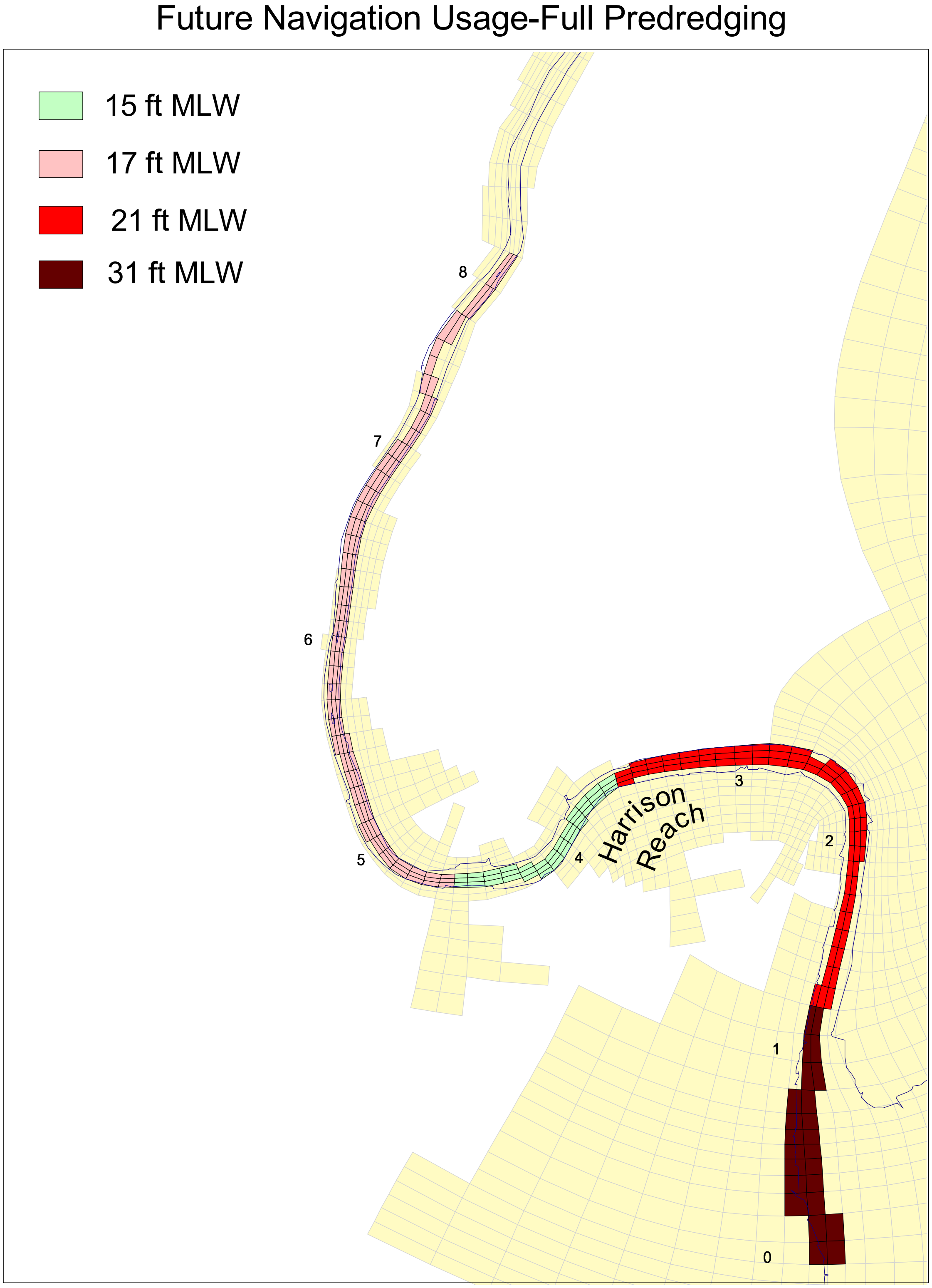

Figure 5-8b. "Future Navigation Usage" areas between RM 0 and RM 8.3.

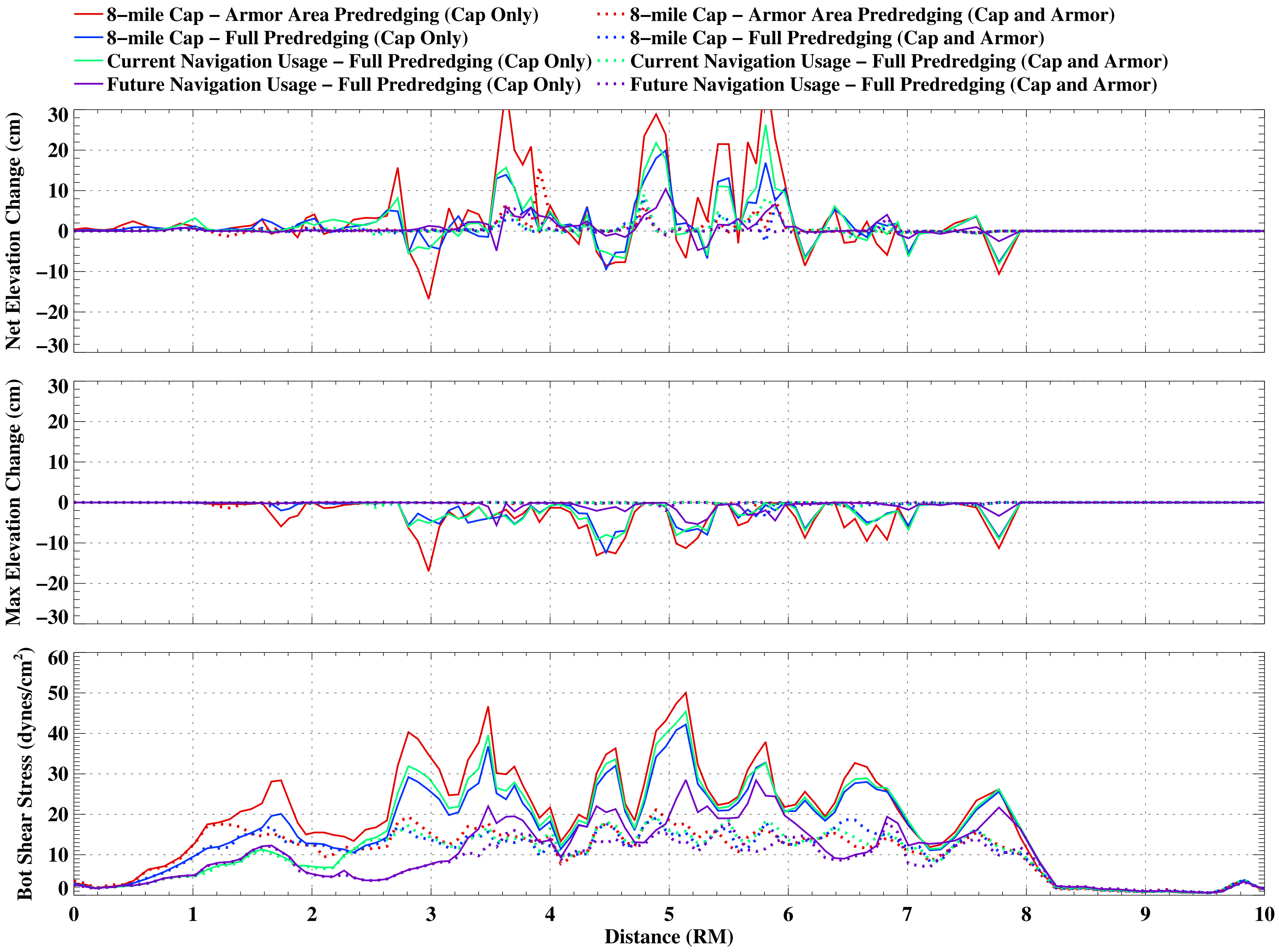

Figure 5-9. Comparisons of cross-river average net bed elevation change, the maximum erosion and bottom shear stress along the river under the different depth conditions and the different capping/armoring scenarios. The 100-year return flow was used for these simulations and upland borrow sand used as the capping material.

SECTION 6

FLOODING ANALYSIS

6.1 FLOW AND STORM SURGE ANALYSES

Daily mean stream flow data for the Passaic River at Little Falls, NJ from USGS (Station #01389500) and historic monthly extreme values of water level from NOAA's Bergen Point (Station #8519483 NY) were downloaded from the agencies' websites. These data sets were used to perform flood and storm surge analyses.

6.1.1 Flow Analysis

Daily mean stream flow data at the Little Falls gauging station are available from 1891 through 2005. The long-term averaged (105 years) flow of the Passaic River measured at this most downstream gauging station is 1,140 cfs. During the past 105 years, the maximum peak flow measured at Little Falls was 31,700 cfs, which was observed on October 10, 1903. During the last few decades, a maximum peak flow of 18,400 cfs was measured on April 7, 1984. On a yearly averaged basis, water year 1902 yielded the largest flow of 2,400 cfs while the driest year, 1965, yielded 270 cfs. Maximum daily flow for each year was extracted from this 105 year data record (Figure 6-1). Figure 6-2 shows the probability distribution of annual maximum flows. The figure indicates that median annual maximum flow of the Passaic River is about 7,000 cfs. The 100-year return flow (plotted at the 99.0th percentile) lies between 18,000 cfs and 24,000 cfs and depends on how one extrapolates the distribution curve beyond the 95th percentile. Determining the 500-year return flow (which occurs at the 99.8th percentile) from this flow probability distribution plot is more difficult to estimate due to lack of data at this high flow range.

Estimation of the 100- and 500-year floods was performed using a parametric flood-frequency curve procedure elaborated in "Methods of Stream-flow Data Analysis" by Andre Leher of Humboldt State University (2005), which is based on the methods suggested by Chow et. el. (1988). Leher suggests two different methods for estimating flow recurrence intervals: (1) Log-Normal and (2) Type 1 Extreme (Gumbel) methods. These procedures are described below:

- Compile a list of water-year annual maximum flows,
- Take common logs (log10) of the annual flows, and
- Compute the mean $\bar{x}$ and standard deviations of the original data, then compute the mean $\bar{x}_I$, standard deviation s_l, and coefficient of skewness g_I of the log-transformed data.

The general form of the equation defining the flows of different recurrence intervals (Q_{Tr}) is

$$Q_{Tr} = \bar{x} + K_T\ s \qquad (6\text{-}1)$$

where K_T is the frequency factor and depends on the probability distribution assumed for the flows.

Log-Normal distribution

For a log-normal fit, the defining equation is:

$$Q_{Tr} = 10^{\bar{x}_l + K_{TL} s_l} \qquad (6\text{-}2)$$

The values of K_{TL} to use in the equation are listed in the table below and the corresponding return-year flows for the Passaic River are shown in Table 6-1.

Table 6-1. Frequency factor K_{TL} used for log-normal recurrence interval computation and the recurrence flows for the Passaic River at Little Falls.

Recurrence interval T_r	Frequency factor	Flow
1.5	-0.439	5,510
2	0.000	6,751
5	0.842	9,968
10	1.282	12,219
25	1.751	15,180
50	2.054	17,465
100	2.326	19,808
200	2.576	22,237
500	2.878	25,572

The computed discharges can be plotted versus recurrence interval on a semi-log or flood frequency paper and fitted with a smooth line

Type I extreme–value (Gumbel) distribution

For an extreme value fit, the defining equation is:

$$Q_{Tr} = \bar{x} + K_{TG}\ s \qquad (6\text{-}3)$$

where $K_{TG} = -\frac{\sqrt{6}}{\pi}\{0.577 + \ln[\ln T_r - \ln(T_r - 1)]\}$ Values for the frequency factor and the computed recurrence flows for the Passaic River are listed in the Table 6-2

Table 6-2. Frequency factor K_{TG} used for Type I Extreme (Gumbel) recurrence interval computation and the recurrence flows for the Passaic River at Little Falls.

Recurrence interval T_r (year)	Frequency factor K_{TG}	Flow Q_{Tr}
1.5	-0.523	5,509
2	-0.164	6,890
5	0.720	10,293
10	1.305	12,544
25	2.044	15,389
50	2.592	17,498
100	3.137	19,596
200	3.679	21,682
500	4.395	24,483

Figure 6-3 shows the results of both the Log-Normal and Type I Extreme methods. Both analyses yield similar results for the 100-year flow, which are 19,808 and 19,596 cfs, respectively; a difference of about one percent. However, due to relatively few records exceeding 20,000 cfs in the past 105 years, the estimations of 500-year flow yield somewhat different results by each method. The Log-Normal method yields 25, 572 cfs and the Type 1 Extreme method yields 24,483 cfs (approximately a 4% difference).

During the study, HydroQual contacted the USGS Trenton Office and sought their advice concerning these estimates. The USGS Trenton Office provided their 100- and 500-year flow estimates as 20,000 and 26,000 cfs, respectively, which were estimated by the Pearson Type III frequency distribution method (USGS, 1982). The USGS estimates were used for the specification of 100- and 500-year flows.

6.1.2 Storm Surge Analysis

Monthly extreme water elevations observed at the NOAA Bergen Point station are available from 1982 through 2003 (Figure 6-4). These extreme water elevations represent storm surges associated with the passage of low-pressure systems through the region. Due to the orientation of the coastlines off New York Harbor, which, in general, run in southwest and northeast directions, persistent northeasterly winds with several days of duration bring coastal waters into the Harbor and can result in coastal flooding. Annual extreme elevations were extracted from the data and processed to estimate the probability distribution of extreme events. The results are shown in Figure 6-5. The plot suggests that the 100-year storm surge elevation lies between 1.84 and 1.92 m above MSL. Based on the Bergen Point data the 500-year storm surge is about 1.96 m above MSL.

Due to the relatively short records at Bergen Point, additional analysis of extreme water elevations was conducted using the data observed at the Battery. This station has more than 50 years of tidal observations and during the existence of the station it recorded one of the highest water levels observed in the New York Harbor region, which is the storm surge related to the passage of Hurricane Donna on September 12, 1960. Hurricane Donna caused extreme water elevations, as much as 2.56 m (8.4 ft) relative to NGVD29, in many parts of the coastal areas around the New York Harbor (Harris, 1963). The highest water level within the LPR was 2.93 m (9.6 ft) relative to NGVD29 near Rutherford, NJ.

In order to justify the use of the Battery data for inferring surge events in the LPR area, a correlation analysis of extreme water elevations at both gauges was conducted. Monthly extreme events observed from 1982 through 2004 were used for this analysis. The results shown in Figure 6-6 indicate that there is a high correlation ($R^2 = 0.96$) between these stations due to proximity. The linear regression also suggests that, in general, the extreme elevations at Bergen Point are about 10 cm higher than those observed at the Battery. The probability distribution of the annual extreme water elevations at the Battery is shown in Figure 6-7. The results suggest that 100- and 500-year storm surges for Bergen Point are 2.4m and 2.67 m above MSL, respectively.

6.1.3 Correlation of flow and storm surge events

Further analysis of flood waters from upstream freshwater inflows resulting from heavy rainfall events and the storm surge elevations was conducted to find out whether any correlations exist between the high river inflows and storm surge events. The monthly extreme water elevations at Bergen Point are plotted against the daily flows of the Passaic River measured at the Little Falls to deduce correlation between high flows and storm surge (Figure 6-8).

The correlation results are shown in Figure 6-9 (upper panel) and the correlation coefficient (R^2) is less than 0.02. Further efforts were conducted to evaluate whether lagged flow data (2nd, 3rd, and 4th day) were correlated with storm surge (remaining panels in Figure 6-9). The correlation coefficients improve when comparing the flow records a few days after the storm surge events. However, the results do not produce a meaningful correlation between the high flow events and storm surge events and it was concluded that there is no direct correlation between them.

6.2 CAPPING AND SIMULATION SCENARIOS

The boundary forcing data of the model include freshwater flows from rivers, and water surface elevation, temperature and salinity at open boundaries. Several model forcing conditions were considered for the capping scenarios:

- 100-year flow,
- 500-year flow,
- 100-year storm surge, and
- 500-year storm surge

The 100- and 500-year flow events were constructed to provide freshwater inflows at Dundee Dam, as two extreme flow conditions. However, the measured freshwater inflow volumes for each flow event account only for the flow measured at Little Falls. The drainage area above Little Falls (780 square miles) accounts for 77 percent of the total Passaic River basin (1,013 square miles). The remaining 23 percent of the drainage area includes the downstream area of the Passaic River below Little Falls (178 square miles) as well as the drainage area of the Saddle River (55 square miles), which enters the Passaic River just downstream of Dundee Dam. The total flow volumes assigned at Dundee Dam were estimated by multiplying by 1.3, which is the ratio of the total drainage area of the Passaic River Basin to the gauged drainage area. The final peak flow volumes for the 100- and 500-year flows are 26,000 and 33,800 cfs, respectively. Although no correlation between flow and storm surge events was found, as discussed in the previous section, this does not mean that this never occurs in nature. It may, however, be unrealistic to assume that the 100- and 500-year flow and storm surge events occur simultaneously. Therefore, it was decided to conduct the model simulations for high flow and storm surge events separately. It should also be noted that modeled estimates of storm surge are based on historical data and do not take into account future increases in sea level elevation.

The harmonic constituents in the New York Harbor were used to generate water surface elevations along open boundaries. A storm surge analysis of water surface elevation data at the Battery was conducted and the 100 and 500-year surge peaks were obtained (2.40 m and 2.67 m above MSL). A storm surge curve observed at the Battery during Hurricane Donna in 1960 which lasted about two days was used for this study. These water elevations were added to the astronomical tide for projection simulations. In order to create the maximum possible water elevation during each simulation, the storm surge peaks were added to the peak spring tide within the simulation period. Constant temperature and salinity were applied to the open boundaries.

Several capping/armoring scenarios were considered in the study with various combinations of capping/armoring areas with different depth conditions:

- Base Case Scenario: using existing bathymetry conditions in the LPR and no capping/armoring.
- "8-mile Cap - Armor Area Pre-Dredging" Scenario: the first 8.3 miles of the LPR were capped with 2 feet of UBS and armored at selected locations with 2 feet of 6-inch angular cobble. Armored areas were to be pre-dredged 2 ft before being capped with sand and then armored with stone. Therefore, the top of armored areas would be level with other areas that are sand capped, and post-remediation depths would be two feet shallower than pre-remediation depths.
- "8-mile Cap – Full Pre-Dredging" Scenario: the bottom of the LPR between RM 0 and RM 8.3 was dredged by 2 feet before capping and 4 feet before capping and armoring. With this configuration, current river depths would be maintained in the capped/armored areas.
- "Current Navigation Usage – Full Pre-Dredging" Scenario: assumed that a 31-ft deep navigation channel would be constructed in the river between RM 0 and RM 1.2, and a 21-ft deep navigation channel between RM 1.2 and RM 2.5. The rest of the upstream section of the river was maintained at the existing bathymetry. The navigation channel depths (*i.e.*, 31 and 21 feet) denote the water depths below MLW to the top of capping/armor layer. The remaining bottom of the LPR between RM 0 and RM 8.3 was dredged by 2 feet before capping and 4 feet before capping and armoring.
- "Future Navigation Usage – Full Pre-Dredging" Scenario: assumed various future navigational channel conditions in the RM 0 through RM 8.3. The breakdown of navigation channel depths at various RM points are:
    - RM 0 – RM 1.2: 31' below MLW
    - RM 1.2 – RM 3.6: 21' below MLW

- RM 3.6 – RM 4.6: 15' below MLW
- RM 4.6 – RM 8.1: 17' below MLW
- RM 8.1 – RM 8.3: existing bathymetry

Under this scenario, the bottom of the LPR between RM 0 and RM 8 was dredged by 2 feet before capping and 4 feet before capping and armoring. The navigation channel depths denote the water depths below MLW to the top of capping/armoring layer.

Figure 6-10 shows the extent of different capping and armoring scenarios. Ten-day simulations were set up for the various capping/armoring scenarios and the forcing conditions (high flow and storm surge). The Base Case Scenario runs were also performed, using the existing bathymetry with no capping or armoring for the 100- and 500-year flows and storm surge events in order to determine any change in the flooding areas under the different capping/armoring and dredging scenarios.

Modification of model bathymetry resulting from capping/armoring activities could change the total water volume in the river, and, therefore, change the distributions of computed water surface elevations and current velocities. In addition, sediment grain size distributions could modify model-computed fields of current velocities and water surface elevations since the bottom drag coefficient in the hydrodynamic model is directly correlated with sediment grain size. Equation (6-4) shows the formulation used to estimate the bottom drag coefficient (C_D) in ECOMSEDZLJ (Blumberg and Mellor, 1987).

$$C_D = \left[\frac{1}{\kappa} \ln(0.5 * Z_b / Z_0) / z_0 \right]^{-2}, \tag{6-4}$$

where z_0 is the bottom roughness, z_b is the thickness of the grid nearest the bottom and κ is the von Karman constant. In the above equation, C_D is a function of hydrodynamic bottom roughness (z_0), which is related to sediment grain size (Kamphuis, 1974). Table 6-3 displays hydrodynamic bottom roughness lengths specified in the LPR model. Using Equation (6-4) and assuming a grid cell depth of 5 m, the corresponding bottom drag coefficients are estimated in Table 6-4.

Table 6-3. Hydrodynamic Bottom Roughness Length (m) under Different Bottom Conditions in the Lower Passaic River

Base Case	0.001
Capping Area	0.001
Armoring Area	0.010

Table 6-4. Bottom Drag Coefficient for a Grid Cell with a 5m Depth under Different Model Bottom Conditions in the Lower Passaic River

Base Case	0.005
Capping Area	0.005
Armoring Area	0.015

6.3 RESULTS

The output variables considered in this section include water surface elevation, bottom velocity, and bottom shear stress. In ECOMSEDZLJ the bottom shear stress is determined by

$$\overline{\tau_b} = \rho_0 C_D |V_b| V_b, \qquad (6\text{-}5)$$

where ρ_0 is the water density and V_b is the bottom velocity. Time-series of water surface elevations, current velocities, and bottom shear stresses at select locations were processed. Figure 6-11 shows the station locations.

Figure 6-12 shows the 500-year flow discharge specified at the upstream boundary and computed water surface elevations for the Base Case Scenario in the Harrison Reach and near the Dundee Dam. The flow event presents a maximum freshwater inflow of 965 m^3/s (33,800 cfs). Corresponding to the extreme flow event, the increase in water surface elevation is most significant near the Dundee Dam, which rises up to 4.0 m above NGVD29 during the peak of the flow, and, at the upstream end of Harrison Reach (RM 5), where the maximum water surface elevation reaches 2.5 m above NGVD29. At the Harrison Reach (RM 3), the maximum water elevation is about 1.7 above NGVD29. Hereafter, all water and land elevations are in meters relative to NGVD29.

6.3.1 Changes in Water Elevations

Maximum values of water surface elevation at each model grid cell were extracted from the model computations during each 10-day simulation period. A summary of along-river variation of the maximum water surface elevation through the entire length of the LPR is shown in Figure 6-13. The figure summarizes the maximum water elevations at different locations in the river under different flow and storm surge conditions in response to various capping and armoring scenarios.

For all simulations, the results indicate that the water surface elevations increase in an upstream direction. Under the Base Case Scenario, which uses the existing depth of the river, the downstream-upstream difference can be as large as 3.6 m during the 100-year flow event and 4.2 m during the 500-year flow event (blue lines in Figure 6-13). However, this increase is mainly limited to the narrow upper section of the river (upstream of RM 8). In the downstream section below RM 8, where the river becomes wider, the increase in the water level during the 100-year flow is computed to be less than 0.5 m between RM 0 and RM 8 and less than 0.8 m during the 500-year flow.

Comparing the "8-mile Cap – Armoring Area Pre-Dredging" Scenario (green lines in Figure 6-13) to the Base Case Scenarios under the existing river depths, it can be seen that the largest water elevation increase occurs immediately upstream of the armored regions, which are around RM 3 and RM 12. This increase is as large as 0.5 m and 0.8 m for the 100 and 500-year flows, respectively. High bottom drag coefficients were used for the armored areas, which were about 3 times larger than those used for the other non-armoring scenarios (Table 6-4). It appears that high bottom drag coefficients in the armored area hinder movement of water downstream and result in the increase of water elevations in upstream locations, *i.e.*, a backwater is generated. These changes in the water elevations in the upstream section of the river result in additional flooding in the low lying areas. The spatial extent of flooding areas due to various capping and armoring scenarios will be discussed below.

Full pre-dredging of 2 to 4 feet in the lower 8.3 miles of the river, where capping (2 feet) and armoring (additional 2 feet) is planned, results in a reduction of about 0.2 to 0.4 m in water elevation rise compared to the non-pre-dredged, *i.e.* existing bathymetry, "8 mile Cap – Armor Area Pre-Dredging" Scenario for both the 100 and 500-year flows. The results reflect the water level change in response to the downstream water depth change, *i.e.* the pre-dredging. The results of water level rise under the "Future Navigation Use – Full Pre-Dredging" Scenario are less than those in the Base Case Scenario, which suggest that deepening some portions of the capping/armoring area could have beneficial effects in reducing the extent of flooding during high flow events. It is noted that there are no significant elevation differences between the “8 mile Cap – Full Pre-Dredging” (red lines in Figure 6-13) and “Current Navigation Use – Full Pre-Dredging” Scenarios (yellow lines in Figure 6-13) for each flow event. The results indicate that channel deepening of the lower 2.5 miles would not significantly change flood stages in upstream locations.

During the 100- and 500-year storm surge events, the upstream-to-downstream difference in water surface elevation is about 0.2 m (the two bottom panels in Figure 6-13). However, water elevations in the LPR rise about 2.8 m and 3.1 m above normal elevation, respectively, for the 100 and 500-year storm surges, which would result in additional flooding in the low lying regions near the mouth and the upstream portions of the river. It was found that during storm surge events the maximum water elevation between RM 3 and RM 8 would be lower under the capping/armoring scenario compared to the Base Case Scenario. It appears that those armored areas with higher bottom roughness would impede the progression of storm surge upstream and, hence, result in lower elevation rise compared to those computed under relatively smooth bottom conditions under the Base Case Scenario. The “Future Navigation Use – Full Pre-Dredging” Scenario would raise water elevations slightly (about 1 cm or less) compared to those computed under the Base Case Scenario. This is due to deepening of the lower 8.3 miles of the LPR, which allows more water to travel upstream with less resistance.

6.3.2 Flooded Areas

The flooded areas in the LPR are determined by comparing water surface elevations in the river to nearby landside digital elevation information during the simulations. Total flooded areas for each simulation are tabulated in Table 6-5, and do not include the in-river areas inundated during normal tides, *i.e.* within river wetting and drying areas under normal tidal elevations.

6.3.2.1 Scenarios During the 100-Year Flow

Figure 6-14 shows the grid cells flooded during the 100-year flow under the Base Case Scenario. Under the Base Case Scenario, the 100-year flow event would flood an area of 499 acres along the river (Table 6-5). During the 100-year flow, the “8 mile Cap - Armor Area Pre-Dredging” Scenario would increase the water elevation by 0.5 m and increase the projected flooding area by 93 acres for a total of 592 acres (Figure 6-15). The additional flooding area under the “8 mile Cap - Full Pre-Dredging” Scenario is projected to occur between RM 5 and RM 12. The “8 mile Cap - Full Pre-Dredging” Scenario would result in a projected flooded area of 523 acres about 69 acres less than computed for the scenario where only the armored area is pre-dredged. The results indicate that pre-dredging of the capping/armoring areas would raise water level less than 0.1 m in the upstream locations (Figure 6-16) compared to those computed under the Base Case Scenario. As indicated in

Figure 6-13, the "Current Navigation Use - Full Pre-Dredging" Scenario, which deepens water depths in the first 2.5 miles of the LPR, would not significantly change the flooding area compared to that computed under "8 mile Cap - Full Pre-Dredging" Scenario. However, the "Future Navigation Use - Full Pre-Dredging" Scenario would only flood 482 acres, and is about 17 acres less than areas projected to flood under the Base Case Scenario (see Figure 6-17 and Table 6-5).

6.3.2.2 Scenarios During the 500-Year Flow

The 500-year flow would raise the upstream water levels as much as 3.8 m under the Base Case Scenario and it would cause flooding of 794 acres, as shown in Figure 6-18. The model results indicate that additional areas downstream of the Dundee Dam, especially between RM 8 and RM 11, would be flooded during the 500-year flow, in comparison to the areas flooded during the 100-year flow under the Base Case Scenario.

During the 500-year flow event, the water elevations would increase about 0.8 m in the area upstream of the capping/armoring region under the "8 mile Cap – Armor Area Pre-Dredging" Scenario (Figure 6-13) compared to those under the Base Case Scenario. This water elevation increase would affect many grid cells near the County Park in Lyndhurst (RM 11) and downstream. Under this "8 mile Cap – Armor Area Pre-Dredging" Scenario, the flooded area is projected to be 880 acres (Figure 6-19), which adds about 86 acres to the flooded area relative to the Base Case Scenario during the 500-year flow.

It is found that pre-dredging of the capping/armoring area would lower the water elevations in the upstream locations (Figure 6-13). On average, the water elevation would increase by less than 0.1 m due to the pre-dredging, compared to those computed under the Base Case Scenario. The total flooded area under the "8 mile Cap – Full Pre-Dredging" Scenario is 822 acres as shown in Figure 6-20. The "Current Navigation Use – Full Pre-Dredging" Scenario would flood essentially the same areas as the "8 mile Cap – Full Pre-Dredging" Scenario, *i.e.*, the deepening of the lower 2.5 miles would have minimal effect as far as flooded area is concerned. However, the "Future Navigation Use – Full Pre-Dredging" Scenario would lower the water elevation along the length of the river and would reduce the flooded area to 767 acres. The flooded areas would be reduced by 27 acres, compared to those under the Base Case Scenario. Comparing the flooded areas under this "Future Navigation Use – Full Pre-Dredging" Scenario to those under the "8 mile Cap – Armor Area Pre-Dredging" Scenario with existing bathymetry, the "Future Navigation Use – Full Pre-Dredging" Scenario would reduce the flooded area by as much as 113 acres (Figure 6-21). It is clear from these results that flooding would be significantly reduced if the deeper channel depths could be maintained in the LPR.

6.3.2.3 Scenarios During Storm Surge Events

The 100- and 500-year storm surges would cause the most flooding between the river mouth and RM 3.5, where land elevations are relatively low. As indicated in Table 6-5, flooded areas during storm surge events are much greater than those under 100-and 500-year flows. The increase in water elevations of as much as 3.0 m would result in the flooding of 1,249 acres and 1,504 acres during 100- and 500-year storm surges, respectively (Figure 6-22 and 6-23). Although most of the flooded areas are in the lower 5 miles of the river, both the low lying areas in the County Park of Lyndhurst and the area just downstream of the Dundee Dam would also be flooded during the extreme storm surge events. As indicated in earlier sections, the scenarios with capped/armored condition result in less maximum water elevation rise compared to those under the Base Case Scenario. However, the differences in the water elevations are less than 0.05 m at most of the locations in the LPR and do not change the flood areas significantly as compared to the Base Case Scenario. It is worthy to note that under the "Future Navigation Use – Full Pre-Dredging" Scenario, where the lower 8.3 miles of the LPR would be deepened to maintain a navigation channel, the maximum water level increases compared to those computed under the Base Case Scenario. However, the increase is less than 0.01 m and has no significant impact on the flooding computations.

Table 6-5. Total Areas (acres) Flooded under Different Simulation Scenarios

	Base Case (Existing Depth)	8 Mile Cap: Armor Area Pre-Dredging	Full Pre-Dredging before Capping/Armoring		
			8 Mile Cap	Current Navigation Use	Future Navigation Use
100-Year Flow	499	592	523	523	482
500-Year Flow	794	880	822	822	767
100-Year Storm Surge	1,249	1,249	1,249	1,249	1,249
500-Year Storm Surge	1,504	1,504	1,504	1,504	1,504

6.4 SENSIVITITY ANALYSES

6.4.1 Sensitivity to Land Surface Elevation

To properly estimate potential flooding areas under different conditions in the LPR basin, the best available shoreline and land elevation information were incorporated into the hydrodynamic model (see Section 2). The initial model land elevations were configured using the 2-foot contour lines from the USACE survey maps. However, even these data resulted in shoreline and land elevation uncertainties of ± 1 foot. Therefore, a sensitivity run was performed, where the land elevations used in the model were reduced by 1 foot, to see how the uncertainty in the shoreline elevation might affect the estimates of the flooding areas. The simulation scenario selected was the "8 mile Cap – Armor Area Pre-Dredging" Scenario. The 100- and 500-year flows at Dundee Dam and predicted tides at the open boundaries of the model were used as model forcing functions.

Figure 6-24 shows the maximum water surface elevation along the LPR during the simulations. In the figure, blue lines are corresponding to the model results obtained with the original shoreline elevation while the red lines are the sensitivity run results obtained with 1 foot lowered land elevation. The model results indicate that lowering the land surface elevations slightly decreases maximum water surface elevations during flood events when compared to the original land elevation configurations (Figure 6-24). On average, the difference between using the original and the modified shoreline elevations is less than few centimeters during the 100- and the 500-year flow events.

Table 6-6 displays the flooded areas and the area changes under different shoreline elevations. Clearly the decrease in land surface elevations results in a larger flooded area. When the estimated land elevations were reduced by 1 foot, the flooded areas were projected to increase by about 25% and 17% during 100- and 500-year flow events, respectively. During the 100-year flow conditions, the additional flooding areas due to 1 foot adjustment of land elevations are limited from RM 8 to RM 12, especially in the relatively flat land near the County Park in Lyndhurst near RM 11 (Figure 6-25). However, under the 500-year flow conditions, most of the additional flooding areas are located from RM 3 to the region immediately upstream of the Harrison Reach (Figure 6-26).

Table 6-6. Total Areas (acres) Flooded under Different Shoreline Elevations.

Sensitivity	Original	Modified	Difference (%)
100-Year Flow	592	738	25
500-Year Flow	880	1,028	17

6.4.2 Sensitivity to Bottom Roughness Length

The AS originally selected as the capping material for this study was found to be easily subject to bedload transport under normal tidal condition during the cap erosion analysis. This was also found to be true for the smaller sand particle sizes for the UBS source. Even moderate tidal currents of about 1 ft/sec would mobilize a portion of the capped material as bedload transport. Under this mode of transport, sand grains would form ripples and dunes depending on the variation of the current speed. This process is not formulated within the current hydrodynamic model algorithms. During the modeling efforts, the bottom roughness of the capping material is assumed to be 0.001 m. Literature values indicate the bottom roughness length of medium to coarse sand would vary from 0.0003 to 0.006 m depending on the height of sand ripples and dunes (Dyer, 1986). In order to estimate the effect of this transient nature of bottom roughness length due to non-cohesive sand capping material, a sensitivity run was conducted with using a value of 0.005. A model run was performed using various bottom roughness lengths: 0.001 for non capped/armored areas, 0.005 for capped areas, and 0.01 for armored areas. Four simulations are conducted: "8 mile Cap – Armor Area Pre-Dredging" Scenario and "8 mile Cap – Full Pre-Dredging" Scenario for 100- and 500-year flow events. The maximum water level rise for these simulations are shown in Figure 6-27. The results indicate that, with higher bottom roughness length, maximum water level rise would increase by 10 to 15 cm for both existing depth and pre-dredged depth conditions.

Table 6-7 summarizes the flooded areas and the area changes under different hydrodynamic roughness lengths. The increase in water elevation rise due to higher bottom roughness results in a larger flooded area. However, the change in the flooded areas were projected to increase only by between 0.5-2.5% and 1.3-2.4% during 100- and 500-year flow events, respectively for both the existing depth and pre-dredged depth conditions, which are relatively small changes. This computation provides a bound on the range of uncertainty in the extent of flooded area associated with transient bottom roughness due to the mobile portions of the sand cap.

Table 6-7. Total Areas (acres) Flooded under Different Hydrodynamic Roughness Lengths of Capped Area

	Maximum Capping/Armoring Existing Bathymetry			Maximum Capping/Armoring Full Pre-Dredging		
	Original	Higher Zo	Difference (%)	Original	Higher Zo	Difference (%)
100-Year Flow	592	595	0.5	523	536	2.5
500-Year Flow	880	891	1.3	822	833	1.4

6.5 FEMA FLOW AND STORM SURGE SIMULATIONS

Two model runs were constructed in order to compare the flood areas computed by ECOMSEDZLJ with those estimated by FEMA. FEMA used 100- and 500-year flow and storm surge conditions estimated by USACE (1972 and 1973) and applied both the flow and storm surge conditions concurrently for the estimation of the flood areas in the LPR.

Following is the summary of the flow and storm surge conditions of the FEMA flood study:

- 100-year condition
  - Flow: 30,200 cfs
  - Storm surge: 10.2 ft (3.1m) ((NGVD29)
- 500-year conditions
  - Flow: 46,200 cfs
  - Storm surge: 12.8 ft (3.9m) (NGVD29)

It is worth noting that FEMA's 500-year flow and storm surge values are about 75% and 30% higher, respectively, than those estimated by HydroQual for use in this study. The model was configured with the above forcing information and simulated for 10 days. Maximum water elevations along the LPR during the 100- and 500-year events are shown in Figure 6-28. The figure also shows the maximum water level rise along the river computed by FEMA. The results indicate that the ECOMSEDZLJ computed water level during the 100 year event rises from 3.1m at the river mouth to 6.0 m at the upstream end of the river.

During the 500 year event, the water level rises from 4.0 m to 7.5m. However, the FEMA results indicate that water level rise during the 100-year event varies from 3.2 m at RM 8 to 6.9m at the upstream end. The FEMA 500-year event shows even more significant water level rise: 3.8m at RM 8 to 8.4m at the upstream end. The two model results show comparable water level rises in the narrow sections of the LPR upstream of RM 8. However, there are still a few underlying differences in the application of two models. The most probable causes of the differences could be:

1) Physical configuration of the river such as hydraulic capacity (channel dimension), bottom resistance, land elevation, etc. As described in Section 2, ECOMSEDZLJ model was configured with most recent USACE survey data for both the river (2004) and land elevations (1995). There are about 10 bridges that are partially or fully submerged during the 500-year flow. These would likely impact the water surface elevation profile significantly. These man-made structures are not considered in ECOMSEDZLJ.

2) Modes of hydraulic computation: steady-state (FEMA) vs. dynamic computation (ECOMSEDZLJ). In steady-state computation, it is assumed that the surge and flow conditions are constant. On the contrary, ECOMSEDZLJ defined a flow curve which reaches the peak flow for only a short period of time (*i.e.* less than few hours).

Figure 6-28 indicates that 500-year FEMA estimated water elevation at RM 8 is about 3.8m, which is the storm surge elevation expected at the mouth of the river. The figure shows that FEMA estimated no elevation change from the mouth of the river to RM 8 whereas ECOMSEDZLJ computed about 0.5m water level rise in the same distance, which suggests another inconsistency between FEMA and ECOMSEDZLJ configuration.

Figures 6-29 and 6-30 show the projected flood areas computed by ECOMSEDZLJ for the 100- and 500-year events. About 2,080 acres and 2,650 acres would be flooded under the 100- and 500-year events using the FEMA-estimated values for flow and storm surge. The model results indicate that most of the downstream locations are flooded during events except some areas where the land elevations are higher than 6m. The ECOMSEDZLJ computed flood areas were compared with the FEMA-estimated 500-year flood areas in the LPR. The approximate FEMA 500-year flood areas in the LPR are about 3,500 acres counting from the mouth of the river. ECOMSEDZLJ computed 500-year flood areas that account for about 75 percent of the area estimated by FEMA. Most of the discrepancies in the flooded areas are found to occur within the first three miles of the river (see Figures 6-29 and 6-30), where the yellow shaded areas are FEMA estimated 500-year flood areas and red shaded areas are the ECOMSEDZLJ computed flood areas. In upstream locations, the ECOMSEDZLJ computed flood areas overlap most of the FEMA estimated areas except for a few locations downstream of the Dundee Dam and the "S" shaped section of the river near the City of Passaic. ECOMSEDZLJ computed flooded areas upstream of RM 3 account for about 75% (1.485 acres out of 1.816 acres) of the area estimated by FEMA.

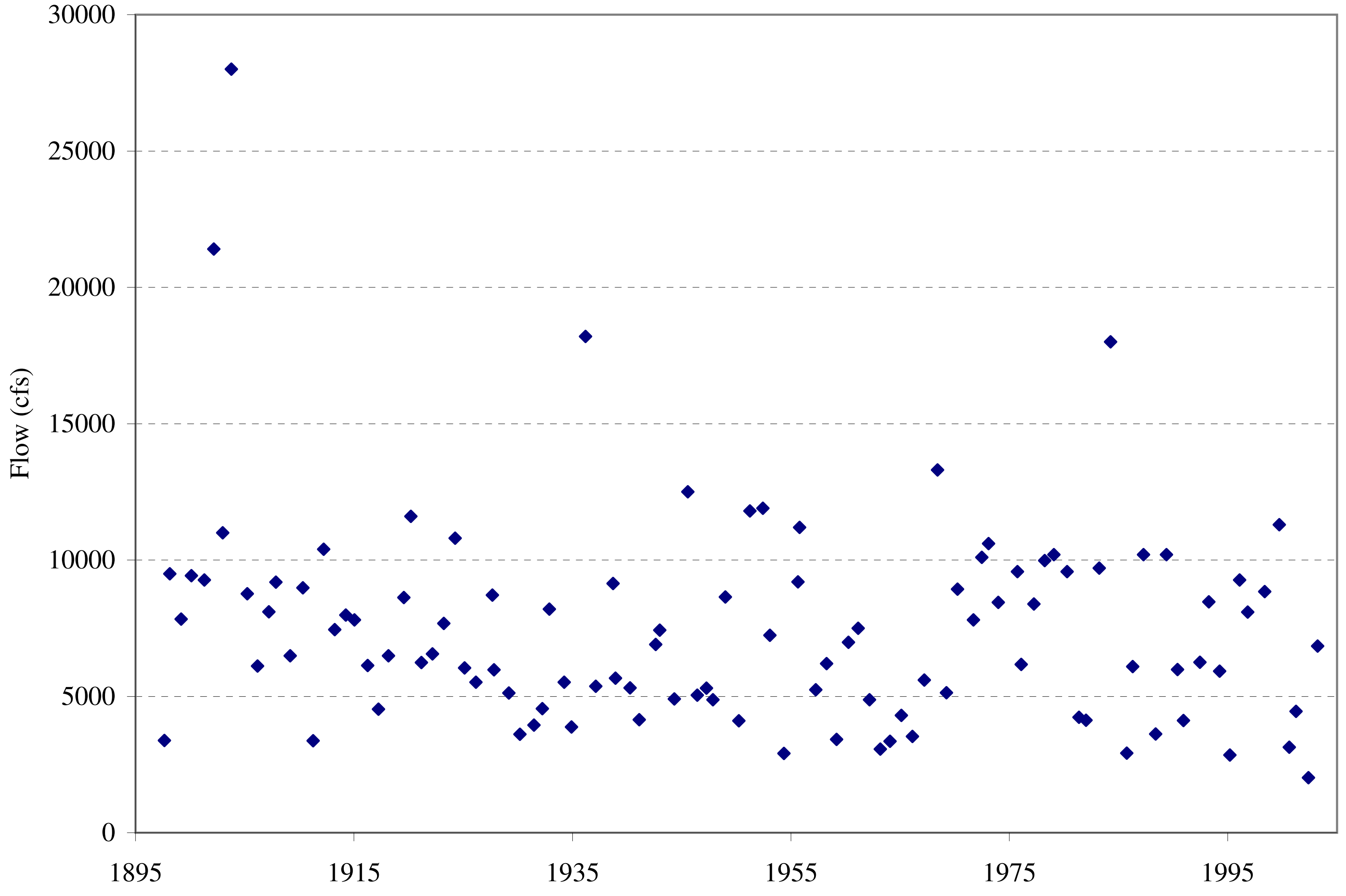

Figure 6-1. Annual maximum daily flows at Little Falls between 1981 and 2005.

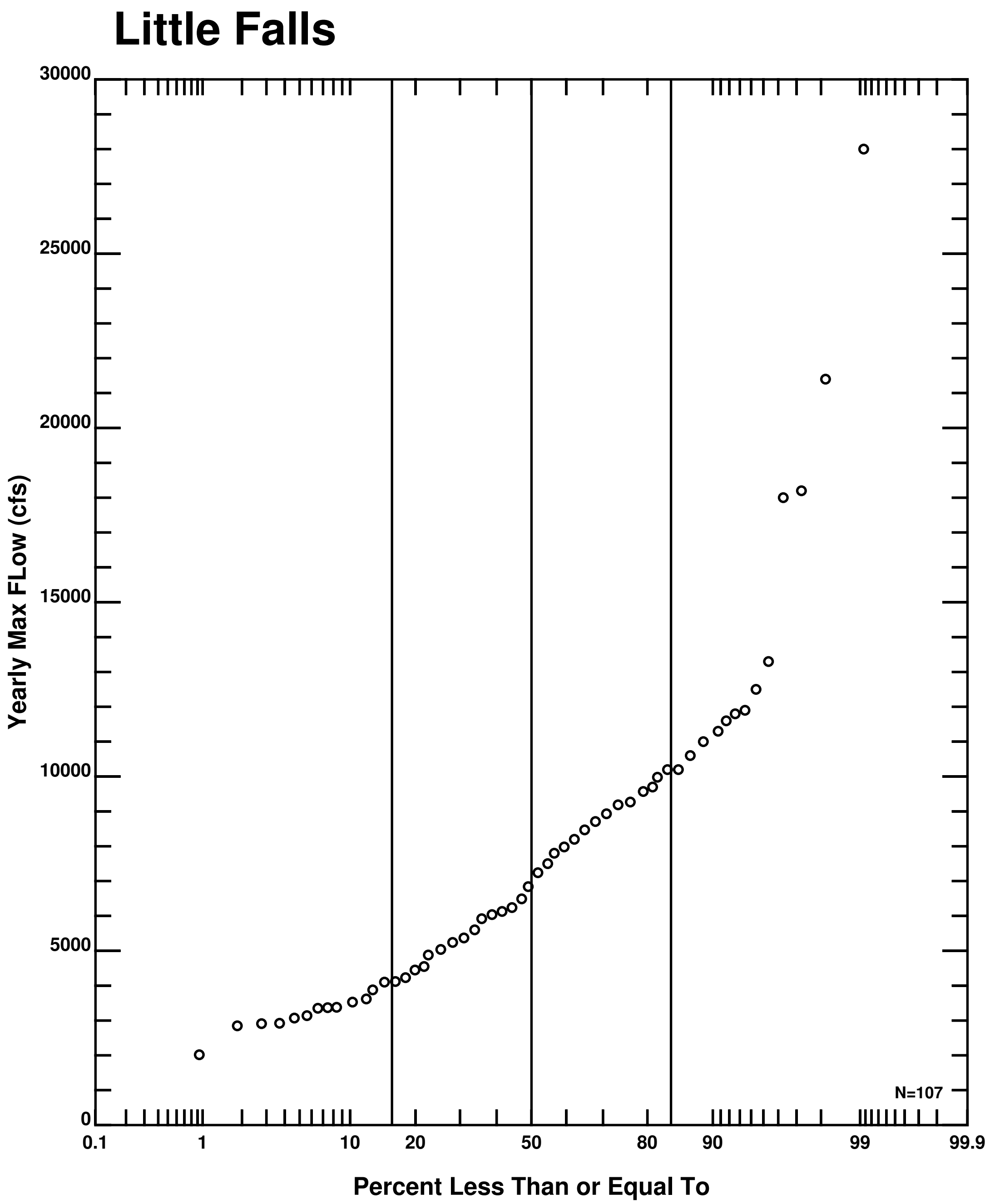

Figure 6-2. Probability distribution of annual maximum flows observed at Little Falls.

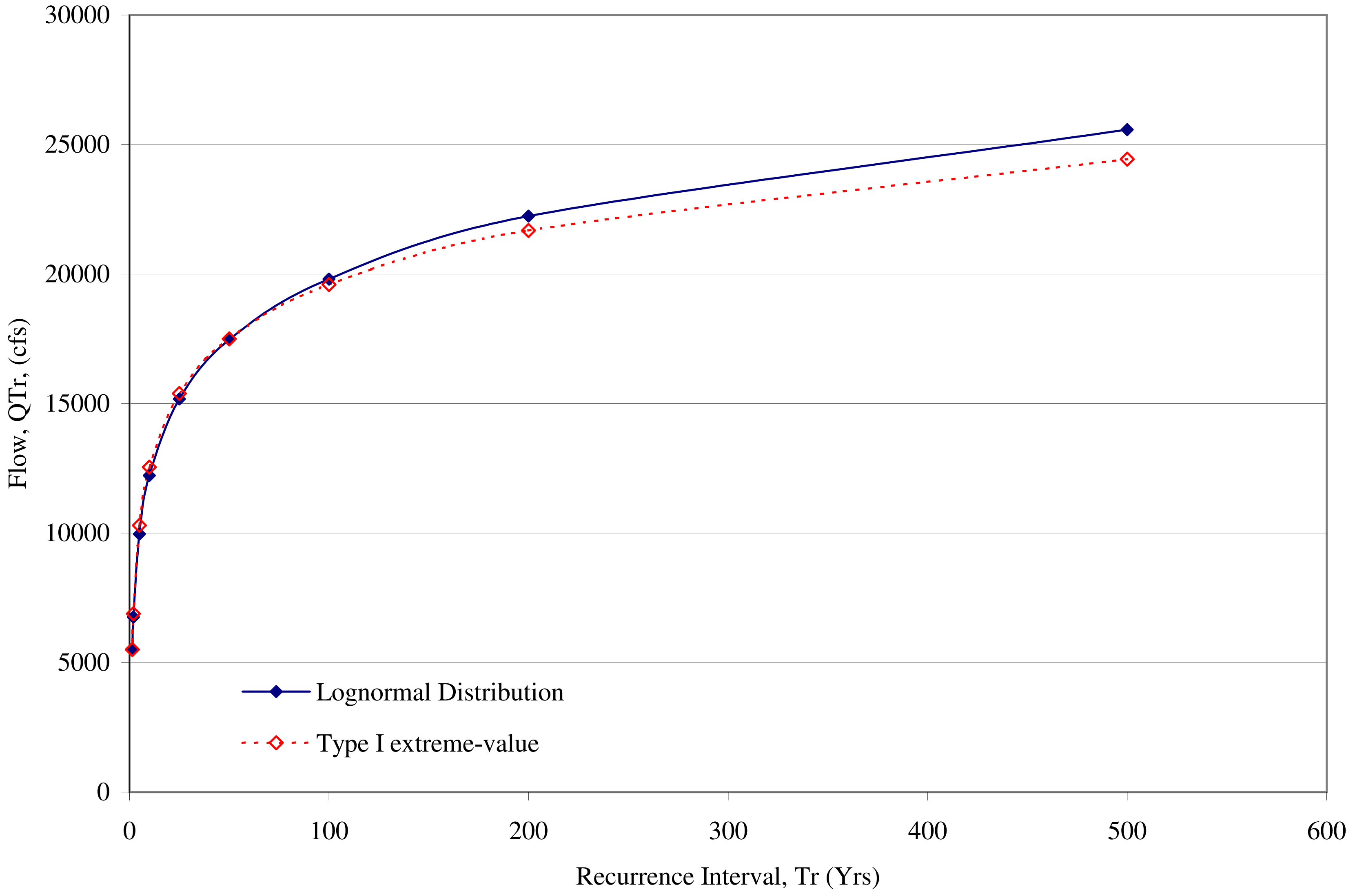

Figure 6-3. Estimated 100- and 500-year flows using Log-Normal and Type 1 Extreme (Gumbel) methods.

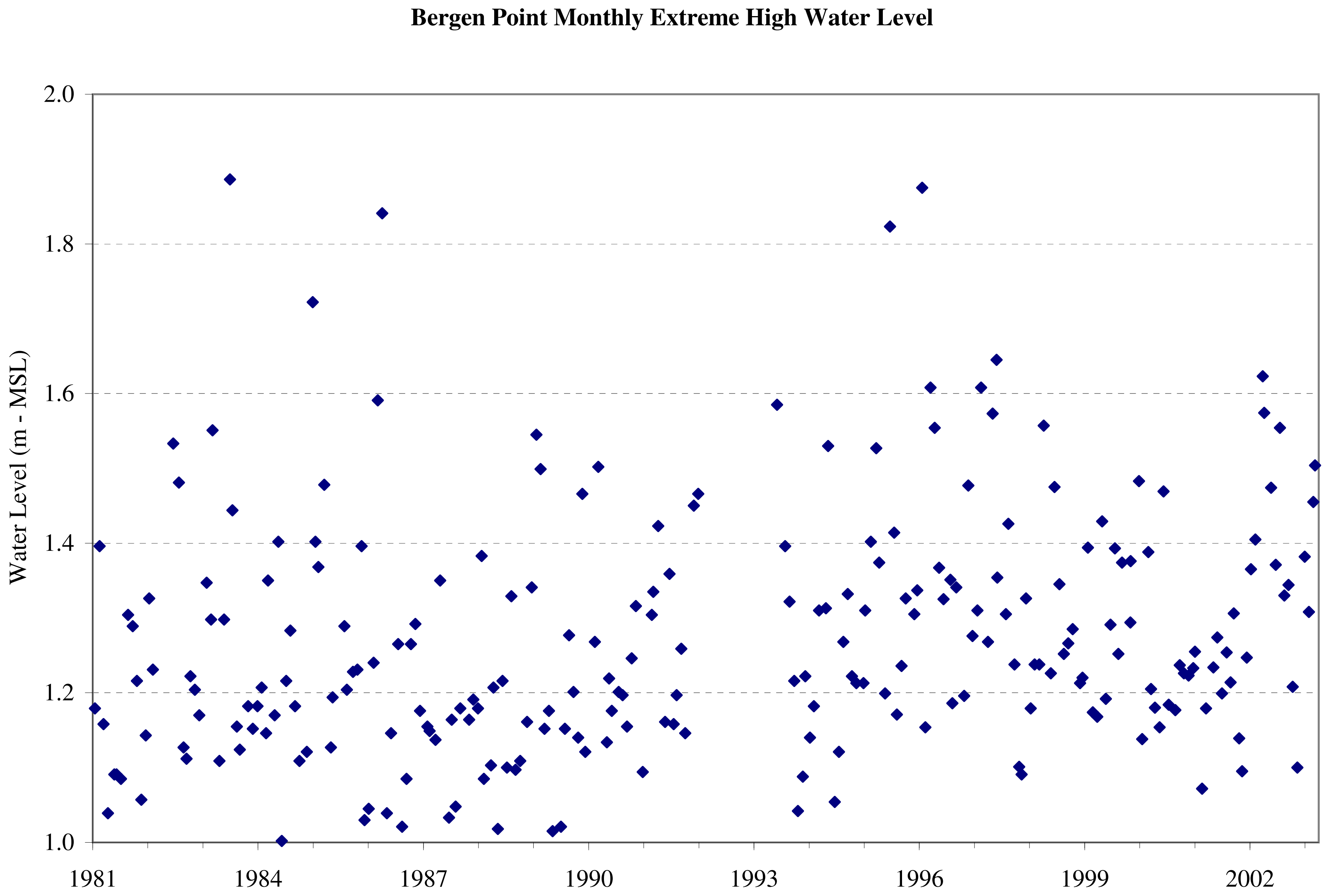

Figure 6-4. Monthly extreme high water levels at Bergen Point between 1982 and 2003.

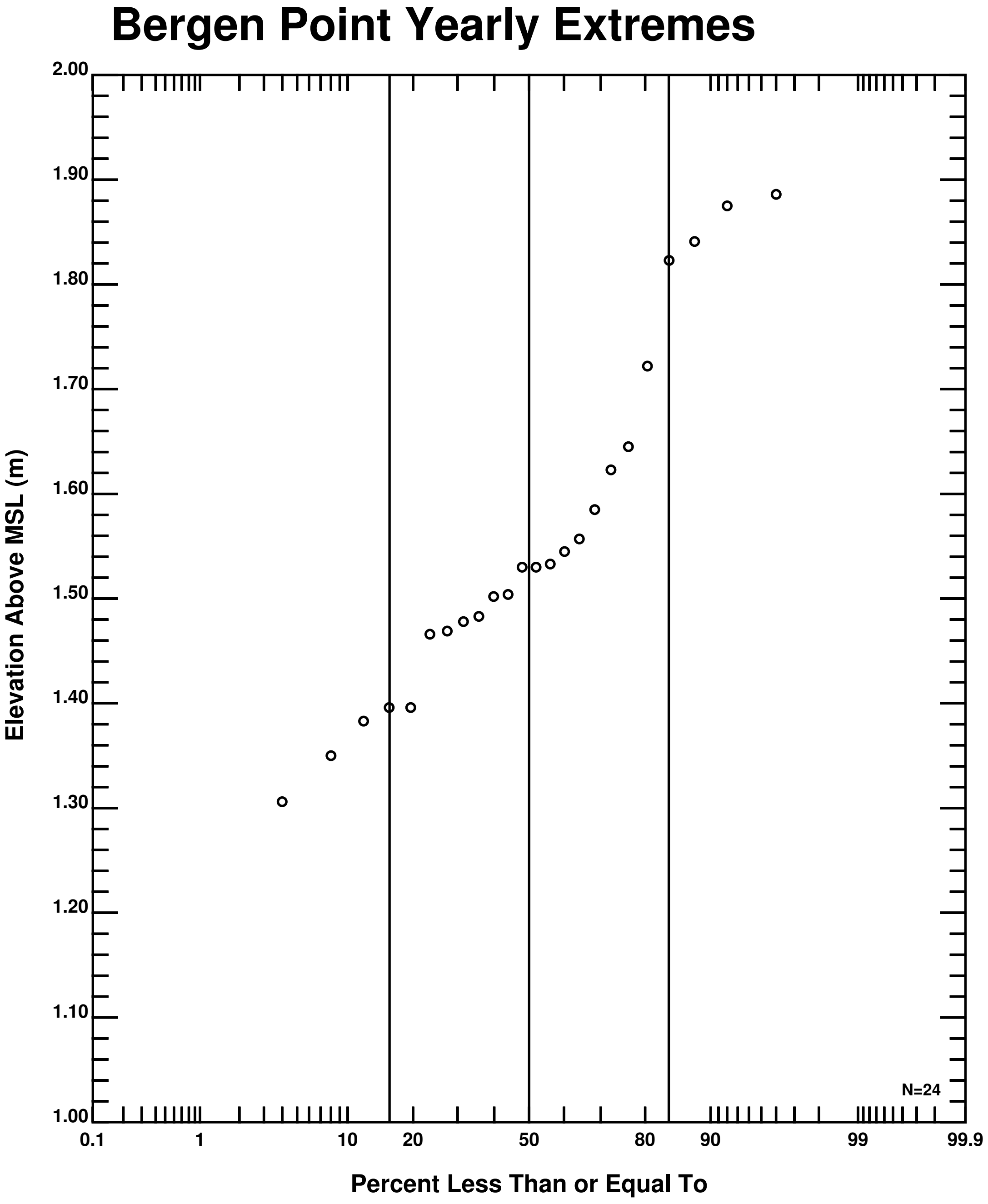

Figure 6-5. Probability distribution of annual extreme elevations observed at Bergen Point.

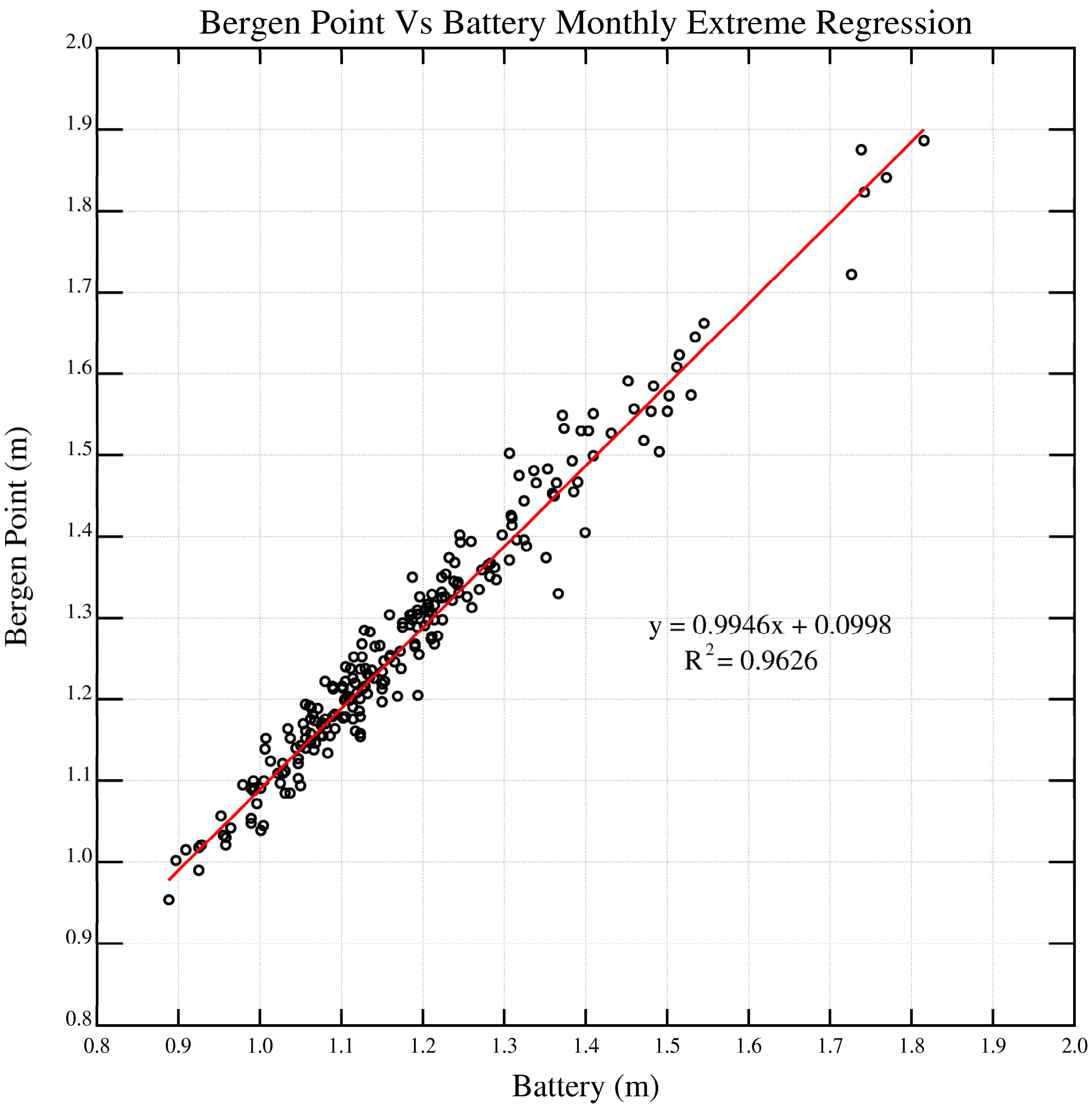

Figure 6-6. Correlation analysis of the monthly extreme water elevations between Bergen Point and the Battery NOAA stations.

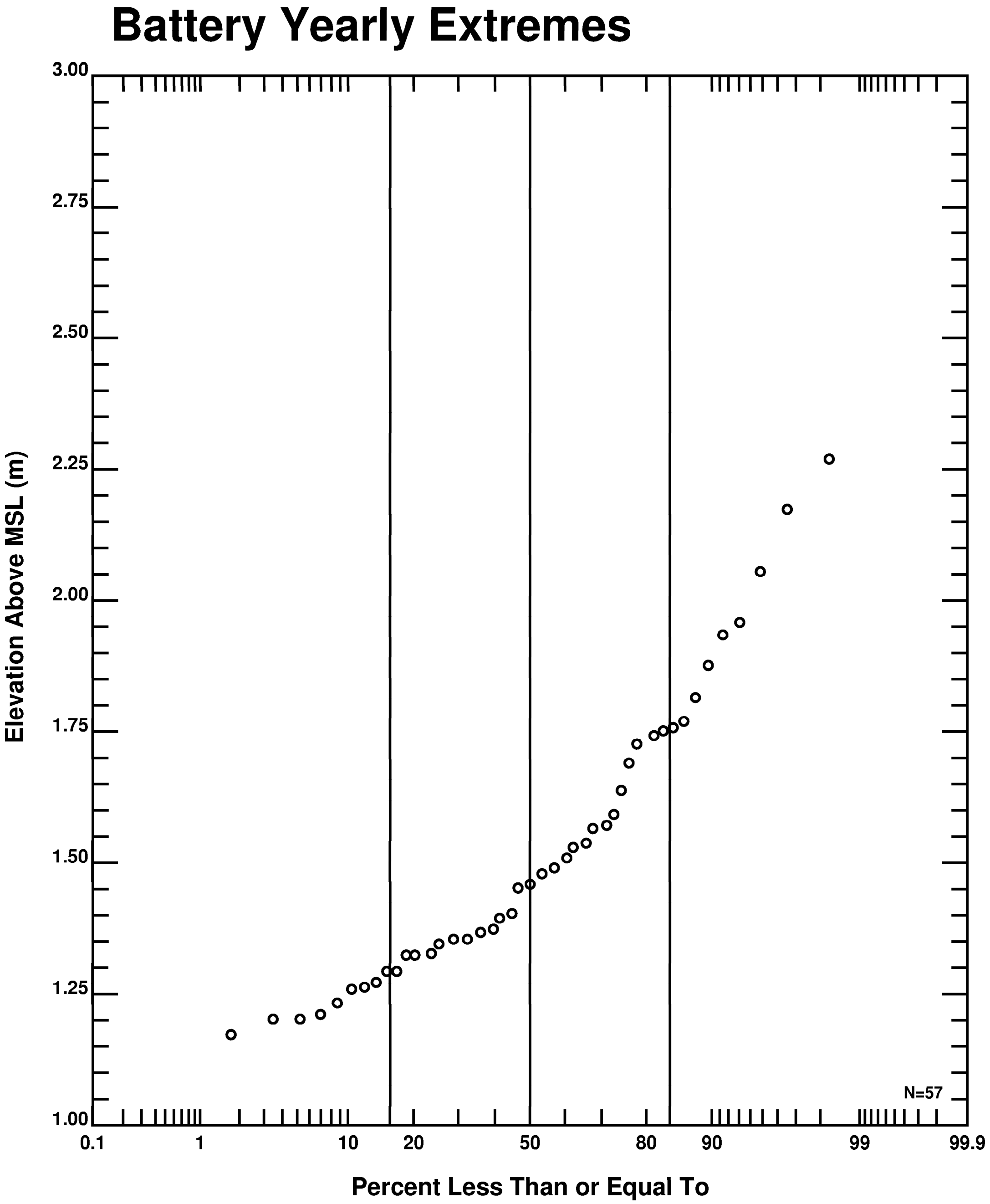

Figure 6-7. Probability distribution of annual extreme elevations observed at the Battery.

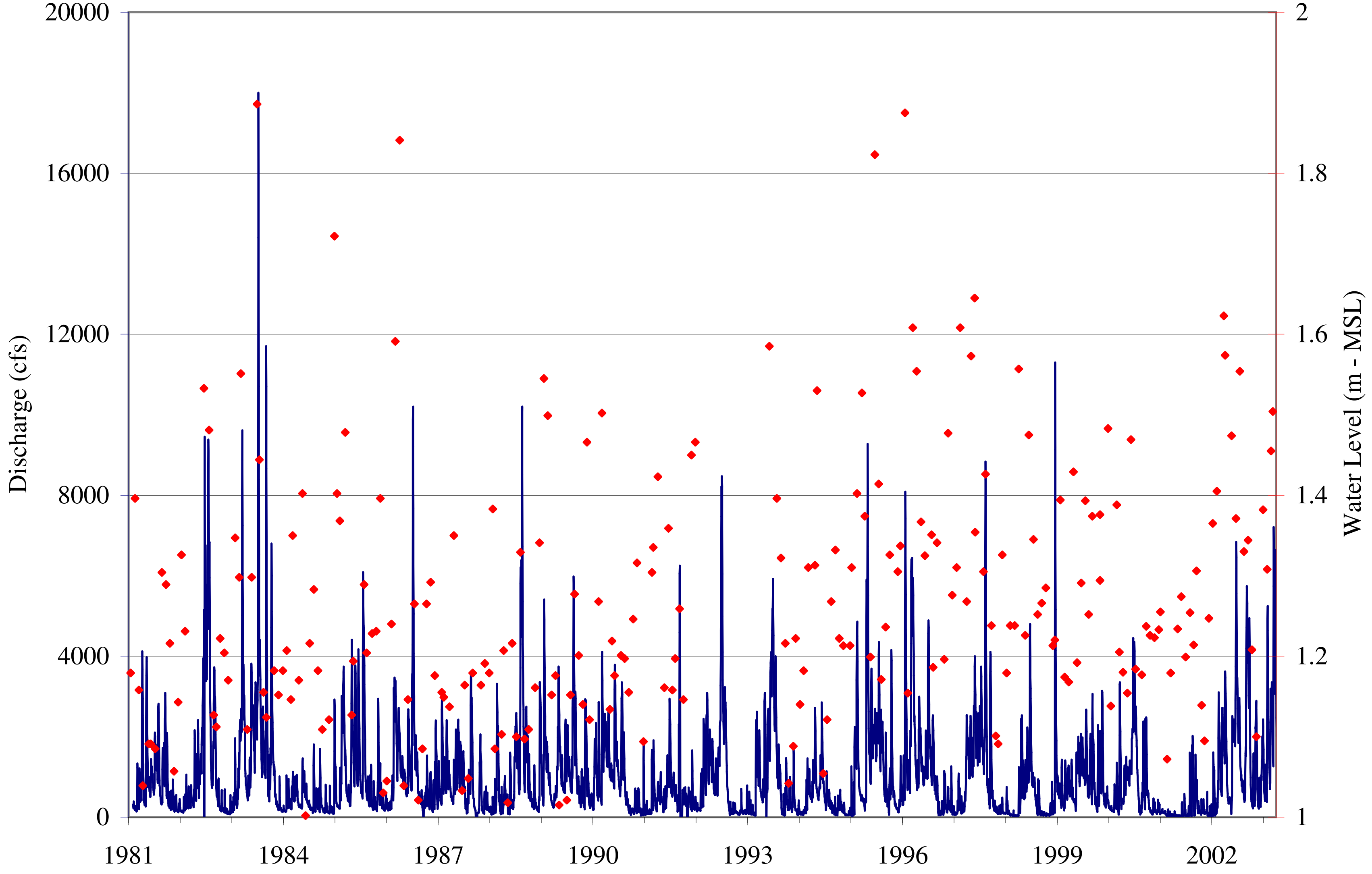

Daily Mean Discharge At Little Falls and Bergen Point
Monthly Extreme High Water Level

Figure 6-8. Daily flows measured at Little Falls and monthly extreme high water levels at Bergen Point between 1982 and 2003.

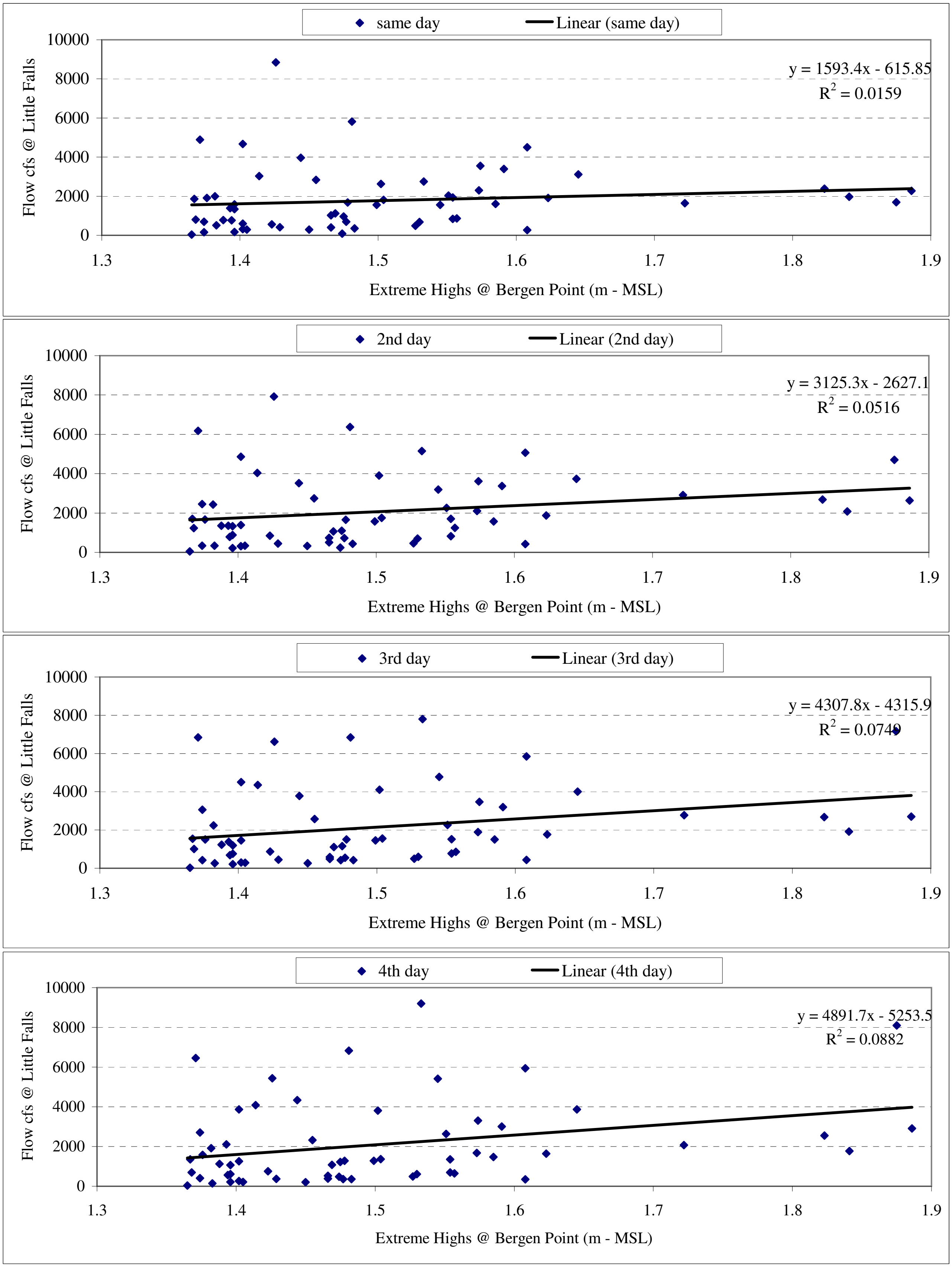

Figure 6-9. Correlation analysis of extreme water levels and daily flows: correlation of same day events (top panel); water level vs. flow of second day(2nd panel); water level vs. flow of third day (3rd panel); water level vs. flow of 4th day (bottom panel).

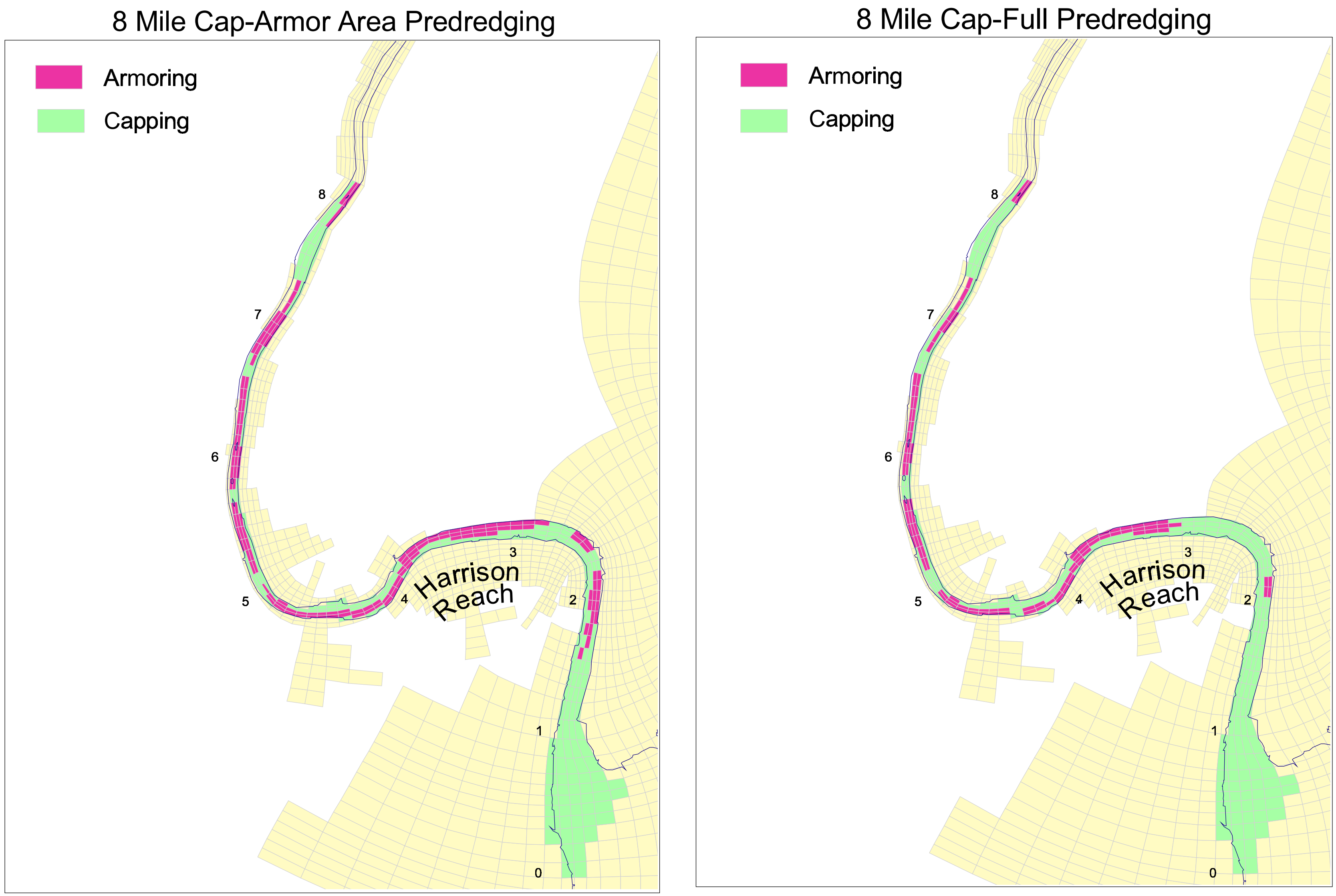

Figure 6-10. Extent of capping/armoring scenarios : capping and armoring areas for 8 mile cap-armor area predredging (left panel) and 8 mile cap-full predredging (right panel) are shown.

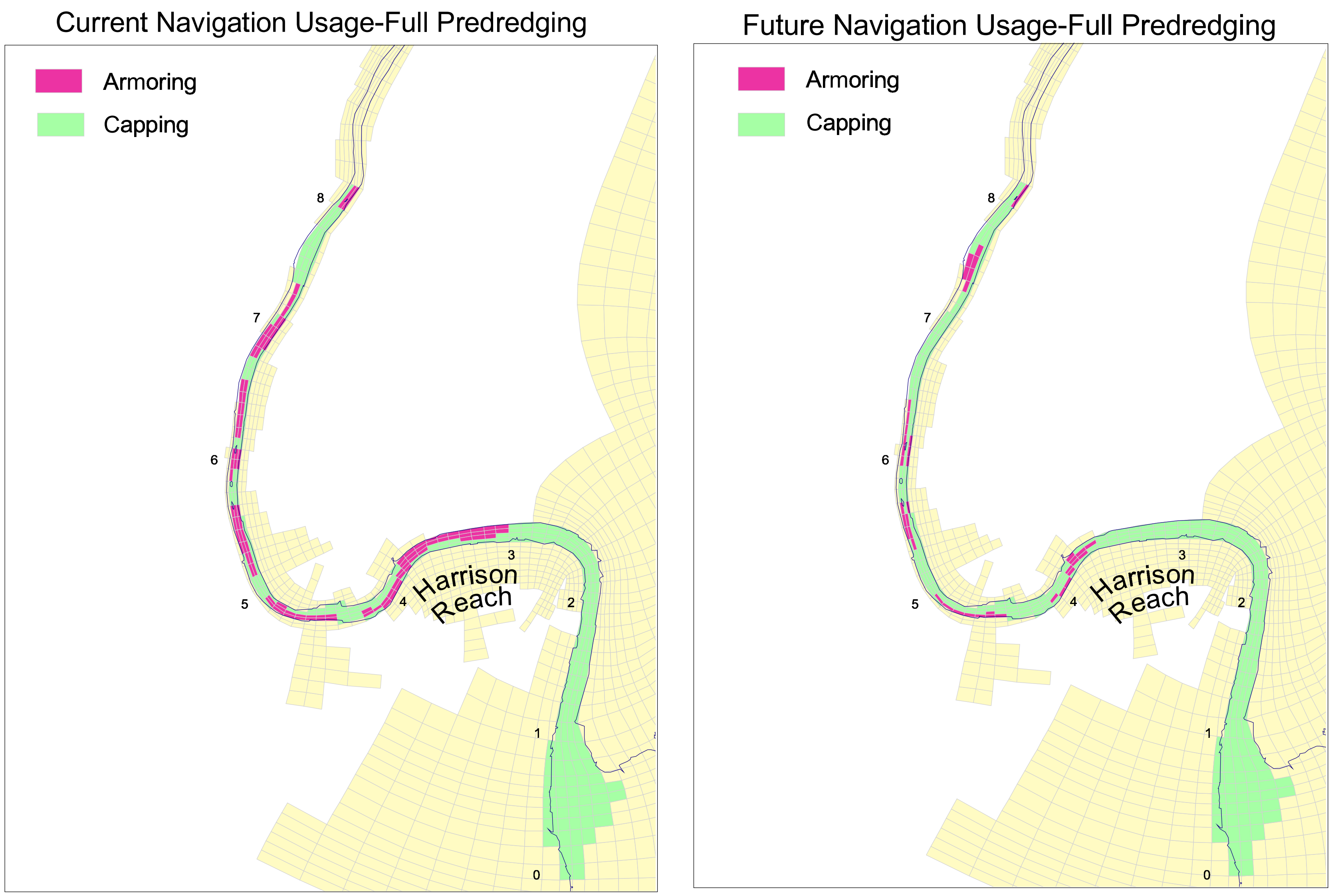
Current Navigation Usage-Full Predredging

Future Navigation Usage-Full Predredging

Figure 6-10. (continued) Extent of capping/armoring scenarios : "Current Navigation Usage" and "Future Navigation Usage" areas are shown.

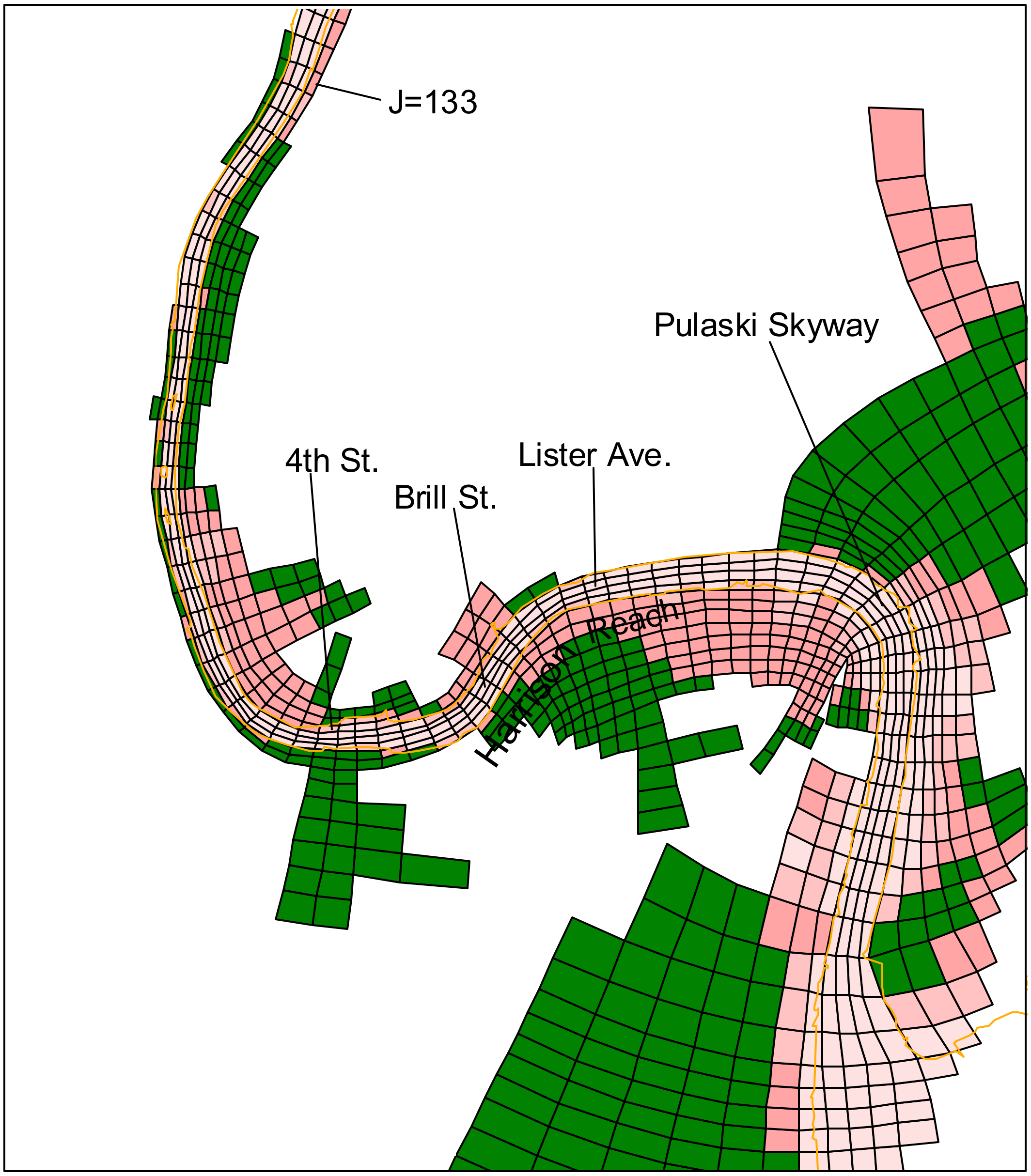

Figure 6-11. Map showing the time series output locations.

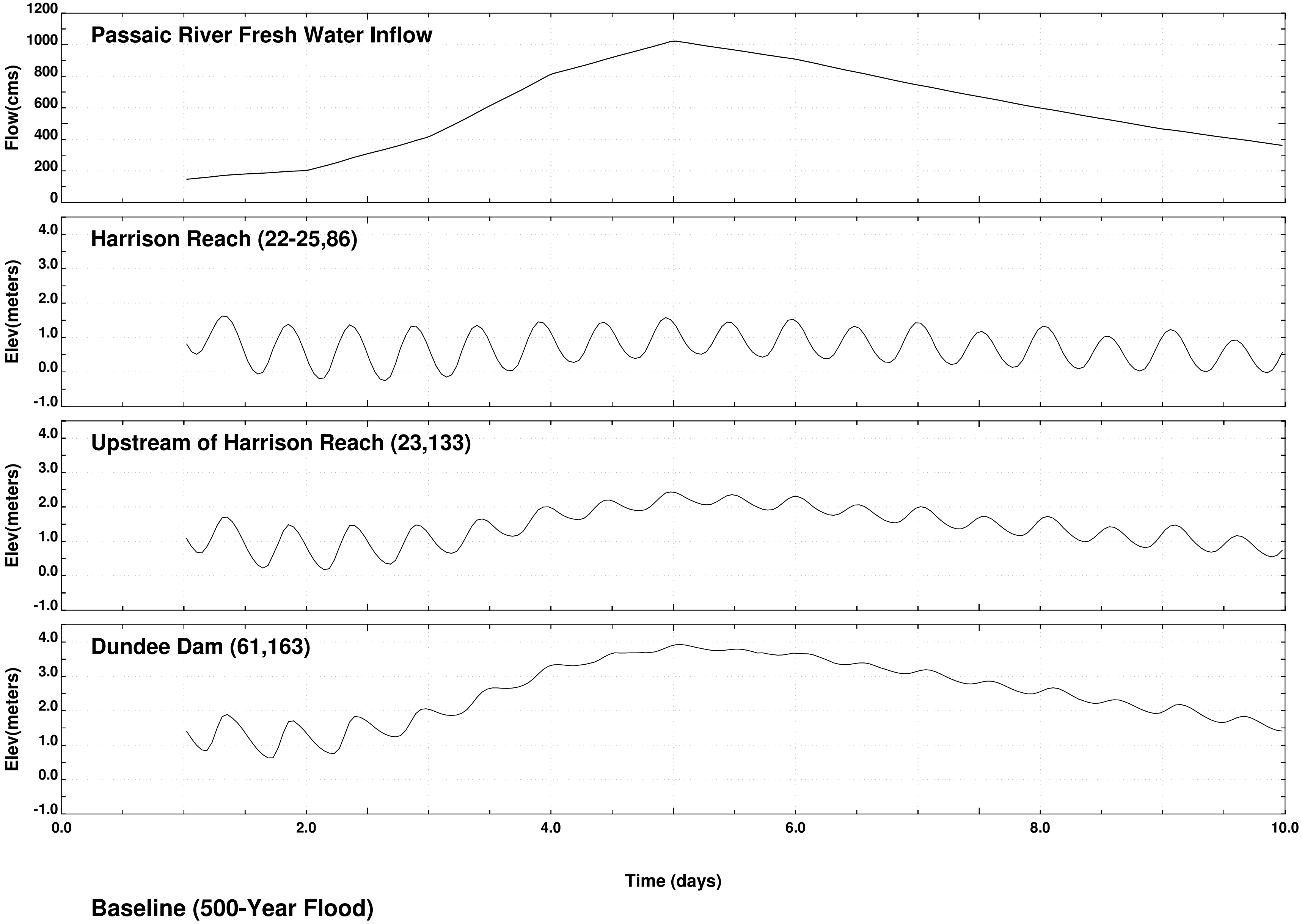

Figure 6-12. The 500-year flow (top panel) and water surface elevation for the Base Case Scenario in Harrison Reach and near Dundee Dam.

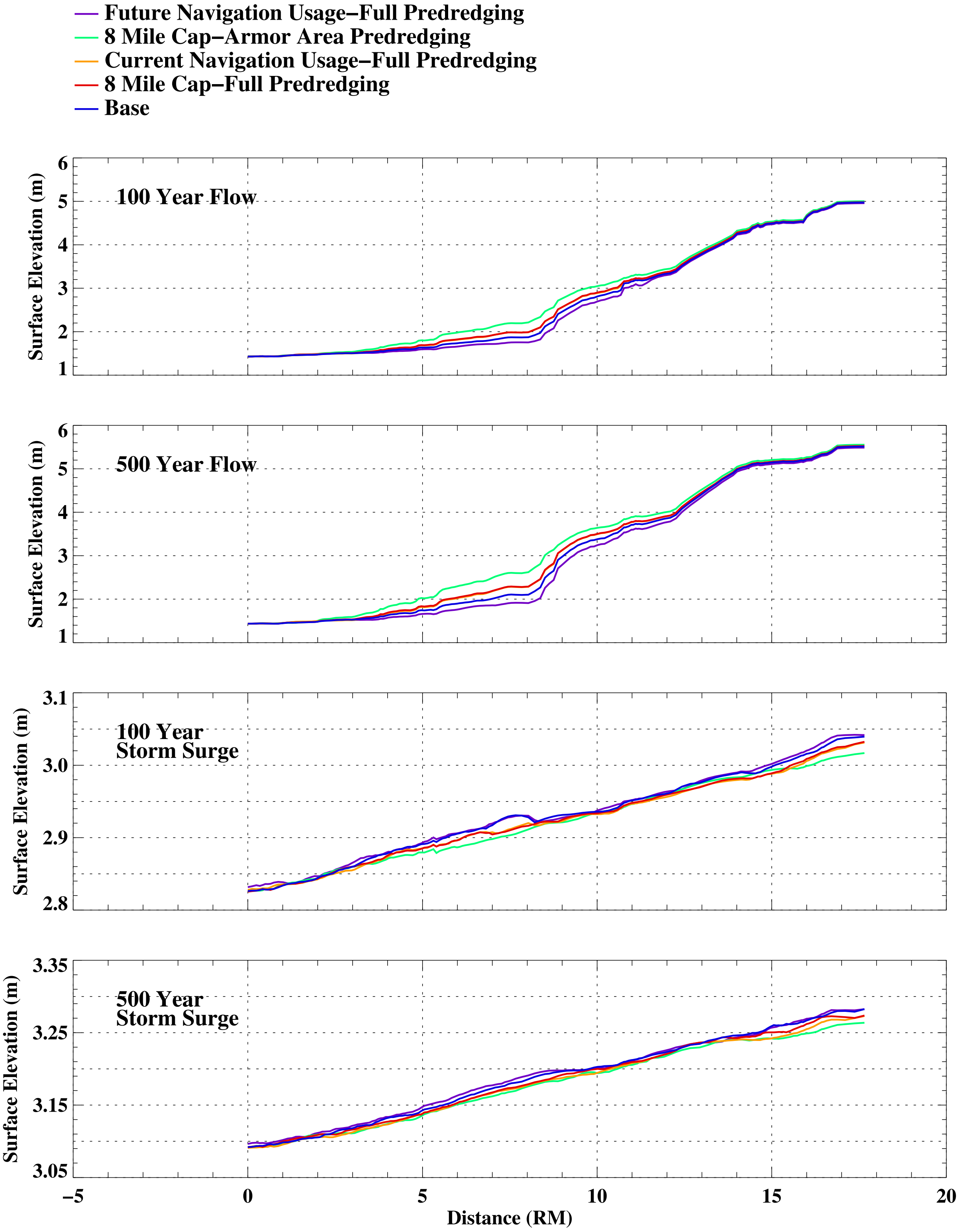

Figure 6-13. Maximum water surface elevations under different simulation scenarios along the Passaic River.

100 Year Flow for Base Case

Figure 6-14. Projected flood area under the Base Case Scenario during the 100-year flow

100 Year Flow for 8 Mile Cap-Armor Area Predredging

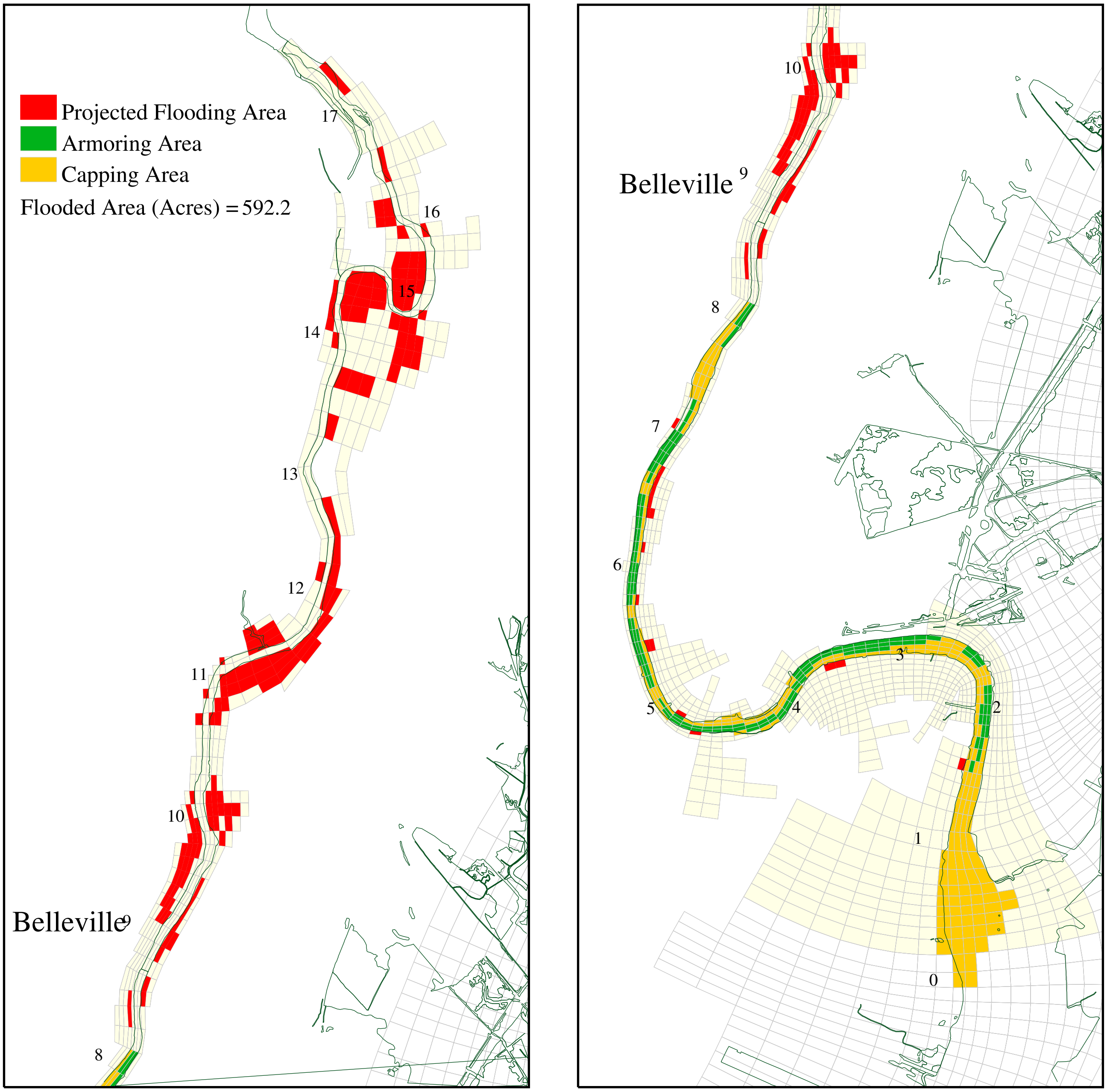

Figure 6-15. Projected flood area under the 8 Mile Cap-Armor Area Predredging Scenario during the 100-year flow.

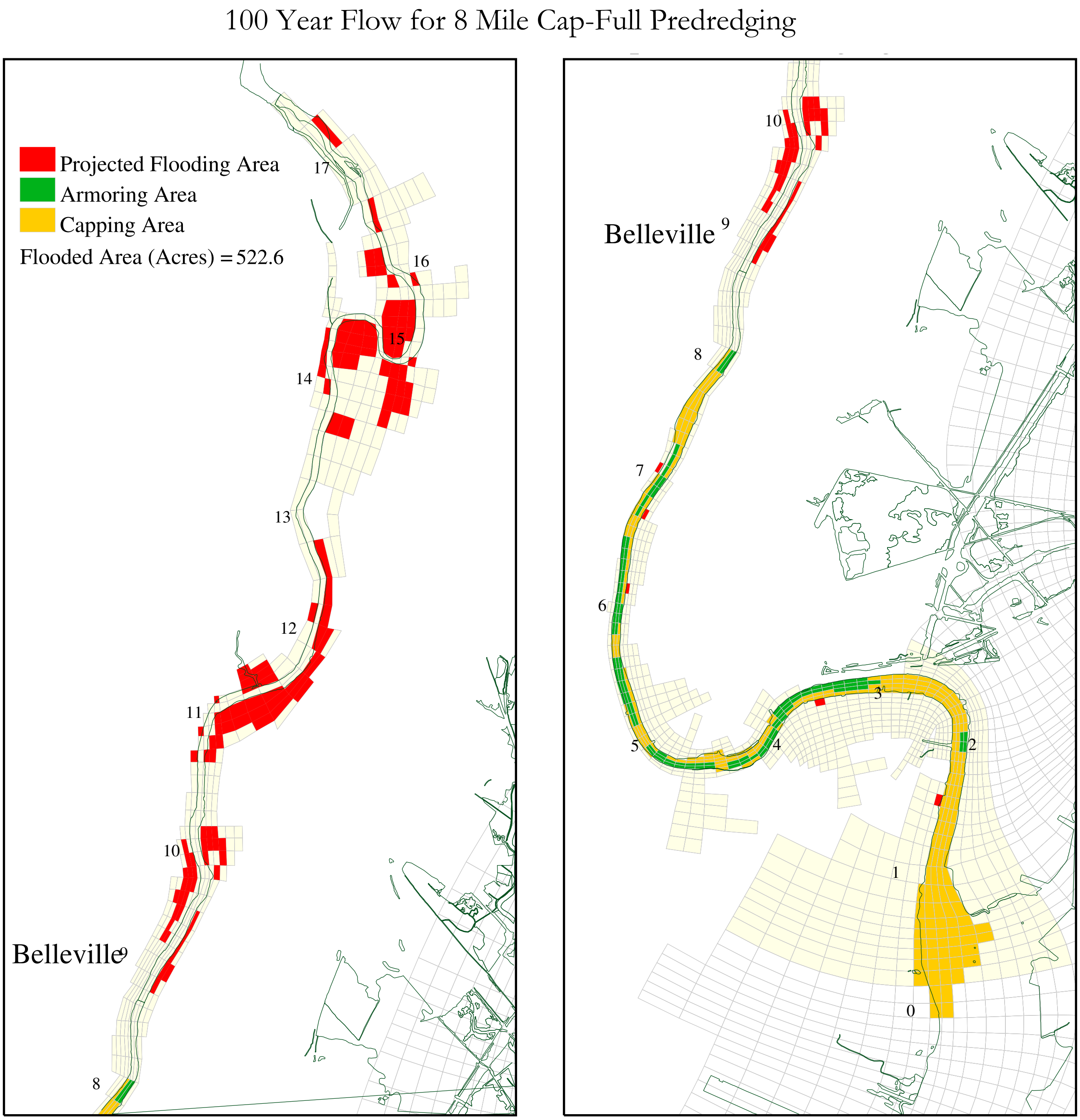

Figure 6-16. Projected flood area under the 8 Mile Cap-Full Predredging Scenario during the 100-year flow.

100 Year Flow for Future Navigation Usage-Full Predredging

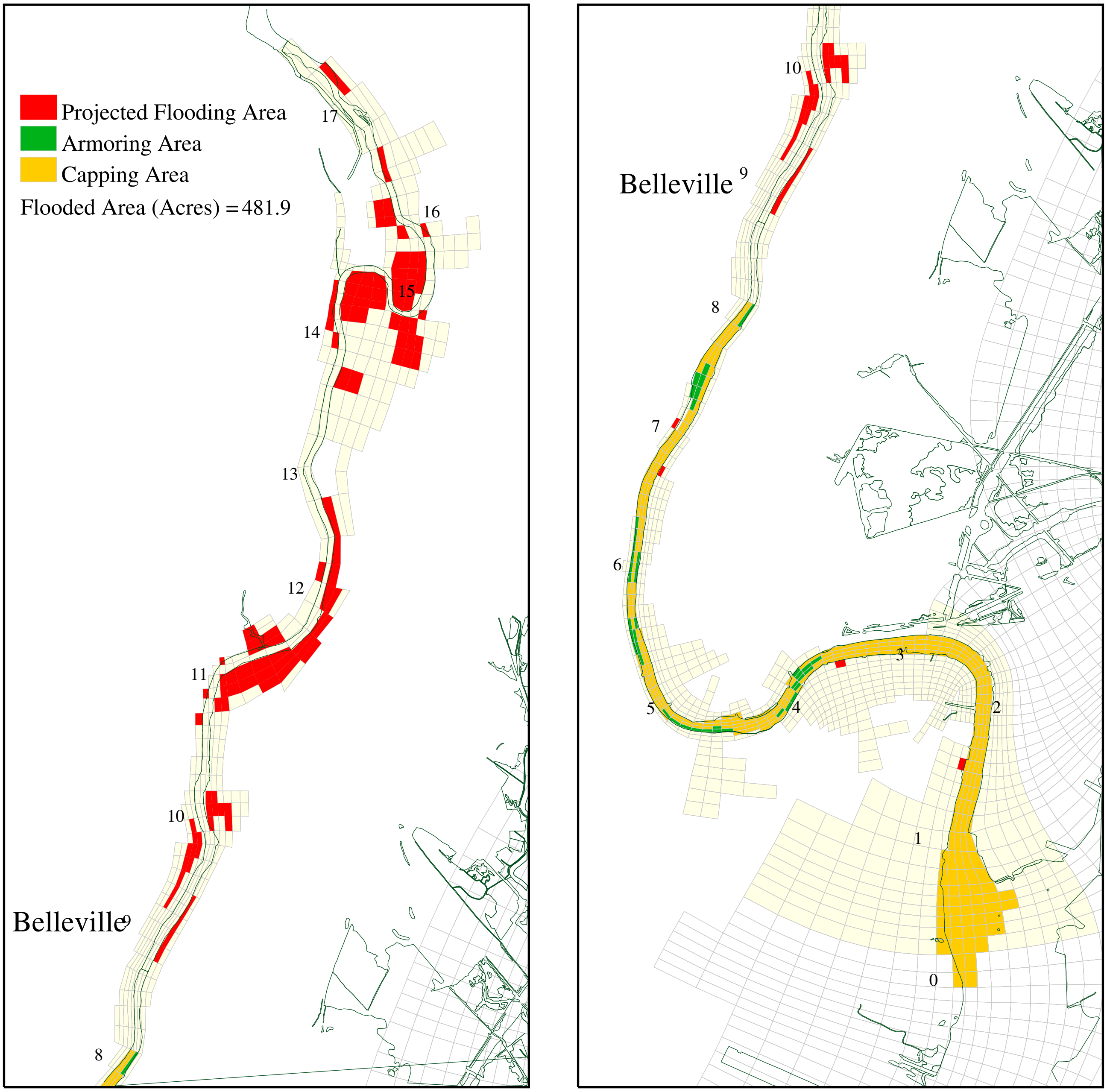

Figure 6-17. Projected flood area under the Future Navigation Usage-Full Predredging Scenario during the 100-year flow.

500 Year Flow for Base Case

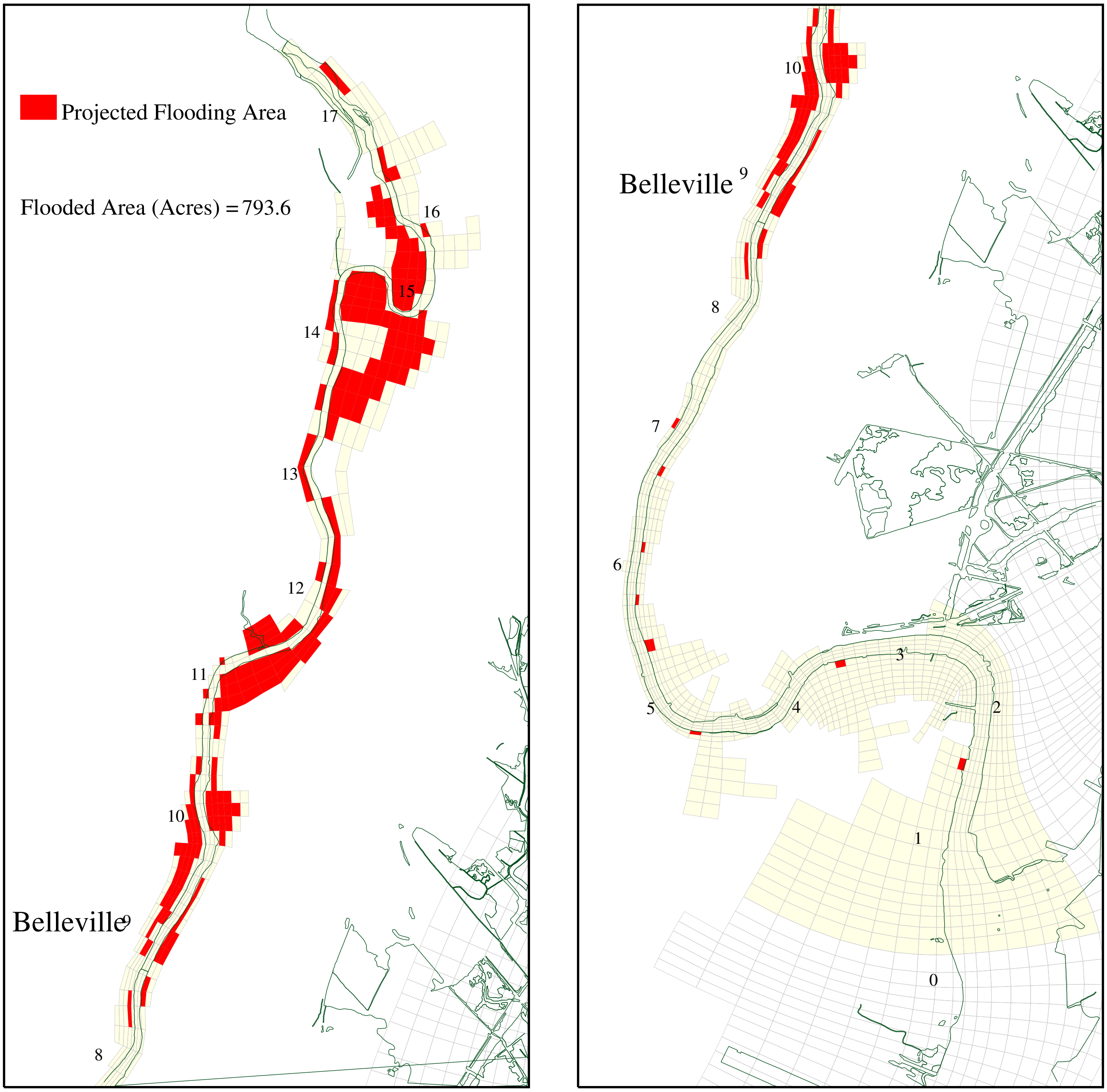

Figure 6-18. Projected flood area under the Base Case Scenario during the 500-year flow.

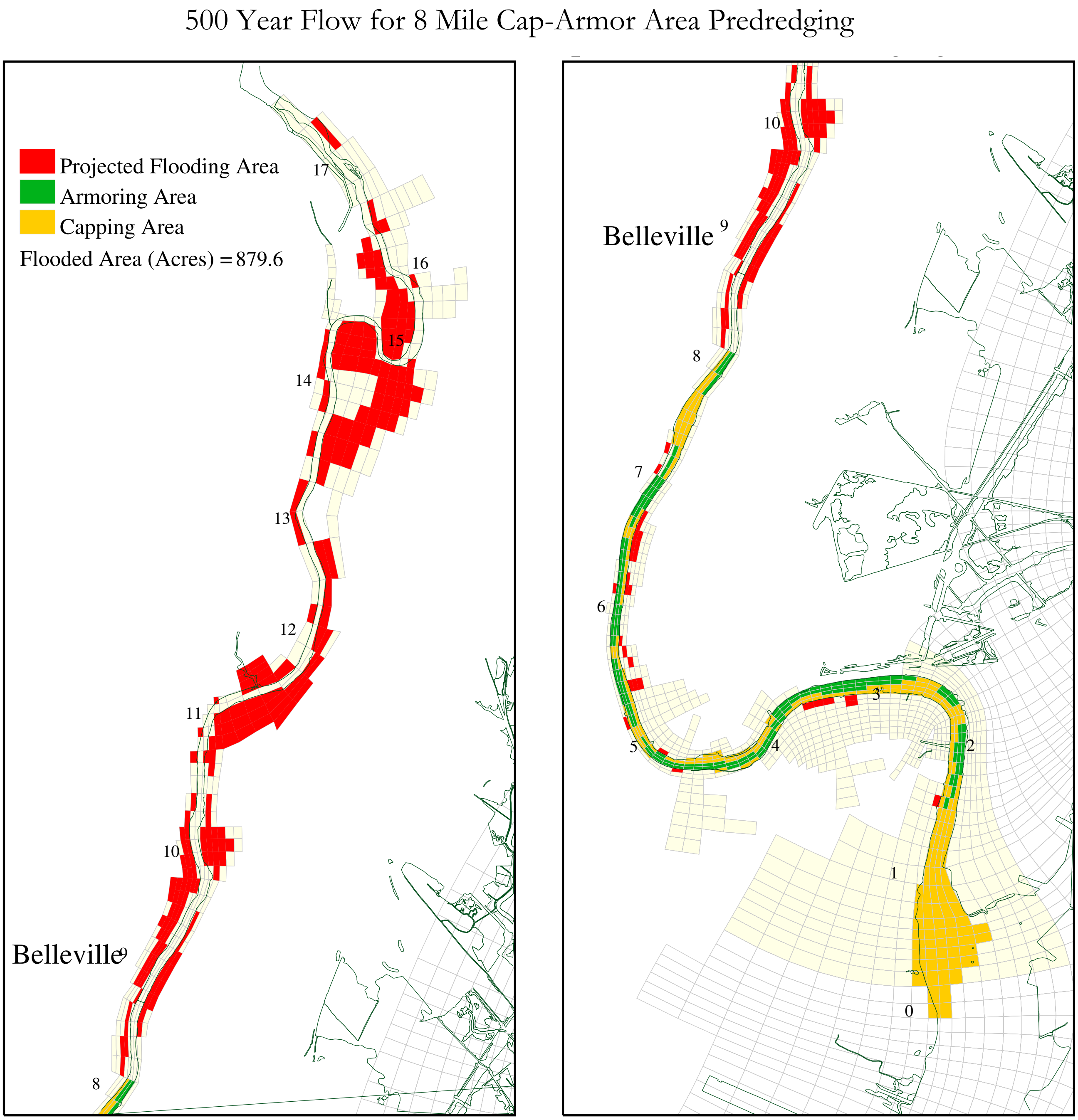

500 Year Flow for 8 Mile Cap-Armor Area Predredging

Figure 6-19. Projected flood area under the 8 Mile Cap-Armor Area Predredging Scenario during the 500-year flow.

500 Year Flow for 8 Mile Cap-Full Predredging

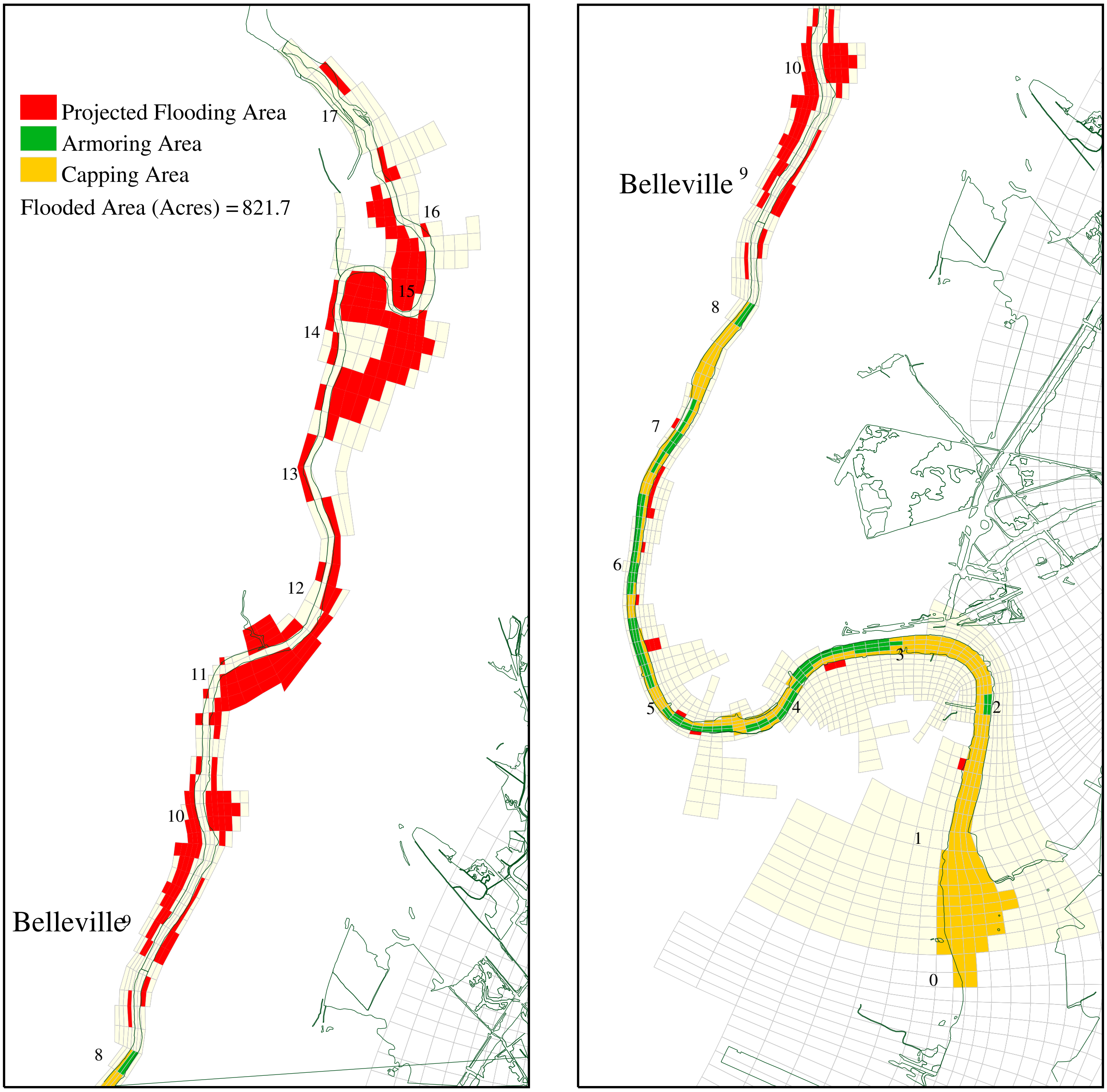

Figure 6-20. Projected flood area under the 8 Mile Cap-Full Predredging Scenario during the 500-year flow.

500 Year Flow for Future Navigation Usage-Full Predredging

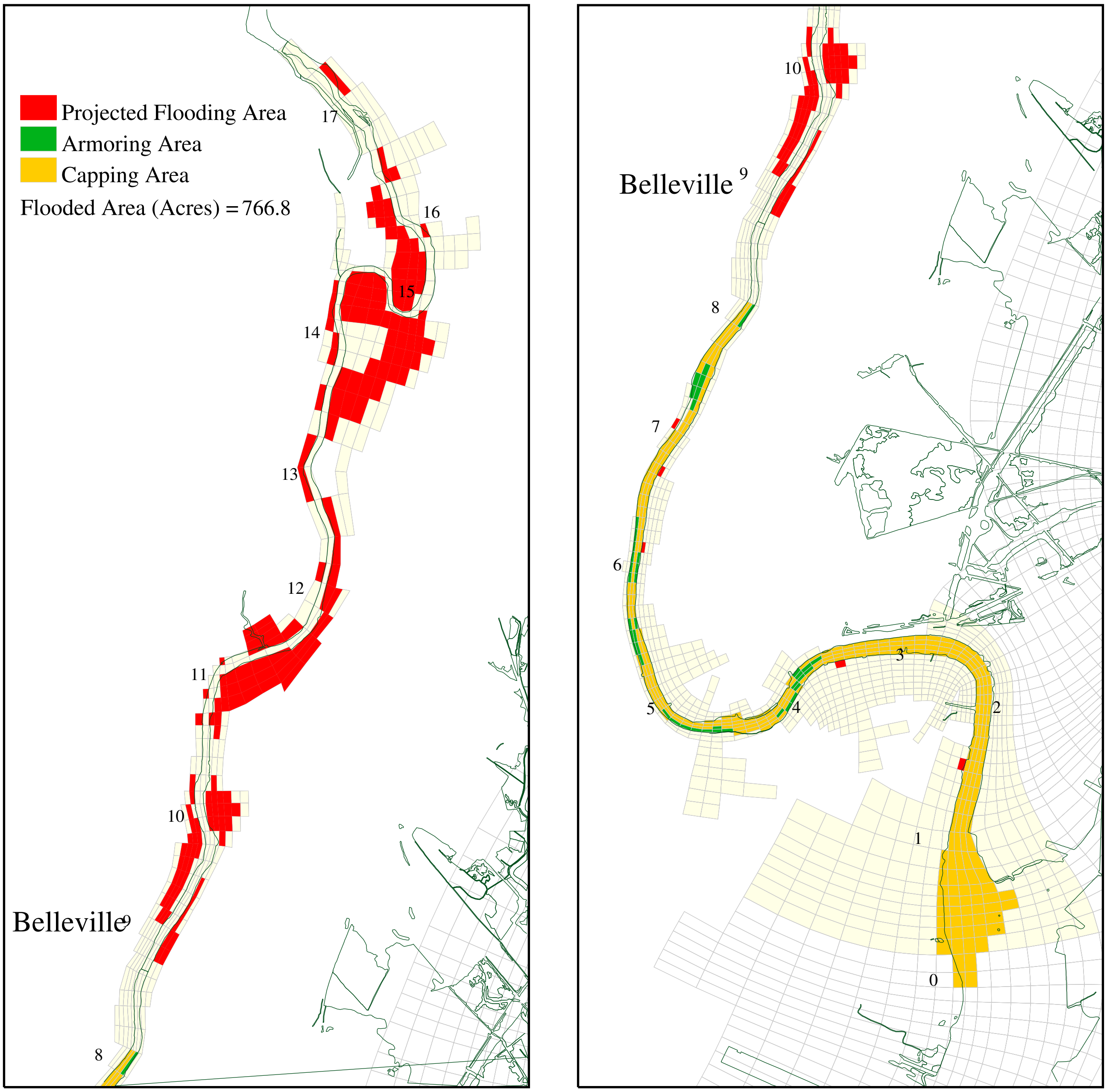

Figure 6-21. Projected flood area under the Future Navigation Usage-Full Predredging Scenario during the 500-year flow.

100 Year Storm Surge for Base Case

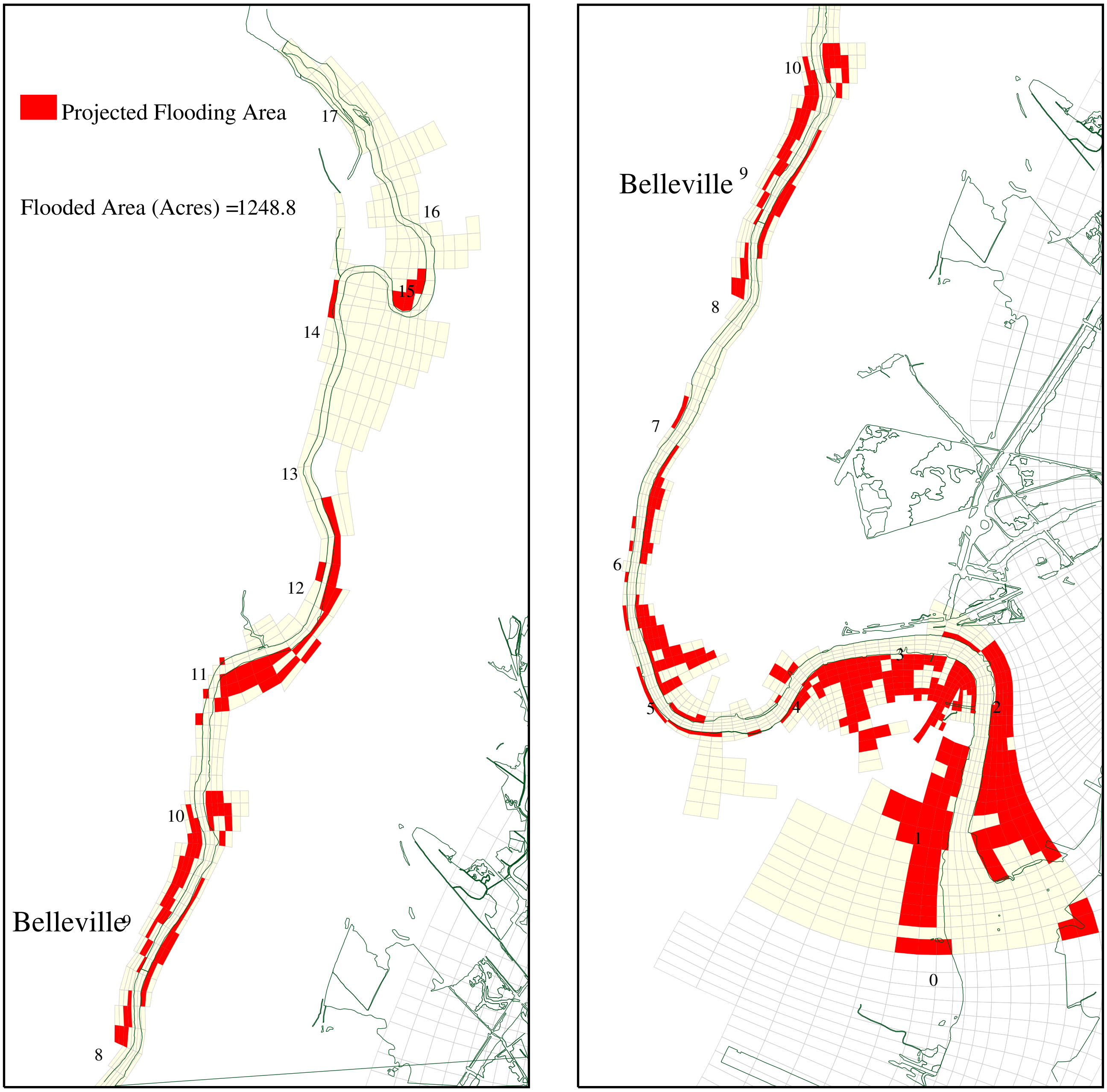

Figure 6-22. Projected flood area under the Base Case Scenario during the 100-year storm surge.

500 Year Storm Surge for Base Case

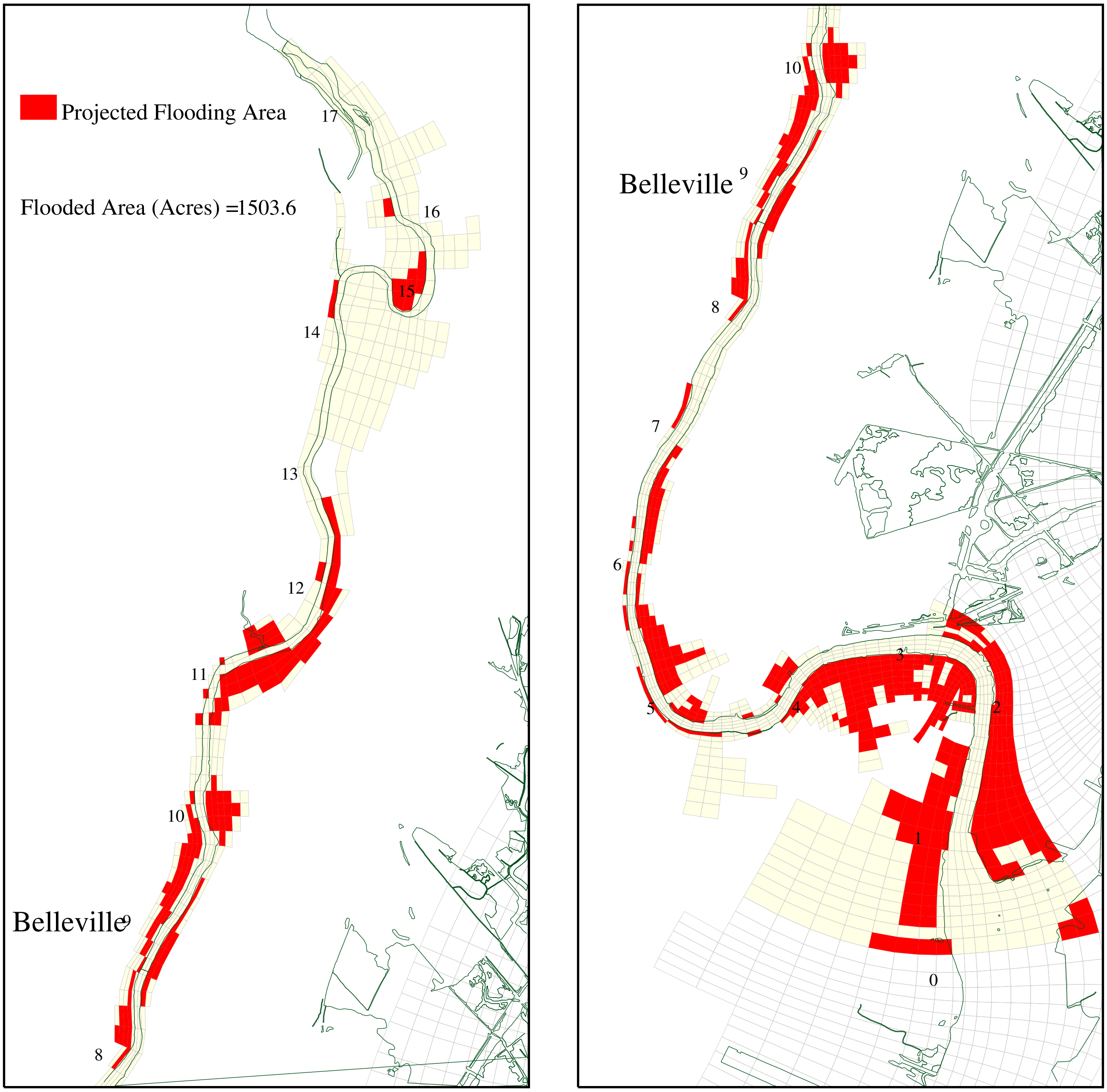

Figure 6-23. Projected flood area under the Base Case Scenario during the 500-year storm surge.

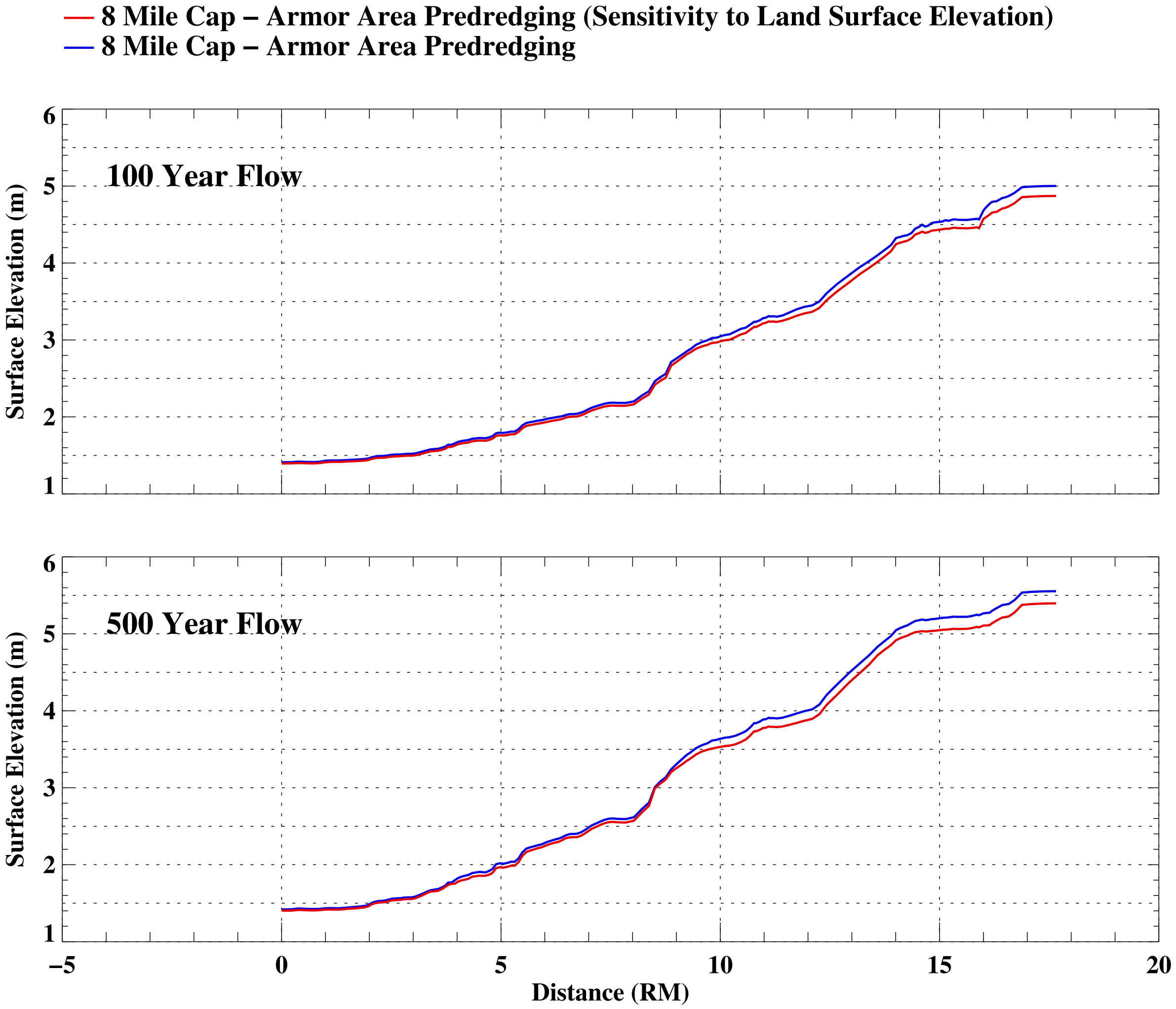

Figure 6-24. Comparison of water surface elevations for land elevation sensitivity runs for the 100-year flow (upper frame) and the 500-year flow (lower frame).

100 Year Flow for 8 Mile Cap-Armor Area Predredging
(Sensitivity to Land Surface Elevation)

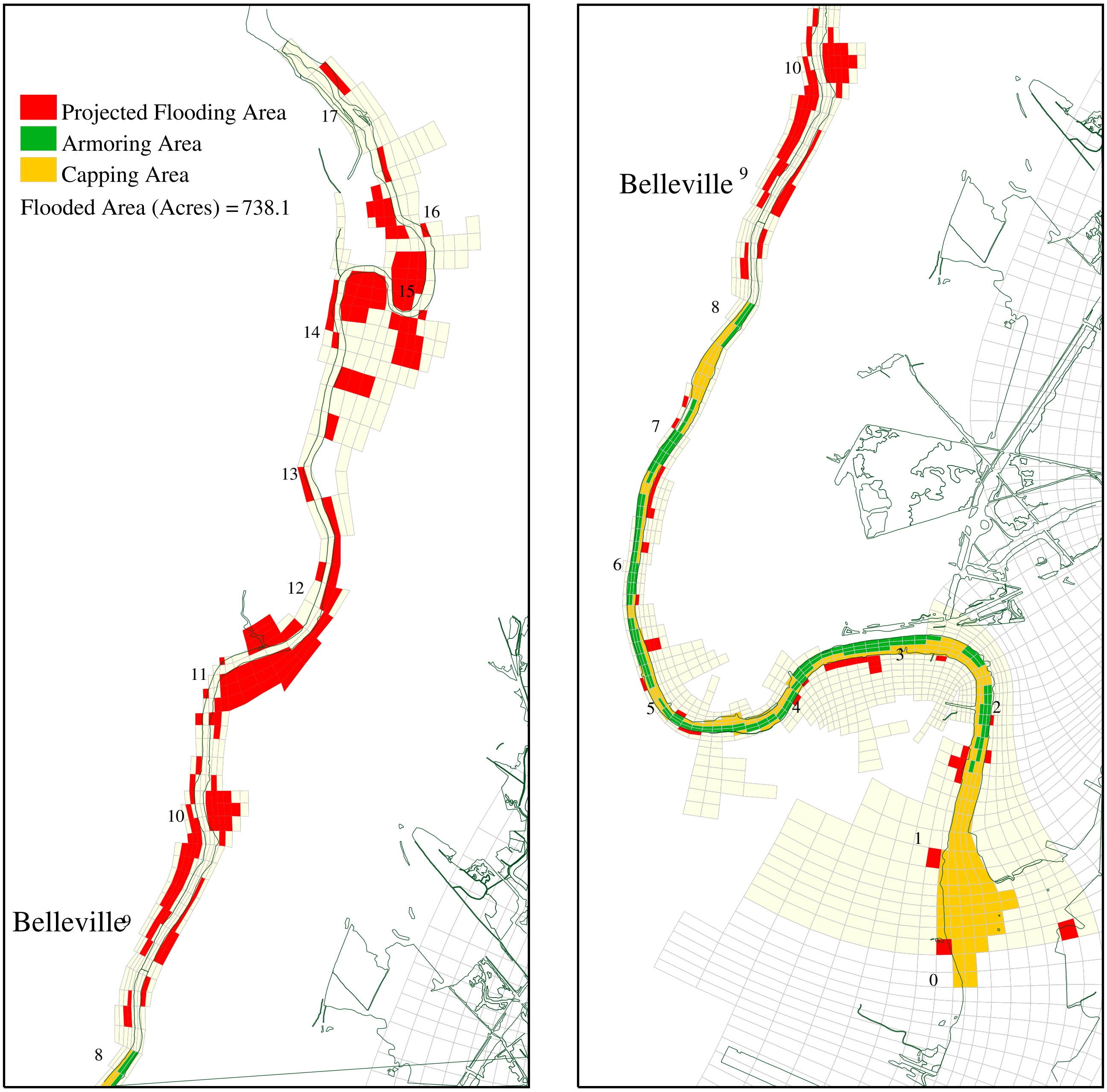

Figure 6-25. Projected flood area with 1 ft lowered land elevation under the 8 Mile Cap-Armor Area Predredging Scenario during the 100-year flow.

500 Year Flow for 8 Mile Cap-Armor Area Predredging
(Sensitivity to Land Surface Elevation)

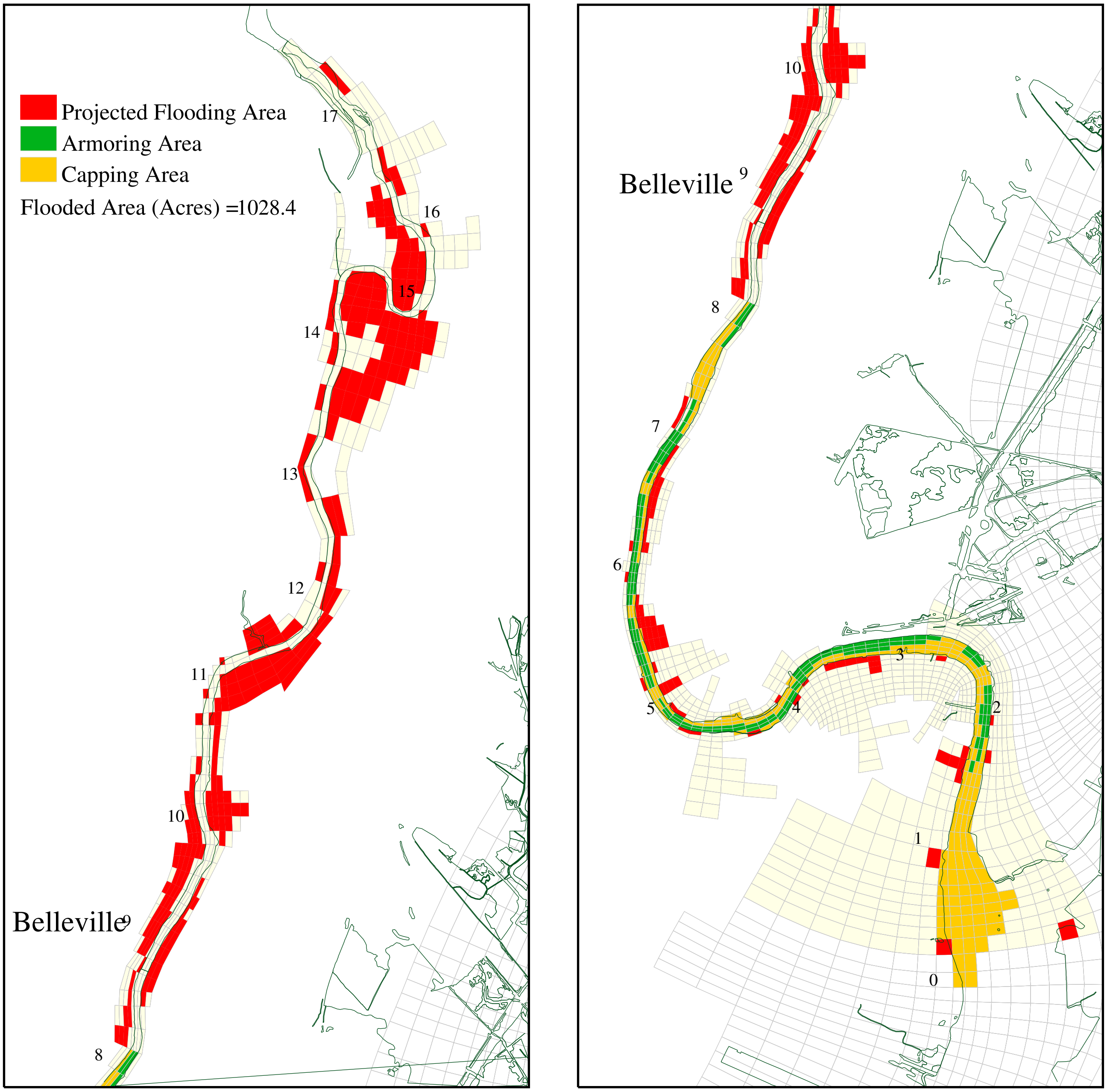

Figure 6-26. Projected flood area with 1 ft lowered land elevation under the 8 Mile Cap-Armor Area Predredging Scenario during the 500-year flow.

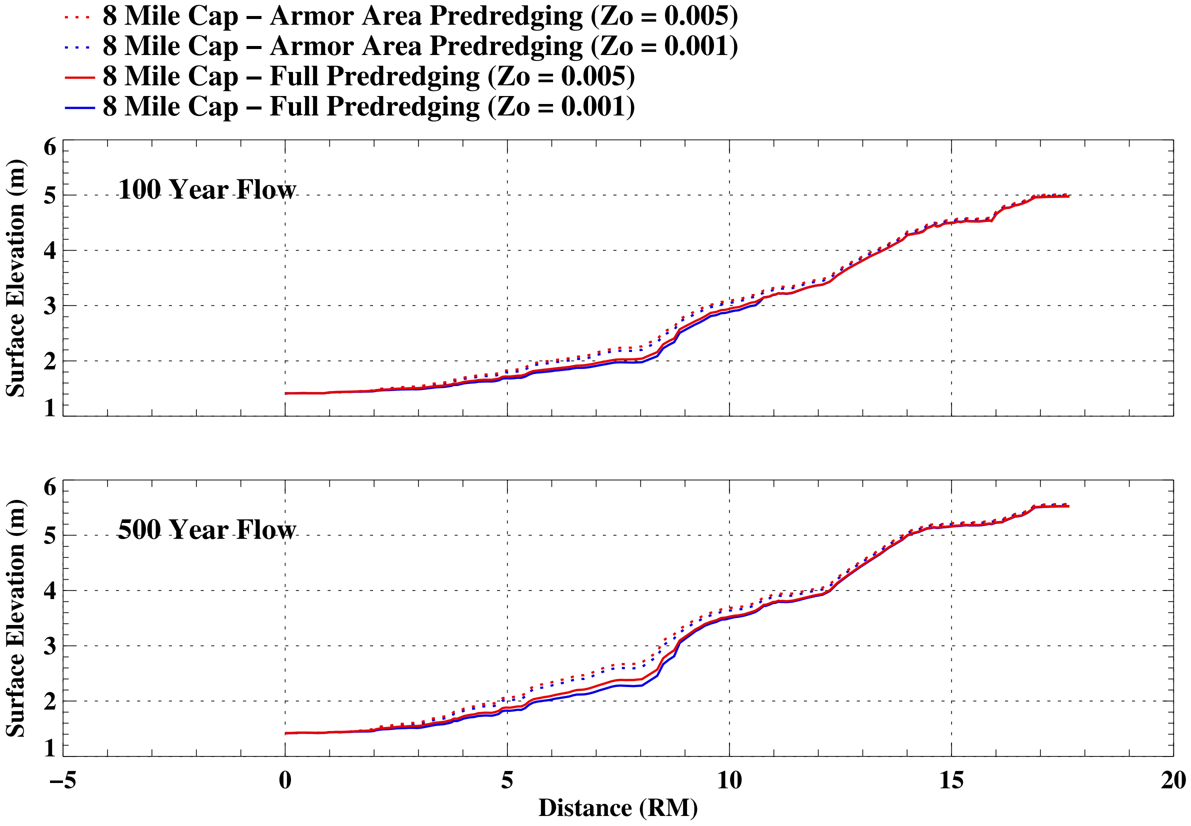

Figure 6-27. Maximum water surface elevations under different bottom roughness lengths along the Lower Passaic river.

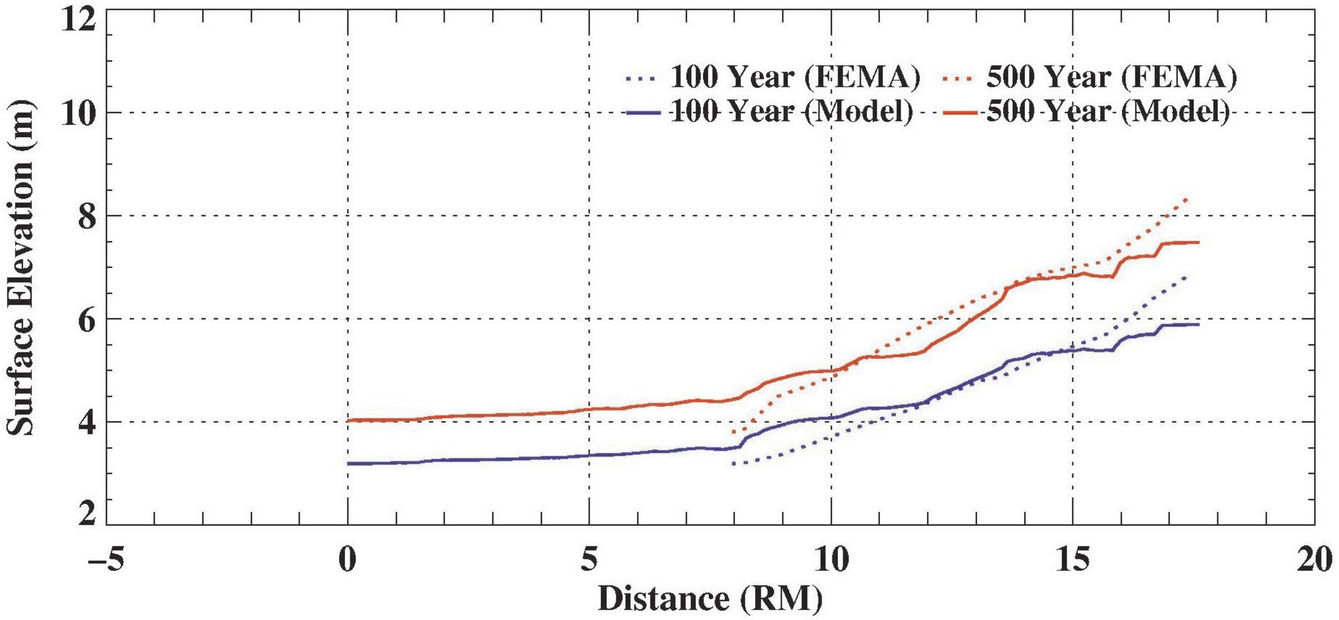

Figure 6-28. Maximum water elevations computed along the Lower Passaic River during the FEMA flood events.

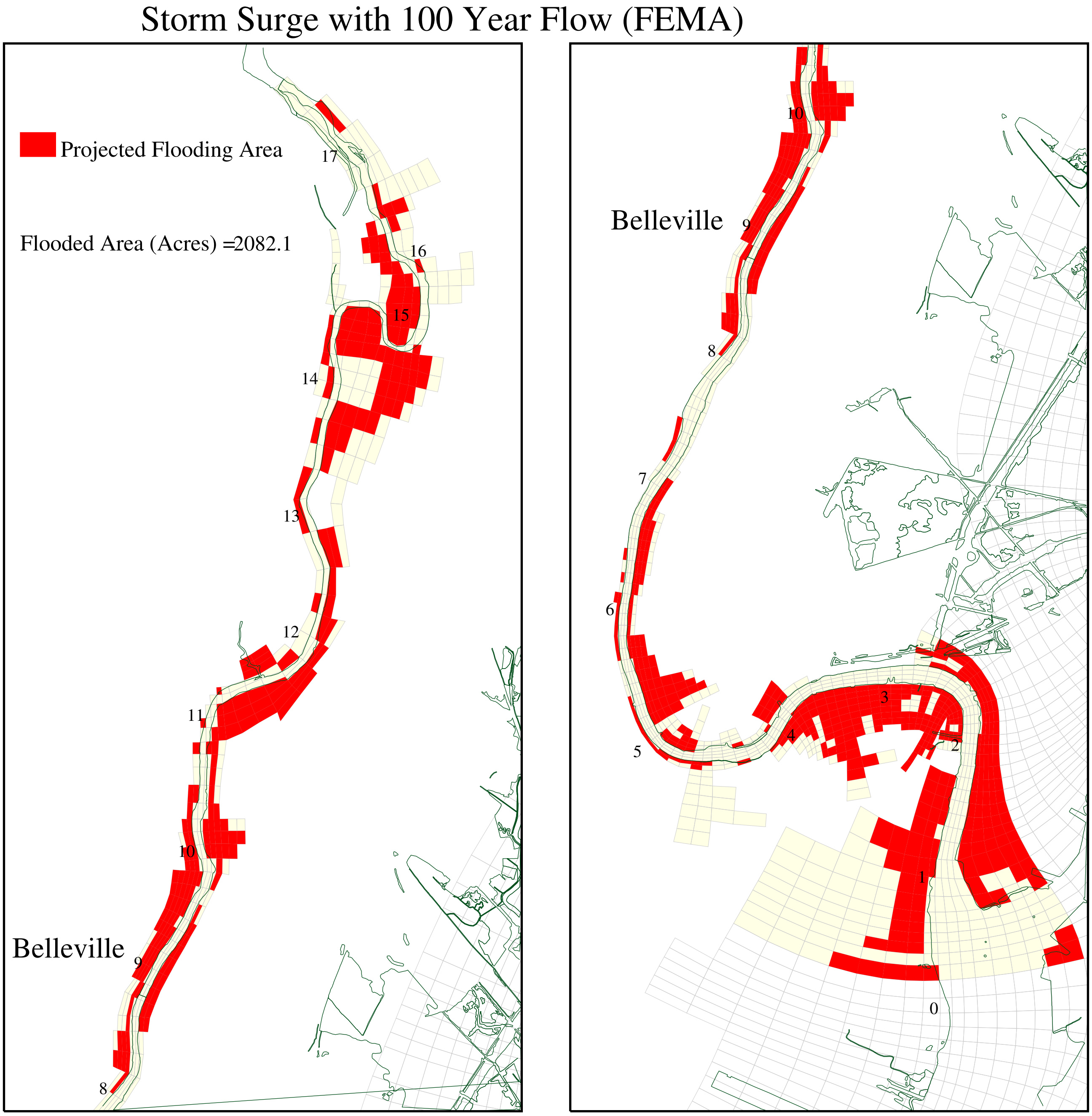

Figure 6-29. Projected flood area during the FEMA 100-year event.

Storm Surge with 500 Year Flow (FEMA)

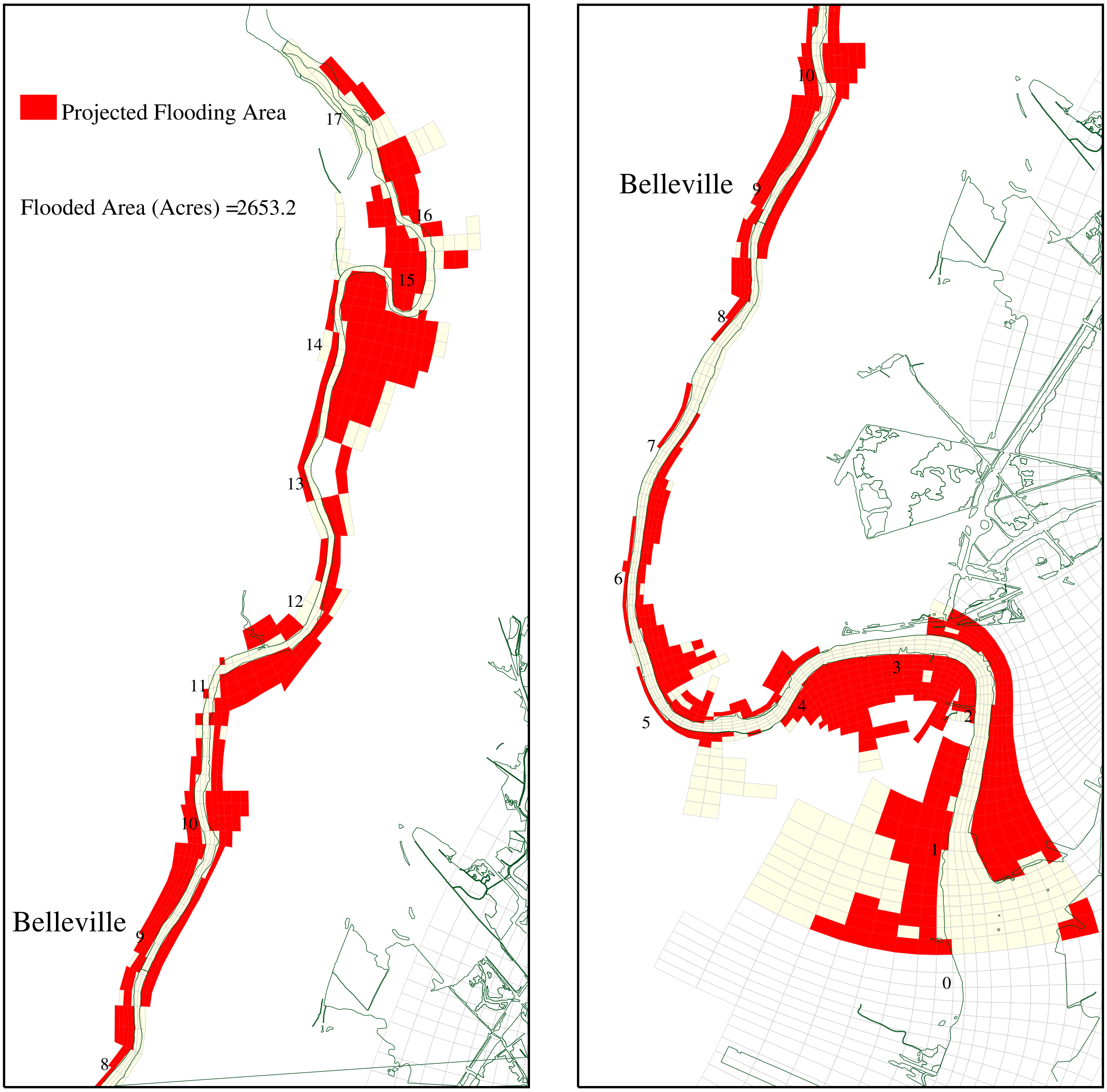

Figure 6-30. Projected flood area during the FEMA 500-year event.

SECTION 7

CONCLUSIONS

A three-dimensional hydrodynamic-sediment transport model was developed to evaluate the migration of cap material that might be placed to remediate sediment contamination in the first 8.3 miles of the LPR. The FEMA 500-year flood plain was included in the model domain and 2 ft contour USACE land survey data were used to configure the elevation of the banks of the LPR and to determine potential flooding areas.

The hydrodynamic model used in this study is an extension of the model developed by HydroQual for use in the LPR and Newark Bay RI/FS (HydroQual, 2007). A model calibration was performed using field survey data collected in the summer of 2004. Model computed water surface elevations, current velocities, and temperature and salinity were compared against observed data. Model validation was conducted using the storm surge data of Hurricane Donna and the observed surge elevations were well reproduced by the model at various locations in the study area. The FEMA 100- and 500-year events were also used for model validation. Although the hydrodynamic model did not exactly reproduce the areas of inundation within the FEMA 500-year flood plain, the model was able to reproduce comparable FEMA computed water level rises and flooding areas in the LPR.

As part of the cap stability/erosion analysis, conducted using the sediment transport model-SEDZLJ, it was found that sands from the Ambrose Channel were highly erodible and thus not suitable for use as a sand cap in the LPR. Instead, it will be necessary to utilize sands from an upland borrow source. These upland sands are comprised of sands with larger particle grain sizes, which are heavier and less subject to the forces of erosion experienced in the LPR. These are, however, areas within the river where it will be necessary to place protective armor (rock cobble) over the sand cap so as to prevent erosion of the cap. This occurs in regions of the river which experience high bottom water velocities with accompanying high bottom shear stress.

Analyses of extreme flow and surge events were also conducted. The 100- and 500-year flows are estimated as 20,000 and 26,000 cfs and the 100- and 500-year storm surges as 2.4 m and 2.67 m above MSL, respectively, in the study area. The model was configured with the 100- and 500-year flow and storm surge events. Four capping/armoring scenarios were evaluated against a Base Case Scenario: 1) 8 mile Cap – Armor Area Pre-Dredging; 2) 8 mile Cap – Full Pre-Dredging; 3) Current Navigation Usage – Full Pre-Dredging; and 4) Future Navigation Usage – Full Pre-Dredging. A summary of the modeling results is as follows:

- Under the Base Case Scenario, the 100 and 500-year flows would inundate areas of 499 and 794 acres, respectively.
- The “8 mile Cap – Armor Area Pre-Dredging” Scenario would increase the water elevation by as much as 0.5 and 0.8 m from those in the Base Case Scenario during the 100- and 500-year flows, respectively. Compared to the Base Case Scenario, the “8 mile Cap – Armor Area Pre-Dredging” Scenario would flood an additional 93 acres during the 100-year flow (total flooded area of 592 acres) and 86 acres during the 500-year flow (total flooded area of 880 acres).
- The “8 mile Cap – Full Pre-Dredging” Scenario would increase the water elevation by 0.1 and 0.2 m, as compared to the Base Case Scenario during the 100- and 500-year flows, respectively. The flooded areas would increase by 24 acres during the 100-year flow (total flooded area of 523 acres) and by 28 acres during the 500-year flow (total flooded area of 822 acres) compared to those computed under the Base Case Scenario.
- The “Current Navigation Usage – Full Pre-Dredging” Scenario would produce similar results to those under the “8 mile Cap – Full Pre-Dredging” Scenario, both for water elevation rise and flooded areas.
- The “Future Navigation Usage – Full Pre-Dredging” Scenario would reduce the maximum water level rise by 0.1 and 0.2 m, compared with the Base Case Scenario during the 100- and 500-year flows, respectively. The flooded areas would decrease by 17 acres during the 100-year flow (total flooded area of 482 acres) and by 27 acres during the 500-year flow (total flooded areas of 767 acres) compared to those computed under the Base Case Scenario.
- Model results indicate that the 100 and 500-year storm surges would cause the maximum flooding in the study area (1,249 and 1,504 acres, respectively, under the Base Case Scenario) and most of the flooding would occur in the low lying areas near the mouth of the river. Different capping/armoring scenarios would not change the flooded areas during the storm surge events, compared to those computed under the Base Case Scenario.
- A few sensitivity runs of the model were conducted to account for the uncertainty of the land elevation by reducing the land elevation by 1 foot and for the uncertainty of the bottom roughness lengths of the upland sand cap material by increasing the bottom roughness lengths by a factor of five. The results suggest that, by lowering the land elevation by 1 foot, the flooding area during the 100- and 500-year flow would increase as much as 25 percent compared to the results using the original land

elevation configuration. A higher bottom roughness length (a value of 0.005) for the sand cap material would result in about a 0.5 to 2.5 % increase in the flooding areas compared to those computed with the value (0.001) used for the flooding analyses.

SECTION 8

REFERENCES

Aqua Survey Inc., 2006, Technical Report, Geophysical Survey, Lower Passaic River Restoration Project, submitted to New Jersey Dept of Transportation - Office of Maritime Resources, Trenton, NJ

Blumberg, A.F. and G.L. Mellor, 1987. A description of a three-dimensional coastal ocean circulation model. In: Three-Dimensional Coastal Ocean Models, Coastal and Estuarine Sciences, 4. N. Heaps, Ed., American Geophysical Union, Washington, D.C., 1-16.

Blumberg, A.F. and L.A. Khan, and J.P. St. John, "Three Dimensional Hydrodynamic Model of New York Harbor Region", J. Hydraulic Engineering, 125, 799-816, 1999

Cheng, N.S., 1997. Simplified settling velocity formula for sediment particle. Journal of Hydraulic Engineering, 123(2):149-152.

Chow, Ven T., D.R. Maidment, and L.W. Mays, 1988. Applied Hydrology, McGraw-Hill.

Dyer, Keith R., 1986. Coastal and Estuarine Sediment Dynamics. John Wiley & Sons, 342p.

Federal Emergency Management Agency, 1996. Q3 Flood Data (CD-ROM).

Guidelines for Determining Flood Flow Frequency. 1982. Bulletin 17B of the Hydrology Subcommittee, Interagency Advisory Committee on Water Data, Office of Water Data Coordination, USGS.

Harris, D. Lee, 1963, Characteristics of the Hurricane Storm Surge. Technical Paper No. 48, U.S. Dept of Commerce, Weather Bureau, Washington, D.C.

HydroQual, Inc., 2004. A Primer for ECOMSED, Version 1.4: Users Manual, Mahwah, NJ. 194 p.

HydroQual, Inc., 2007, Hydrodynamic Modeling Report, Lower Passaic River Restoration Project, submitted to US Environmental Protection Agency Region 2 and US Army Corps of Engineers, Kansas City District.

Jones, C. and W. Lick, 2001. Contaminant flux due to sediment erosion. *Proceedings of the 7th International Conference: Estuarine and Coastal Modeling*, 280–293.

Kamphuis, J.W., 1974, Determination of sand roughness for fixed beds. J. Hydraulics Reseach, 12:193-203.

Leher, Andre, 2005. Handout notes "Methods of Stream-flow Data Analysis", Humboldt State University.

Little, W.C. and P.G. Mayer, 1972. The role of sediment gradation on channel armoring. Publication No. ERC-0672, School of Civil Engineering in Cooperation with Environmental Research Center, Georgia Institute of Technology, Atlanta, GA. 1-104.

Roberts, J., R. Jepsen, D. Gotthard, and W. Lick, 1998. Effects of particle size and bulk density on erosion of quartz particles. Journal of Hydraulic Engineering, 124(12):1261-1267.

USACE, 1972. Passaic River Report, New York District

USACE, 1973. Supplement Report: Passaic River Survey Report for Water Resource Development, New York, NY

Van Rijn, L., 1984. Sediment transport, part II: Suspended Load Transport. Journal of Hydraulic Engineering, 110(11):1431-1456.

ATTACHMENT A

SEDZLJ INCORPORATION INTO ECOMSEDZLJ

Sea Engineering, Inc.
200 Washington St. Suite 210
Santa Cruz, CA 95060
Voice: 831.421.0871
Fax: 831.421.0875

□□□ Jim Fitzpatrick

□□□□ □ Craig Jones

□□□ Ed Garland, Nicholas Kim

□□□□□ September 25, 2006

□□□ SEDZLJ incorporation into ECOM

Sediment Transport Model Implementation

As part of the Lower Passaic River Restoration Project, HydroQual and the Technical Advisory Committee (TAC) decided to implement a pre-existing, peer-reviewed (Jones and Lick, 2001) sediment transport model into HydroQual's hydrodynamic model, ECOM. SEDZLJ uses measured sediment erosion data as the basis for modeling sediment transport in a system. Rather than attempt to reconstruct a computer code equivalent to SEDZLJ using information contained in the Jones and Lick paper, it was determined to be more expedient and cost-effective for Sea Engineering, Inc. (SEI) to incorporate SEDZLJ into ECOM. This technical memo outlines the completion of the first two sub-tasks of the sediment transport modeling effort. The sub-tasks are:

> **Model Code Integration:** SEI will implement the existing version of SEDZLJ into HydroQual's current hydrodynamic/sediment transport model, ECOMSED. HydroQual will provide SEI with a copy of the current version of the ECOMSED computer code, User's Guide and a model input file that has been used in testing and conducting quality control checks for the performance of the ECOMSED model.
>
> **Model Code Verfication:** As part of the implementation process SEI will verify that the SEDZLJ code has been properly implemented within ECOMSED by simulating and reproducing the laboratory data set generated by Little and Mayer (1972).

Model Code Integration

The SEDZLJ code was integrated into the ECOM model to accomplish two goals. The first goal is to calculate the net flux of sediments (g/cm^2/s) at the sediment/water interface due to erosion and deposition. The second goal is to calculate bedload transport of sand sized sediments on the computational grid. Water column transport of sediments is unchanged from the current ECOM implementation with the exception of allowing more than two size classes.

The integration was accomplished through the inclusion of multiple subroutines to handle the input and calculation of the above processes. Figure 1 is a flowchart illustrating the main features of the model integration. Point "A" calls the SEDZLJ input routines, point "B" calls the water column transport routines from ECOM to transport all size classes of sediment utilized, and point "C" calls the routines to calculate the sediment flux and the bedload transport. The implementation of this structure allows for easy integration while preserving the main structure of ECOM. The model structure indicated has been verified to fit into the ECOM structure and operate with no variable conflicts or input conflicts. Full variable definitions and input file descriptions will be provided upon finalization of SEDZLJ implementation.

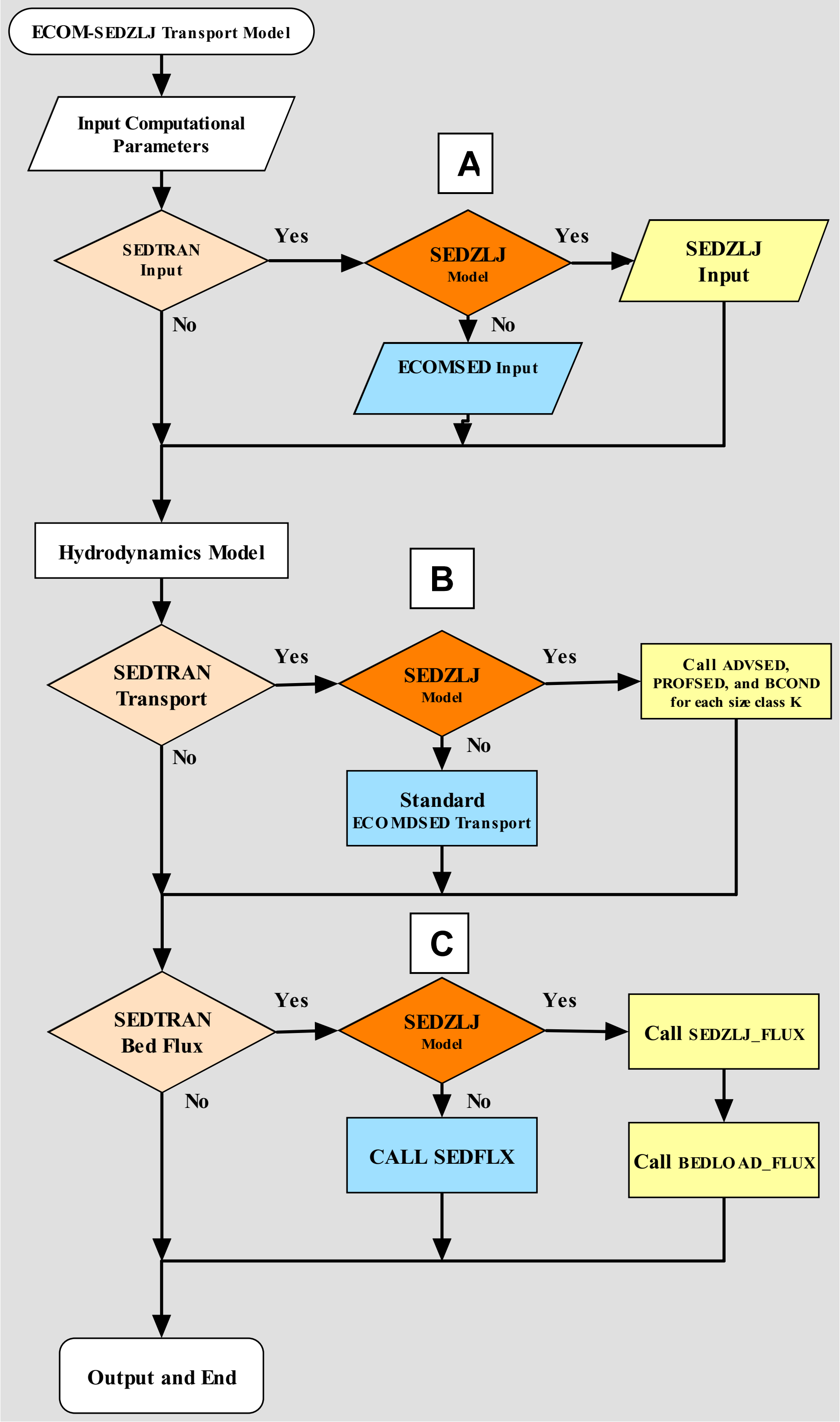

Figure 1. Flow chart illustrating main points of SEDLZJ Integration into ECOM

Model Code Verification

The evaluation and validation of the SEDZLJ implementation (ECOM-SEDZLJ) required modeling a set of well-documented physical experiments. Little and Mayer (1972) conducted detailed measurements of non-cohesive bed-armoring and transport in a straight flume. This case was utilized as a verification here because the bed-armoring and transport processes in the experimental setup require the utilization of critical algorithms in the sediment transport model. No detailed cohesive data sets for model verification exist at this time, so the model framework is only validated with non-cohesive data.

In the experiment, a flume 12.2 m long and 0.6 m wide was filled with a distribution of sand and gravel sediments. Clear water was then run over the sediment bed at a flow rate of 0.016 m^3/s. The eroded sediment was collected at the outlet of the flume, and the sediment transport rate was determined. When the sediment transport rate had decreased to 1 percent of the beginning transport rate, the bed was assumed to be fully armored and the experiment was ended. The full armoring of the sediment bed occurred in 75.5 hours. The final armored bed particle size distribution of the sediment surface was then measured by means of a wax cast.

The experiment was simulated with ECOM-SEDZLJ. Thirteen elements with a downstream dimension of 100 cm and cross-stream dimension of 60 cm were used to discretize the domain. The initial sediment distribution in the model was set equal to the distribution in the flume experiments. The sediment bed comprised 9 size classes selected to accurately represent the sediment bed in the experiment. Table 1 shows the 9 size classes used in the model and their corresponding properties of settling speed, w_s, critical shear stress for erosion, t_{ce}, and critical shear stress for suspension, t_{cs}. Data from the Roberts et al. (1998) Sedflume studies on quartz were used to define the erosion rates and critical shear stresses for sediments in the model. The coefficient of friction was set such that the measured shear stress of 1.0 N/m^2 was reproduced in the model.

Table 1. Sediment size class properties used for Little and Mayer (1972) study.

Particle Size (m)	Initial Bed Percentage by Mass	w_s (cm/s)	$_{ce}$ (N/m^2)	$_{cs}$ (N/m^2)
125	2	0.9	0.15	0.15
222	8	2.25	0.24	0.26
432	23	5.2	0.33	0.45
1020	32	11.3	0.425	2.12
2000	11	18.01	0.93	5.36
2400	8	20.18	0.97	6.73
3000	6	23.07	1.2	8.79
4000	6	27.25	1.6	12.26
6000	4	34.13	2.48	19.2

Model Results

The model was run for 75.5 hr with a time step of 0.1 s. The model shows good agreement with the experimental data. In the first few hours, there is a rapid increase in the average particle size from 1,600 to 2,500 m; this is followed by a much slower rate of increase to a little above 2,500 m by the end of the experiment. Associated with this increase, is a four order-of-magnitude decrease in erosion rate. The reason for this decrease is that the finer particle sizes are eroded from the sediment bed while the coarser particles are left behind, thereby increasing the average particle size of the bed and decreasing the erosion rates. This is responsible for the drop in the net transport rate of sediments from the channel, and is consistent with bed coarsening as discussed earlier. Initially the transport is almost equally bedload and suspended load, but as the bed coarsens the transport rate becomes almost exclusively bedload. This armoring process is expected since coarse particles, incapable of suspension at this shear stress, are concentrated in the bed. The modeled and measured transport rate and average particle size are shown in Figure 2 as a function of time.

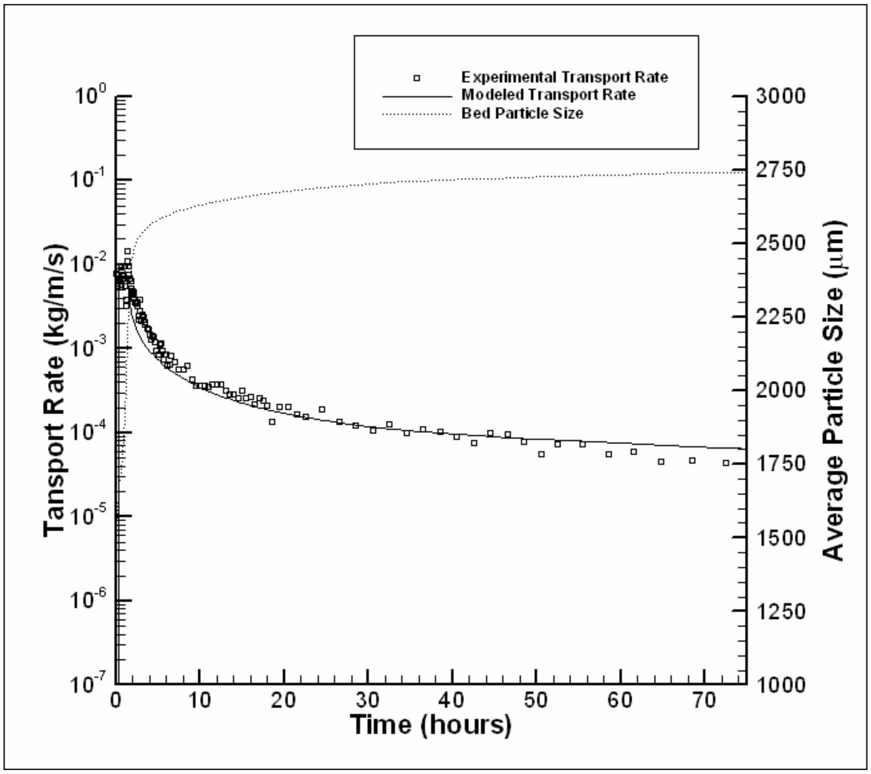

Figure 2. Modeled vs. measured transport rates and average particle size as a function of time.

A comparison is also made between the final particle size distribution in the active layer of the model and the particle size distribution of the surface of the bed in the experiment. Although the distributions are not identical, the final d_{50} was 2,750 μm in the model and 3,200 μm in the experiment yielding a difference of 14 percent. Discrepancies between the two distributions are most evident at smaller particle sizes.

The results from this model show good overall agreement with the data and trends observed in the experiments. Such agreement indicates that the model accurately estimates the erosion, transport, and subsequent coarsening of a sediment bed.

ATTACHMENT B

BED ELEVATION CHANGES, MAXIMUM EROSION AND BOTTOM SHEAR STRESSES FOR AMBROSE SAND CAP

Figure B-1a. Plan view of the net elevation change under the 1-year return flow conditions (Ambrose sand used as the capping material).

Figure B-1b. Plan view of the maximum erosion under the 1-year return flow conditions (Ambrose sand used as the capping material).

Figure B-1c. Plan view of the bottom shear stress under the 1-year return flow conditions (Ambrose sand used as the capping material).

Figure B-2a. Plan view of the net elevation change under the 25-year return flow conditions (Ambrose sand used as the capping material).

Figure B-2b. Plan view of the maximum erosion under the 25-year return flow conditions (Ambrose sand used as the capping material).

Figure B-2c. Plan view of the bottom shear stress under the 25-year return flow conditions (Ambrose sand used as the capping material).

Figure B-3a. Plan view of the net elevation change under the 100-year return flow conditions (Ambrose sand used as the capping material).

Figure B-3b. Plan view of the maximum erosion under the 100-year return flow conditions (Ambrose sand used as the capping material).

Figure B-3c. Plan view of the bottom shear stress under the 100-year return flow conditions (Ambrose sand used as the capping material).

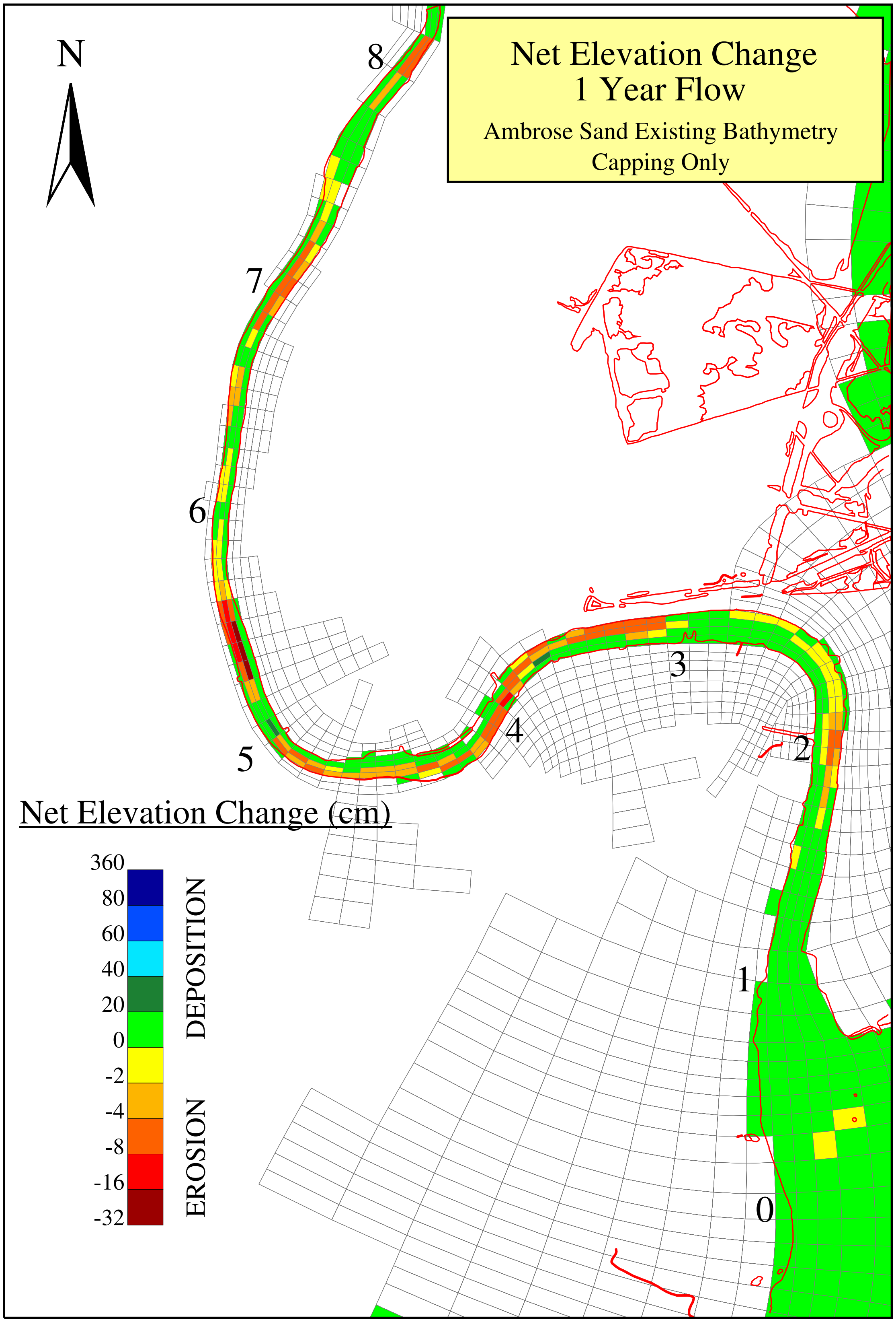

Figure B-1a. Plan view of the net elevation change under the 1-year return flow conditions (Ambrose sand used as the capping material).

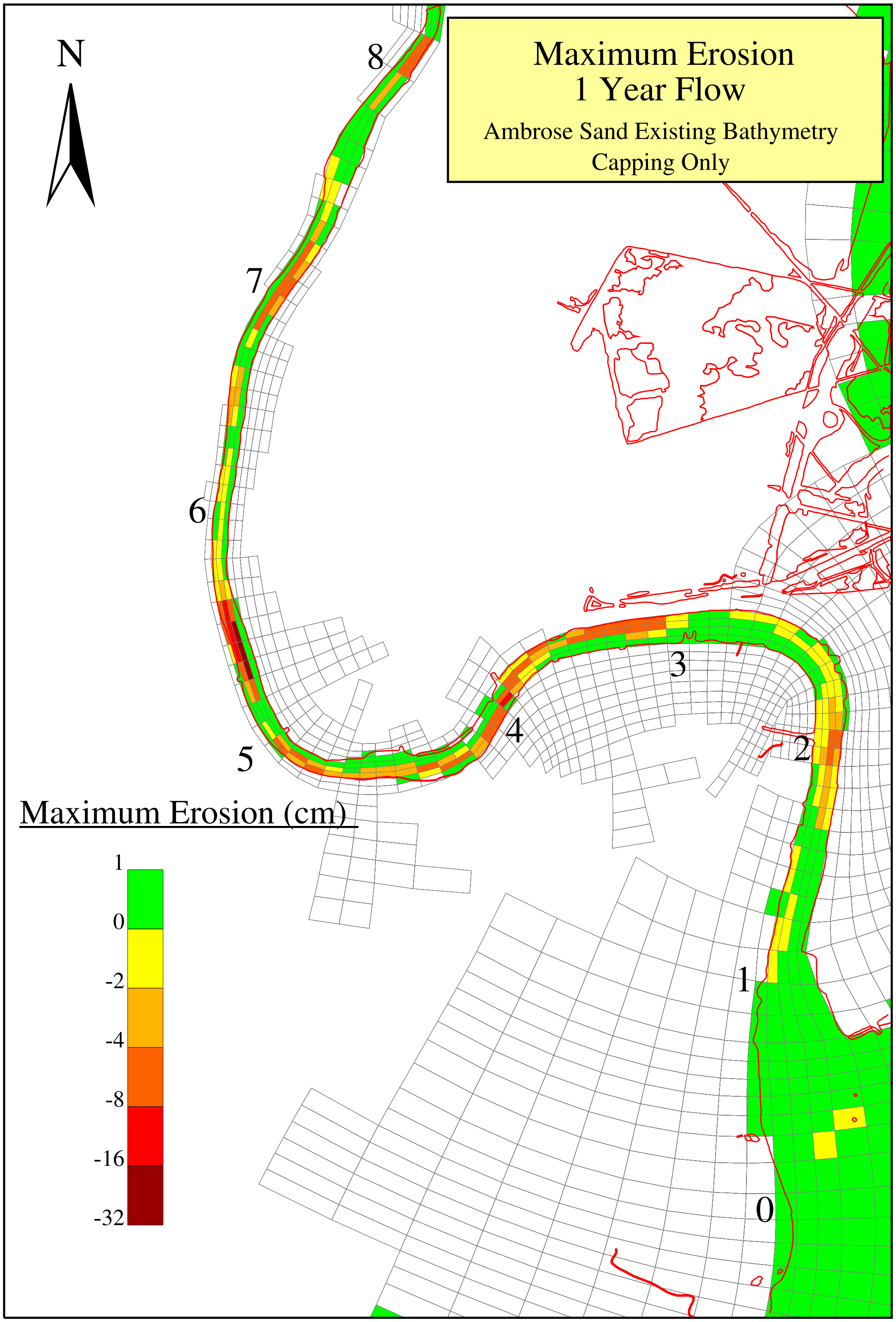

Figure B-1b. Plan view of the maximum erosion under the 1-year return flow conditions (Ambrose sand used as the capping material).

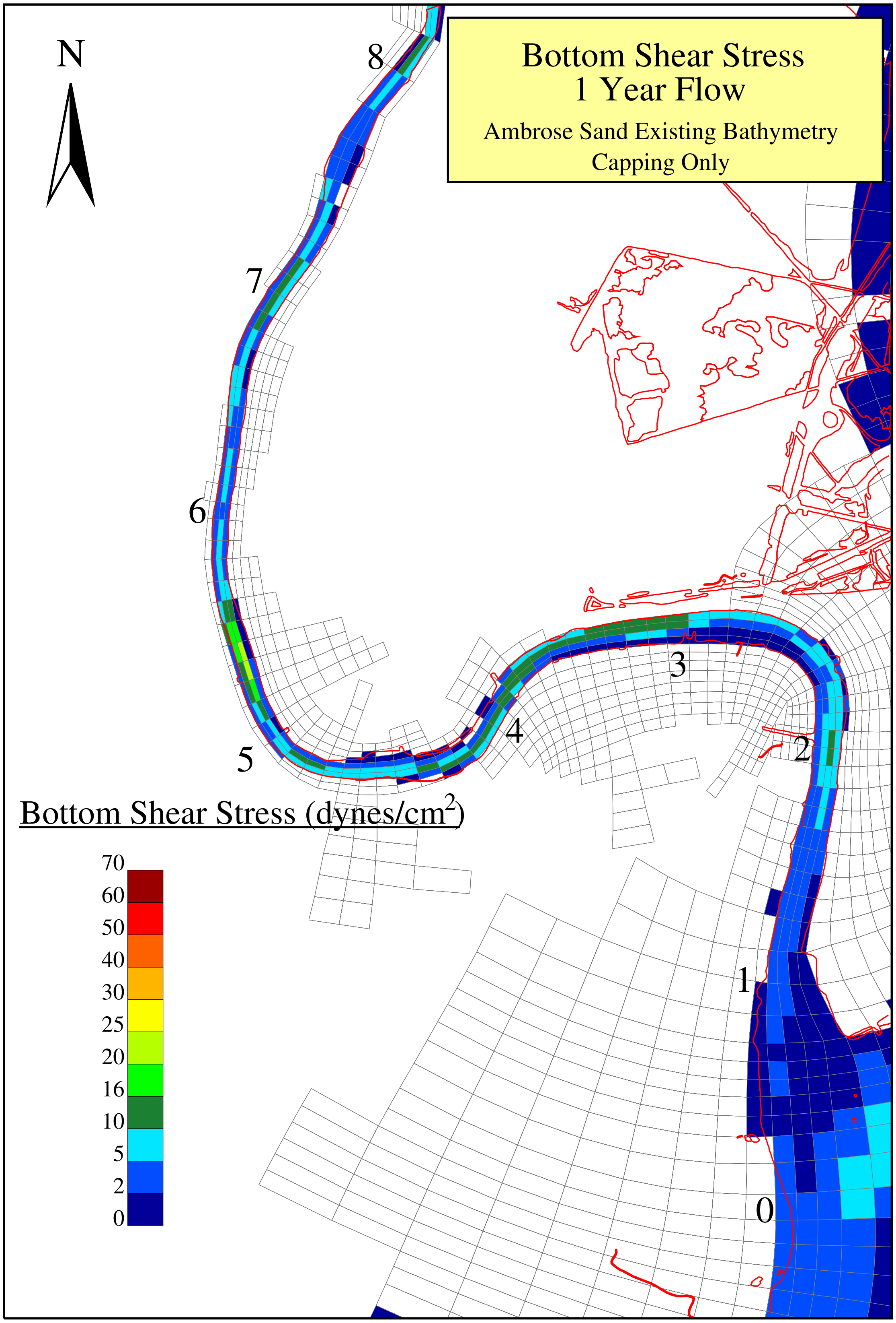

Figure B-1c. Plan view of the bottom shear stress under the 1-year return flow conditions (Ambrose sand used as the capping material).

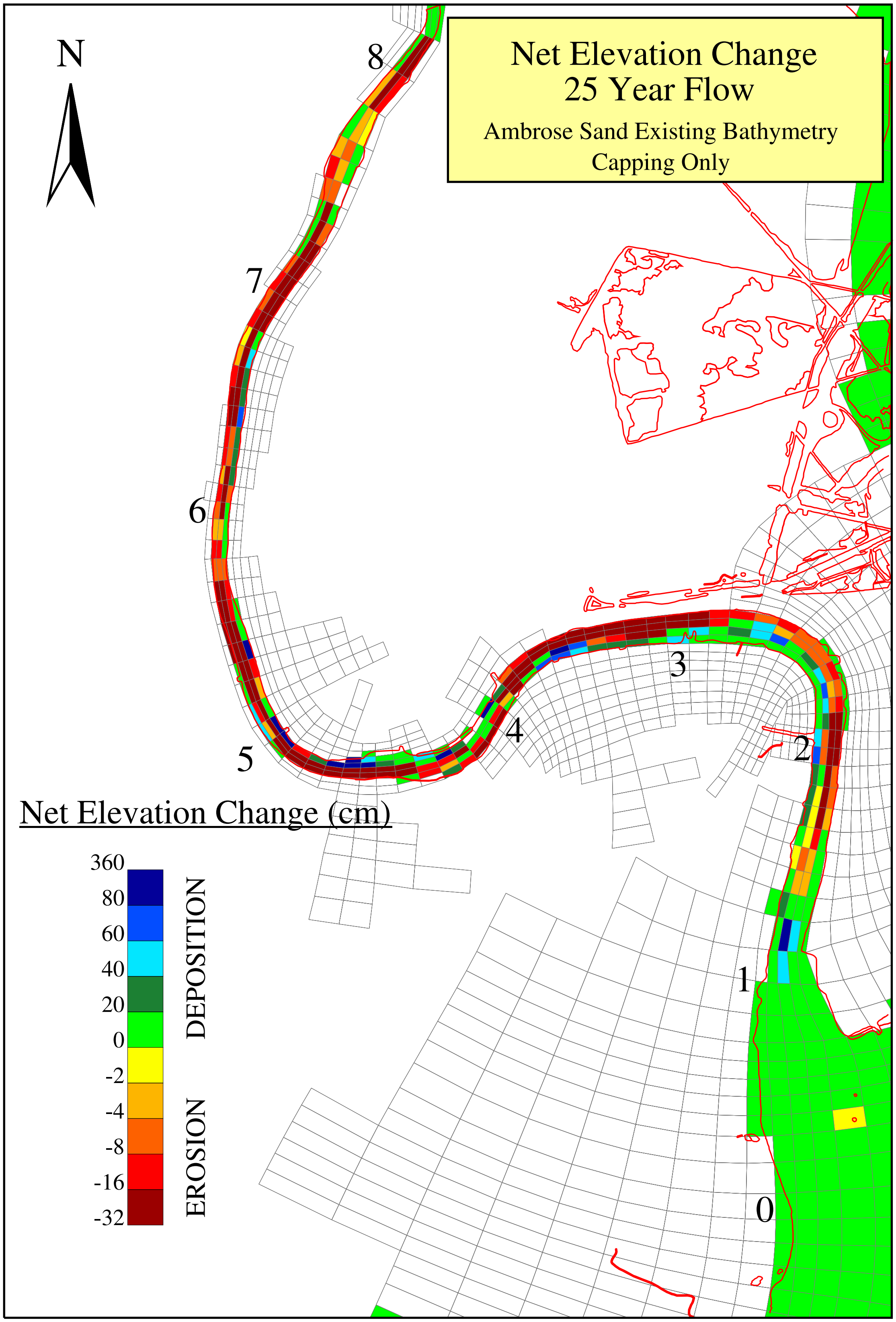

Figure B-2a. Plan view of the net elevation change under the 25-year return flow conditions (Ambrose sand used as the capping material).

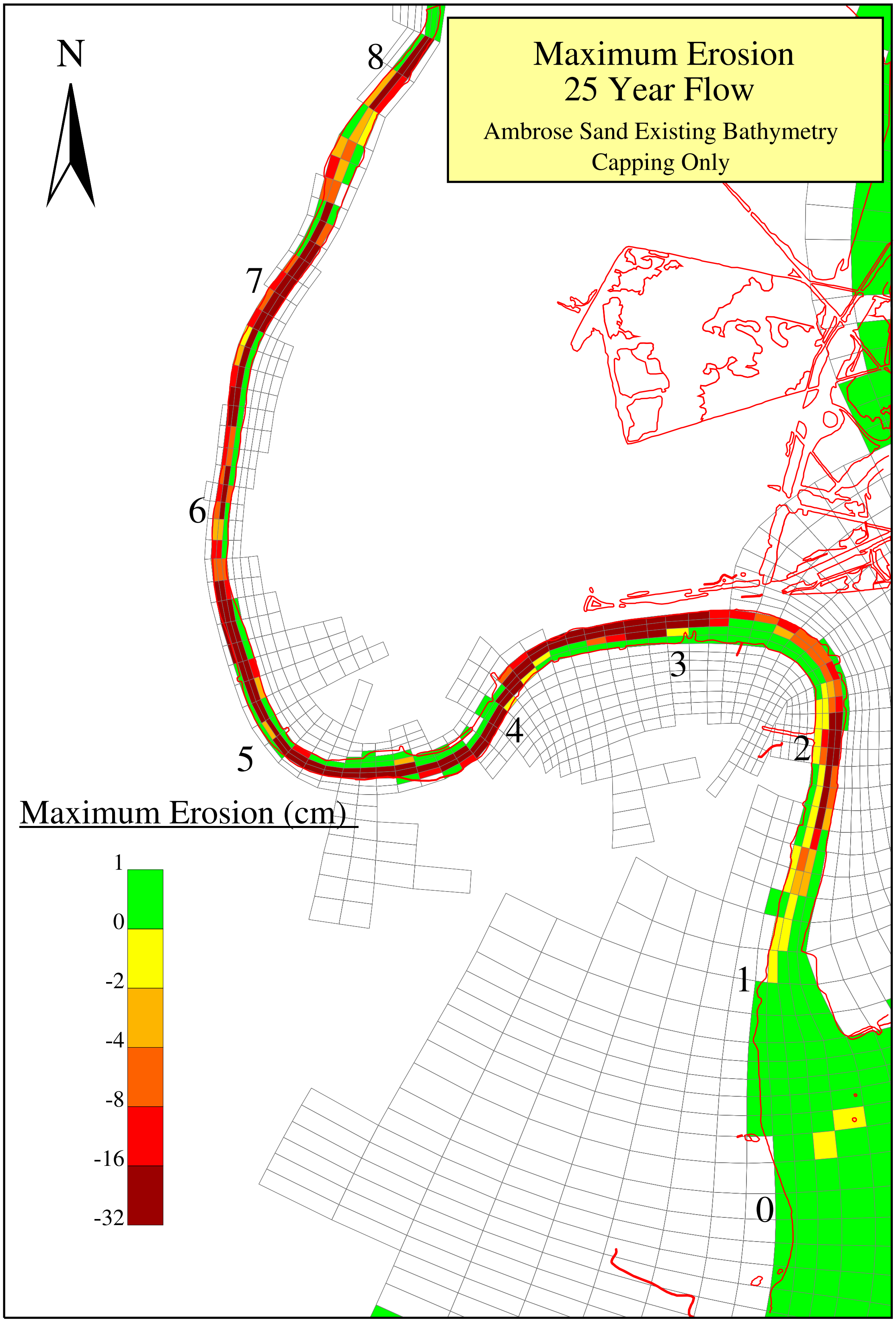

Figure B-2b. Plan view of the maximum erosion under the 25-year return flow conditions (Ambrose sand used as the capping material).

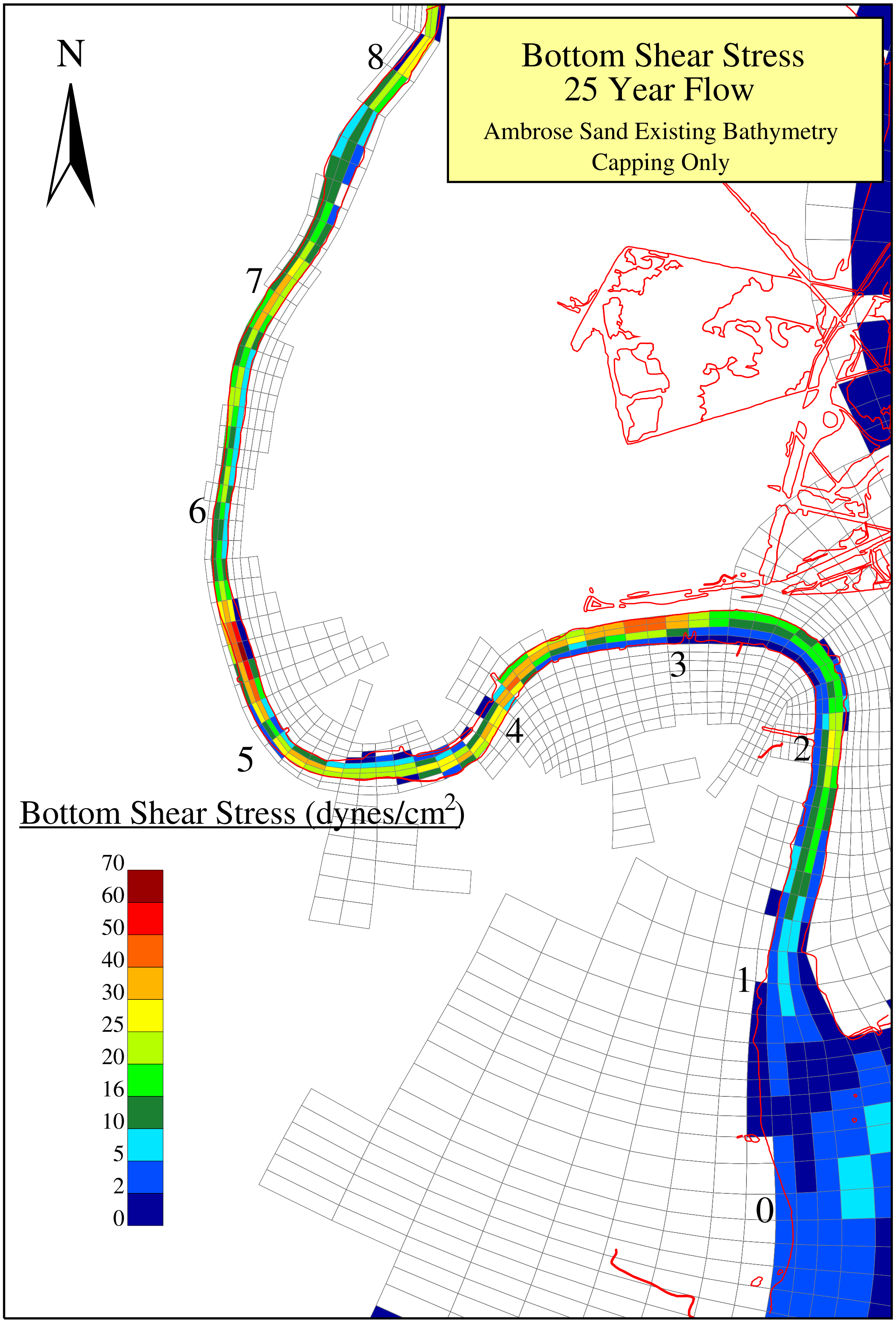

Figure B-2c. Plan view of the bottom shear stress under the 25-year return flow conditions (Ambrose sand used as the capping material).

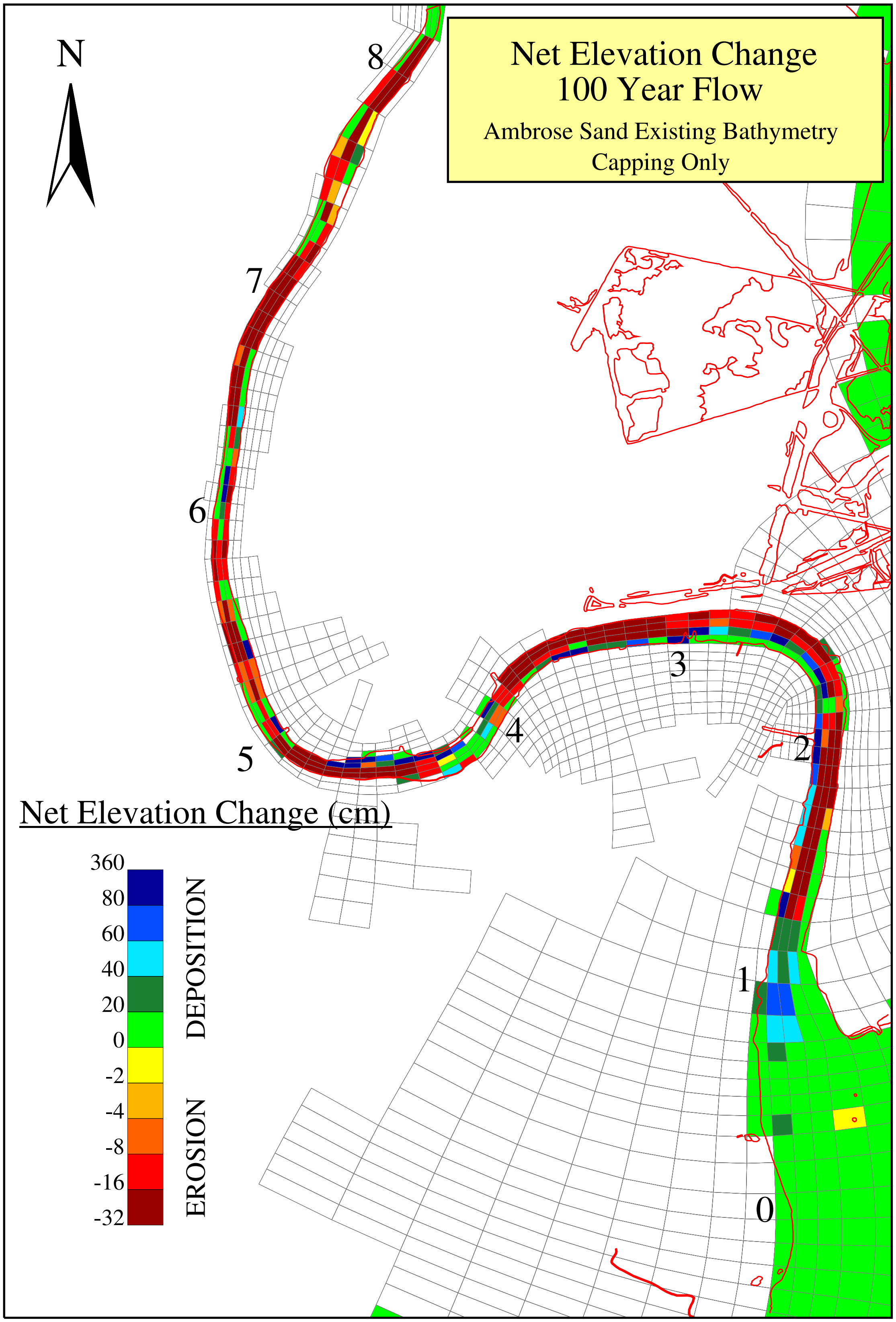

Figure B-3a. Plan view of the net elevation change under the 100-year return flow conditions (Ambrose sand used as the capping material).

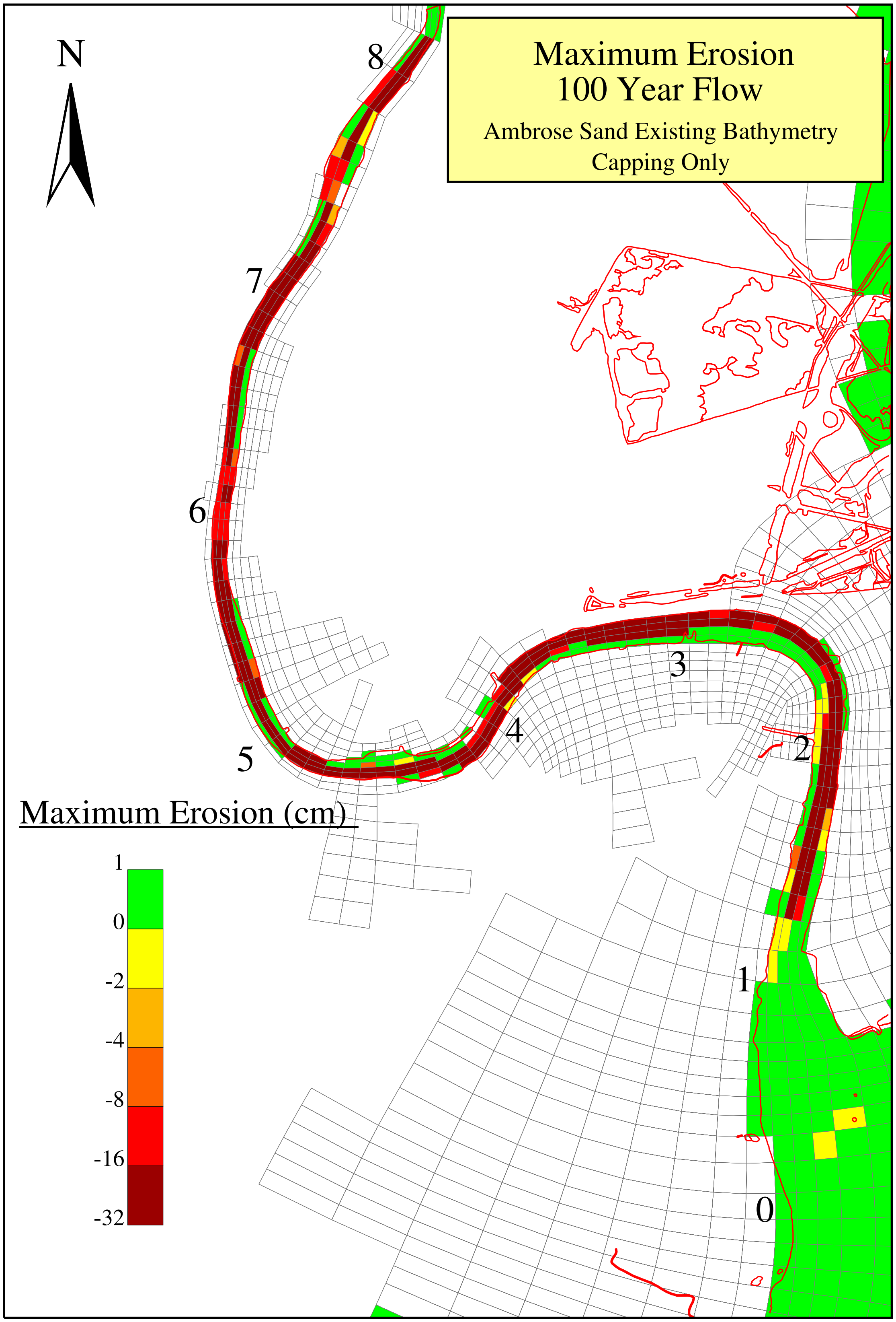

Figure B-3b. Plan view of the maximum erosion under the 100-year return flow conditions (Ambrose sand used as the capping material).

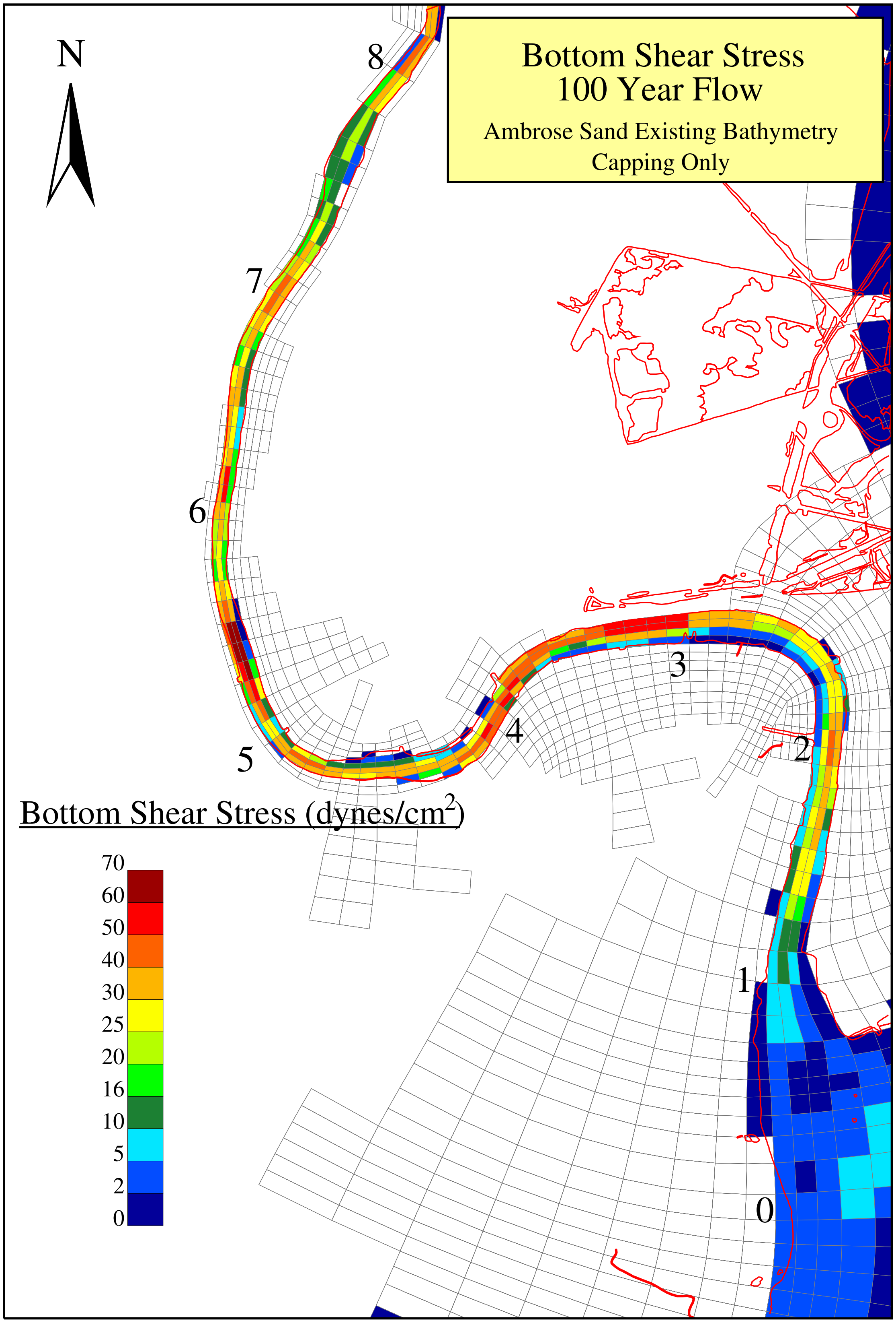

Figure B-3c. Plan view of the bottom shear stress under the 100-year return flow conditions (Ambrose sand used as the capping material).

ATTACHMENT C

BED ELEVATION CHANGES, MAXIMUM EROSION AND BOTTOM SHEAR STRESSES FOR UPLAND BORROW SAND CAP

Figure C-1a. Plan view of the net elevation change under the 1-month return flow conditions (Upland Borrow sand used as the capping material).

Figure C-1b. Plan view of the maximum erosion under the 1-month return flow conditions (Upland Borrow sand used as the capping material).

Figure C-1c. Plan view of the bottom shear stress under the 1-month return flow conditions (Upland Borrow sand used as the capping material).

Figure C-2a. Plan view of the net elevation change under the 6-month return flow conditions (Upland Borrow sand used as the capping material).

Figure C-2b. Plan view of the maximum erosion under the 6-month return flow conditions (Upland Borrow sand used as the capping material).

Figure C-2c. Plan view of the bottom shear stress under the 6-month return flow conditions (Upland Borrow sand used as the capping material).

Figure C-3a. Plan view of the net elevation change under the 1-year return flow conditions (Upland Borrow sand used as the capping material).

Figure C-3b. Plan view of the maximum erosion under the 1-year return flow conditions (Upland Borrow sand used as the capping material).

Figure C-3c. Plan view of the bottom shear stress under the 1-year return flow conditions (Upland Borrow sand used as the capping material).

Figure C-4a. Plan view of the net elevation change under the 2-year return flow conditions (Upland Borrow sand used as the capping material).

Figure C-4b. Plan view of the maximum erosion under the 2-year return flow conditions (Upland Borrow sand used as the capping material).

Figure C-4c. Plan view of the bottom shear stress under the 2-year return flow conditions (Upland Borrow sand used as the capping material).

Figure C-5a. Plan view of the net elevation change under the 5-year return flow conditions

(Upland Borrow sand used as the capping material).
Figure C-5b. Plan view of the maximum erosion under the 5-year return flow conditions (Upland Borrow sand used as the capping material).

Figure C-5c. Plan view of the bottom shear stress under the 5-year return flow conditions (Upland Borrow sand used as the capping material).

Figure C-6a. Plan view of the net elevation change under the 10-year return flow conditions (Upland Borrow sand used as the capping material).

Figure C-6b. Plan view of the maximum erosion under the 10-year return flow conditions (Upland Borrow sand used as the capping material).

Figure C-6c. Plan view of the bottom shear stress under the 10-year return flow conditions (Upland Borrow sand used as the capping material).

Figure C-7a. Plan view of the net elevation change under the 25-year return flow conditions (Upland Borrow sand used as the capping material).

Figure C-7b. Plan view of the maximum erosion under the 25-year return flow conditions (Upland Borrow sand used as the capping material).

Figure C-7c. Plan view of the bottom shear stress under the 25-year return flow conditions (Upland Borrow sand used as the capping material).

Figure C-8a. Plan view of the net elevation change under the 50-year return flow conditions (Upland Borrow sand used as the capping material).

Figure C-8b. Plan view of the maximum erosion under the 50-year return flow conditions (Upland Borrow sand used as the capping material).

Figure C-8c. Plan view of the bottom shear stress under the 50-year return flow conditions (Upland Borrow sand used as the capping material).

Figure C-9a. Plan view of the net elevation change under the 100-year return flow conditions (Upland Borrow sand used as the capping material).

Figure C-9b. Plan view of the maximum erosion under the 100-year return flow conditions (Upland Borrow sand used as the capping material).

Figure C-9c. Plan view of the bottom shear stress under the 100-year return flow conditions (Upland Borrow sand used as the capping material).

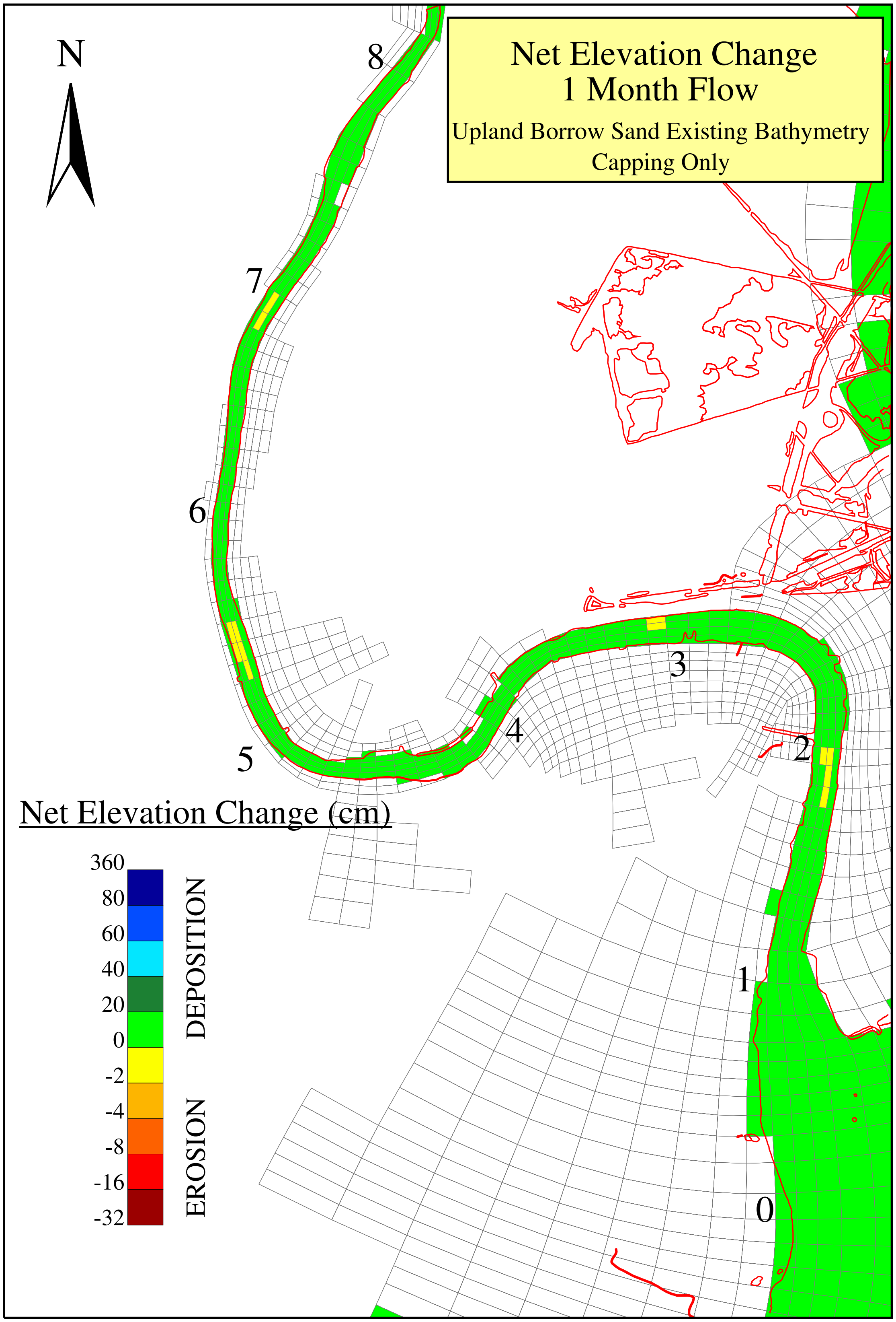

Figure C-1a. Plan view of the net elevation change under the 1-month return flow conditions (Upland Borrow sand used as the capping material).

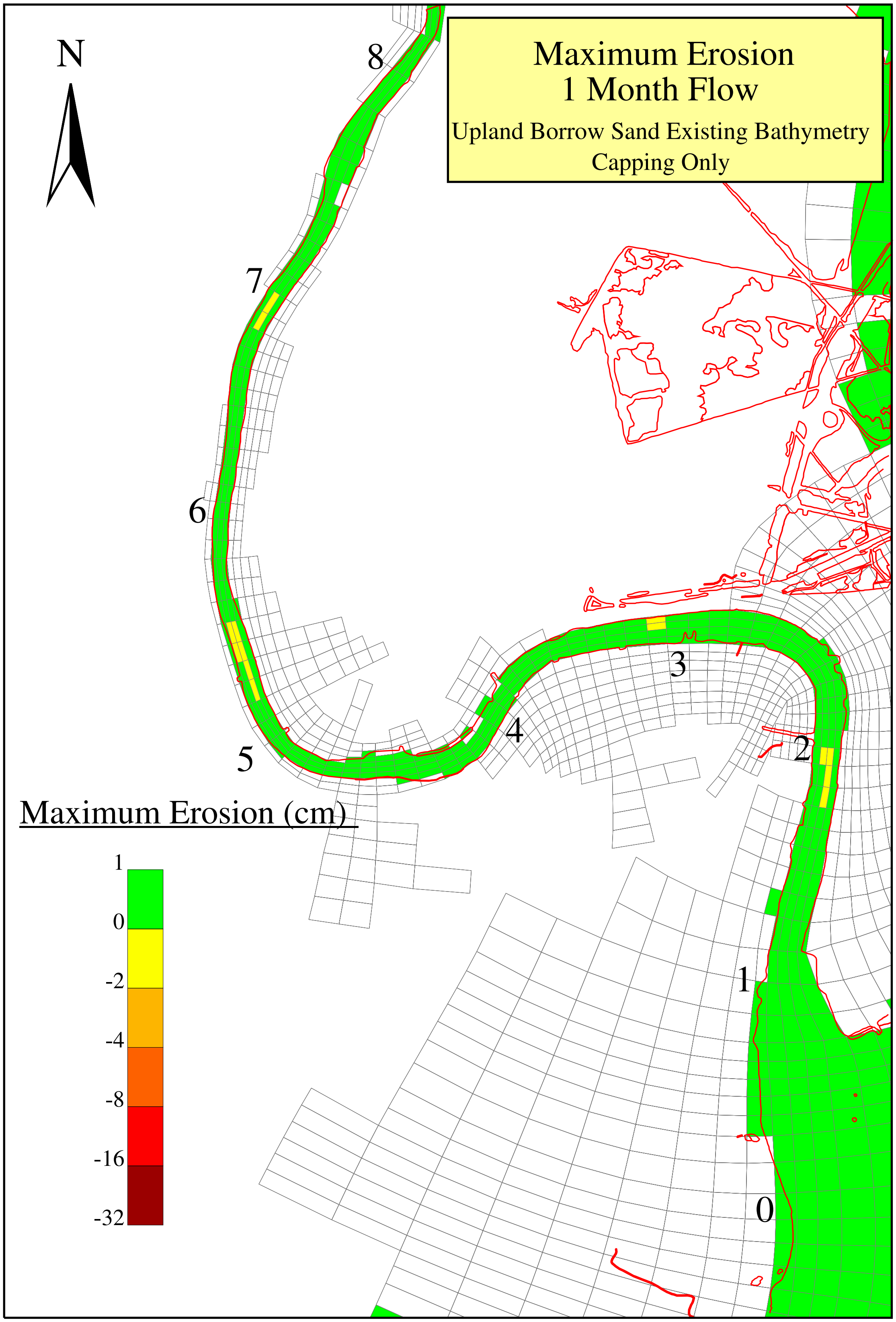

Figure C-1b. Plan view of the maximum erosion under the 1-month return flow conditions (Upland Borrow sand used as the capping material).

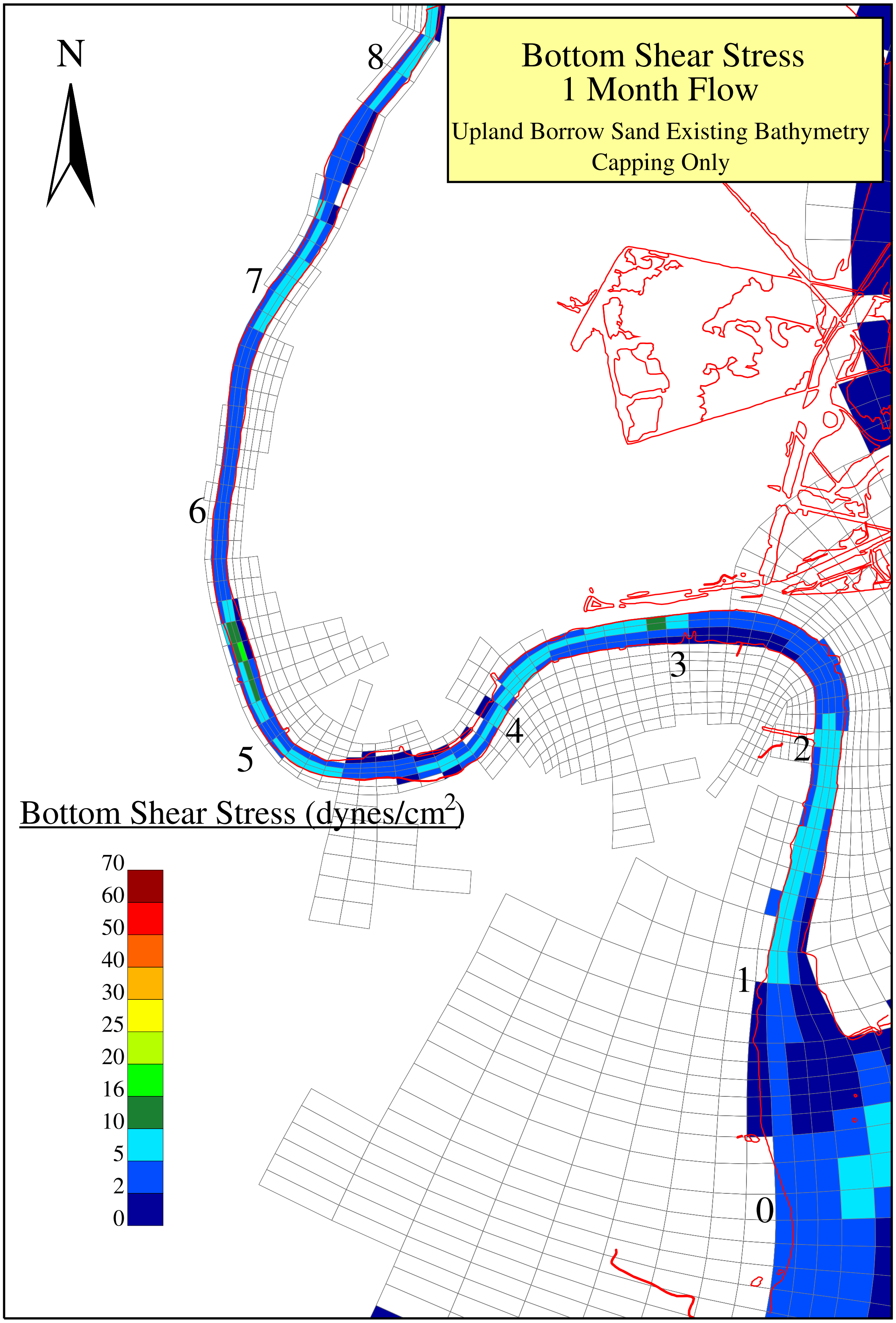

Figure C-1c. Plan view of the bottom shear stress under the 1-month return flow conditions (Upland Borrow sand used as the capping material).

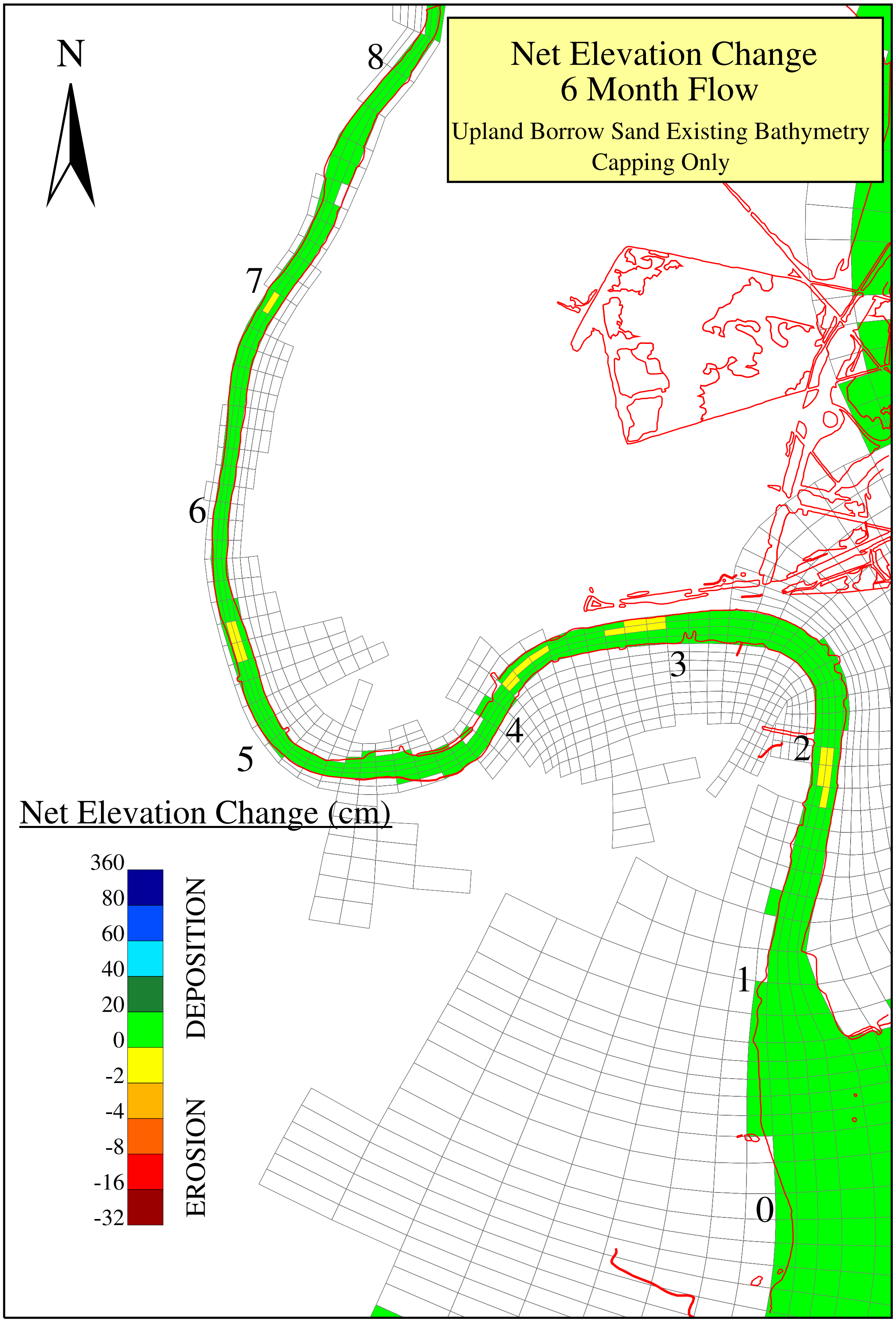

Figure C-2a. Plan view of the net elevation change under the 6-month return flow conditions (Upland Borrow sand used as the capping material).

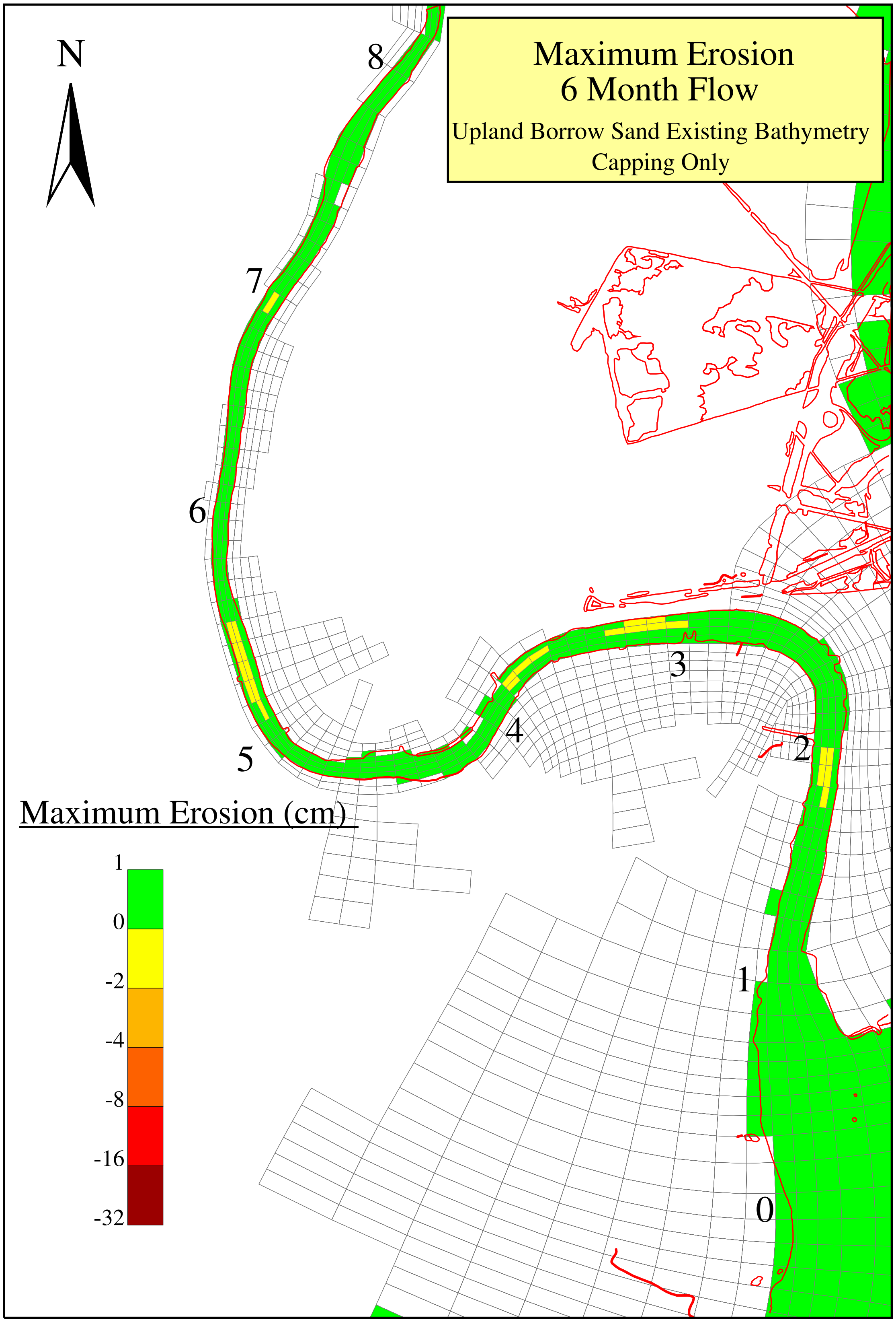

Figure C-2b. Plan view of the maximum erosion under the 6-month return flow conditions (Upland Borrow sand used as the capping material).

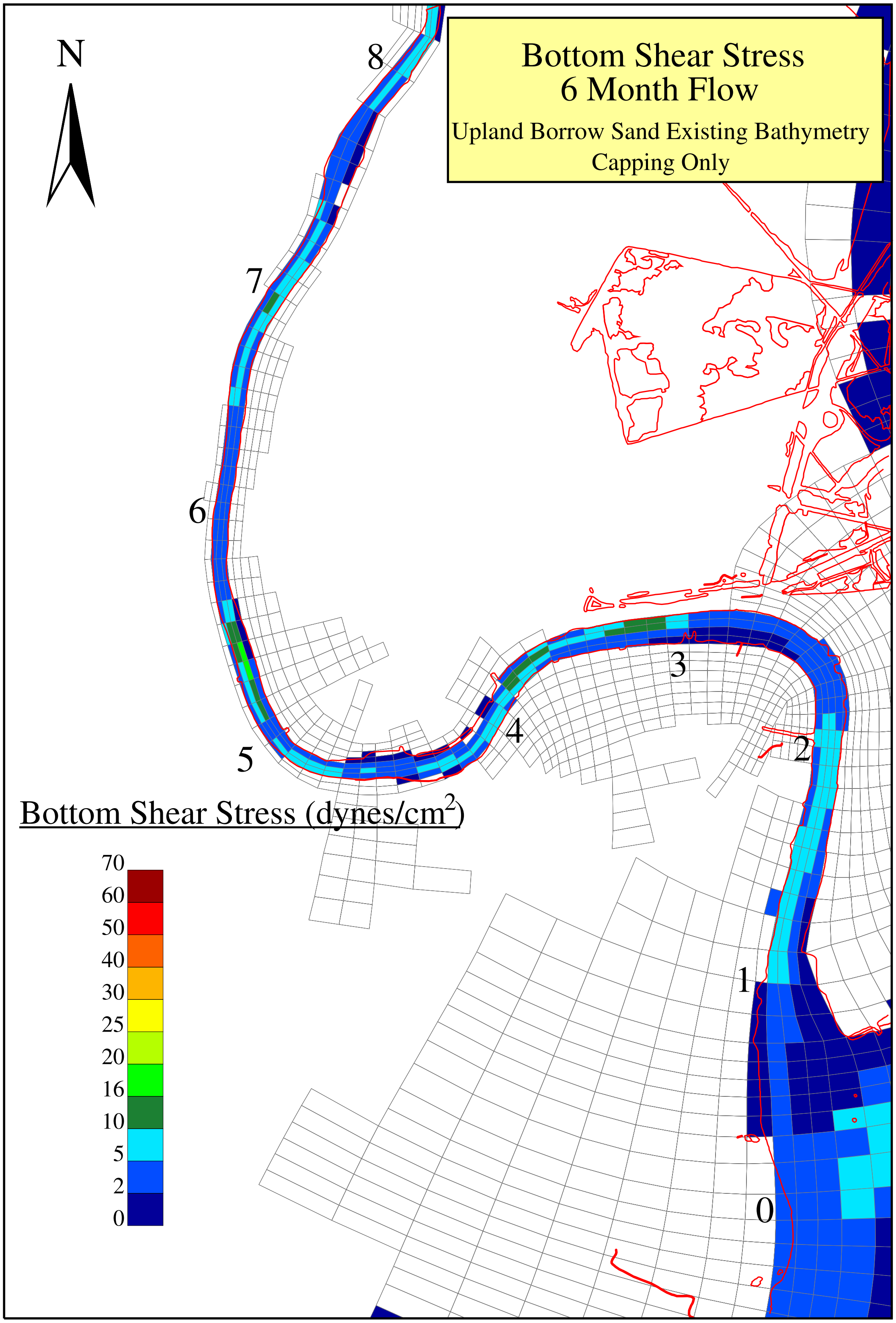

Figure C-2c. Plan view of the bottom shear stress under the 6-month return flow conditions (Upland Borrow sand used as the capping material).

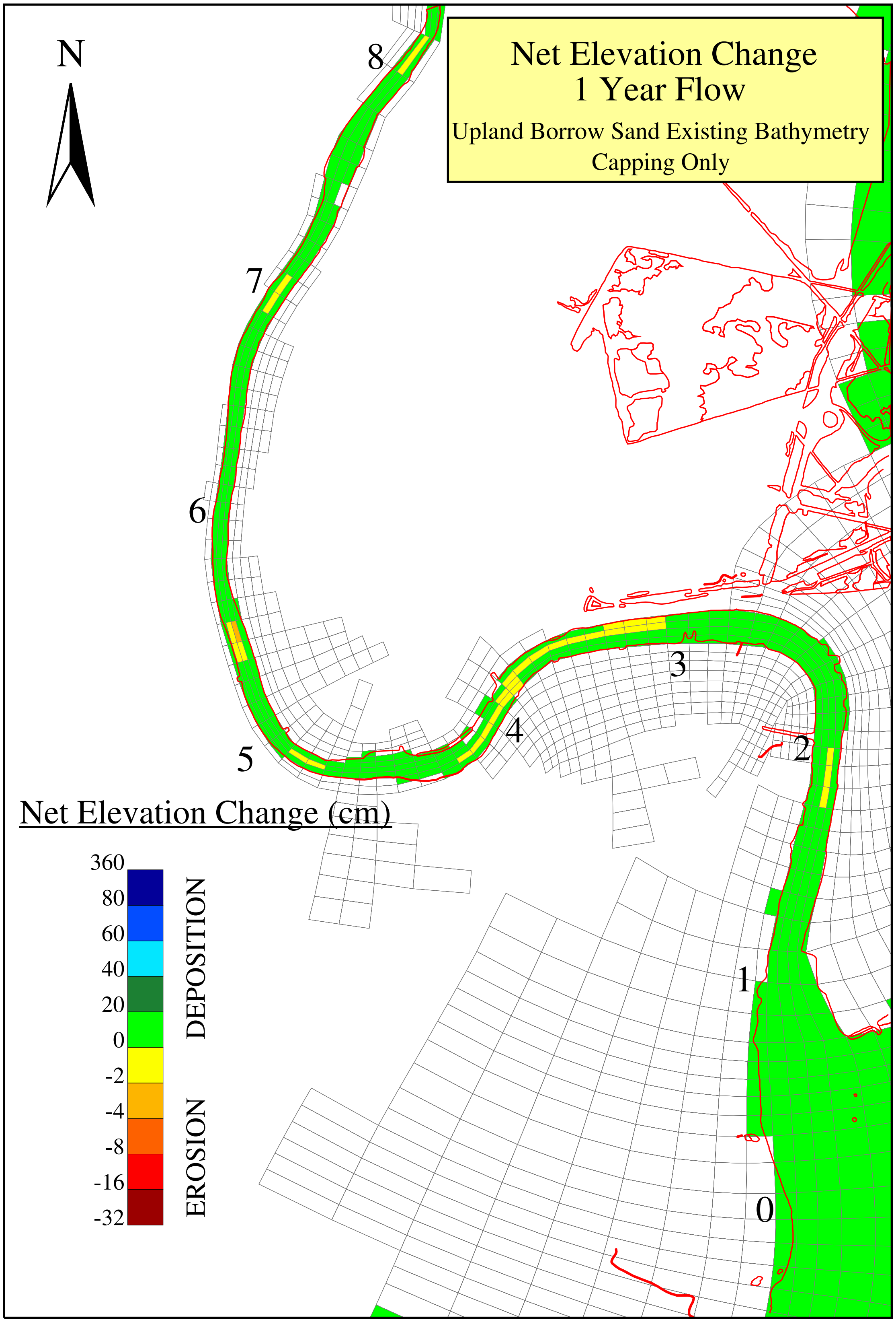

Figure C-3a. Plan view of the net elevation change under the 1-year return flow conditions (Upland Borrow sand used as the capping material).

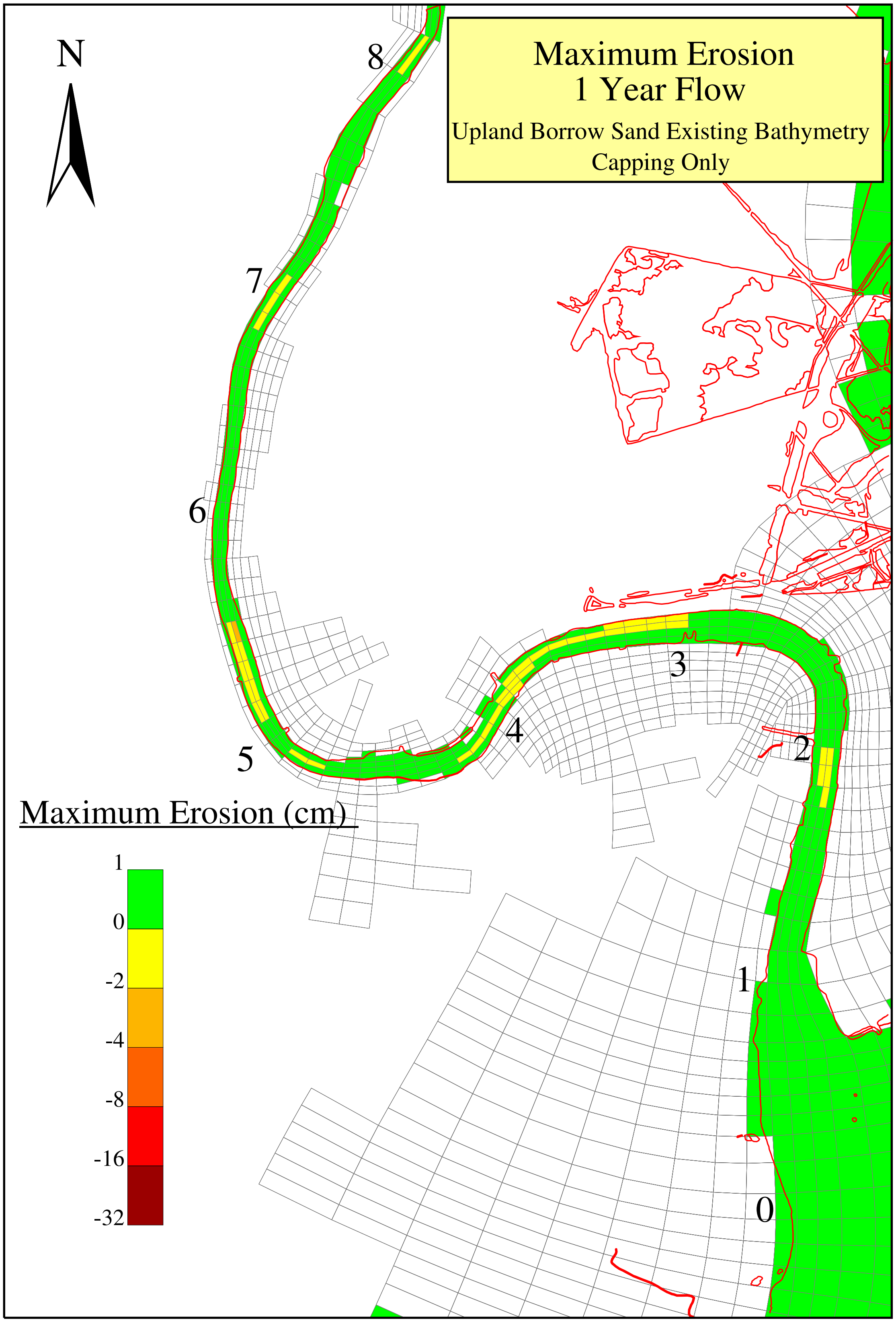

Figure C-3b. Plan view of the maximum erosion under the 1-year return flow conditions (Upland Borrow sand used as the capping material).

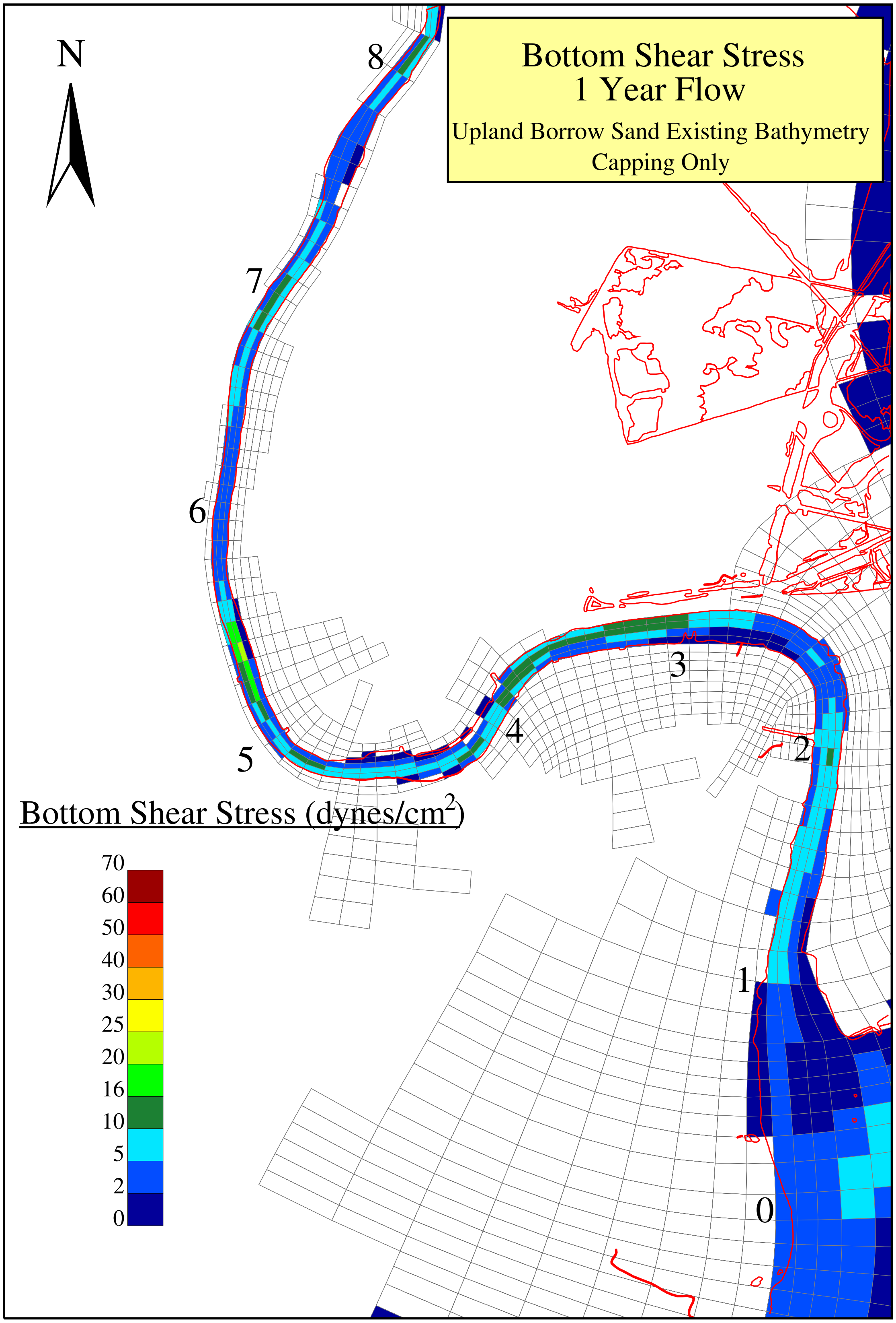

Figure C-3c. Plan view of the bottom shear stress under the 1-year return flow conditions (Upland Borrow sand used as the capping material).

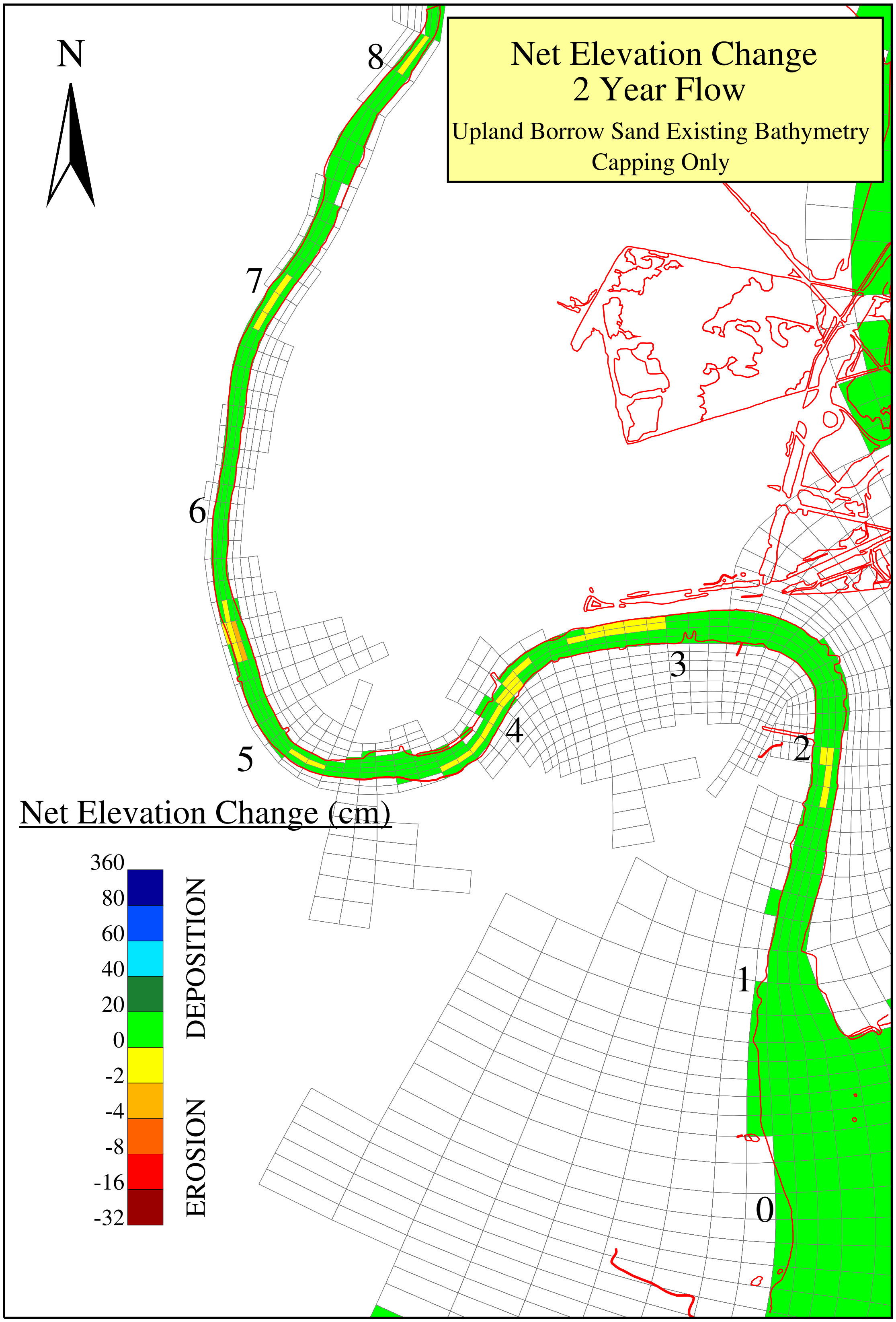

Figure C-4a. Plan view of the net elevation change under the 2-year return flow conditions (Upland Borrow sand used as the capping material).

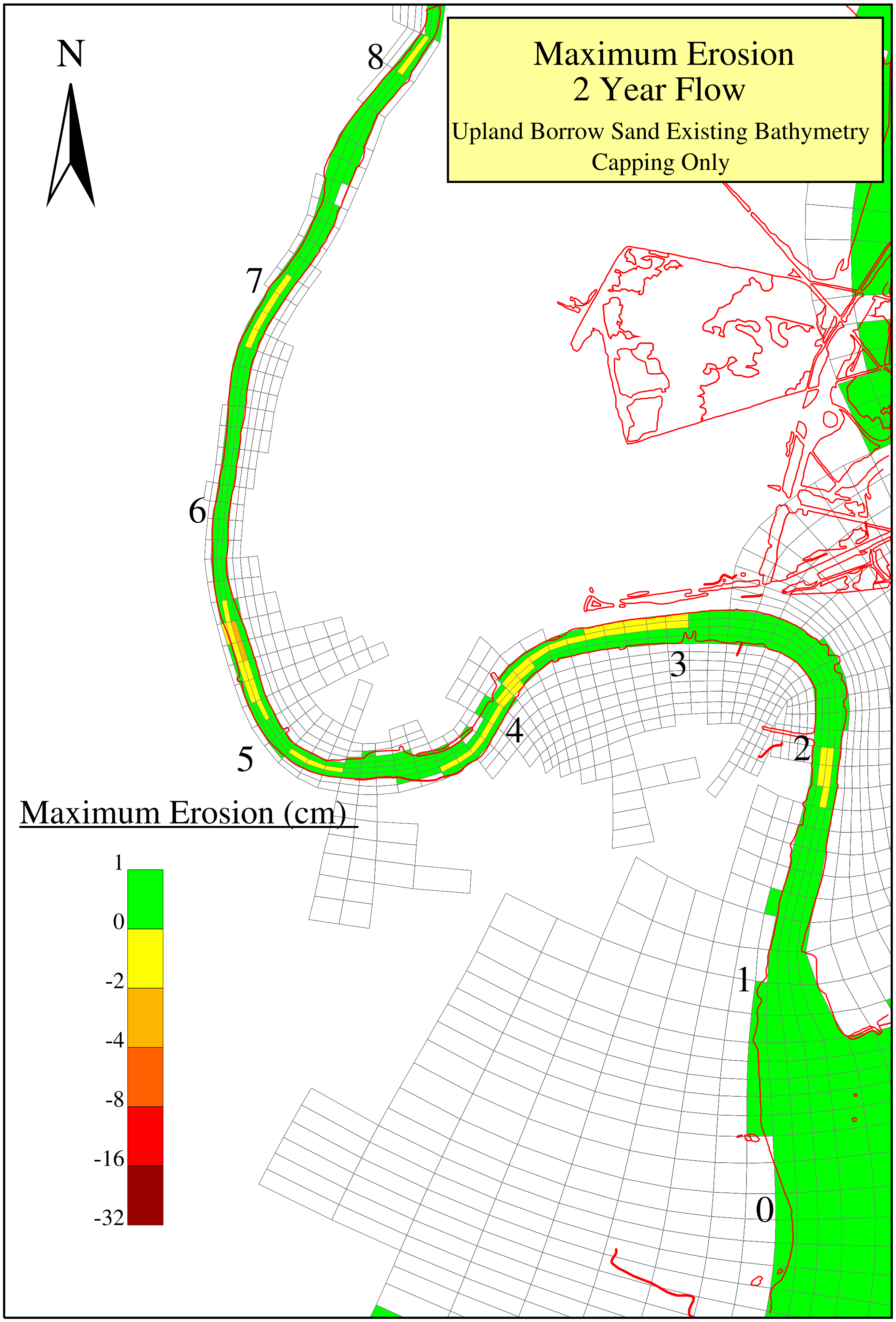

Figure C-4b. Plan view of the maximum erosion under the 2-year return flow conditions (Upland Borrow sand used as the capping material).

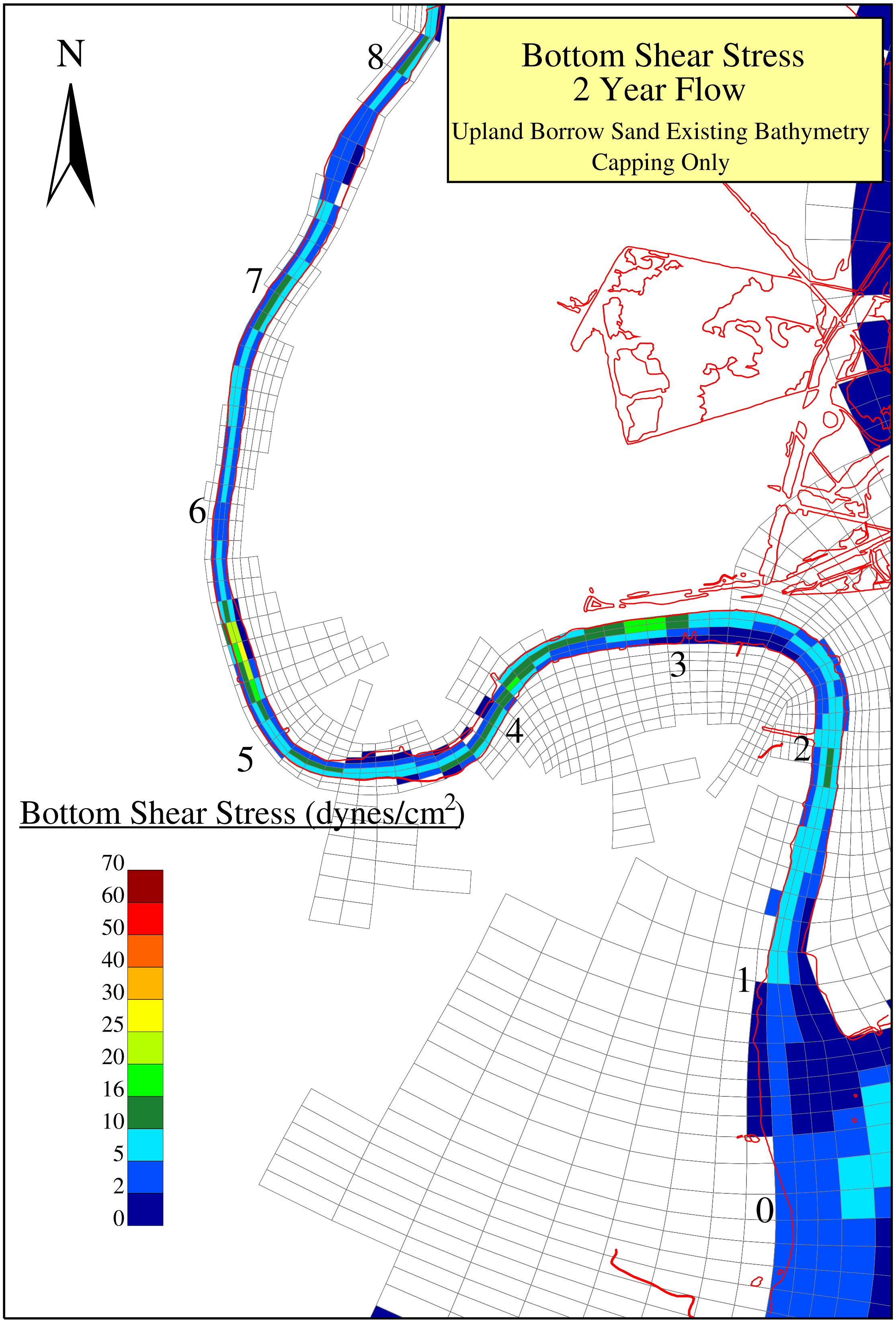

Figure C-4c. Plan view of the bottom shear stress under the 2-year return flow conditions (Upland Borrow sand used as the capping material).

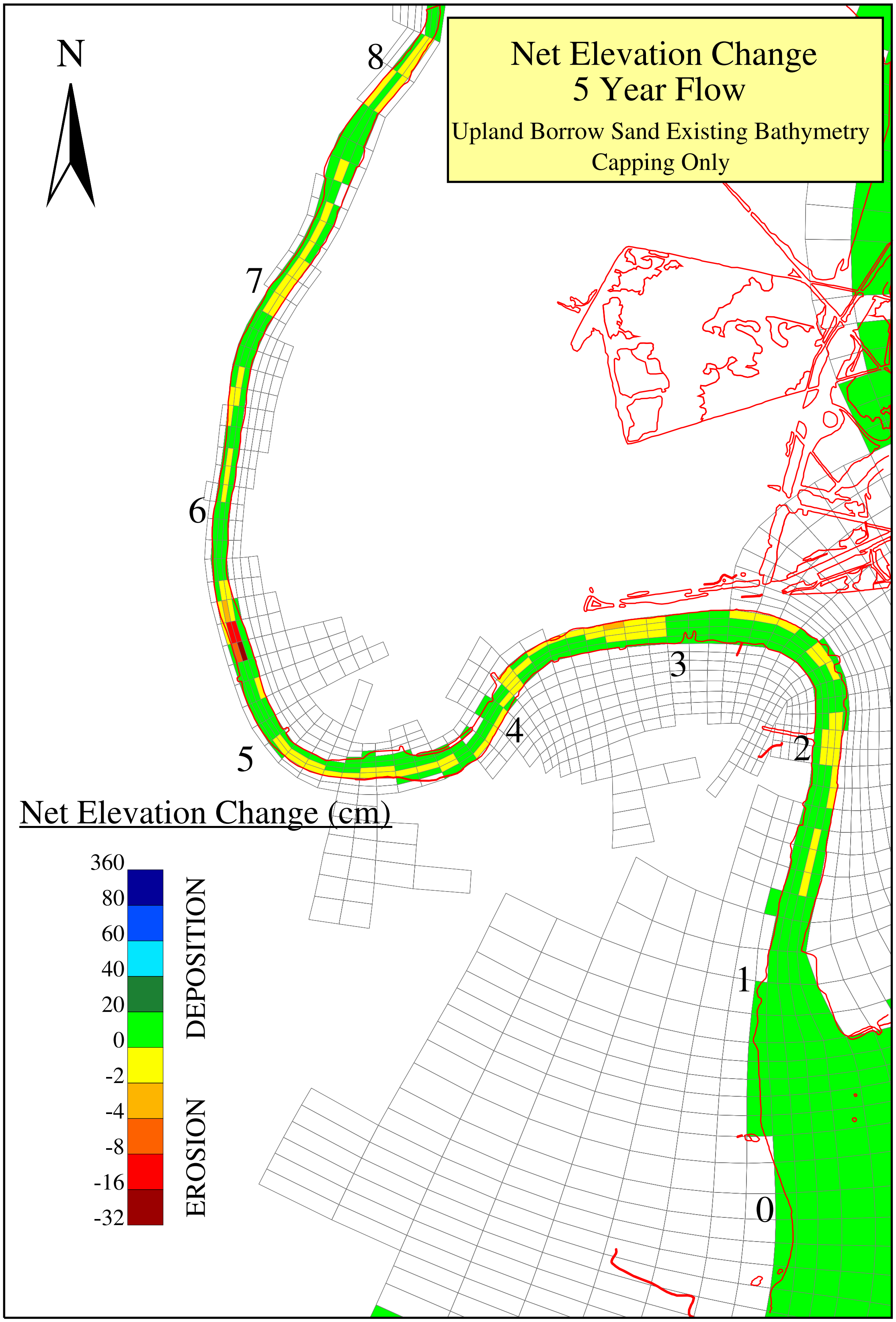

Figure C-5a. Plan view of the net elevation change under the 5-year return flow conditions (Upland Borrow sand used as the capping material).

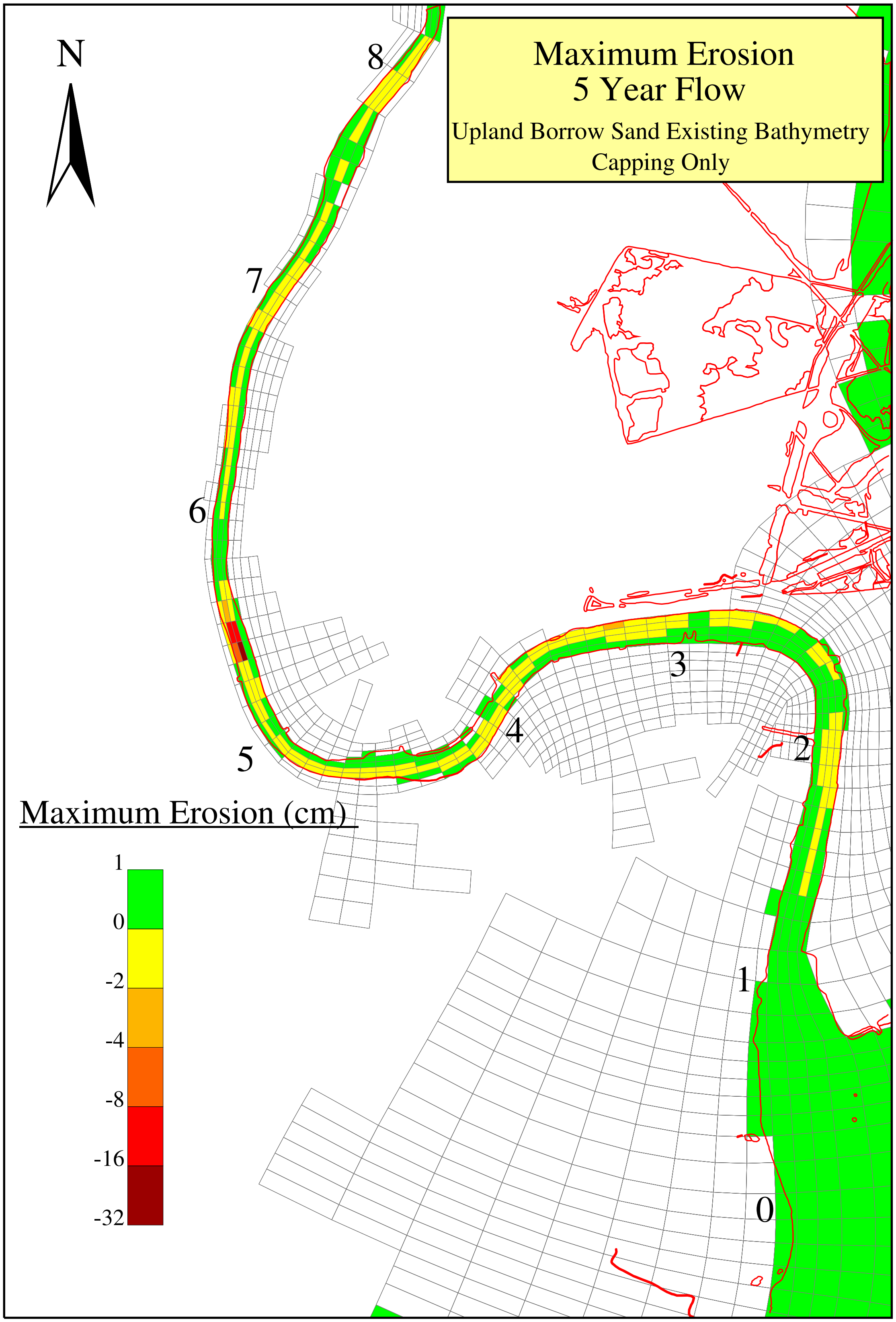

Figure C-5b. Plan view of the maximum erosion under the 5-year return flow conditions (Upland Borrow sand used as the capping material).

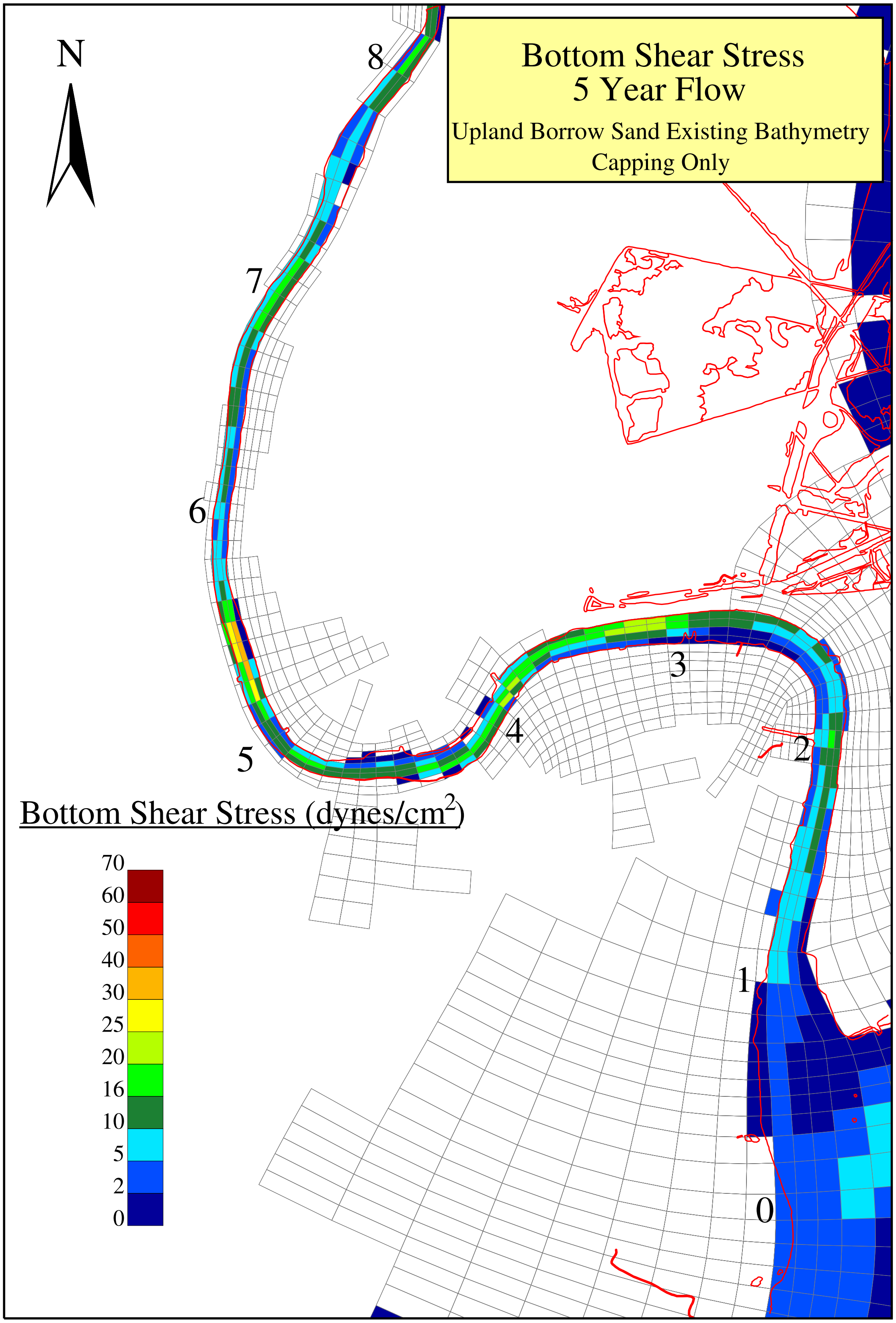

Figure C-5c. Plan view of the bottom shear stress under the 5-year return flow conditions (Upland Borrow sand used as the capping material).

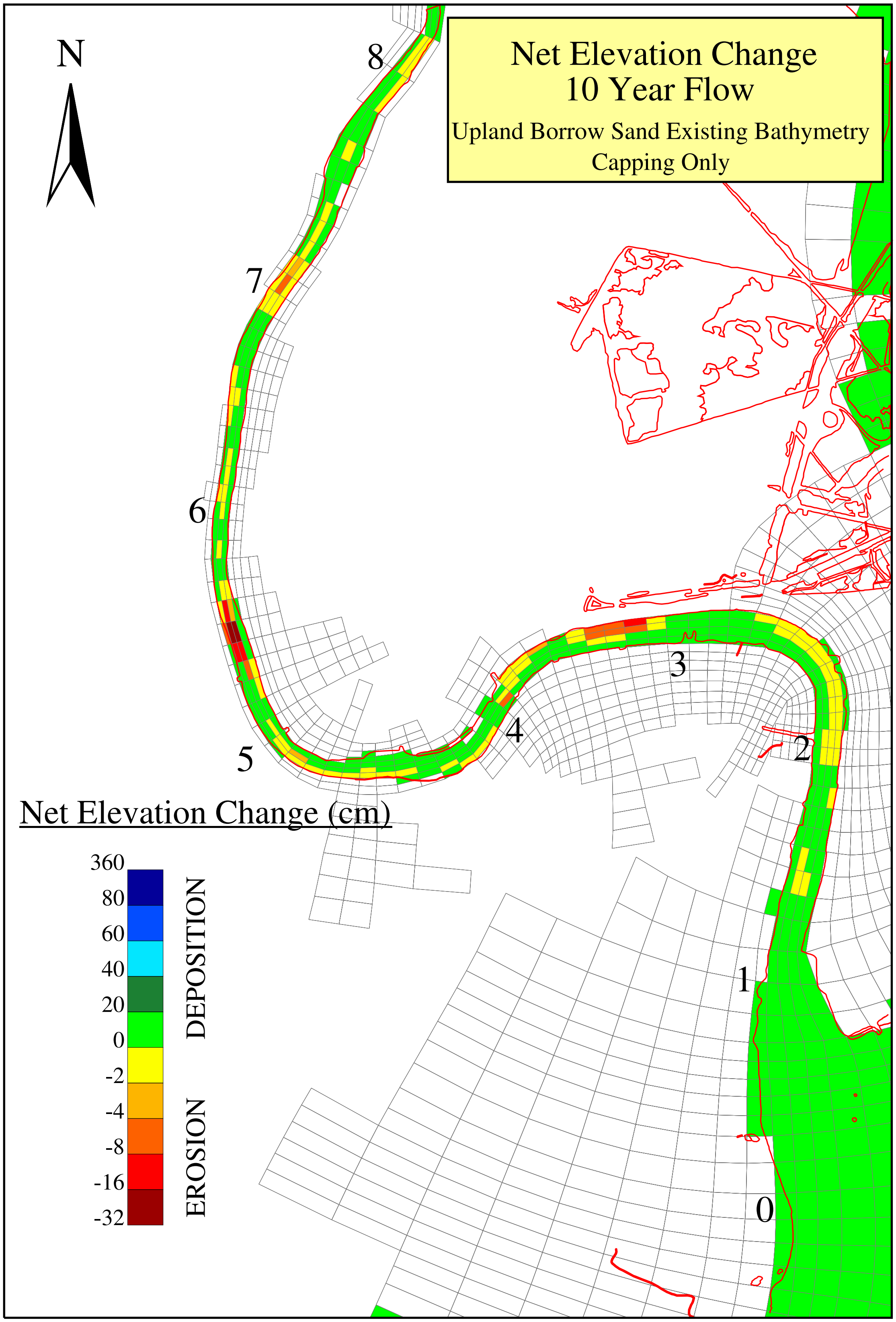

Figure C-6a. Plan view of the net elevation change under the 10-year return flow conditions (Upland Borrow sand used as the capping material).

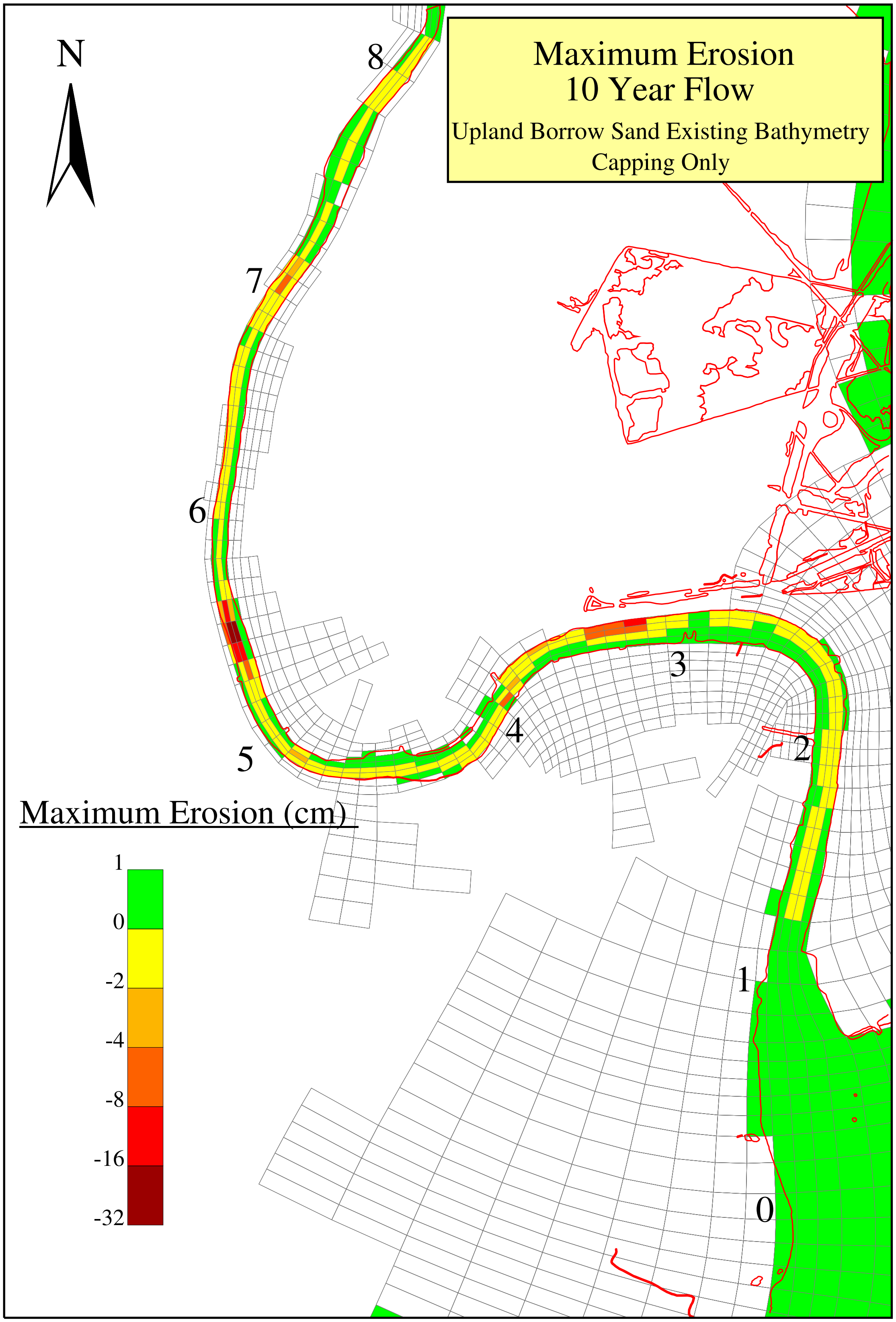

Figure C-6b. Plan view of the maximum erosion under the 10-year return flow conditions (Upland Borrow sand used as the capping material).

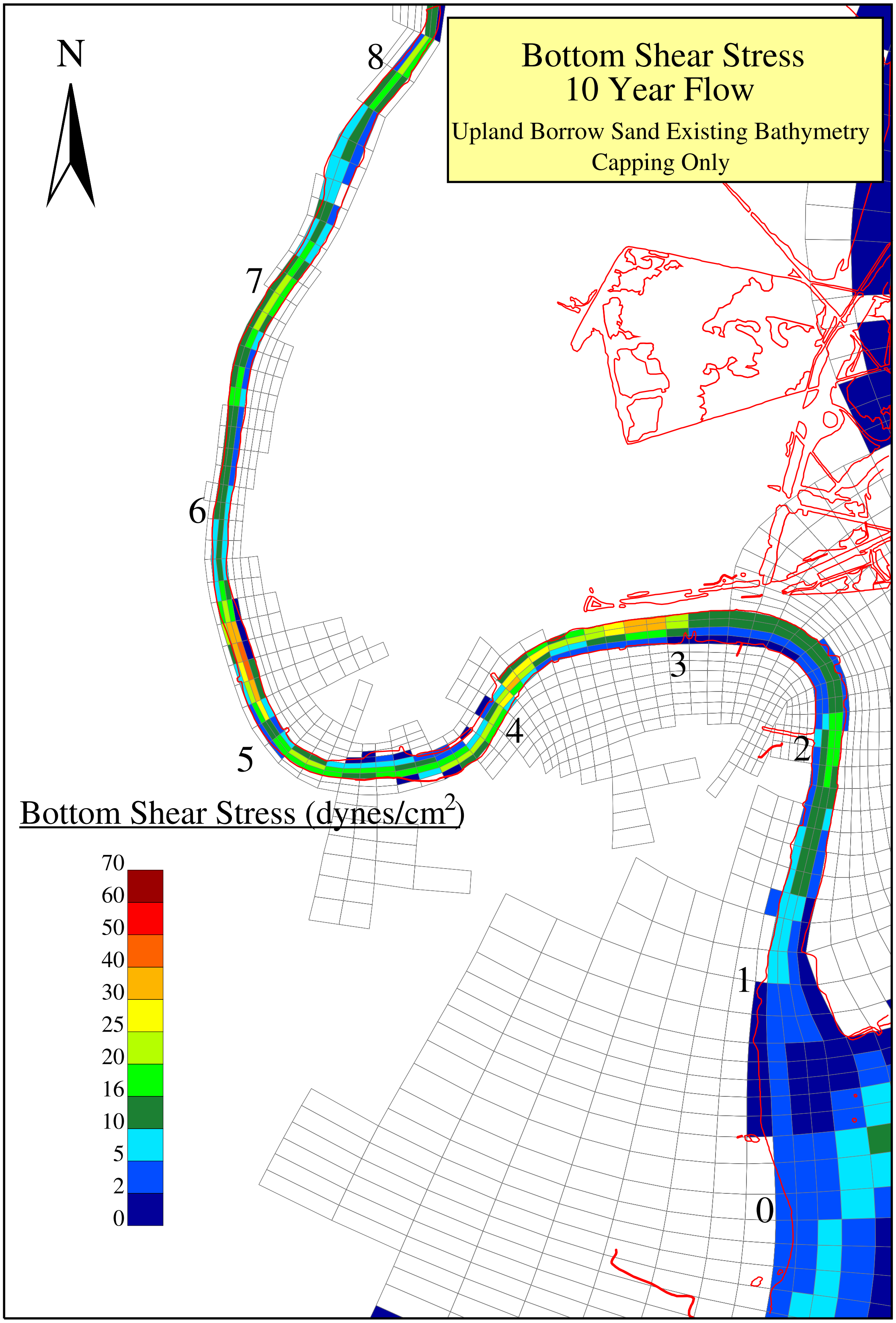

Figure C-6c. Plan view of the bottom shear stress under the 10-year return flow conditions (Upland Borrow sand used as the capping material).

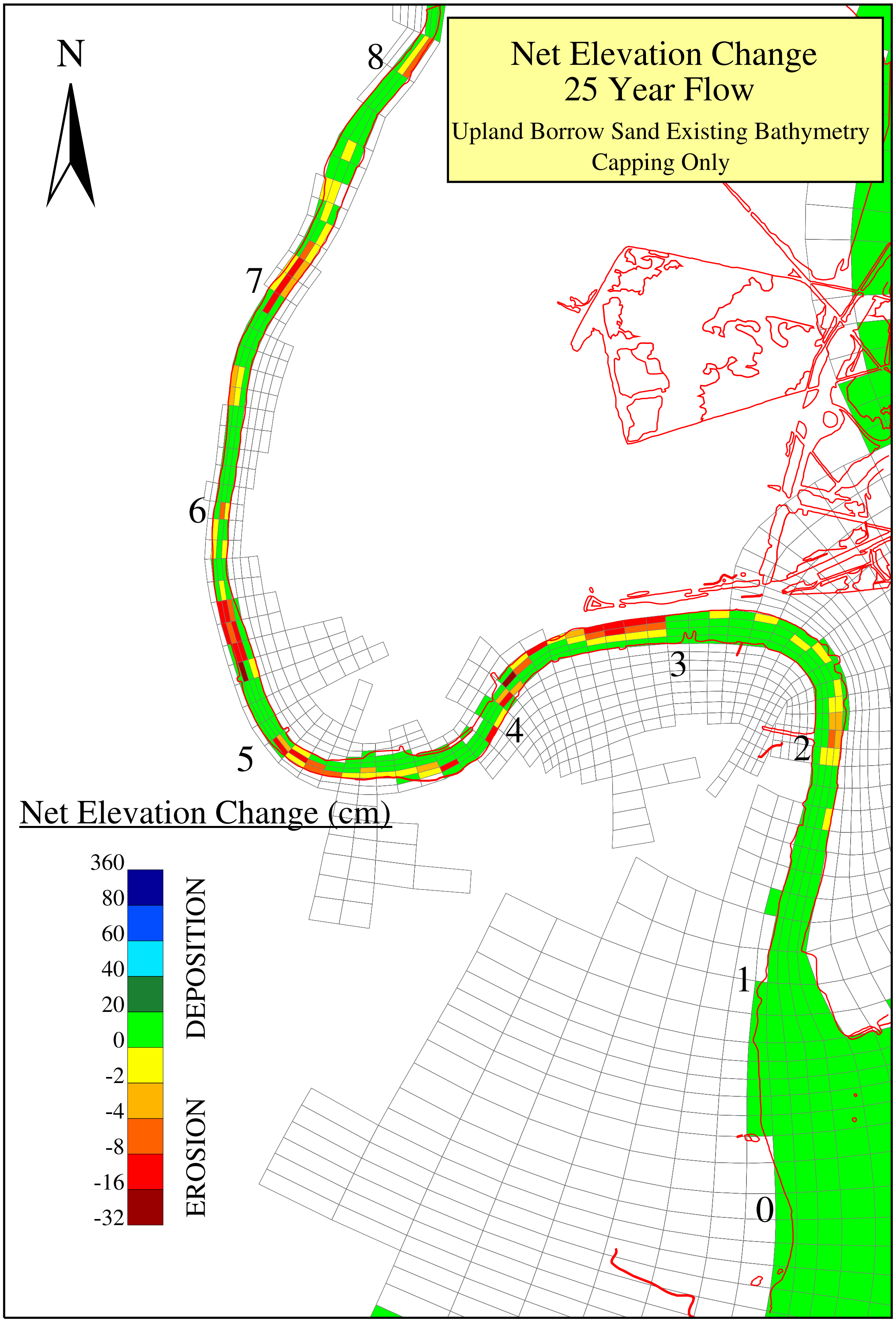

Figure C-7a. Plan view of the net elevation change under the 25-year return flow conditions (Upland Borrow sand used as the capping material).

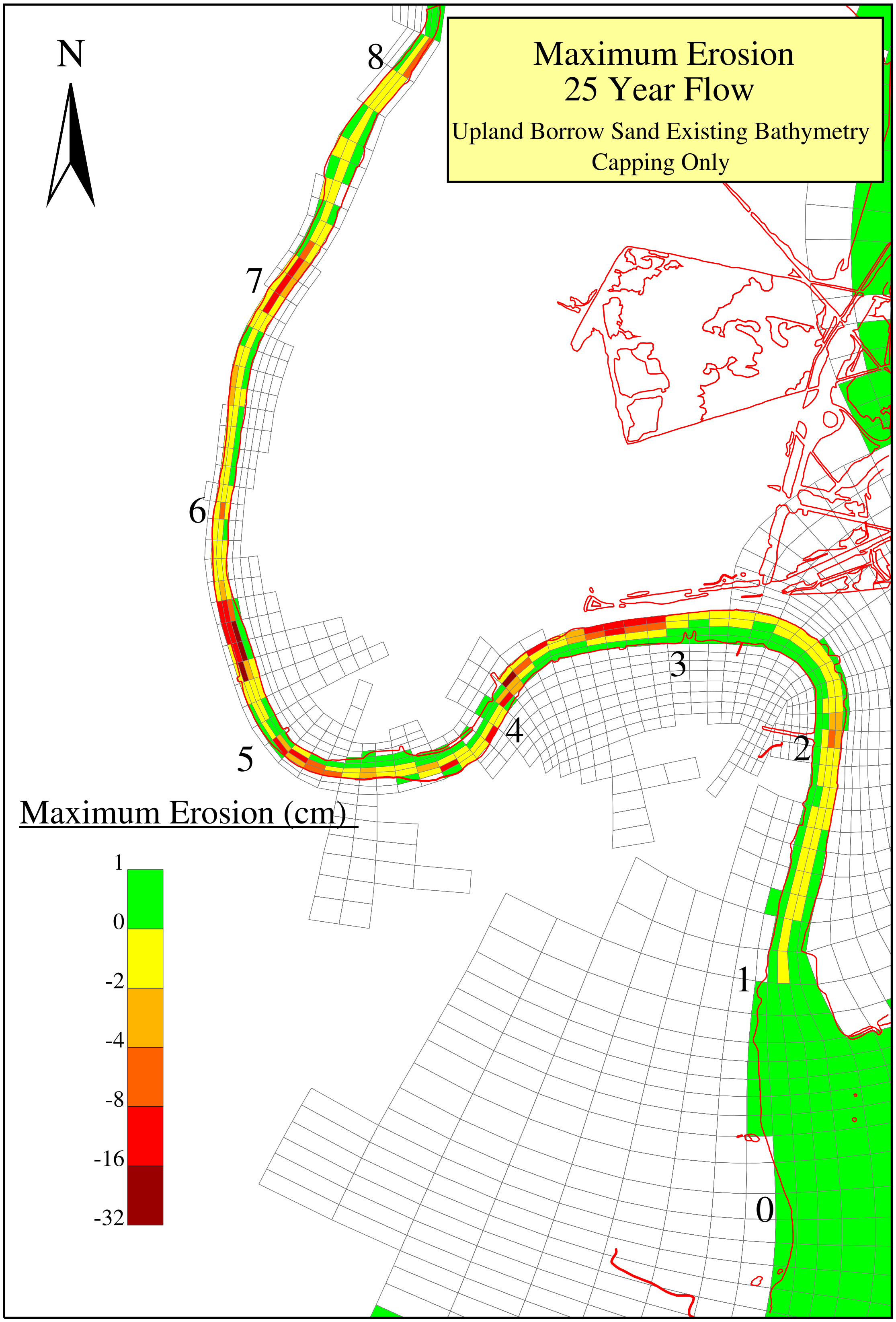

Figure C-7b. Plan view of the maximum erosion under the 25-year return flow conditions (Upland Borrow sand used as the capping material).

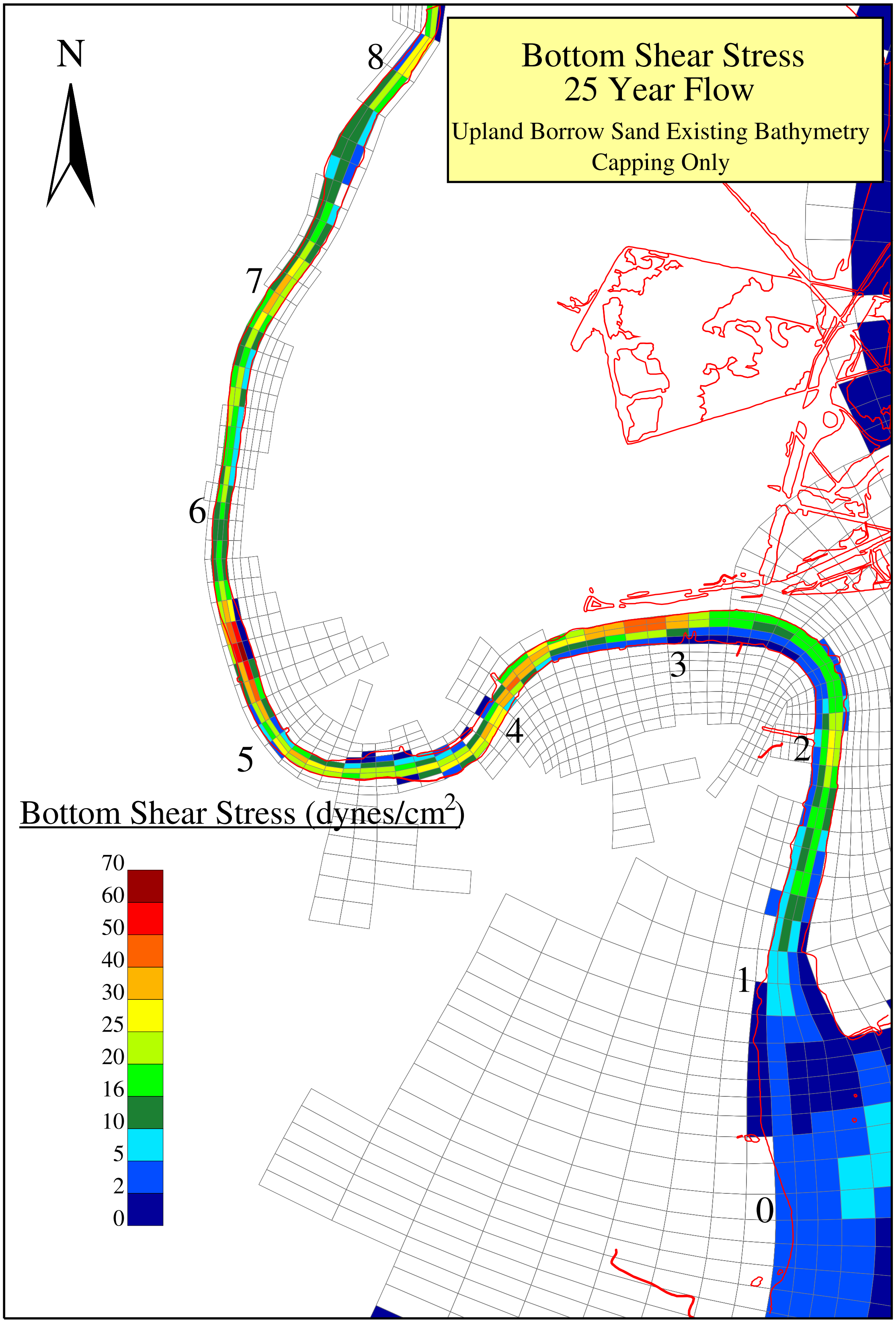

Figure C-7c. Plan view of the bottom shear stress under the 25-year return flow conditions (Upland Borrow sand used as the capping material).

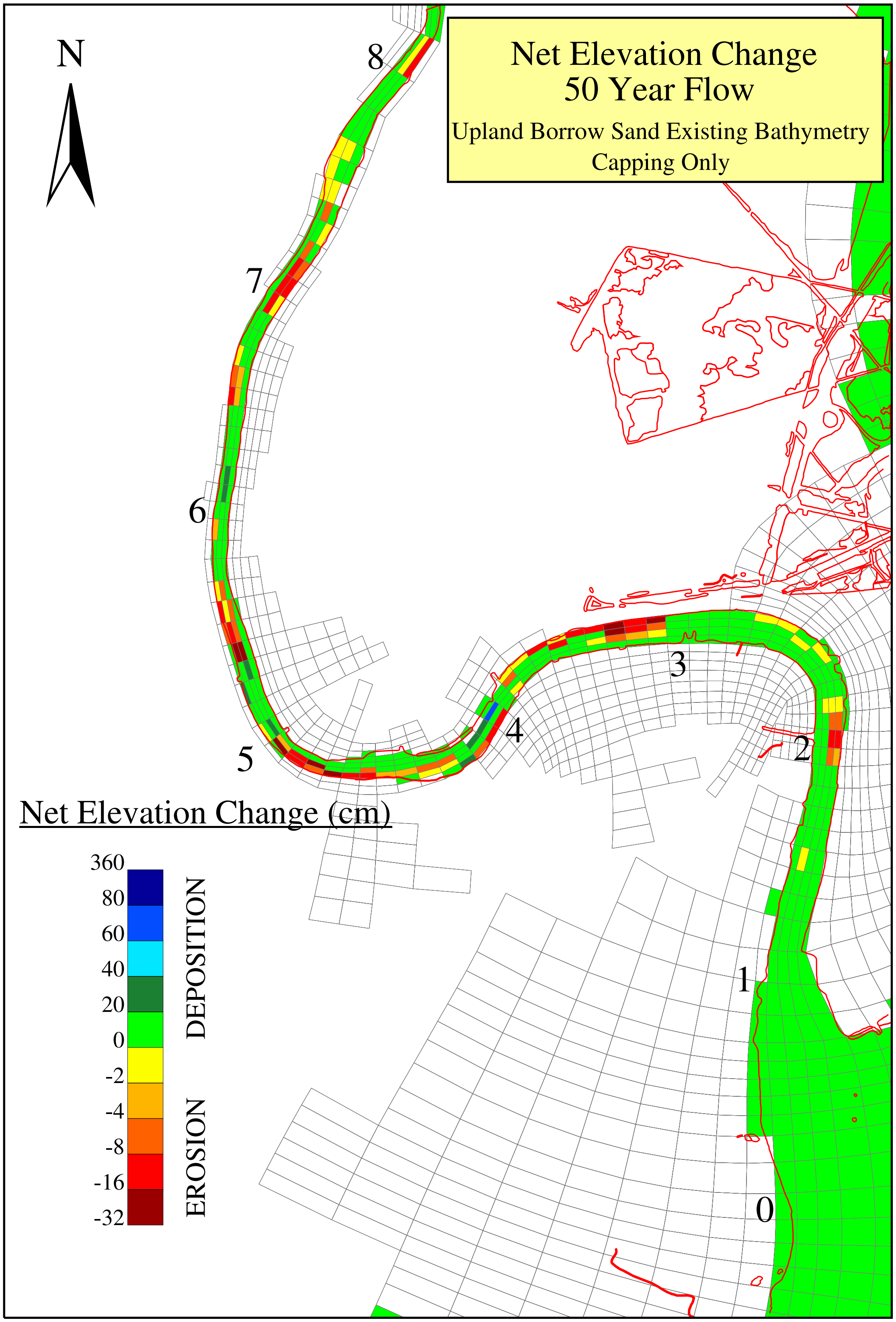

Figure C-8a. Plan view of the net elevation change under the 50-year return flow conditions (Upland Borrow sand used as the capping material).

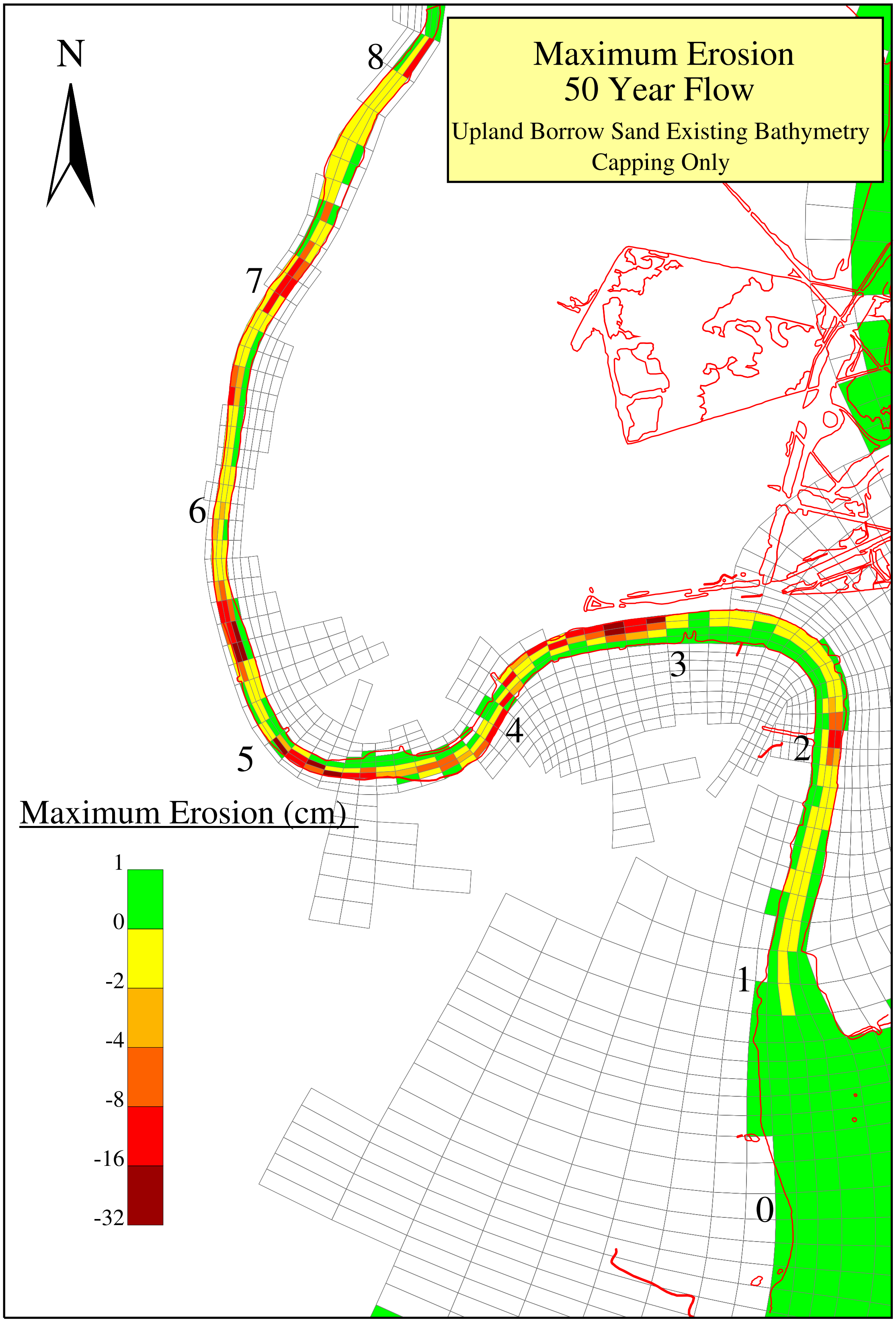

Figure C-8b. Plan view of the maximum erosion under the 50-year return flow conditions (Upland Borrow sand used as the capping material).

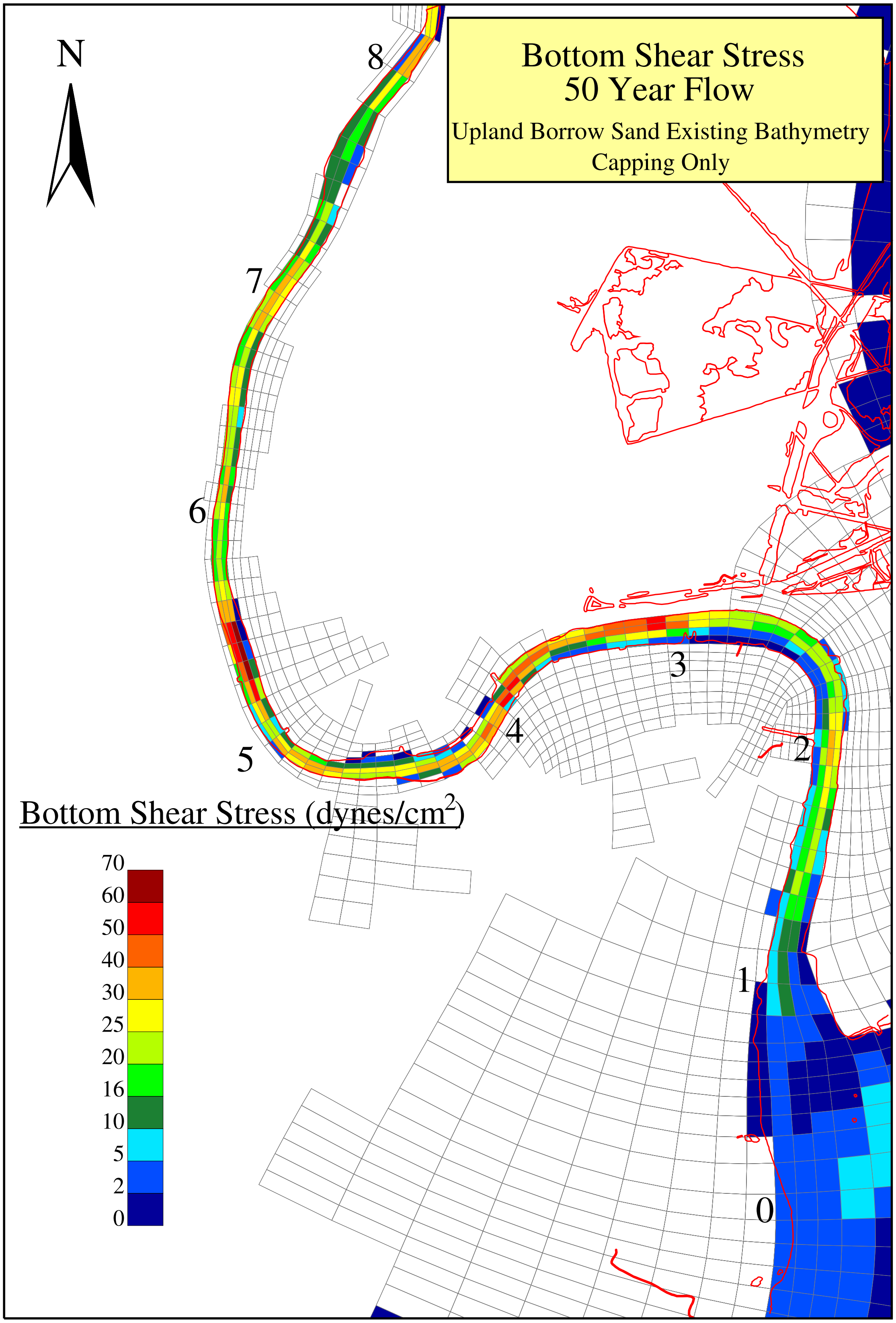

Figure C-8c. Plan view of the bottom shear stress under the 50-year return flow conditions (Upland Borrow sand used as the capping material).

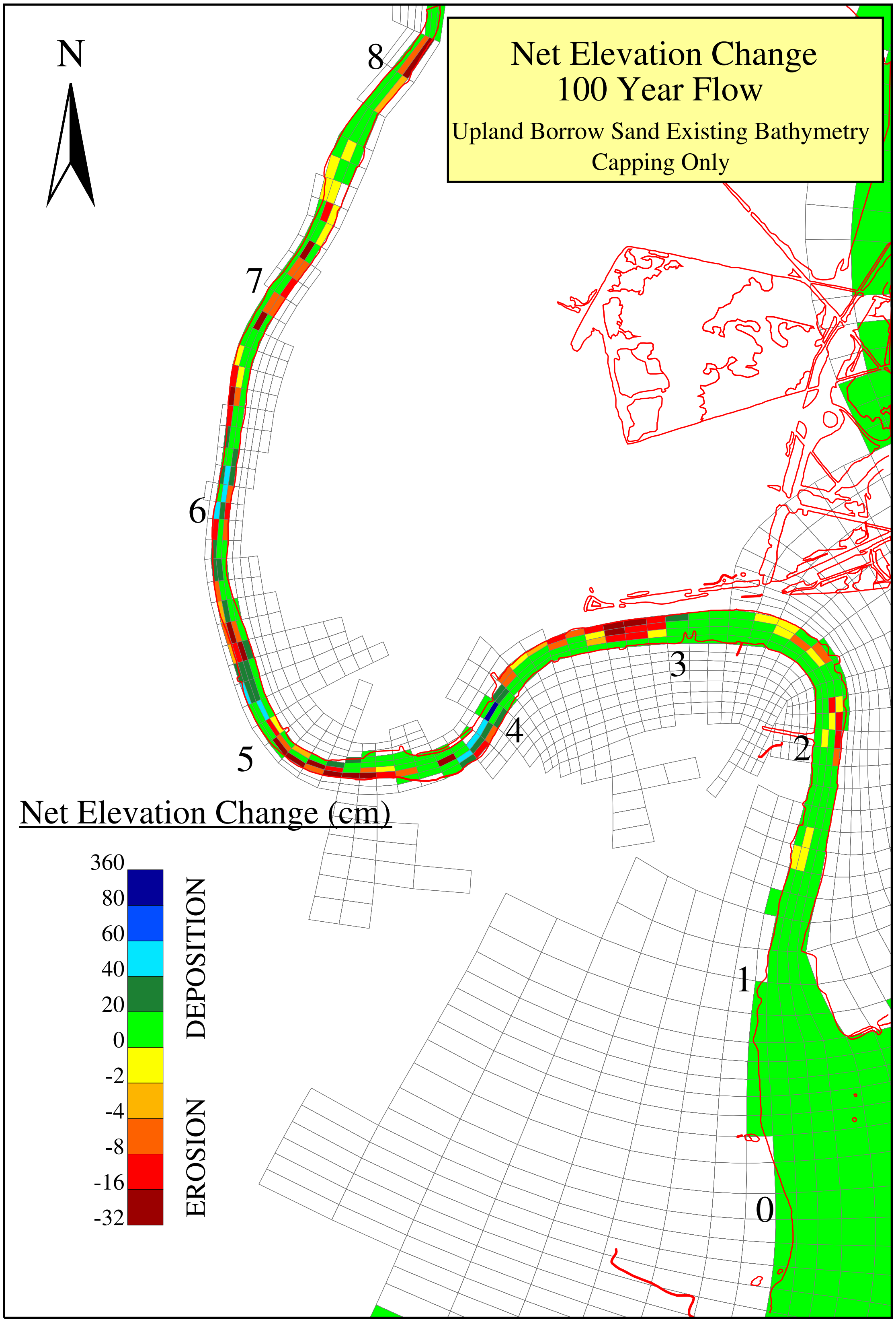

Figure C-9a. Plan view of the net elevation change under the 100-year return flow conditions (Upland Borrow sand used as the capping material).

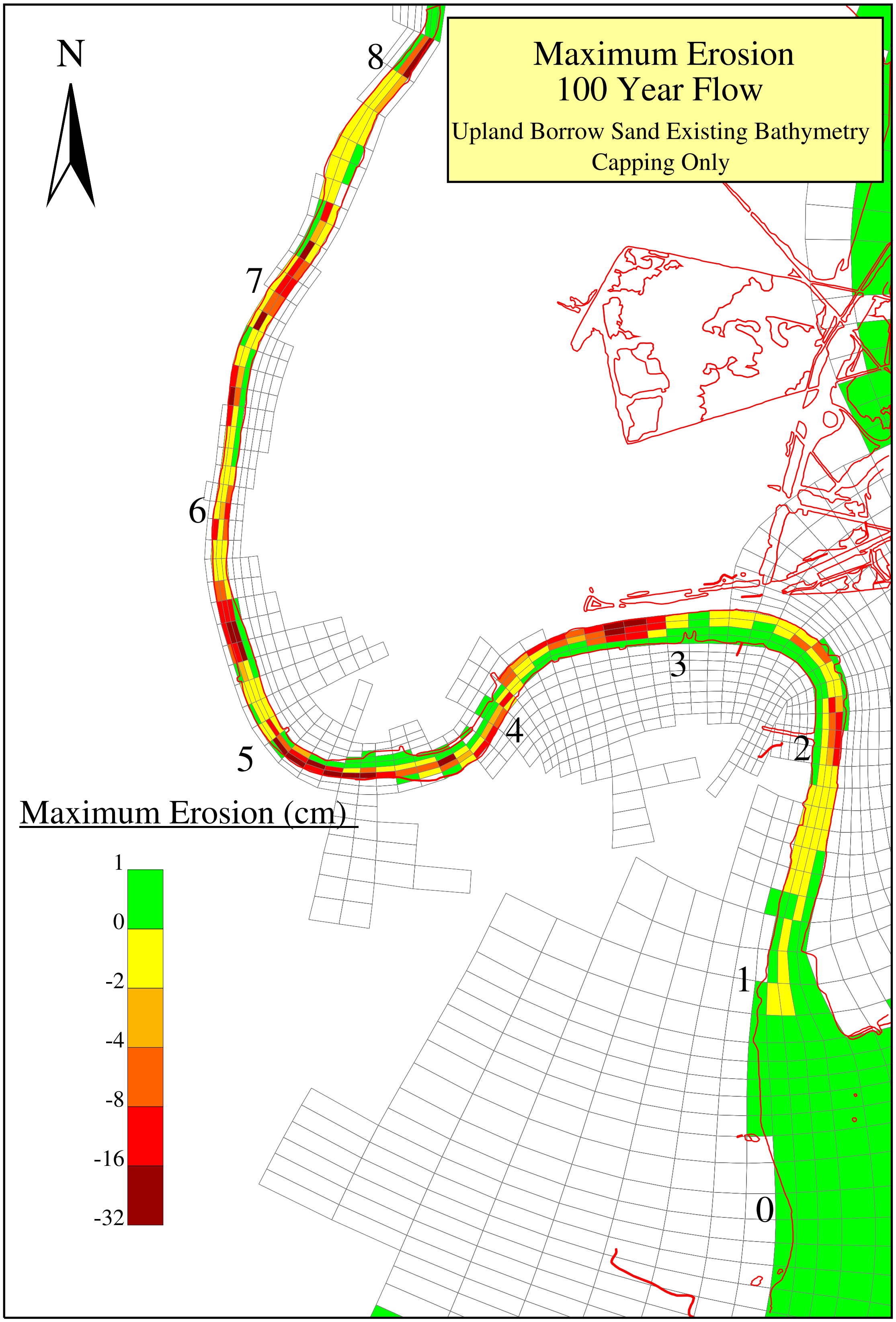

Figure C-9b. Plan view of the maximum erosion under the 100-year return flow conditions (Upland Borrow sand used as the capping material).

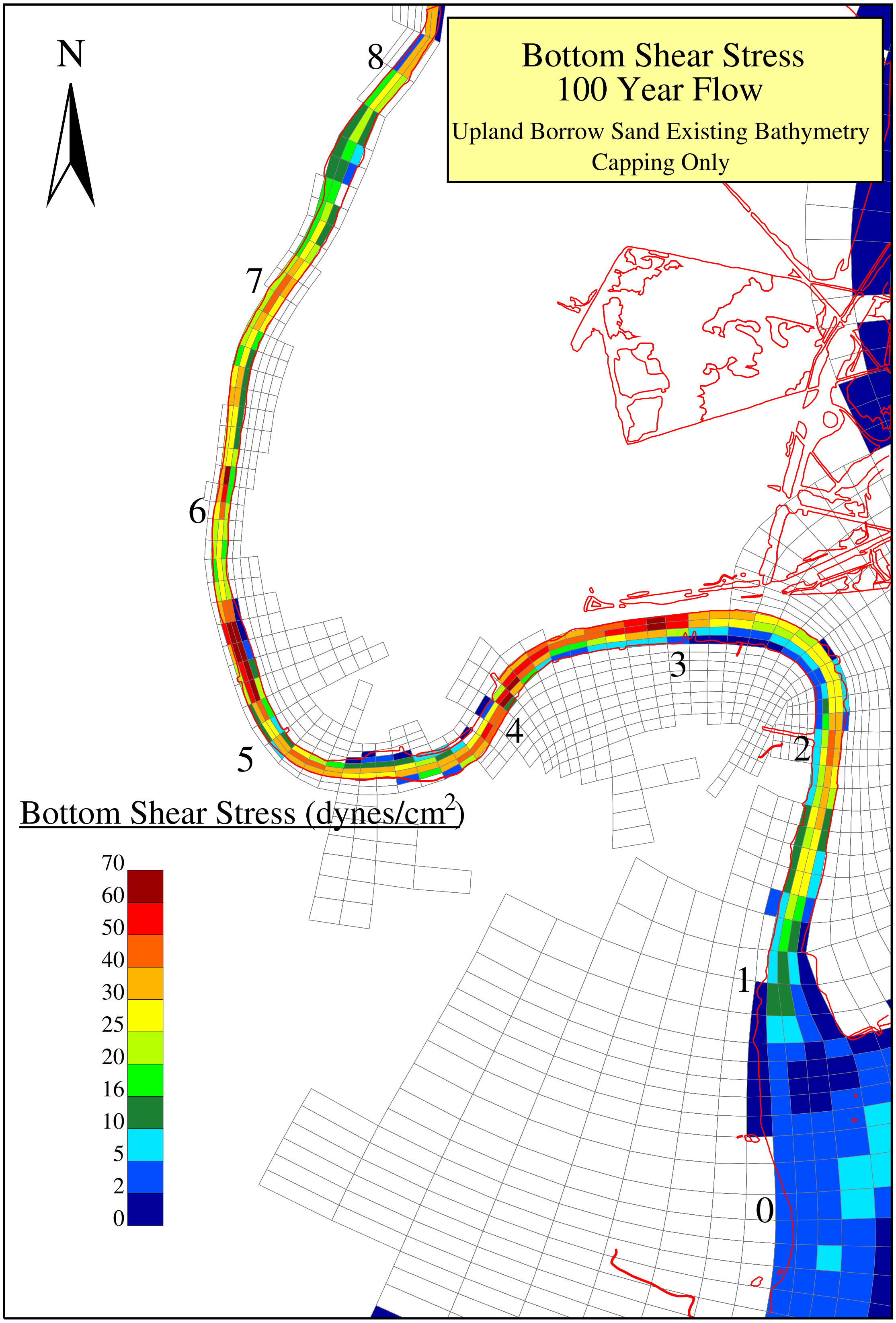

Figure C-9c. Plan view of the bottom shear stress under the 100-year return flow conditions (Upland Borrow sand used as the capping material).

ATTACHMENT D

BED ELEVATION CHANGES, MAXIMUM EROSION AND BOTTOM SHEAR STRESSES UNDER DIFFERENT DEPTH AND CAPPING/ARMORING SCENARIOS

Figure D-1a. Plan view of the net elevation change under 8-Mile Cap-Armor Area Predredging (Capping only) scenario.

Figure D-1b. Plan view of the maximum erosion under 8-Mile Cap-Armor Area Predredging (Capping only) scenario.

Figure D-1c. Plan view of the bottom shear stress under 8-Mile Cap-Armor Area Predredging (Capping only) scenario.

Figure D-2a. Plan view of the net elevation change under 8-Mile Cap-Armor Area Predredging (Capping and Armoring) scenario.

Figure D-2b. Plan view of the maximum erosion under 8-Mile Cap-Armor Area Predredging (Capping and Armoring) scenario.

Figure D-2c. Plan view of the bottom shear stress under 8-Mile Cap-Armor Area Predredging (Capping and Armoring) scenario.

Figure D-3a. Plan view of the net elevation change under 8-Mile Cap-Full Predredging (Capping only) scenario.

Figure D-3b. Plan view of the maximum erosion under 8-Mile Cap-Full Predredging (Capping only) scenario.

Figure D-3c. Plan view of the bottom shear stress under 8-Mile Cap-Full Predredging (Capping only) scenario.

Figure D-4a. Plan view of the net elevation change under 8-Mile Cap-Full Predredging (Capping and Armoring) scenario.

Figure D-4b. Plan view of the net maximum erosion under 8-Mile Cap-Full Predredging (Capping and Armoring) scenario.

Figure D-4c. Plan view of the bottom shear stress under 8-Mile Cap-Full Predredging (Capping and Armoring) scenario.

Figure D-5a. Plan view of the net elevation change under Current Navigation Usage-Full Predredging (Capping only) scenario.

Figure D-5b. Plan view of the maximum erosion under Current Navigation Usage-Full Predredging (Capping only) scenario

Figure D-5c. Plan view of the bottom shear stress under Current Navigation Usage-Full Predredging (Capping only) scenario

Figure D-6a. Plan view of the net elevation change under Current Navigation Usage-Full Predredging (Capping and Armoring) scenario.

Figure D-6b. Plan view of the maximum erosion under Current Navigation Usage-Full Predredging (Capping and Armoring) scenario.

Figure D-6c. Plan view of the bottom shear stress under Current Navigation Usage-Full Predredging (Capping and Armoring) scenario.

Figure D-7a. Plan view of the net elevation change under Future Navigation Usage-Full Predredging (Capping only) scenario.

Figure D-7b. Plan view of the maximum erosion under Future Navigation Usage-Full Predredging (Capping only) scenario.

Figure D-7c. Plan view of the bottom shear stress under Future Navigation Usage-Full Predredging (Capping only) scenario

Figure D-8a. Plan view of the net elevation change under Future Navigation Usage-Full Predredging (Capping and Armoring) scenario.

Figure D-8b. Plan view of the maximum erosion under Future Navigation Usage-Full Predredging (Capping and Armoring) scenario.

Figure D-8c. Plan view of the bottom shear stress under Future Navigation Usage-Full Predredging (Capping and Armoring) scenario.

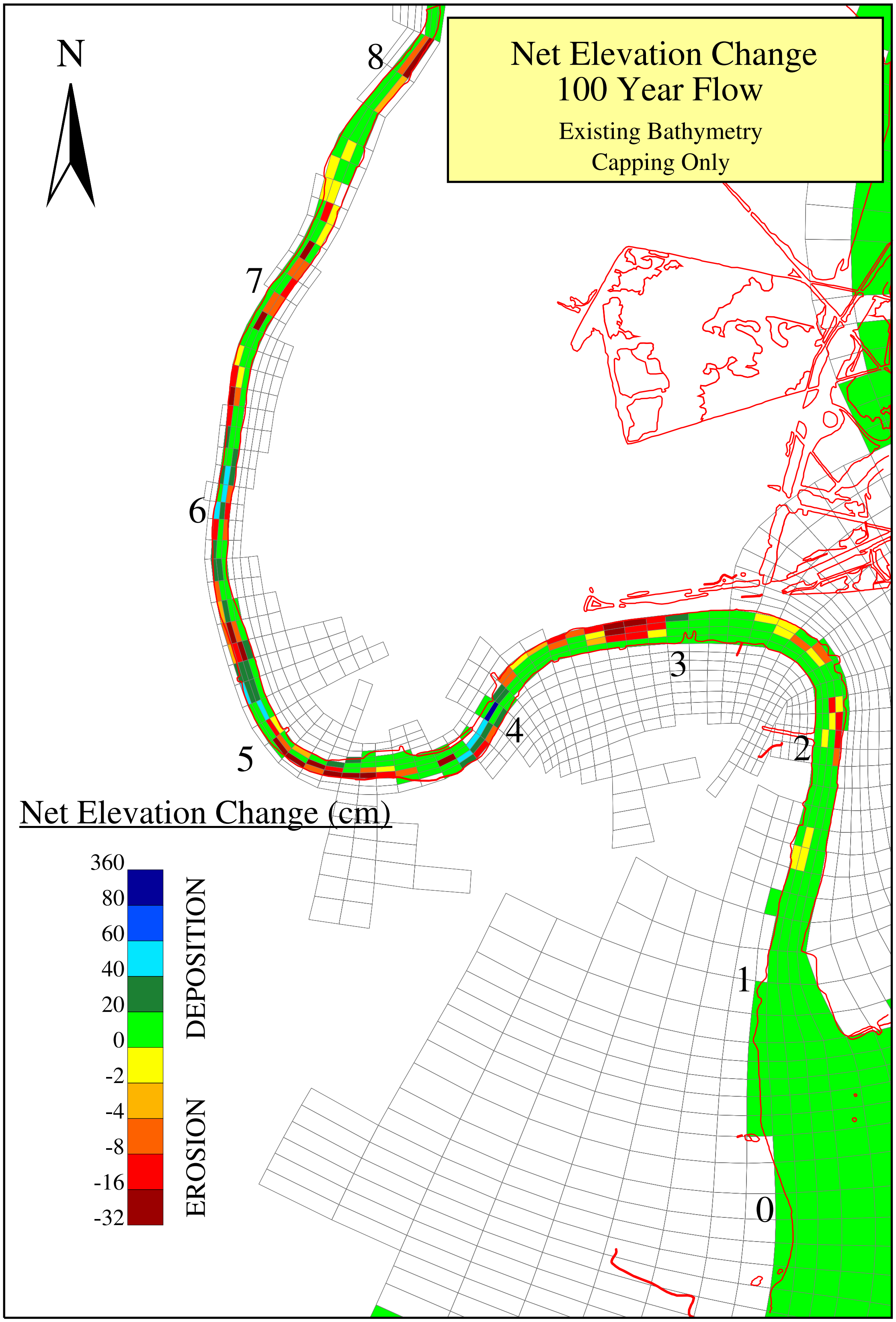

Figure D-1a. Plan view of the net elevation change under 8-Mile Cap-Armor Area Predredging (Capping only) scenario.

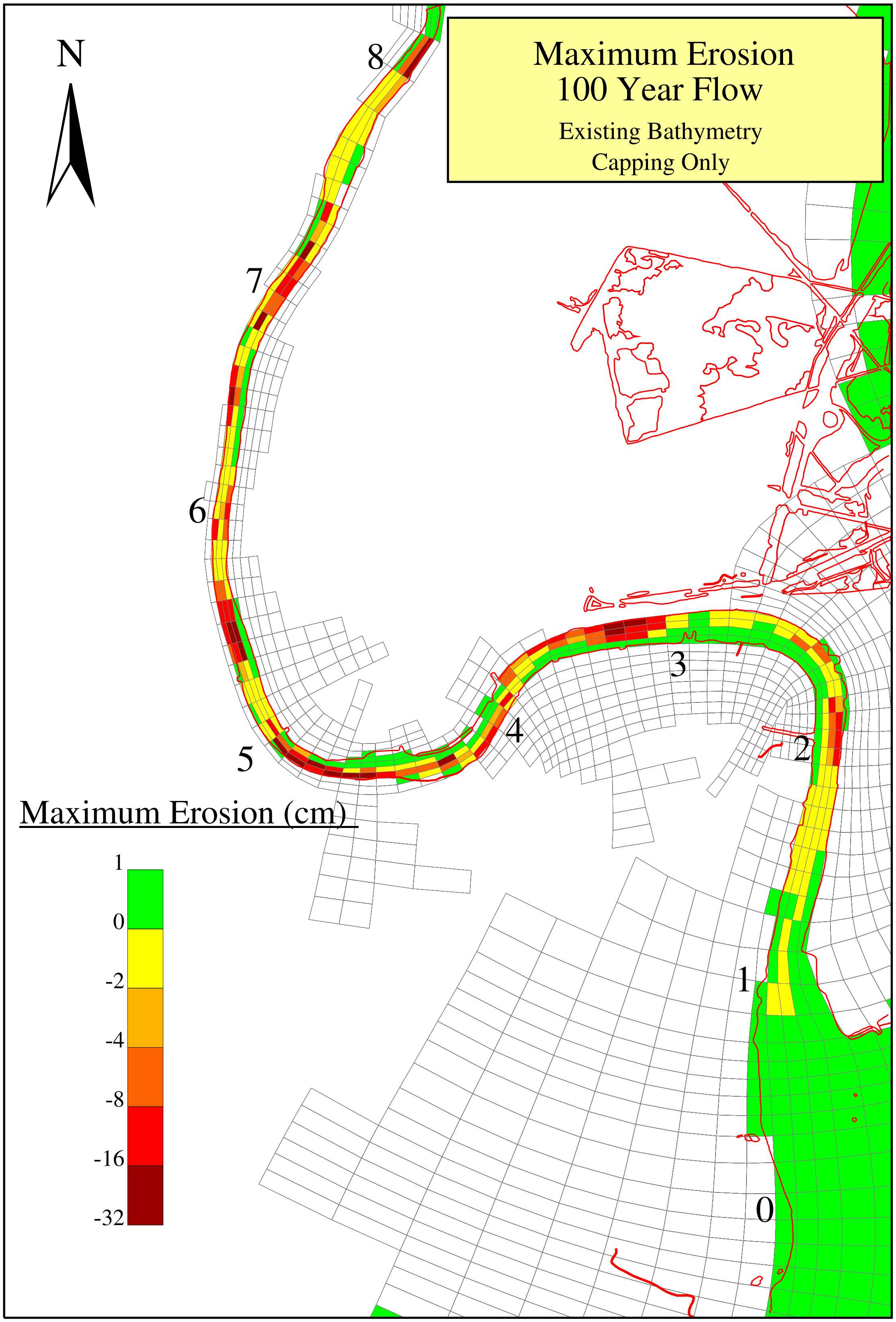

Figure D-1b. Plan view of the maximum erosion under 8-Mile Cap-Armor Area Predredging (Capping only) scenario.

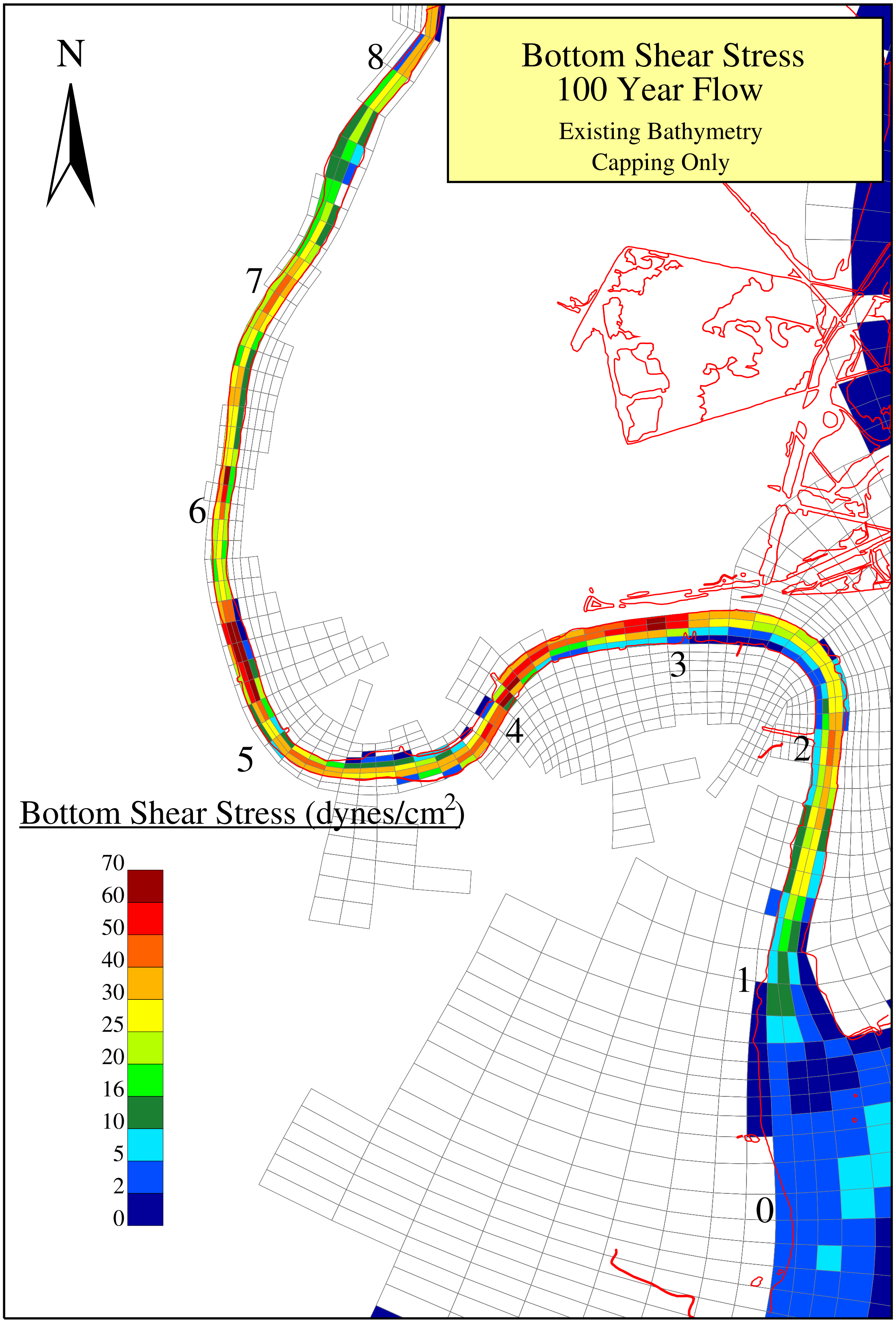

Figure D-1c. Plan view of the bottom shear stress under 8-Mile Cap-Armor Area Predredging (Capping only) scenario.

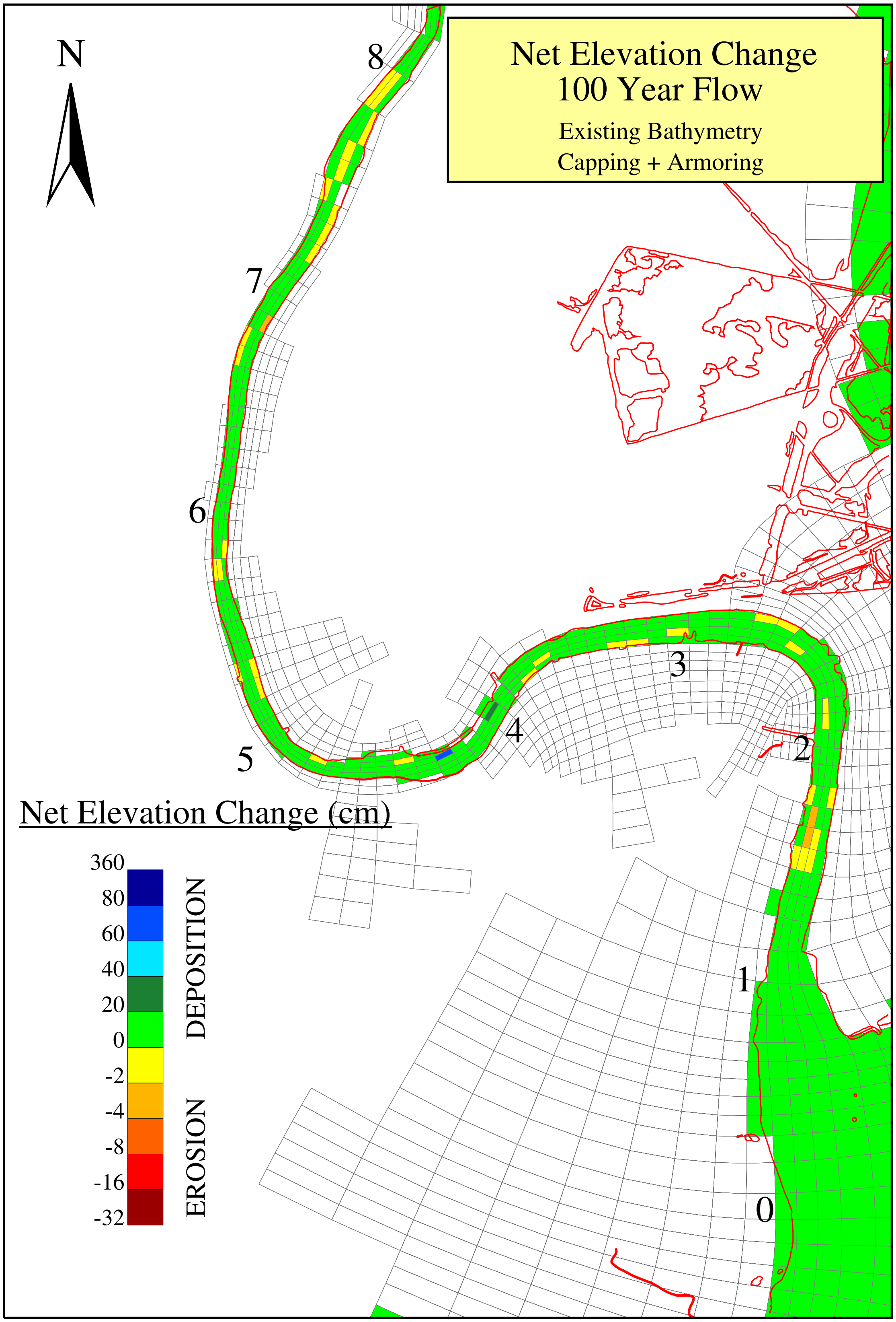

Figure D-2a. Plan view of the net elevation change under 8-Mile Cap-Armor Area Predredging (Capping and Armoring) scenario.

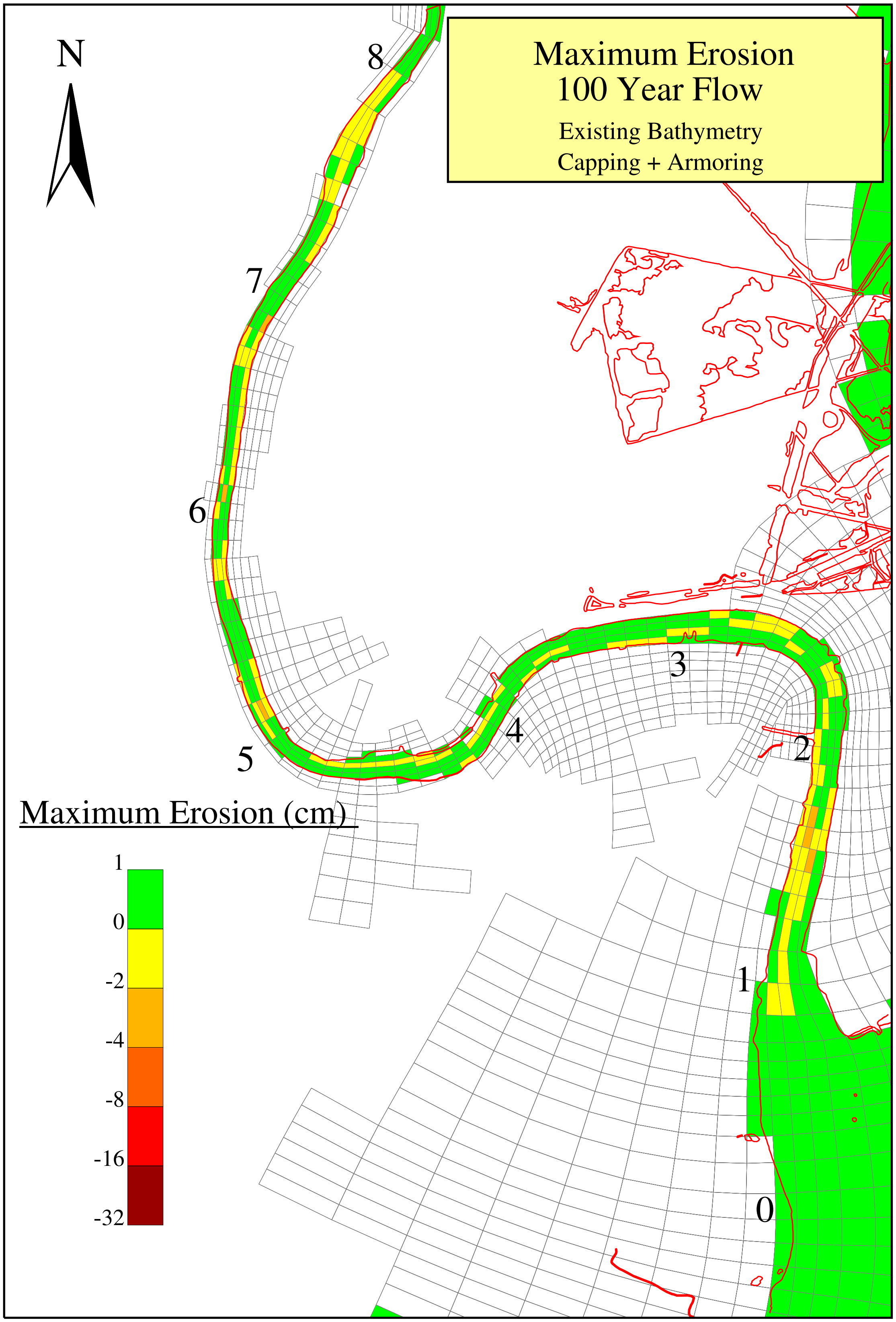

Figure D-2b. Plan view of the maximum erosion under 8-Mile Cap-Armor Area Predredging (Capping and Armoring) scenario.

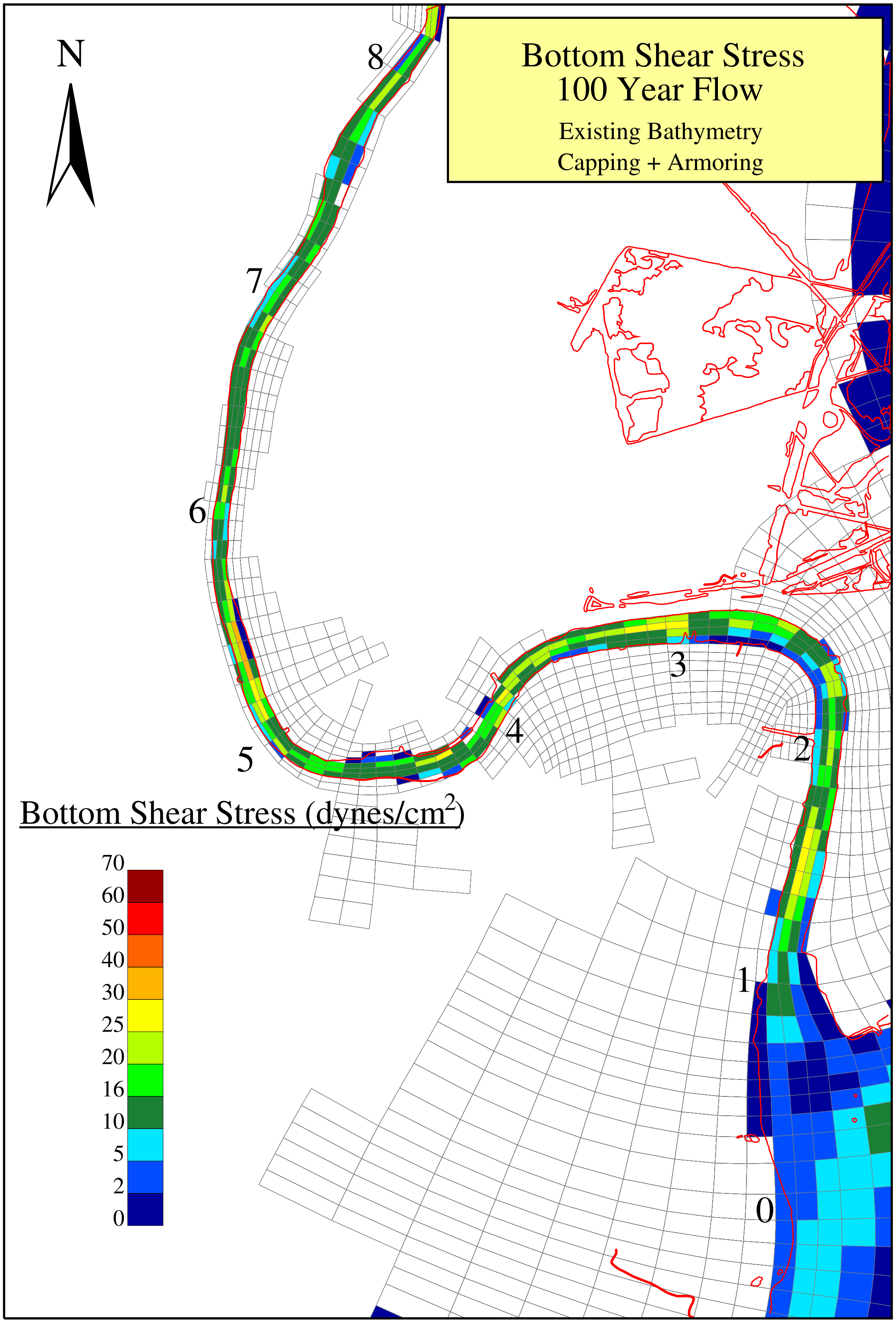

Figure D-2c. Plan view of the bottom shear stress under 8-Mile Cap-Armor Area Predredging (Capping and Armoring) scenario.

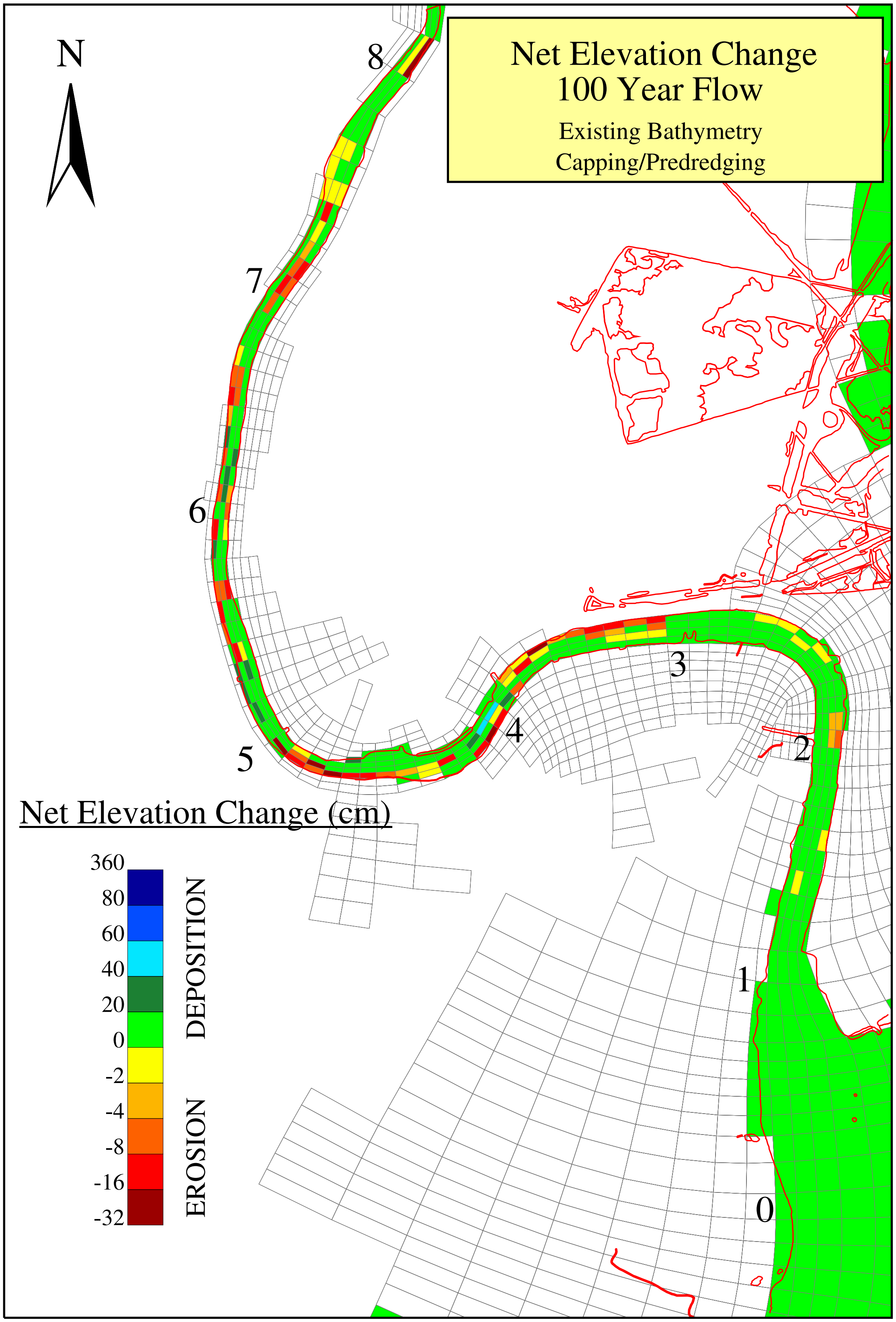

Figure D-3a. Plan view of the net elevation change under 8-Mile Cap-Full Predredging (Capping only) scenario.

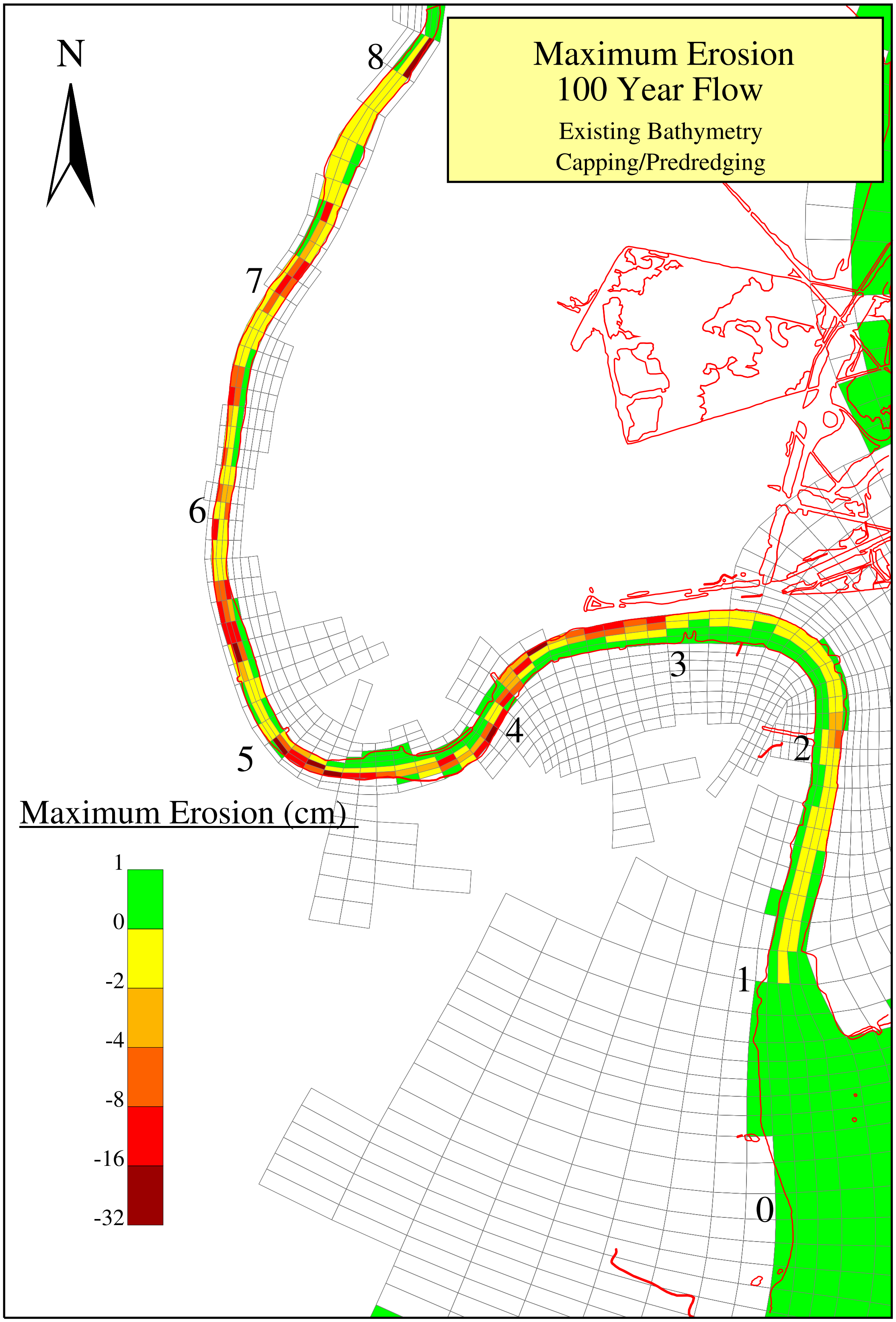

Figure D-3b. Plan view of the maximum erosion under 8-Mile Cap-Full Predredging (Capping only) scenario.

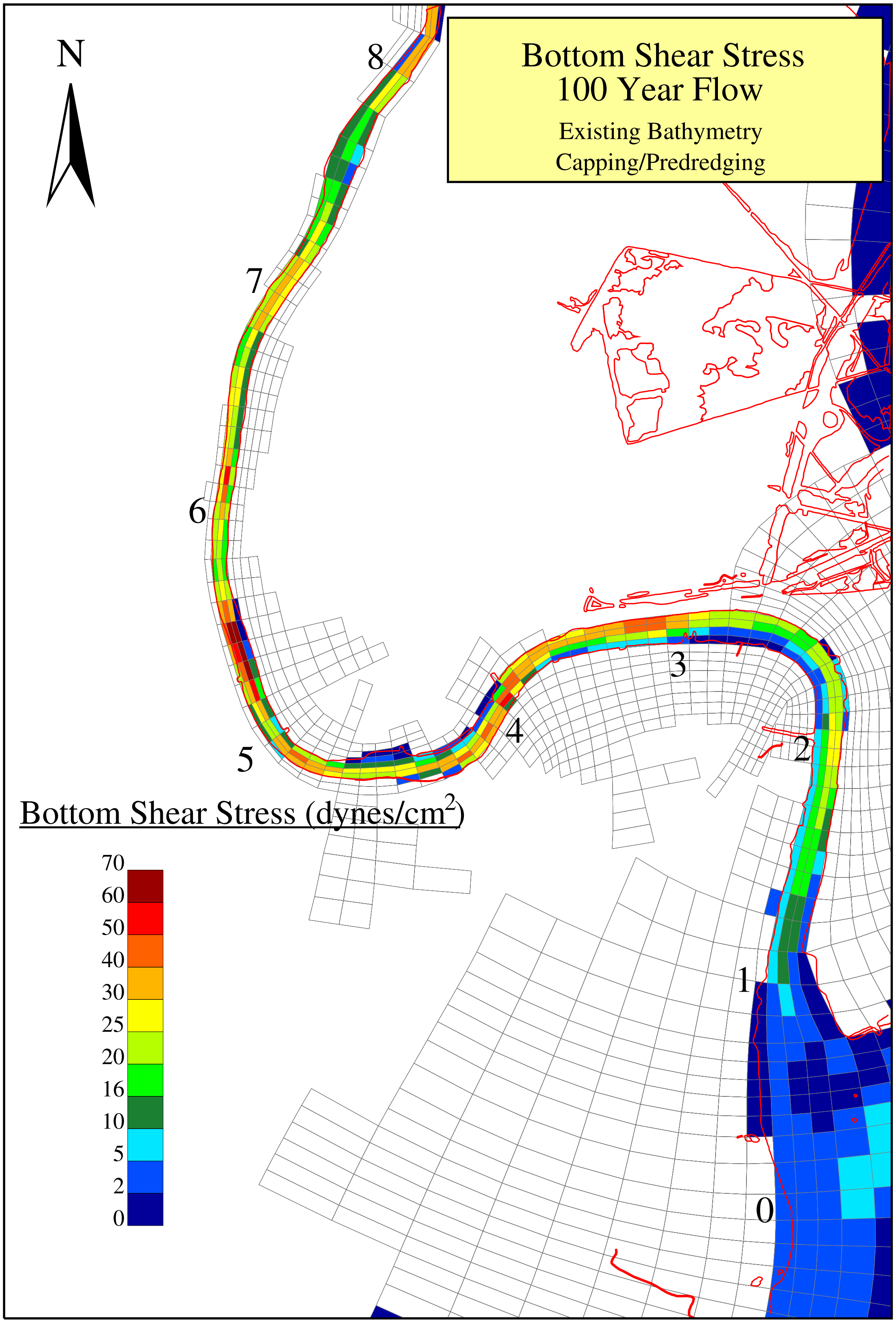

Figure D-3c. Plan view of the bottom shear stress under 8-Mile Cap-Full Predredging (Capping only) scenario.

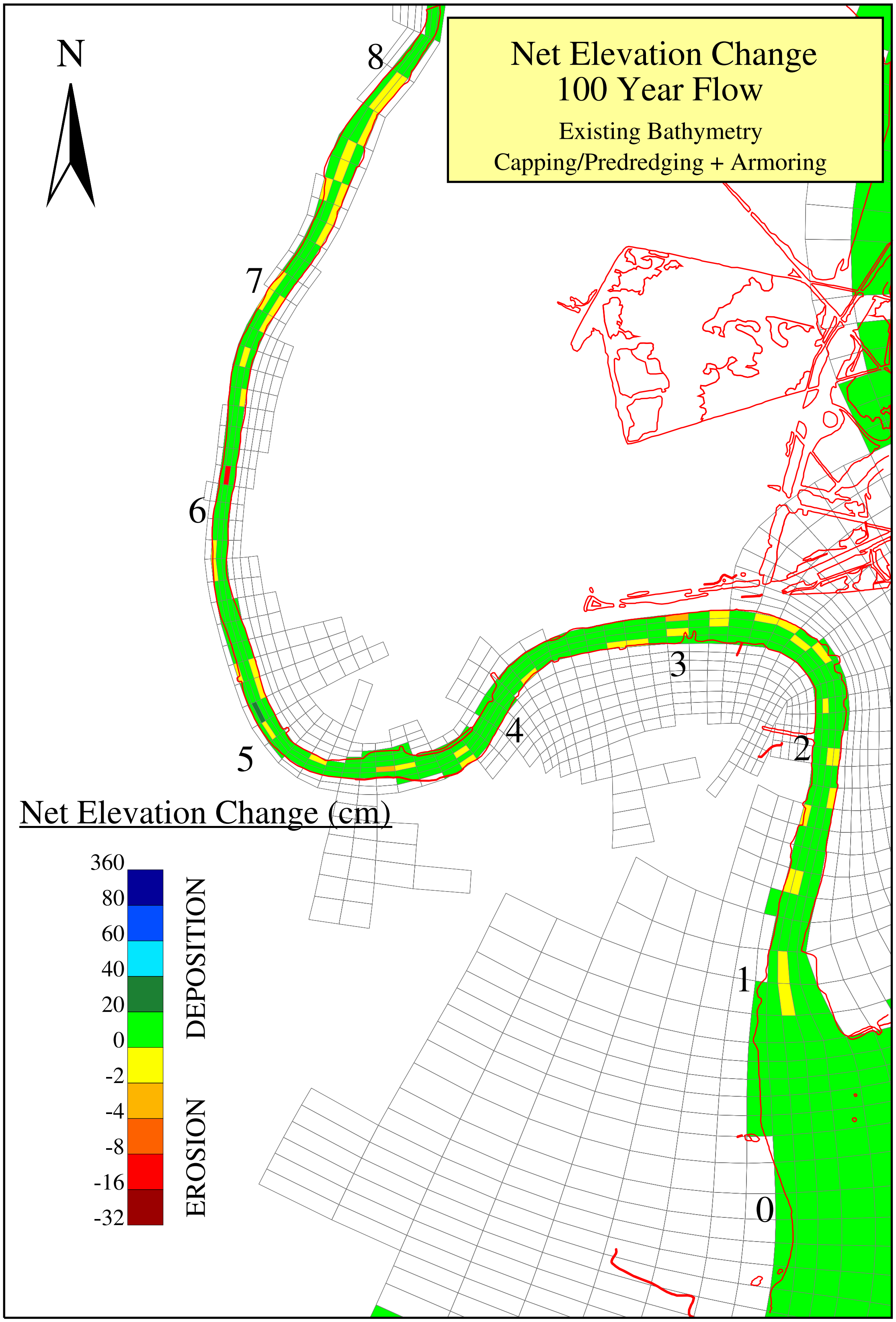

Figure D-4a. Plan view of the net elevation change under 8-Mile Cap-Full Predredging (Capping and Armoring) scenario.

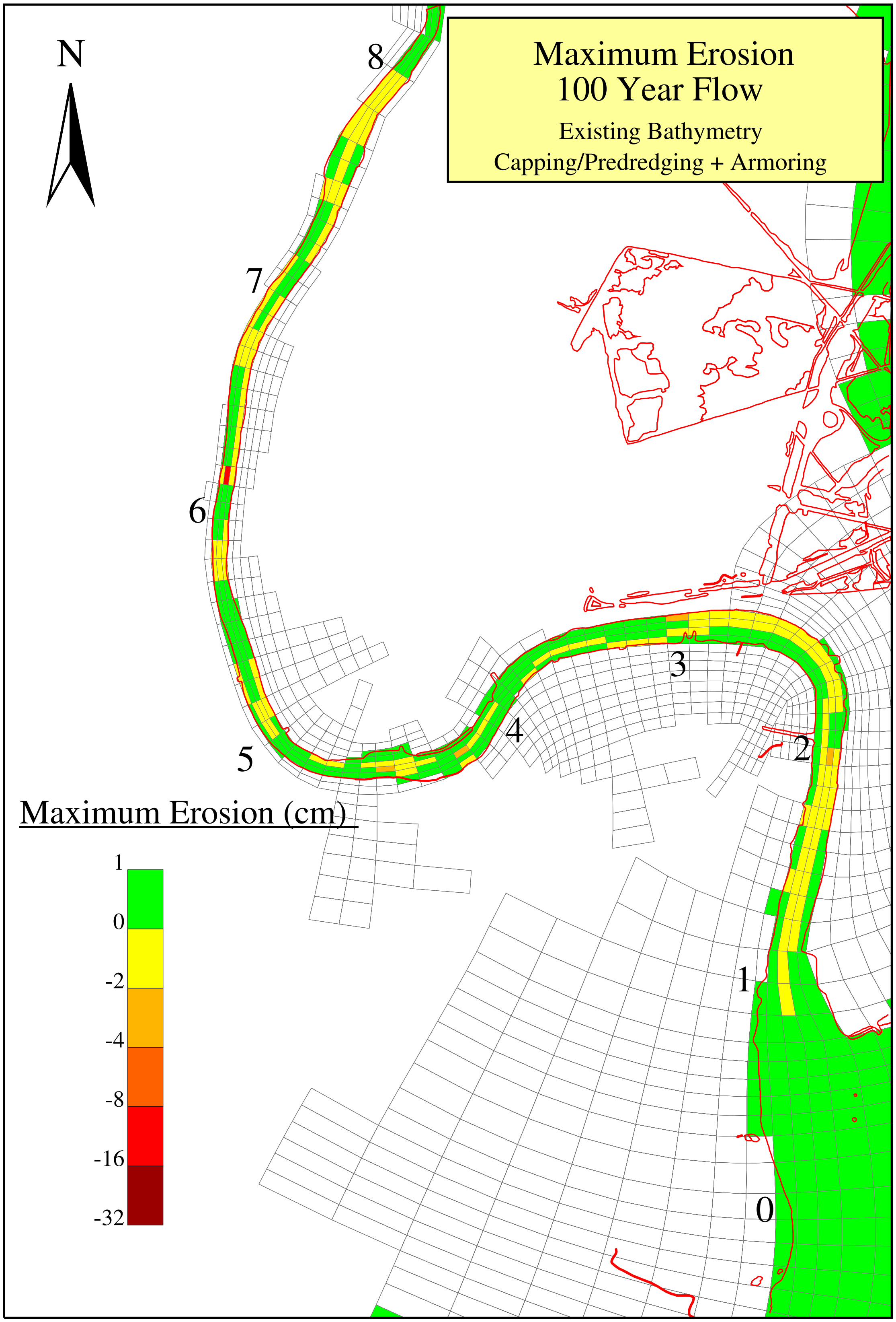

Figure D-4b. Plan view of the maximum erosion under 8-Mile Cap-Full Predredging (Capping and Armoring) scenario.

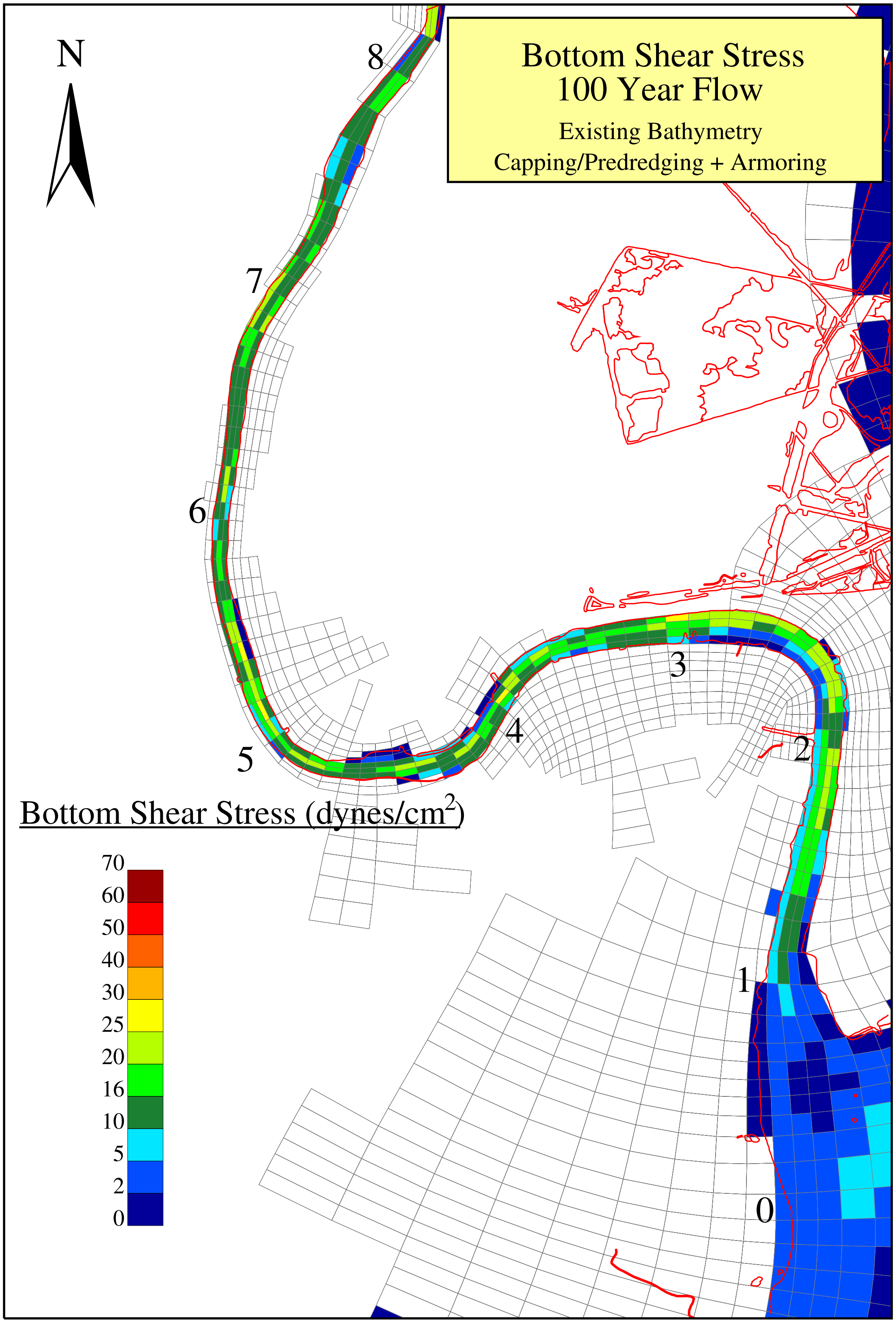

Figure D-4c. Plan view of the bottom shear stress under 8-Mile Cap-Full Predredging (Capping and Armoring) scenario.

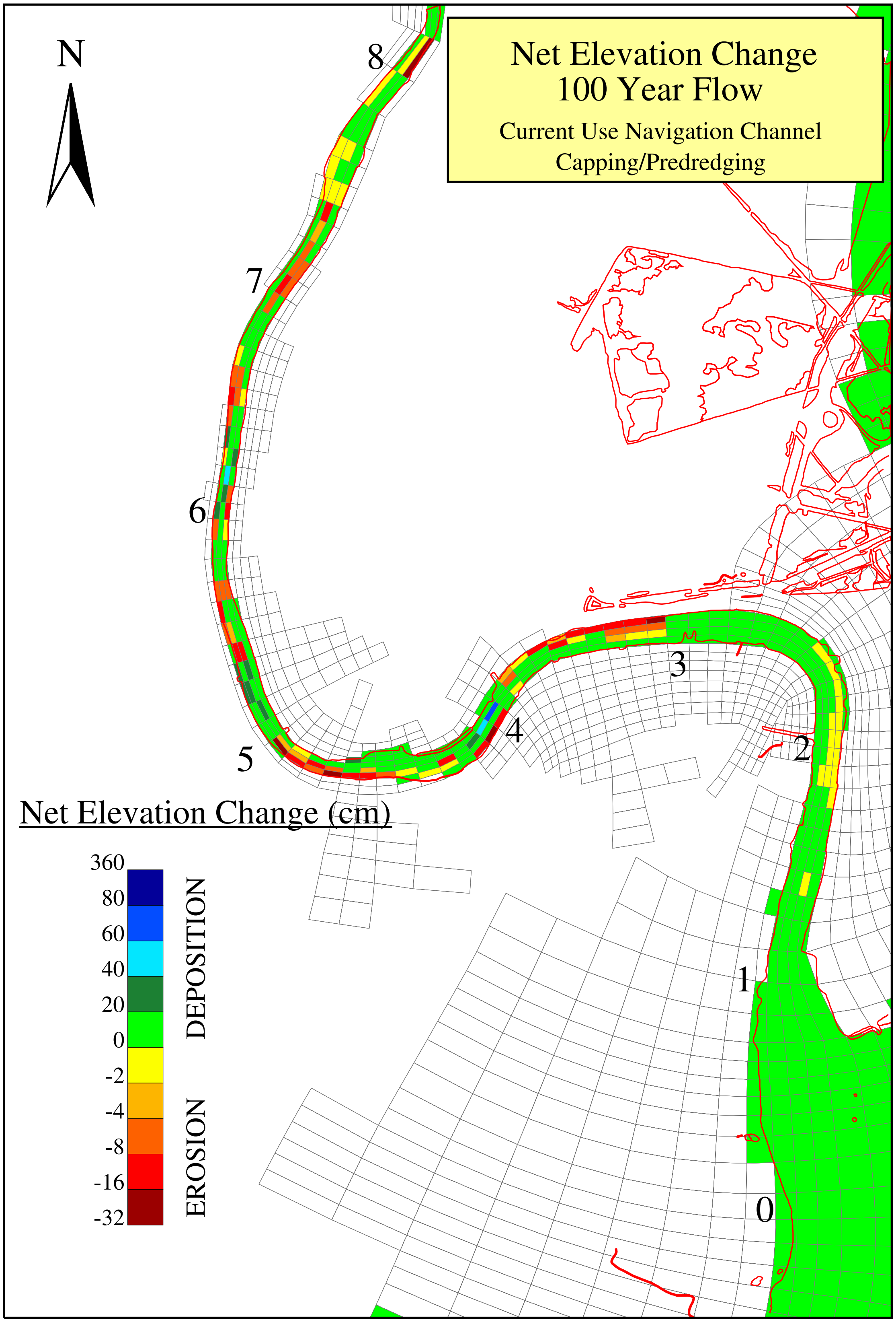

Figure D-5a. Plan view of the net elevation change under Current Navigation Usage-Full Predredging (Capping only) scenario.

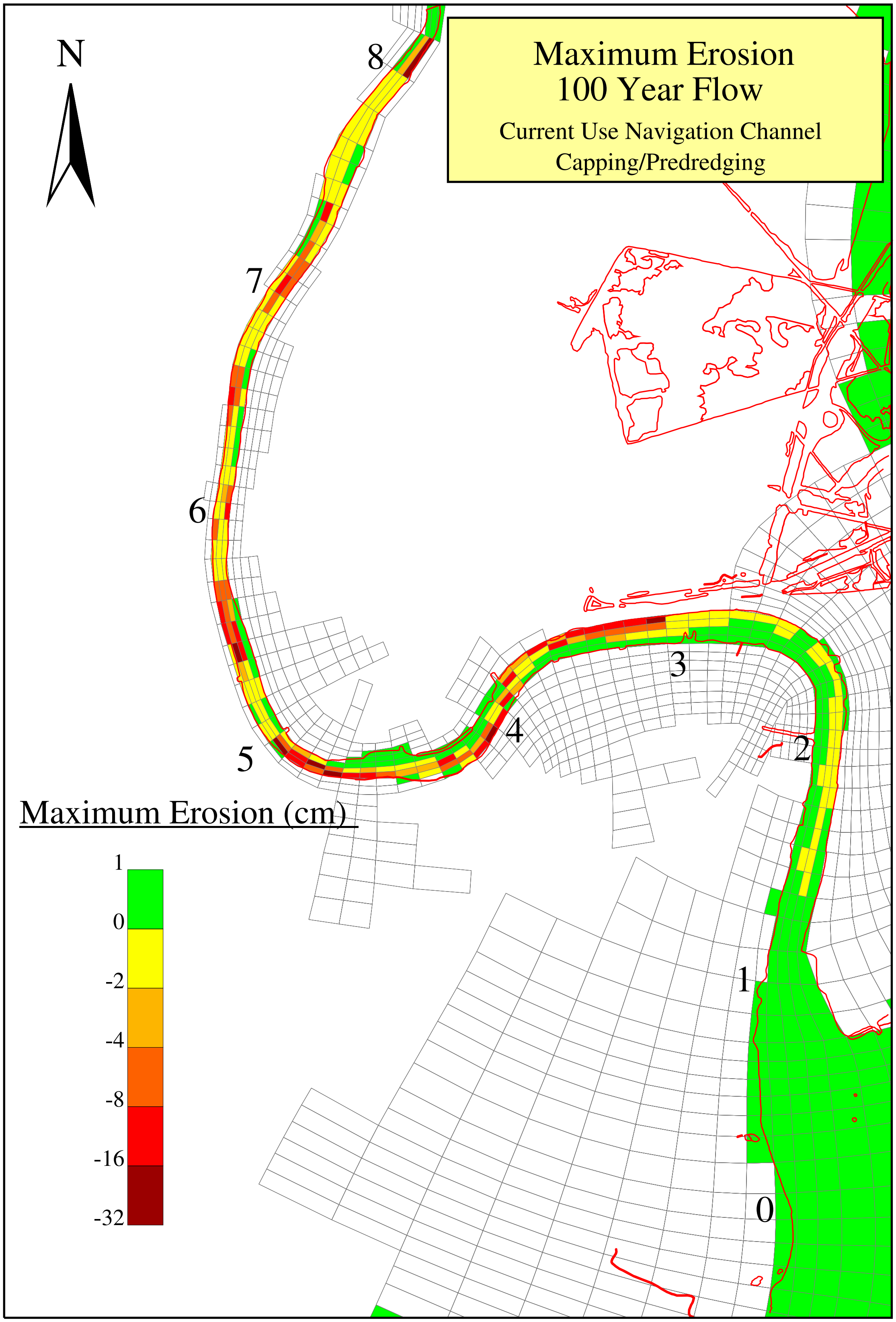

Figure D-5b. Plan view of the maximum erosion under Current Navigation Usage-Full Predredging (Capping only) scenario

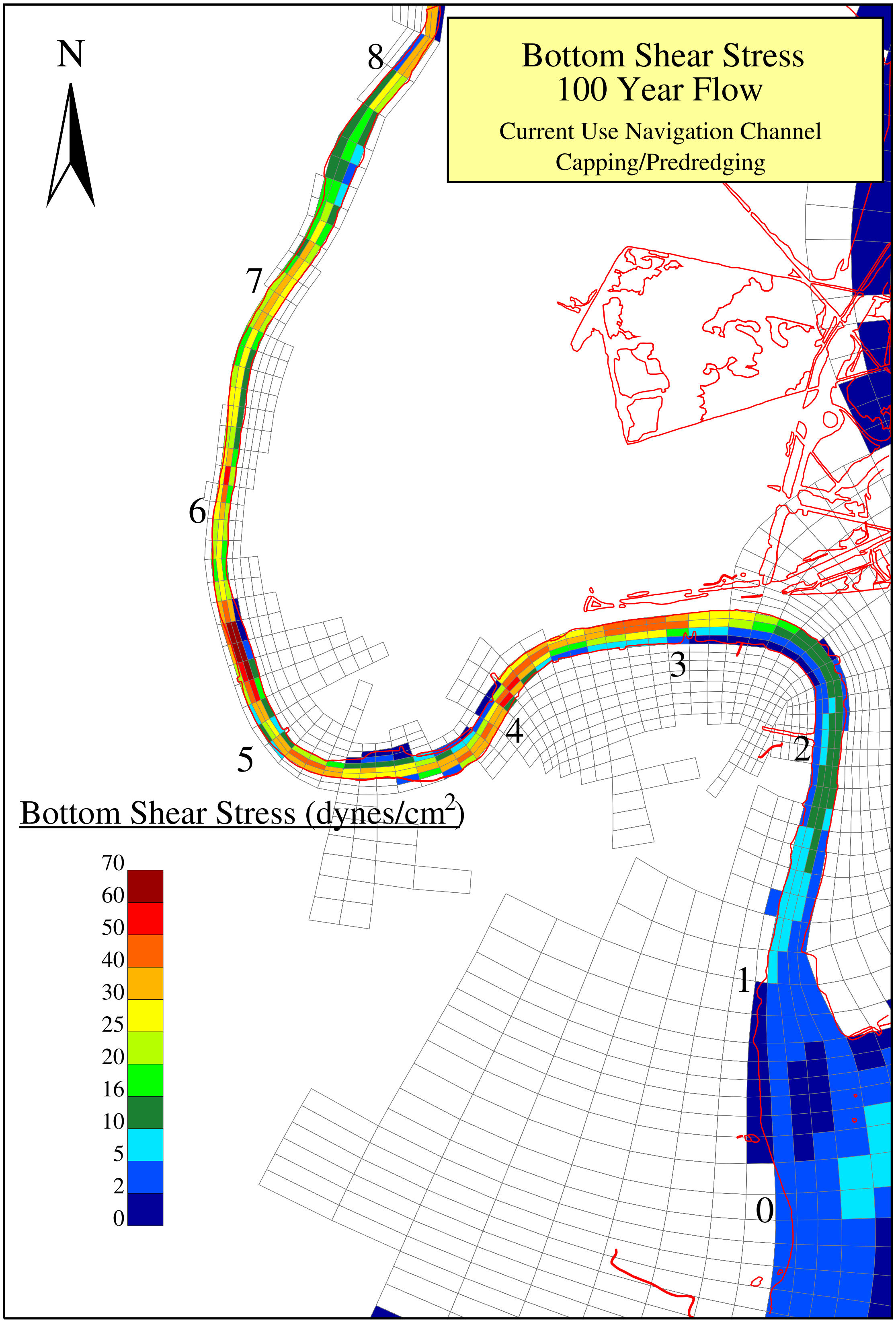

Figure D-5c. Plan view of the bottom shear stress under Current Navigation Usage-Full Predredging (Capping only) scenario

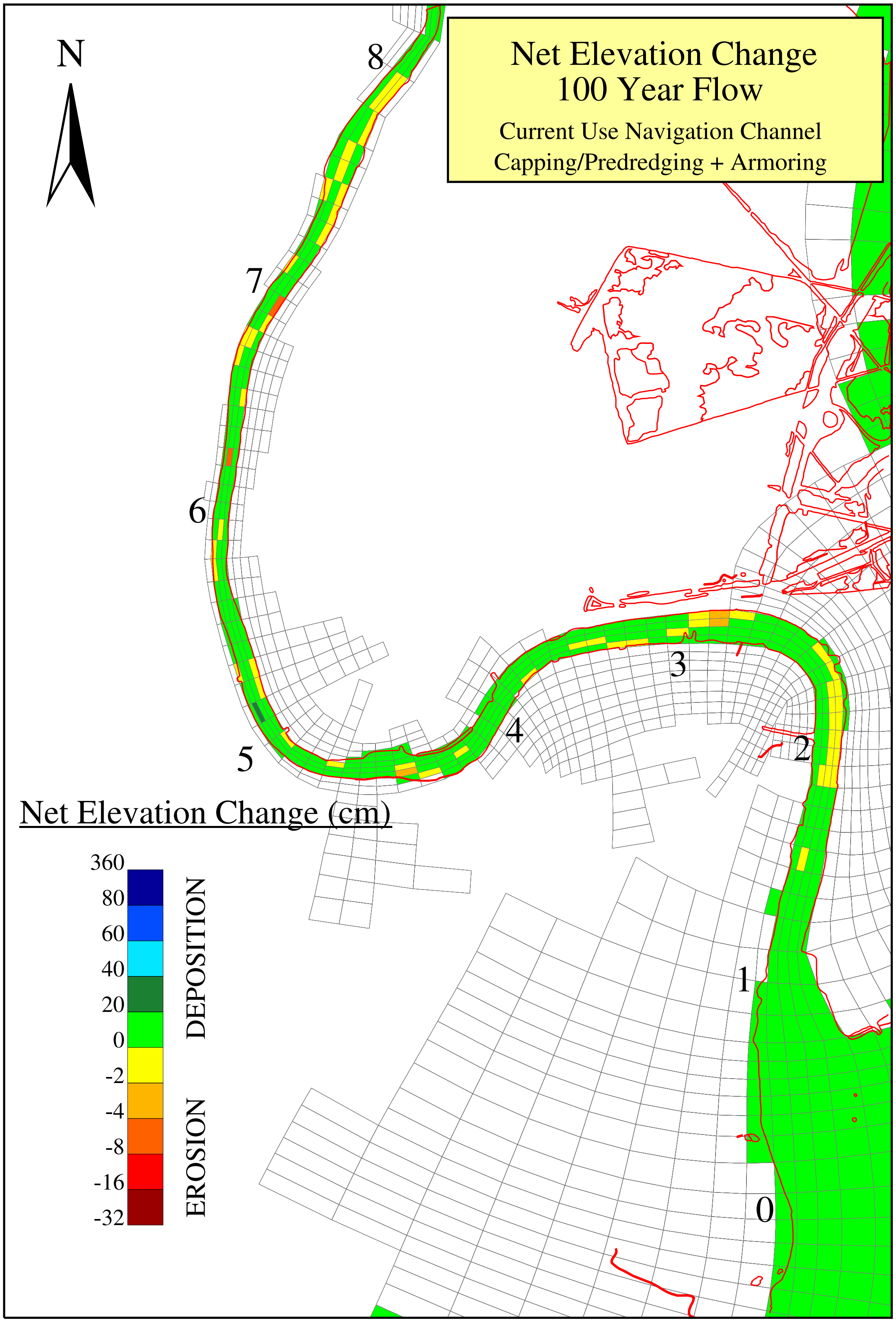

Figure D-6a. Plan view of the net elevation change under Current Navigation Usage-Full Predredging (Capping and Armoring) scenario.

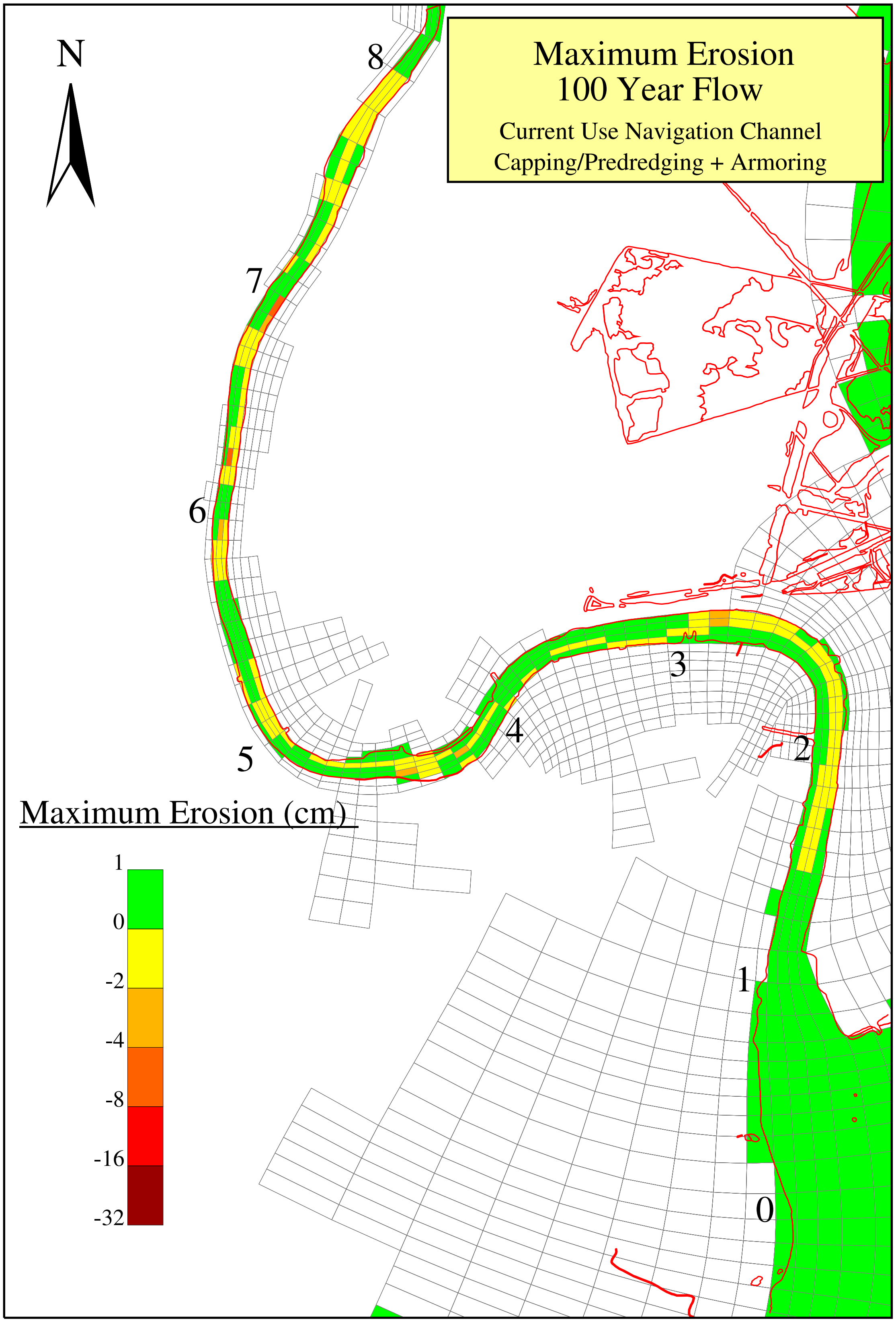

Figure D-6b. Plan view of the maximum erosion under Current Navigation Usage-Full Predredging (Capping and Armoring) scenario.

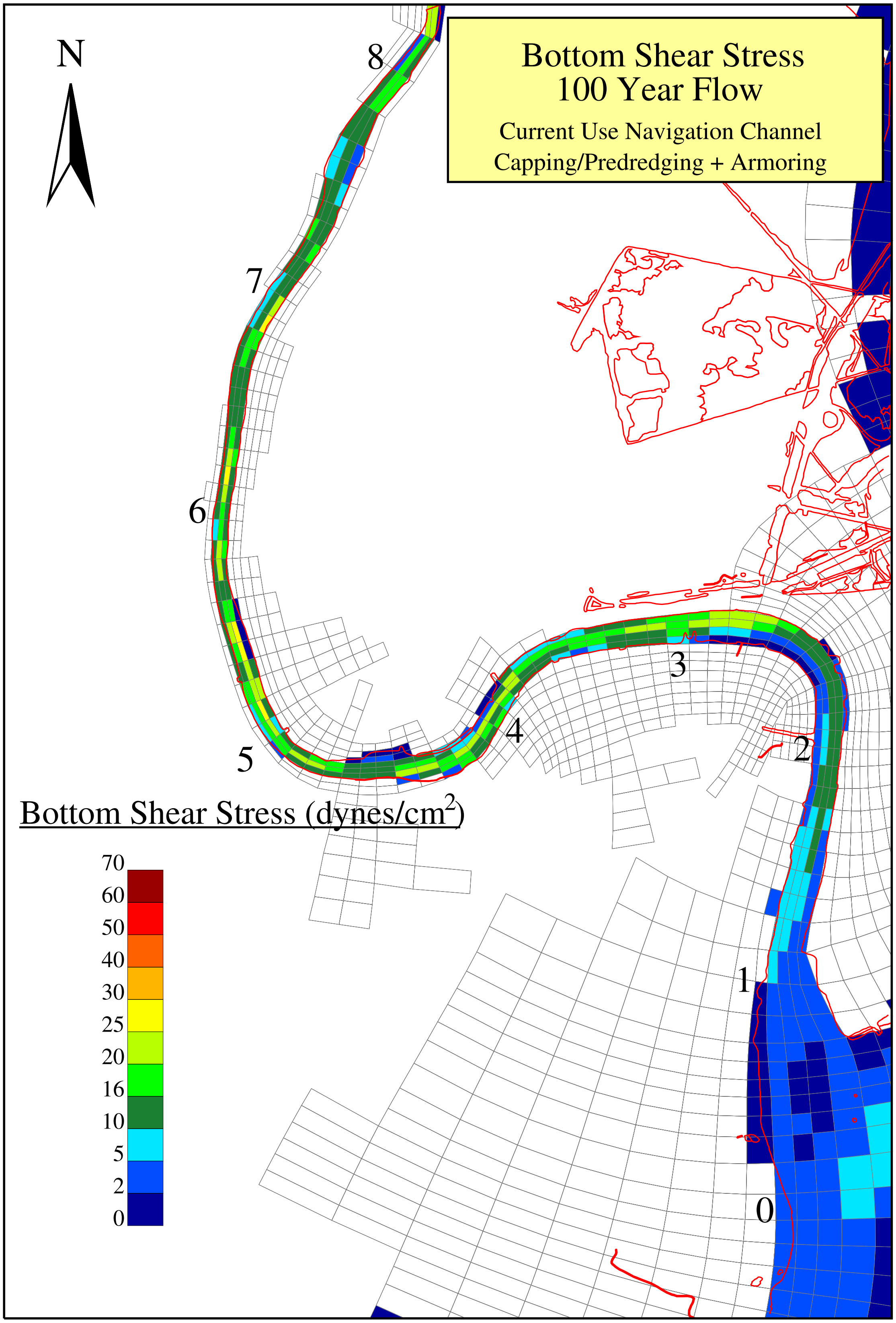

Figure D-6c. Plan view of the bottom shear stress under Current Navigation Usage-Full Predredging (Capping and Armoring) scenario.

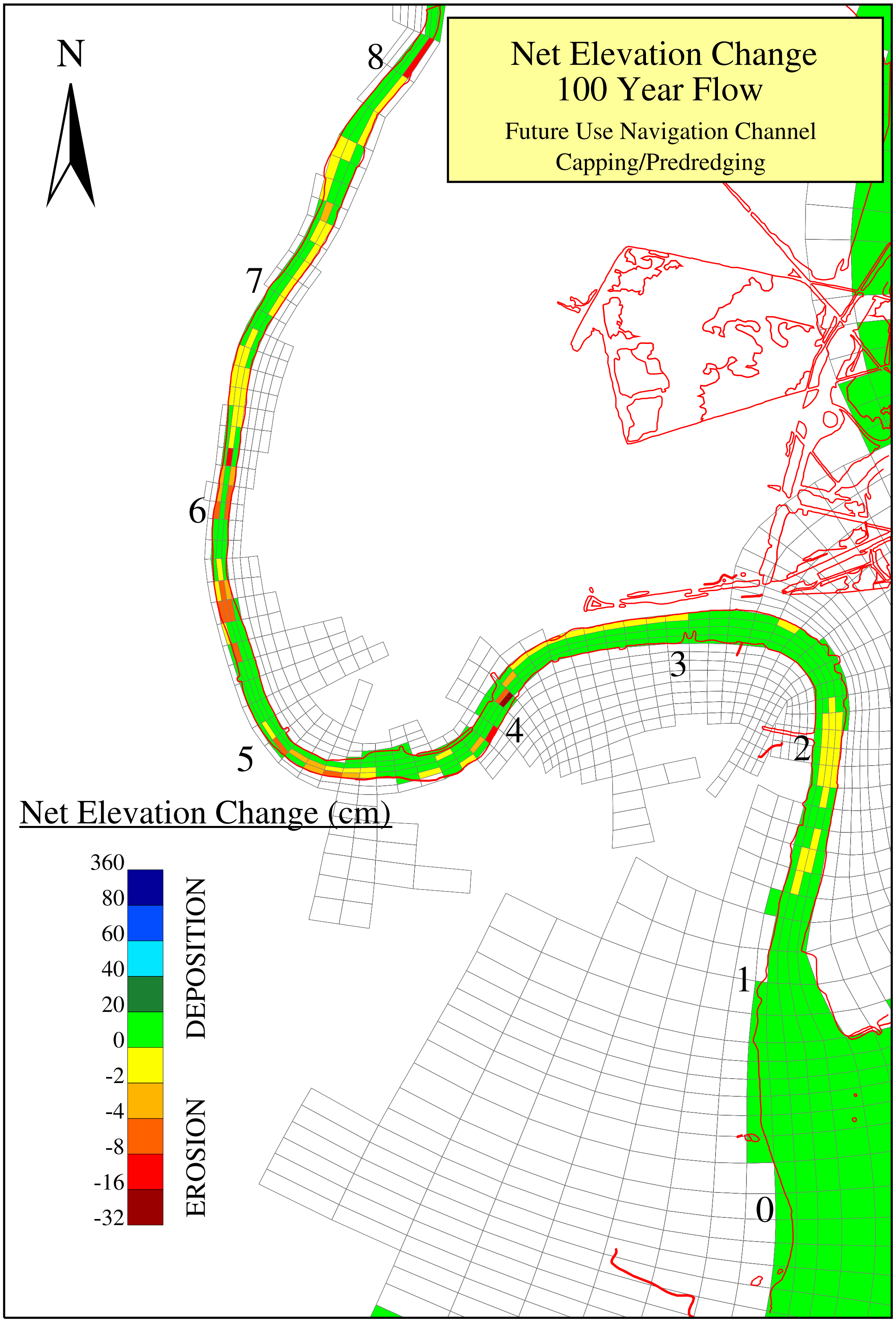

Figure D-7a. Plan view of the net elevation change under Future Navigation Usage-Full Predredging (Capping only) scenario.

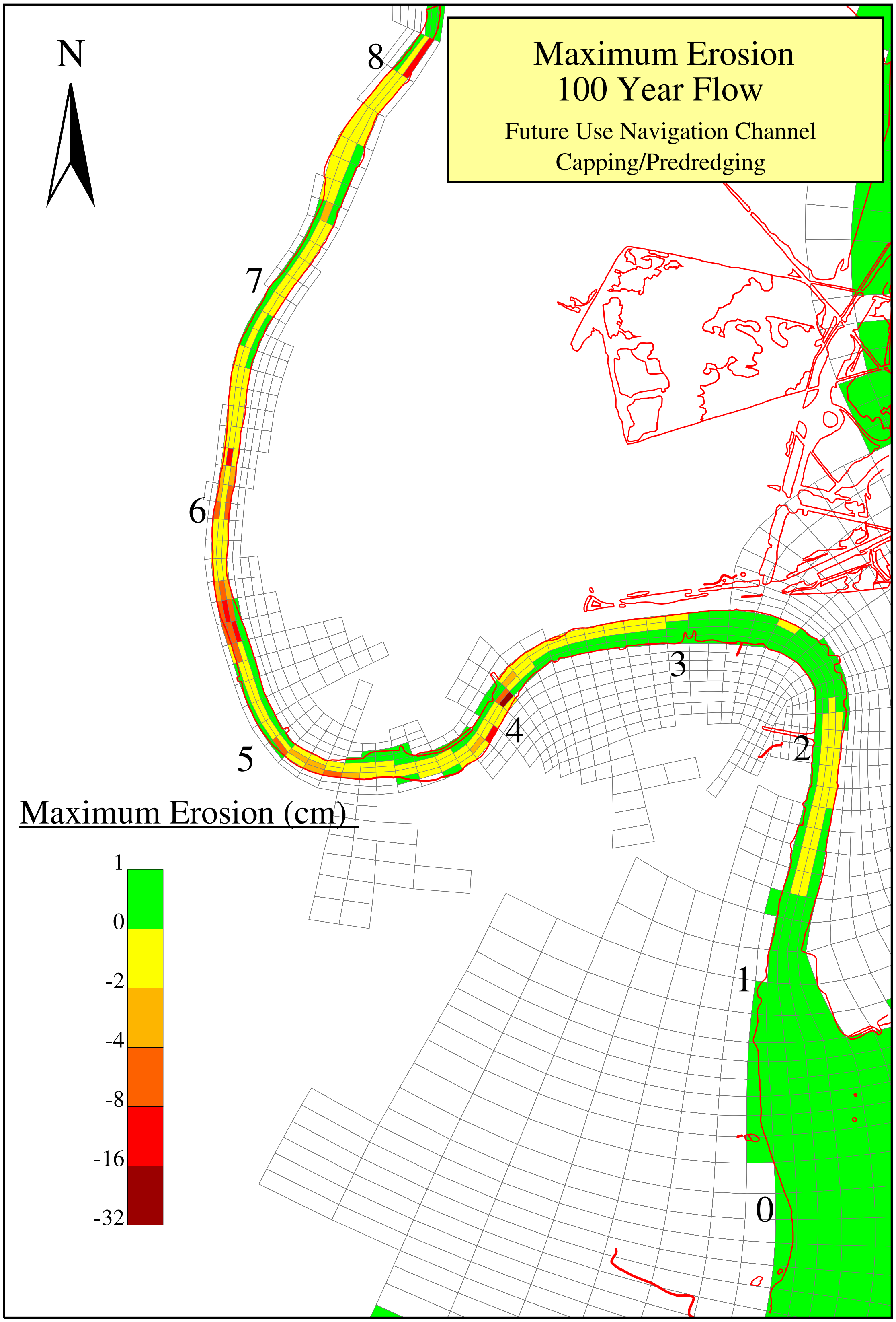

Figure D-7b. Plan view of the maximum erosion under Future Navigation Usage-Full Predredging (Capping only) scenario.

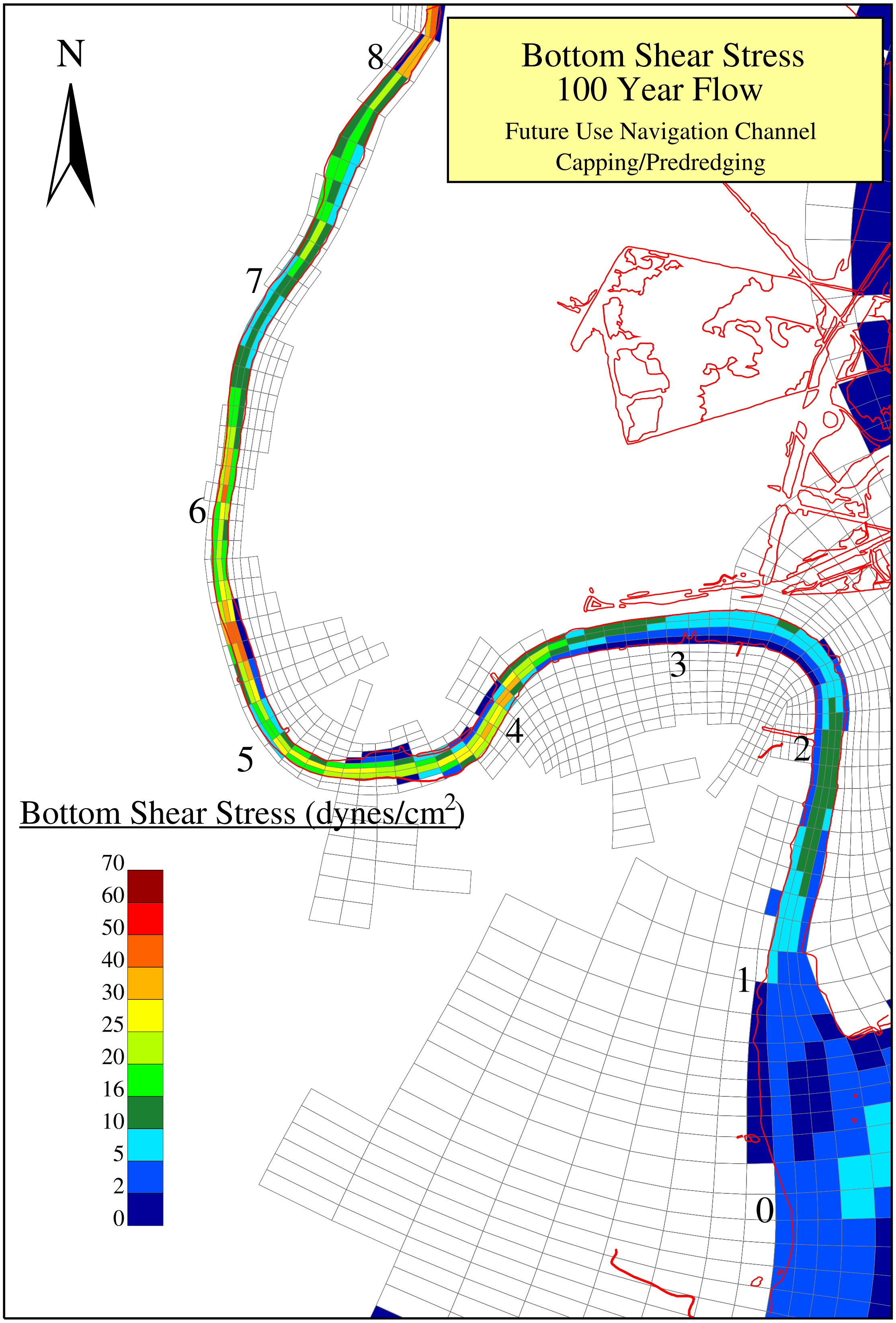

Figure D-7c. Plan view of the bottom shear stress under Future Navigation Usage-Full Predredging (Capping only) scenario

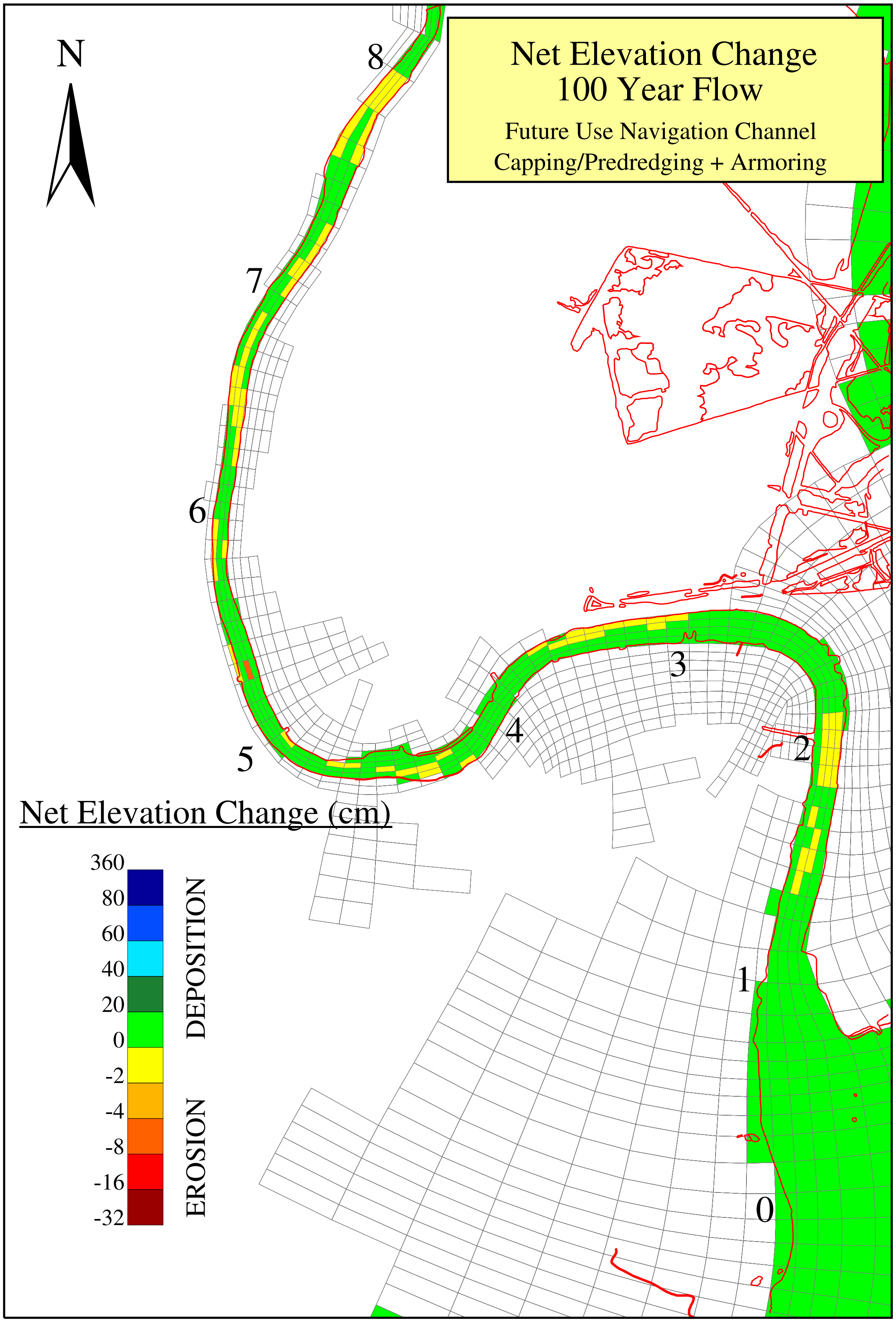

Figure D-8a. Plan view of the net elevation change under Future Navigation Usage-Full Predredging (Capping and Armoring) scenario.

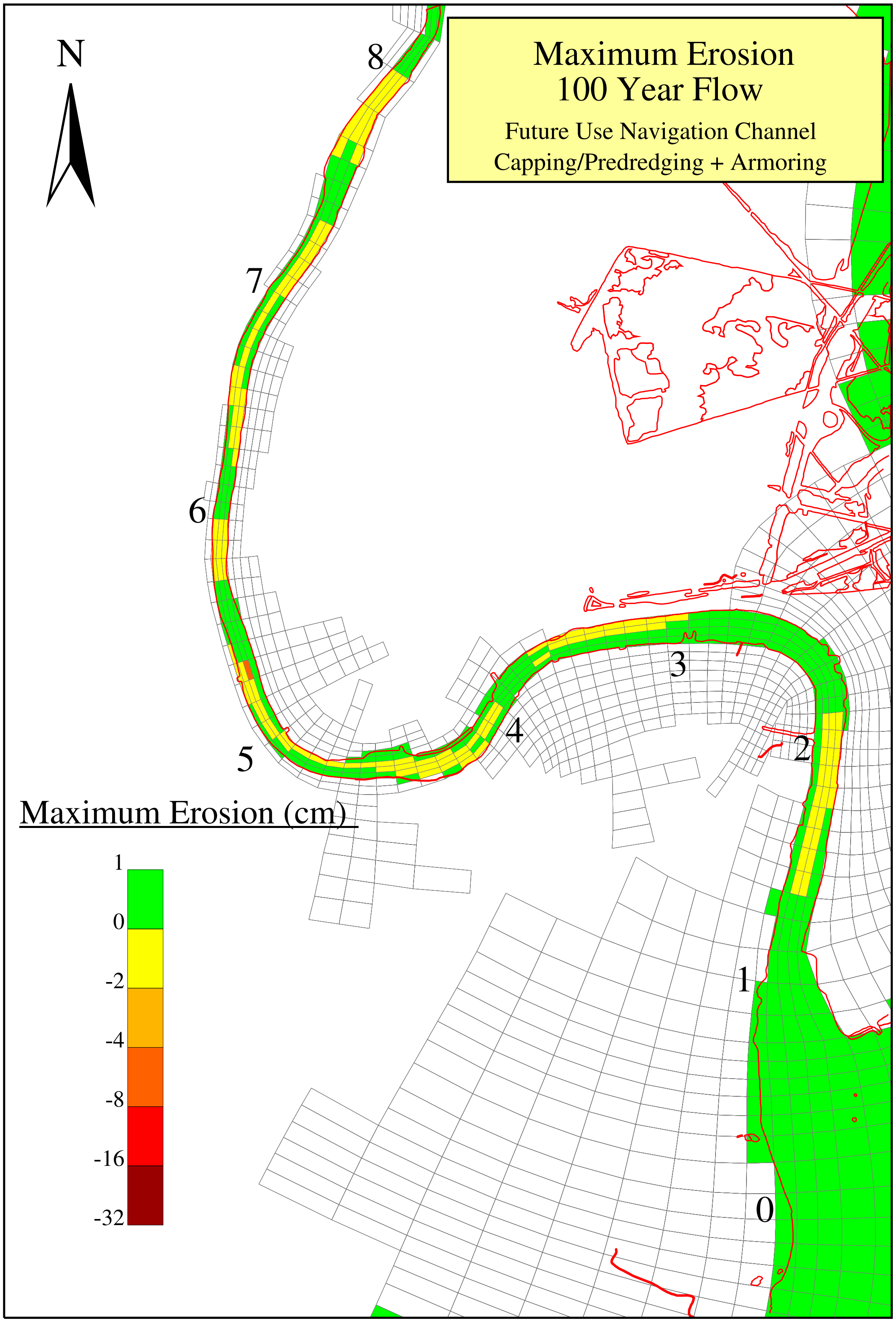

Figure D-8b. Plan view of the maximum erosion under Future Navigation Usage-Full Predredging (Capping and Armoring) scenario.

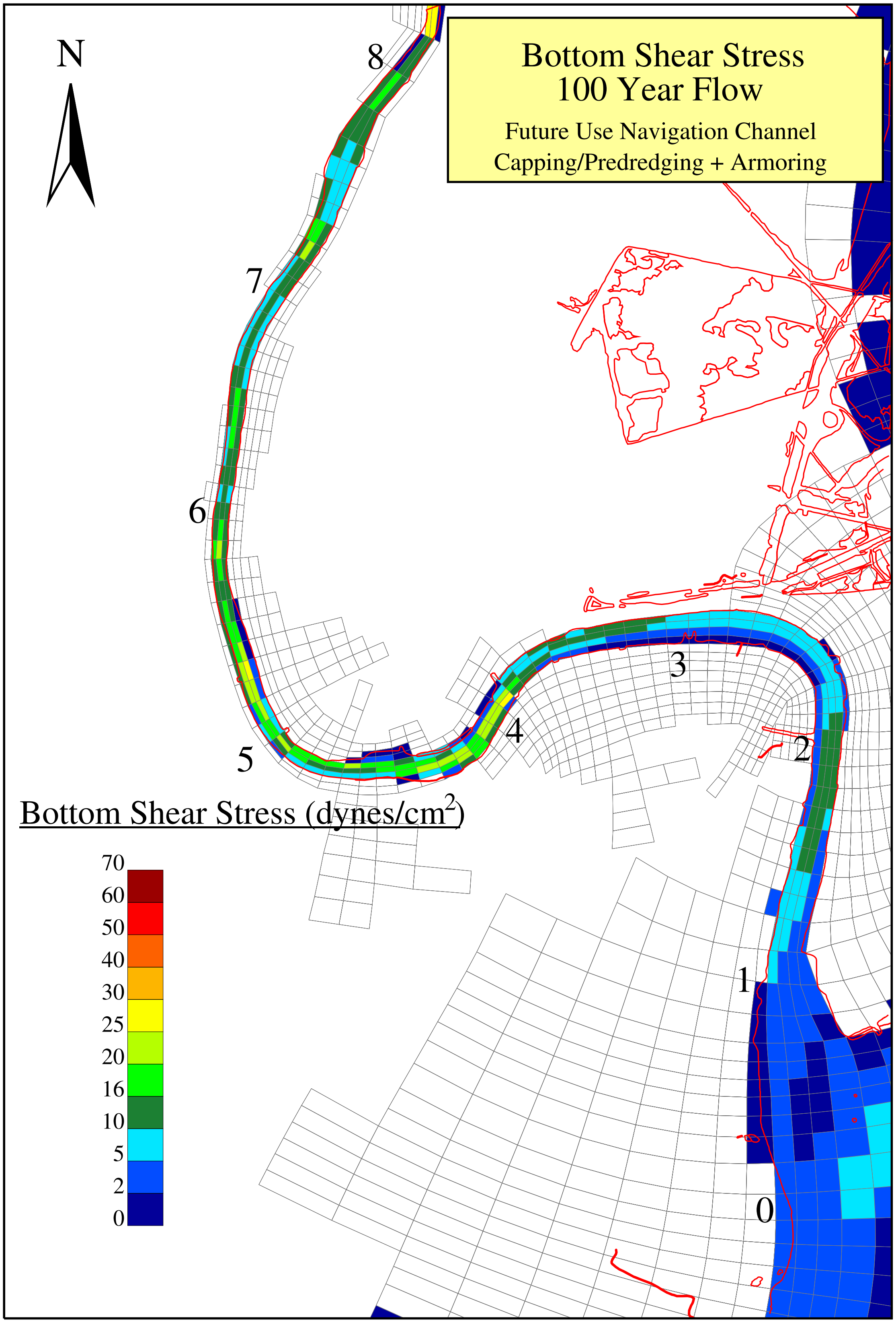

Figure D-8c. Plan view of the bottom shear stress under FutureNavigation Usage-Full Predredging (Capping and Armoring) scenario.